Integrative Chemistry based morphosyntheses of hierarchical composite materials for photovoltaic, photocatalysis and photoluminescence applications

by

Natacha Monique Frédérique Kinadjian

A thesis

presented to the University of Waterloo

in fulfillment of the

thesis requirement for the degree of

Doctor of Philosophy

in

Chemical Engineering

Waterloo, Ontario, Canada, 2014

Abstract

The main objective of this PhD project is to synthetize functional materials bearing hierarchical architectures and specific properties from the nanoscale to the macroscale. For this purpose, we use a transversal and cross-disciplinary method called Integrative Chemistry, which combines chemistry, physical chemistry of complex fluids, and biomimetic processes. This method allows us to control the shape and the structure of the materials at all scales and so to obtain tailor-made hybrid inorganic-organic complex architectures. In consequence, it is possible to design the materials as a function of the structure and properties required. In this project, we decided to investigate how photovoltaic, photocatalytic and photoluminescence properties can be modified/upgraded by a fine control of material hierarchical structure.

The first project included the synthesis of macroscopic fibers of zinc oxide (ZnO) nanorods. We studied how the photoluminescence properties (in absorption and emission) could be tuned as a function of the alignment of the nanorods inside the fibers.

In a second project, TiO_2 macroscopic fibers bearing a hierarchical porosity were synthesized by integrating a multi-scale approach. These fibers have been tested for their photocatalytic performances. Several compositions of solutions were preliminary tested in order to optimize the photocatalytic properties, overall, and the influence of different structural parameters was illustrated. From these results, the structural parameters were tuned (surface roughness, porosity, diameter) and it was possible to synthesize TiO_2 macroscopic fibers using a continuous spinning process. These fibers present photocatalytic performance which are similar or even higher than those of the commercial product.

Finally, we were interested in Dye-Sensitized Solar Cells (DSSCs). The major drawback of these cells is their short lifetime due to the leakage of the liquid electrolyte. Unlike most of the research conducted on this topic, we decided to explore the possibility to design and assemble a full solid state DSSC. As a result, my personal work was dedicated to investigate the Polypyrrole which can be used as electrolyte and/or as electrode in these cells. Swollen Liquid Crystals (SLCs) were used as a nanoreactor for the chemical polymerization of pyrrole with the aim to obtain *in fine* aqueous suspensions of PPy nanosheets that could shaped as thin films. Films obtained with these solutions on glass substrates are expected to be smooth.

Acknowledgments

I would like to thank all the people who contributed to the realization of this PhD project. This PhD project took place between three laboratories in three different countries: the Centre de Recherche Paul Pascal (CRPP) in Bordeaux (France), the University of Waterloo (Canada), and the Laboratoire de Chimie Inorganique Structurale/Groupe de Recherche en Energie par les Matériaux (LCIS-GreenMat) in Liège (Belgium). I would like to thank the directors of these laboratories - Philippe Richetti (CRPP), Eric Prouzet (Waterloo), and Rudi Cloots (LCIS-GreenMat) – for letting me experimenting in their building. More especially, I thank Philippe Richetti for accepting the role of president for my PhD defense jury.

I would like to express all my gratitude to all the people who accepted to be part of my PhD defense jury: Mr. Patrick Davidson and Mr. Cédric Boissière, "les rapporteurs" for their time and their comments, Mr. Pavle Radovanovic, Mr. Yuning Li, and Mrs. Aiping Yu, for accepting to judge this work.

The work described in this manuscript is the result of three years and a half of research that have been conducted in an international context, this project being part of the IDS-FunMat program. Besides the three laboratories involved in this project, some collaboration with other laboratories and other teams in CRPP have been created in order to conduct this project in a successful manner. I would like to thank all the people who helped me in these laboratories and outside, the researchers, the engineers, the technicians, the students (PhD, Master, etc), and the people in the administrations. I will always be grateful for your support, your encouragement and your sympathy, without you, I could not have written this manuscript.

I thank my supervisors who help me during this adventure who allowed me to work on a very interesting topic both in a scientific and a personal point of view: Rénal Backov, Catherine Henrist and Eric Prouzet. I measure the privilege that you offer me to work on so many scientific aspects all along my PhD project, and moreover, to do so in an international context, which allowed me to observe the difference in the academic system between those countries. Rénal, I do not know how to thank you for your admirable management both in a scientific and a human point of view. Your support during the past three years during difficult moments, your unwavering optimism, your advice, and your honesty (both compliments and criticism), allowed me to give the best of myself until the defense. Catherine, thank you for joining this adventure and for your advice. I will not forget your precious help when I was in Liège and on the review of the manuscript, without which some mistakes could have remained … Eric, thank you for presenting me the program in a first place and for letting me experimenting in your lab.

I would like to thank warmly all the members of the IDS-FunMat governing board and affiliated –Laurent Servant, Marianne Delmas, Audrey Sidobre, Jean Etourneau, Stéphane Carlotti, Thierry Tassaing, Bernhard Zeimetz- for their help and their patience. I know that all the administrative problems inherent to international programs were not easy to solve, and I am grateful of your implication in these problems and of solving them. I thank more especially Laurent Servant who took some time to discuss with me during difficult moments.

As this PhD project "did not fit in the box" for most of the administration matters, I would like to thank all the people who contributed to the smooth progress of this project in Waterloo: Sue Horton, Susanna Fiorelli and Judy Caron. I also thank Elysabeth Hortholland at CRPP as well as Martine Lovato and Catherine Dassis in Liège.

My PhD project led me to collaborate with other laboratories outside of the three main ones. In this context I would like to thank Corinne Chanéac, Olivier Durupthy and Fabien Dufour (LCMCP) for the TiO_2 nanorods synthesis. I thank Mickael Le Bechec and Sylvie Lacombe (IPREM) for the TiO_2 fibers photocatalysis characterization. I also would like to thank Beatriz Juliàn-Lopez (Universitad Jaume I) for her help in the characterization of the ZnO fibers for photoluminescence application and for helping me analyzing the results.

I thank Elisabeth Sellier and Michel Martineau (CREMEM) for TEM and SEM experiments, Odile Babot (ISM) for BET analyses and Eric Lebraud (ICMCB) for XRD experiments.

I thank the team NICE (MaFIC), Céline Leroy (DSSCs), Isabelle Ly (freeze-fracture-TEM), Marie-France Achard (SAXS), Alain Derré (ATG), Maryse Maugey, Serge Ravaine and Hanbin Zheng for the latex particles, Gilles Sigaud (DSC), Ahmed Bentaleb (SAXS), Frédéric Nallet (SAXS), Jean-Christophe Loudet, Philippe Poulin, Wilfried Néri, Martin, Vivien, Aurore, Clémence et Ludivine.

Also, in Belgium I would like to thank Gopala Krishna who showed me how to assemble a DSSC and who helped me characterizing some of them, Frédéric Stevens for his advice and his support, Pierre Colson and Jennyfer Dewalque for their kindness and this nice time spent in Sorrento, Seb (le grand) for his help in the lab, his kindness and his good mood!

More generally, I would like to thank all the staff in CRPP and in Liège, and all the students in these three laboratories. More especially, I would like to thank all my office mates: Aiat, Manal, Haleema, Andrew and of course Edgar in Canada, Frédéric, Mélanie and Gopala in Belgium, and Maryse and Vivien in CRPP. I also would like to thank the people I shared the lab with: Fred, Aurore and Jonathan. Thank you for supporting me during these years!

I thank all the people in CRPP who helped me, Nathalie T., Lionel C. et Stéphane B., Nadine L., Frédéric L. and Stéphanie E., Béatrice D., Elysabeth H. et Josianne P., Anne F., Sandrine M., Philippe H. et Jean-Luc L., Lionel B. et Pascal M., Philippe B., Emmanuel T. and Jean-Yves J.

I would like to thank all the people with who I could share nice moments inside or outside of the lab. Here I think about all the IDS-FunMat students and the unforgettable diner and summers schools where we had some fun (Mercedes, Hanbin, Mathilde, Maryna, Alex, Uyxing, Wiljan (affiliated), Marie, Edgar, Camille, Dan, An, Erin, etc, sorry for the ones I forgot but 3 years is a lot!) ! I will definitely remember the karaoke in Annecy! I thank all the people I had lunch with: Edgar, Camille, Dan, Erin, Uyxing in Canada, Fred S., Tiziana, Marie, Mathilde (number 1, 2 and 3!), Zeynep, Daniela and all the LCIS GreenMat lab in Liège, Véronique, Nadine, Maxime, Eric, Mathieu, Clémence, Ludivine, Olivier, Ie-Rang (thanks for the apartment!), Eva, Aurore, Martin, Vivien, and the new ones Pauline, Mélodie, Marion, Vincent, Pierre, Jonathan, Romain… in Bordeaux, I definitely needed these breaks!

Finally, it is with a lot of affection that I would like to thank my family who has always supported me since the beginning, more especially my parents without who nothing would have been possible. Thank you for your love, your support and your trust. I thank my closest and oldest friends : Laëtitia, Léonor, Damien who came all the way to Bordeaux for my defensebut also Mélanie, my temporary roommates and hosts. Of course, I would like to thank my boyfriend Matthieu who lived from very close the PhD thesis and who came all the way to Canada to help me cheer up! Thank you a million times!

To my family, my friends, my boyfriend and to my father.
To my mother and my grandmother who are gone too soon…

Table of Contents

Preface

Shapes and functionalities are certainly the most effective tools employed when considering reaction modes involved in nature and biologic systems. Chemical sciences, historically speaking, firstly focused on composition of matter rather than on its shape. Thus, this is only in the middle of the XIX century that emerged the notion of "isomery" where the molecular structural formulae took the relay of the global one. Today, the notion of "shapes" is of primary importance in chemical science. For instance we can take the case of carbon where fullerenes and nanotubes (single and multi-walls) are offering divergent properties when compared with graphite or diamond. We can also take the notion of "host and guest" employed in molecular science and more precisely in supramolecular chemistry. Today, the society high standard specific needs are pleading for chemists to conceive entities more and more complex, multi-scales, multifunctional and enable of developing a certain degree of autonomy, taking inspiration from *Mother Nature*. The chemical paths employed to generate such complex architectures which bear a certain degree of complexity and certainly interdisciplinary, bio-inspired or not. In the field of bio-inspired materials "integrative synthesis" has been proposed by S. Mann as "*the use of self-assembled organic templates (transcriptive synthesis), cooperative assemblies of templates and building blocks (synergistic synthesis), spatially restricted reaction fields (morpho-synthesis), and combinations of these approaches (integrative synthesis) in the area of sol-gel chemistry*".[1] This approach was further refined by C. Sanchez who summarized perfectly the outstanding revolution in modern material chemistry: "*recent data (...) have led to new understanding of organic–organic or organic–mineral interfaces, allowing the controlled design of new materials with complex or hierarchical structures. Synthetic pathways (...) concern (i) transcription, using pre-organized or self-assembled molecular or supramolecular moulds of an organic (possibly biological) or inorganic nature, used as templates to construct the material by nanocasting and nanolithographic processes; (ii) synergetic assembly, co-assembling molecular precursors and molecular moulds in situ; (iii) morphosynthesis, using chemical transformations in confined geometries (microemulsions, micelles and vesicles) to produce complex structures; and (iv) integrative synthesis, which combines all the previous methods to produce materials having complex morphologies*".[2] This concept was finally fully theorized when enouncing the concept of "Integrative Chemistry" as "*the integration of the sol-gel process,* *inorganic chemistry, lyotropic mesophases, supramolecular architectures, air-liquid foams, biliquid foams, external fields, organic polymers, nanofunctionalization and nanotexturation, (...) [, which] offers the possibility of achieving new architectures at various length scales and with enhanced properties*."[3] Hence, *Integrative Chemistry* can be understood as a method for material design where the initial bricks, relevant from many domains of chemical sciences, are connected and assembled with the help of different driving forces (strong but static covalent bonds, weak but dynamic intermolecular interactions) with the help of multi-scale reaction and structuring mechanisms. In this regard and conceptually speaking, *Integrative Chemistry* is certainly the link between the notions of "complexity in chemistry"[4] and the bio-inspired integrative synthesis.

It is in this vein of *Integrative Chemistry* that this PhD dissertation takes place. We will treat sol-gel chemistry, polymer chemistry, along with the use of external macroscopic shaping modes such as extrusion or spin coating and intrinsic ones, as mesoscopic lyotrope mesophases templates. The whole synthetic modes will be driven to trigger enhanced properties of advanced functional materials either in the fields of photonic, heterogeneous photocatalysis and photovoltaic.

The first Chapter thus describes the general context and the issues related to the synthesis of functional materials bearing hierarchical architectures. At first, we focus on nanoparticles syntheses that constitute the nano-building blocks. In second, we discuss on mesoscopic and macroscopic shaping modes that can be used to obtain the final architecture. Finally, we briefly introduce how the internal structure of the material (crystalline structure for inorganic materials and chain structure for organic materials) affects their properties.

During this PhD project, we have been attached to synthesize functional materials answering to different objectives. The overall progression is iterative, where each new objective comprises a new parameter compare to the previous one.

The first project described in Chapter 2 aims to validate the general “nano-manufacturing” concept based on integrative chemistry by synthesizing zinc oxide (ZnO)/ polyvinyl alcohol (PVA) macroscopic fibers. For this project, a swiveling synergy between the ZnO nanorods of a same macroscopic fiber is created in order to tune their mechanical and photoluminescence properties (in absorption and emission). Especially, we discuss how the anisotropy of both components (material AND process) modify the final properties in a synergetic way.[5]

In a second project, we introduce a new level of synergy, not only based on interactions between components within a same fiber, but also induced between the materials composing the fiber and the environment (air flux). More specifically, the influence of shape and nanostructure on properties and process performance based on photocatalytic applications is illustrated.

In Chapter 3, we report the synthesis of TiO_2 macroscopic fibers bearing a hierarchical porosity, through an integrative multi-scale approach. In this case, we study the influence of the fibers structural parameters on their photocatalytic properties, the structural parameters being adjusted by varying the formulation.[6] From these results, the best formulation to obtain the highest photocatalytic performance is determined. Even though the performances cannot compare with the commercial product, the main goal of this study was to explore how new synthetic paths – investigated in the following chapter – can help to improve the photocatalytic properties through a "*knowledge-based design of functional materials*" method, as defined by W. Jaegermann (TUD, Germany, personal communication) instead of a pure trial and error one.

This approach, with the clear identification of meaningful parameters, results in Chapter 4, in an improved synthesis method of catalytic fibers, which allowed us increasing photocatalytic performances, by modifying overall the fiber hierarchical shape by on reducing their diameter and increasing their porosity. The first part of this chapter is dedicated toward a new manufacturing protocol which involves a spinneret smaller than the one used in Chap.3 and the addition of polymer beads inside the starting solution, in order to enhance both surface interaction and porosity. In a second part, we adapt a semi-industrial process, currently used for the synthesis of Carbon nanotubes/PVA fibers, in order to reduce again the fibers diameter. In this part, the structure/property relationship is discussed.

The last step, which is the multiscale integration of nanostructured functional materials within devices, is illustrated in Chapter 5. In this Chapter, polypyrrole (PPy), a conducting polymer, is synthesized using Swollen Liquid Crystals (SLCs) as a nanoreactor used for the chemical polymerization of pyrrole.[7] For this purpose, a detailed study of the SLCs partial phase diagram is conducted. The objective here is to obtain *in fine* aqueous suspensions of PPy nanosheets that can be shaped as thin film or conducting patterns. As PPy can be used both as the electrolyte and the counter-electrode of a full solid state Dye-Sensitized Solar Cell (DSSC), one of the perspectives could be to integrate this component in such devices.

Chapter 1: General context and objectives

As explained in the preface, materials properties are highly dependent on their architectures. This phenomenon can be observed in nature where we can find materials which possess architectures which confer to the organisms the best properties according to their need. For example, diatom frustuls take advantage of their hierarchical porosity to ensure an optimized matter transport. Also, nacre will be organized in flat-like calcium carbonate sheets in order to increase its mechanical properties and to possess optical properties (iridescence). In this chapter, we will present some techniques which allow designing materials architecture on demand. The first part being dedicated towards nanoparticles syntheses and the second part dedicated towards mesoscopic and macroscopic shaping modes. In a third part, we will briefly introduce how the internal structure of the material (crystalline structure for inorganic materials and chain structure for organic materials) affects their properties.

I. Soft and « sol-gel » chemistry applied at the synthesis of nanoparticles

I.1. Nano-particles syntheses without templating

I.1.1. « Sol-gel » chemistry

I.1.1.1. Hydrolysis and condensation reactions

This paragraph will present briefly the “sol-gel” synthesis process, which is frequently used for material design going from the “solution to oxides”. The information presented in this part has been in part extracted from the PhD thesis of N. Brun[1] and C. Leroy.[2] A more detailed explanation of this synthetic path can be found in the books of Livage *et. al.*,[3,4] Brinker *et. al.*,[5] Hench *et. al.*[6] and Jolivet *et. al.*[7] The illustrations presented in this section are mostly referenced from the book by Brinker.

The so called “sol-gel” process represents in its strict definition an inorganic polymerization in solution. In this case, the sol is a colloidal dispersion (particles size in the range of 1-1000 nm) made of either of molecular precursors that behave as monomers, or of pre-synthesized nanoparticles acting as nanobuilding blocks, or a mixture of both. In most cases, the precursors used in this reaction are metallic alkoxides (like $Ti(OR)_4$ for TiO_2 precursor), which will first react with water. This reaction is called the hydrolysis reaction (Figure 1) and, during this step, alkyl groups (-OR) are progressively substituted by hydroxyl groups (-OH) in order to make the species more reactive for the second step, that is, the propagation reaction, known as condensation. In order to achieve the hydrolysis reaction, the metallic alkoxide will be first solvated by dipolar molecules. Then a nucleophilic substitution reaction will occur and lead to the elimination of an alkyl group *via* the formation of the parent alcohol, as a result of a proton transfer.

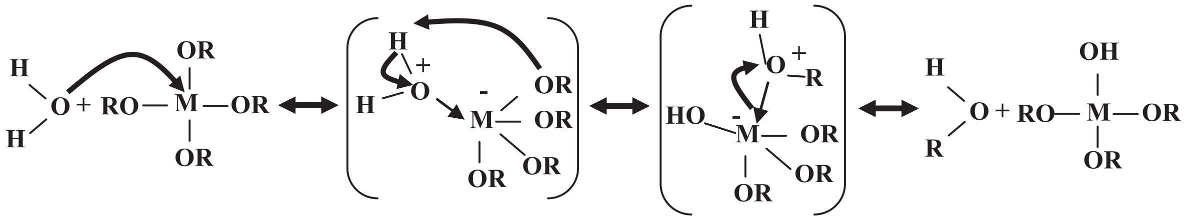

Figure 1. Hydrolysis reaction mechanism for an M $(OR)_4$ alkoxyde type.

Depending on the initial precursor solvation and on the way it eliminates the protons, the chemical formula of the hydrolyzed precursor becomes $[MX_{n-m}O_mH_{2m-h}]^{(z-n+m-h)+}$, M being the transition metal, X an alkyl (OR), a halide or an oxyhalide, *n* the maximal number of coordinates, *m* the number of coordinating water molecule, *z* the cation charge, and *h* the hydrolysis rate $(0 \leq h \leq 2m)$. Depending on the *h* value, the precursor can be either an aquo complex $[MX_{n-m}(OH_2)_m]^{(z-n+m)+}$ for h=0, a hydroxo-aquo complex $[MX_{n-m}(OH_2)_{m-x}(OH)_x]^{(z-n+m-x)+}$ for h<m, or a hydroxo complex $[MX_{n-m}(OH)_m]^{(n-z)-}$ for h=m, an oxo-hydroxo complex $[MX_{n-m}(OH)_{m-x}(O)_x]^{(n+x-z)-}$ for h>m, or an oxy complex $[MX_{n-m}O_m]^{(n+m-z)-}$ for h=2m. In consequence, the cation charge and the pH of the solution are the determinant parameters of the hydrolysis rate, and so of the chemical formula of the hydrolyzed precursor (Figure 2).

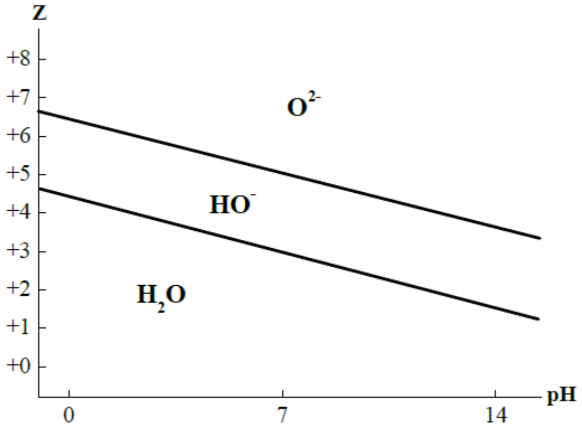

Figure 2. Schematical representation of the stability domain of aquo, hydroxo and oxo ligands according to the pH of the solution and the cation electric charge.[7]

Once the alkoxides have been totally or partially hydrolyzed and contain hydroxyl groups, they can react with each other through the condensation reaction. In the case of $Ti(OR)_4$, the precursor will immediately react in water, exothermically as the initial tetrahedral coordination of Ti is unsaturated (Ti can possess a coordination of up to 6). Four mechanisms of condensation reaction can occur: alkoxolation, oxolation, alcoholation and olation respectively presented in Figure 3.a-d.

Unlike the alkoxolation and the oxolation reactions, the alcoholation and the olation reactions can take advantage of the unsaturated molecular structure to create the inorganic network. The alkoxolation and the olation take place between one hydrolyzed and one non-hydrolyzed alkoxide, whereas the oxolation occurs between two hydrolyzed alkoxides and the alcoholation between two non-hydrolyzed precursors.

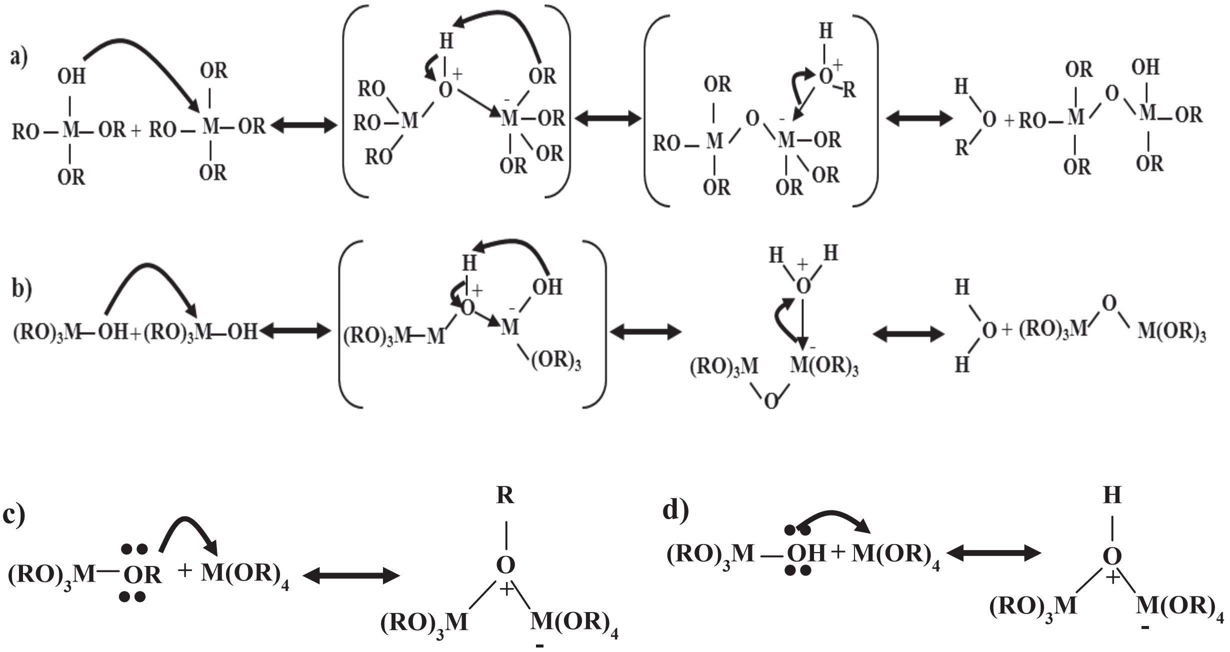

Figure 3. Condensation reaction mechanisms of a $M(OR)_4$ alkoxyde type, (a) alkoxolation, (b) oxolation, (c) alcoholation and (d) olation.

These single molecular reactions preside all reaction mechanisms occurring during a sol-gel process, starting from molecular precursors to final solid materials. Therefore, the fine control of these reactions, all along the different stages of a sol-gel reaction, is essential to control the final materials shape obtained through this technique.

I.1.1.2. Nanoparticles synthesis by sol-gel method and controlling parameters

The first step in the nanoparticles synthesis is the formation of a “zero-charge” precursor with at least one hydroxo group, obtained from the initial pre-hydrolyzed precursors that had been added into the reaction medium. Once such a hydrolyzed precursor is obtained, the lack of electrostatic charges will avoid the electrostatic repulsions between precursors, and the presence of the hydroxo group will allow the intermolecular coordination between precursors.

At this stage, the condensation reaction kinetic is really low due to the small amount of hydrolyzed precursors in solution. As soon as the amount of these hydrolyzed precursors reaches a critical concentration, the formation of a solid phase can take place. The formation of solid *nuclei* (germ) is observed, which will constitute the second step of the nanoparticles synthesis, known as the nucleation-and-growth mechanism. Beyond this stage, hydrolyzed precursors can either create new nuclei, or react with pre-existing germs and contribute to their growth. The first option is more costly in energy because a new liquid/solid interface has to be created with a positive enthalpy, whereas the second is only relevant to the chemical reaction with a negative reaction enthalpy. As the *nuclei* appear or grow, a consumption of the hydrolyzed precursors is observed, which can contribute to lower the concentration in precursors below the critical value required for the creation of new *nuclei*. At this stage, there is a competition between the kinetics of creation of hydrolyzed precursors and that of their consumption in the formation, or growth of the solid phase.

The third step corresponds to the growth of these *nuclei*. During this step, it is also possible to observe the formation of new *nuclei* in parallel to the growth of the ones already present in solution. The formation of new *nuclei* happens if the concentration in hydrolyzed precursors is still above the critical concentration, and it will depend on the kinetics of the hydrolysis and condensation reactions. Indeed, if the initial hydrolysis reaction is much faster than the condensation reaction, the hydrolyzed precursors will not be consumed fast enough and new *nuclei* will be formed. In the contrary, if the condensation reaction is much faster than the hydrolysis reaction, only few *nuclei* will be formed at the beginning. Besides, all new hydrolyzed precursors, as they appear, will be consumed by the particle growth before they reach again the critical concentration required for the formation of new *nuclei*. With this condition, the nucleation of particle seeds will happen in a first step, and all these seeds will grow in parallel, leading to a final colloidal solution made of monodisperse particles. If both nucleation and particle growth are allowed to happen concomitantly, a colloidal solution made of polydisperse particles will be obtained.

Once all precursors have reacted and the solid phase is formed, there is finally a fourth step called the aging process, that includes three important mechanisms that can drastically affect the structure/properties/processing of the final solid material: (i) an internal evolution of the metal oxide framework with a continuous dehydration via oxolation reactions, (ii) a particle size evolution through Oswald ripening where larger particles grow at the expenses of smaller one as a result of differences in the surface energy of the liquid/solid curved interfaces, and (iii) the formation of aggregates resulting from solid-solid physical interactions and helped with the environmental hydrostatic pressure.

From this description we can conclude that several parameters will be determining for the final size and shape of the nanoparticles. These parameters that are:

1. The choice of the metallic cation and the nature of its ligands is an important parameter in controlling the kinetics of hydrolysis-condensation reaction. Nucleophilic attack of a metal center by the hydroxo group of another precursor is the key factor in the condensation reaction, but it can happen only if there is a “good” leaving group to balance the additional coordination resulting from condensation. Control of both nucleophilic attack and coordination balance is hence a key factor in controlling overall the reaction.
2. For reactions involving metal alkoxides, the solvent is usually an alcohol, and water is used as a reagent for the controlled hydrolysis of the alkoxide. Hence, pH is important as it allows us to control the hydrolysis and condensation reactions kinetics by activating catalytic acid or basic mechanisms. At low pH, the hydrolysis reaction will be favored compared to the condensation reaction, which will be the opposite at high pH. In consequence, small nanoparticles will be obtained when the pH is very low. As a result, in order to synthetized 10 nm TiO_2 particles, we will operate the reaction in acidic conditions (see Chapter 3).
3. The temperature allows for a thermodynamic control of the reactions kinetics (the higher the temperature, the higher the reactions kinetics).
4. The solvent nature is also important because changing its polarity will modify its ability to exchange protons (or not), hence will affect the substitution mechanism.

5. Finally, an increase in the precursor concentration can also cause an increase of the reactions kinetics due to the higher probability of the “collision” of two precursors in solution.

In this part, the general principles of the sol-gel chemistry have been presented. Under mild temperature conditions and without additives such as surfactants, this method leads either to gel (polymeric network containing the inorganic component) or spherical particles, depending on the control parameters listed above. As it has been discussed in this paragraph, the reaction is influenced by five major parameters that direct the particles nucleation and growth. In this PhD project, we adapted these parameters in order to, not only synthesize spherical nanoparticles, but also to synthesize anisotropic ones. In this context, we adapted mostly the pH of the solution, the nature of the ligands by adding shape controller, and/or on the temperature and pressure of the system by using hydrothermal reactions. In the next paragraph, we describe how the use of shape controller in sol-gel syntheses can allow one to switch from isotropic to anisotropic particles.

I.1.2. The influence of the ligands: shape controller

Shape controllers are components that allow controlling the shape of the final nanoparticles by favoring preferential direction growth compared to others as a result of modifying the intrinsic particles surface tension γ_s. Shape controllers are generally organic molecules presenting specific ending groups like amino groups ($-NH_2$) or carboxylate groups ($-COO-$) which have a high affinity with the metallic cation.[8,9] Once these groups are in presence of the metallic precursor in solution, they will form complexes with the metallic cation, and by doing so, modify the cation ligands.

Moreover, some ligands have the property to absorb preferentially onto some crystallographic planes than others because they match better the surface charge density, which results in surface poisoning that prevents the particle growth perpendicularly to the grafted plane. As a consequence, it is possible to design the crystallographic structure of the particles and/or their shape. By doing so, not only the hydrolysis/condensation reactions kinetics between precursors are modified (see part I.1.1.2) because of the presence of new ligands, but also the growth direction. The growth direction is here affected by the modification of the reaction between precursors and particle surface due to the presence and the nature of the ligands. For example, Zheng *et al.*[10] performed a study to show the influence on the capping agent (shape controller) alone on silver particles shape. They demonstrate that the addition of citrate or poly(vinyl pyrrolidone) (PVP) in solution allowed them to selectively and routinely obtain either nanoscale octahedrons enclosed by {111} facets, or nanocubes/nanobars covered by {100} facets respectively (Figure 4).

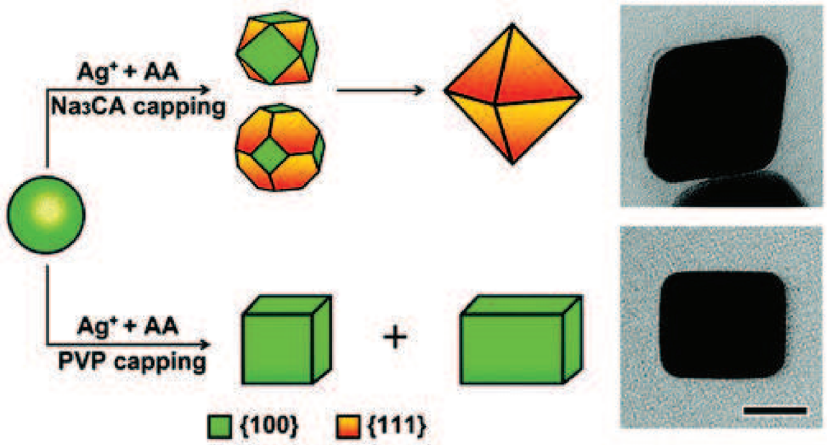

Figure 4. Schematic representation of the synthetic pathways for the selective synthesis of either nanocubes or nanoscale octahedrons of silver nanoparticles by varying the nature of the shape controller (scale bar: 20nm).[10]

The use of shape controllers is really efficient to shape nanoparticles, but the reaction itself can be hampered by these ligands, and an additional driving force is often required to induce and propagate the reaction. Therefore, many studies in the literature report on the use of various heat sources such as hydrothermal, solvothermal, microwave and thermo-plasma syntheses. These techniques are described in the following paragraph.

I.1.3. The influence of the temperature

I.1.3.1. Hydrothermal and solvothermal syntheses

Hydrothermal synthesis refers to a synthesis taking place in an aqueous medium at a temperature over 100°C and at a pressure above 1bar. To perform such syntheses, it is necessary to place the solution in a container that is able to resist at high pressure and high temperature in order to avoid any leakage or breakage during the synthesis. Typically, the solution is placed into a Telfon-lined stainless steel autoclave. Solvothermal synthesis refers to a synthesis that takes place under the same conditions but in a solvent different than water. Hydrothermal or solvothermal methods are stated as special type of chemical transport reaction. These methods are widely used in the preparation of nanostructures presenting specific shapes like 1D structure (nanorods, nanotubes, or nanowires), nanoflowers, and nanoplates (see Figure 5).[11–13] The principal interest of this technique is to increase the solubility of the solids in solution by generating a higher temperature and pressure above the critical point of the solvent. These thermodynamic critical conditions allow almost every solid can become soluble or sensitive in different solvents.

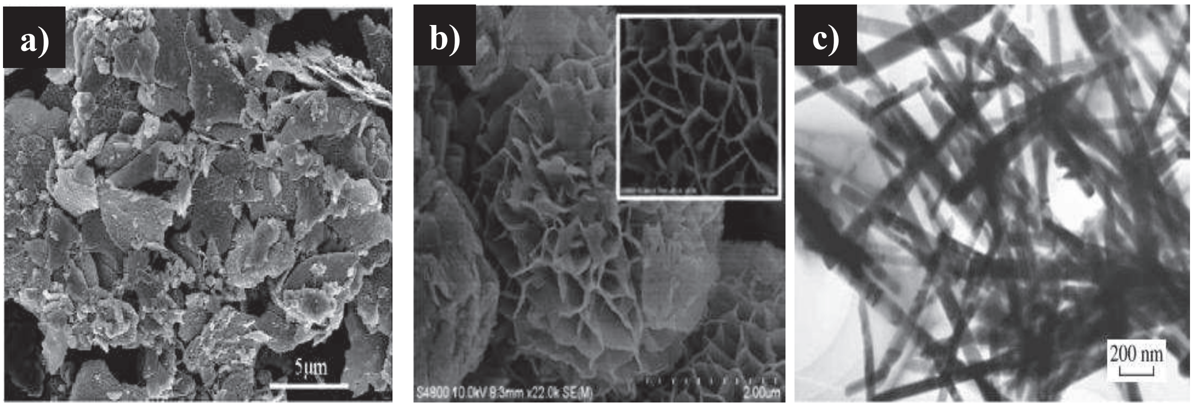

Figure 5. Some examples of SEM images of structures obtained through hydrothermal syntheses: a) $CuInSe_2$ nanoplates, b) $ZnIn_2S_4$ “marigold” flowers and c) ZnO nanorods.[11–13]

There are three main strategies to obtain crystals during hydrothermal synthesis.[14] The temperature gradient method is the most standard method used for hydrothermal syntheses. In this configuration, the reaction products are transported usually from the highest temperature region (highest solubility) to the lowest temperature region (lowest solubility). This method is especially convenient to recover the final product as the temperature gradient leads to the separation of the reaction products. It has been observed that certain-metastable phases are formed only in temperature gradients. With another method, the isothermal one, the reaction is carried out at a constant temperature whith no temperature gradient. This method is usually used for simple syntheses that do not require high transport efficiency. The temperature-decrease method is a variation of the temperature gradient method. In this case, the cooling of the container will induce a separation of the desired phase (saturated at a higher temperature) from the rest of the solution upon cooling.

Shape controllers can be added to the starting solution than will undergo the hydrothermal/ solvothermal synthesis in order to obtain specific shapes.[15] Although this method presents many advantages for the synthesis of solid oxides, the time of the reaction is generally high and it can only work in batches. However, industrial zeolites are usually prepared *via* this route in large quantities. In order to reduce the time of the synthesis, new methods have been developed like microwaves assisted synthesis or thermo-plasma synthesis.

I.1.3.2. Microwave-assisted syntheses

As for hydrothermal syntheses, microwave (MW)-assisted syntheses heat the solution in a confined environment in order to create specific crystal structures with specific shapes.[16] For this type of synthesis, the heating process will occur through two main processes:

- the ***dipolar polarization***, which consists in the dipoles motion due to the change of direction of the electric field; it works generally well with polar solvent or reagents,
- the ***ionic conduction***, consisting in ions movement and collision due to the change of direction of the electric field; it works with the charged particles in solution.

When MW crosses a solution, dipoles present in this solution tend to align with the electric field. As this field oscillates, dipoles try to re-align along the alternating electric-field streamlines which creates both molecular friction (caused by the dipoles movement) and dielectric losses, which are converted into heat. On the other hand, the ions within the solution will move along with the change in direction of the electric field, which results in movement and collision, generating heat too. Here, the ability of the dipoles and the ions to follow the change of direction of the electric field will determine the amount of heat being generated. At too low frequency, the dipoles and the ions can realign with the electric field, and no heat is generated. At too high frequency, the dipoles and the ions have no time to align/oscillate/move properly and their movements are dramatically reduced, which results in a decreasing of the amount of heat being produced. In order to generate a maximum of heat for a minimum of power, the electric field must be adapted to switch directions just before the dipoles are perfectly aligned. The frequency of the MW must therefore be chosen carefully.

Compared to hydrothermal synthesis, the heat produced by MW does not involve a convection process and is a result of a local molecular phenomenon, which makes the heating much more homogeneous. In consequence, using MW dielectric heating as a non-classical energy source has been shown to dramatically reduce processing times, increase the reproducibility, increase product yields, and enhance product purity (by preventing unwanted side reactions) or material properties.[17]

This method aim to replace conventional methods as hydrothermal syntheses, and literature reports already on numerous structures, initially prepared by hydrothermal/solvothermal syntheses, which were reproduced with MW assisted synthesis by now (Figure 6).[18–20]

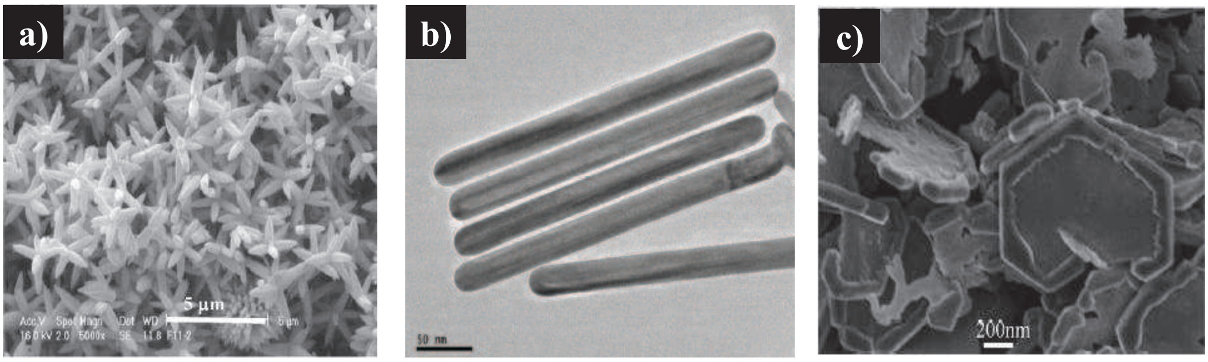

Figure 6. Some examples of SEM images of structures obtained through Microwave assisted syntheses: a) ZnO nanoflowers[18], b) Au nanorods[19] and c) Cu nanoplates.[20]

I.1.3.3. Thermo-plasma assisted syntheses

Nanoparticles can also be designed with more exotic techniques such as thermo-plasma assisted syntheses. The principle of the technique is described in the following by taking as example the synthesis of TiO_2 nanoparticles. First, a blowtorch creates a gas plasma that hits a target containing the reaction precursor (titanium in our case). Fine titanium particles ejected in the reaction chamber by this process will react with the oxygen, which is introduced in the chamber as the reagent in order to form TiO_2 nanoparticles.

This technique is generally used when tailor-made particles presenting specific phases and morphologies are needed. Among others, this technique was used to synthsize TiO_2 nanoparticles with high precision and reproducibility as demonstrated in the study of Banerjee *et al.*[21]. In particular, they demonstrated that the phase ratio between the anatase phase and the rutile phase could be tuned with the pressure of the chamber. This method could be then used to understand the influence of each phase on photocatalytic or photovoltaic properties.

However, this method is quite expensive and can only be used in application where the quality of the final product is more important than its price. For these reasons, hydrothermal/ solvothermal and MW assisted syntheses are preferentially used.

In this part, we have seen that there are several techniques that allow us to design both the nature and the morphology of the nanoparticles, just by changing the physics and the chemistry of the solutions (ligands, pH, temperature, etc). However, other ways of designing the shape and the texture of the nanoparticles have been explored by using other molecules/particles as template for the growth of the particles. In the following part, we aim to give a general overview of these techniques.

I.2. Nano-particles syntheses using templates

In this part we will discuss about the main types of templates that exist in the literature. There are divided in two majors groups, the first one called “hard templates” and the other one called “soft templates”. The template can act on the particles shape and texture in two different ways: either the particles will grow onto/around the template (internal mold) and will adopt its shape and texture, or the template will act as a confinement mold, within which particles will grow and will be restricted by this external mold. The second pathway is generally used to build macroscopic structure that act as a template for nanoparticles being synthesized within, and we will not discuss it in this section. Here we will limit the discussion on the methods to control nanoparticles morphology. Additional descriptions are discussed in part II.

I.2.1. « Hard templating »

Hard templates refer to solid and rigid templates. They are either discrete nanoparticles (internal mold), or mesoscoporous or macroscoporous structures (external mold).

I.2.1.1. Discrete nanoparticles

Discrete nanoparticles are used for the synthesis of hollow particles that grow around the template, this later being further removed to create an internal porous space. They exhibit usually the same morphology as the template. Literature describes numerous porous materials synthesized with the help of polymer beads as a template. Due to their ability to interact with most of the sol-gel syntheses precursors, and since they can be easily eliminated by calcination, they are widely used for the synthesis of inorganic hollow spheres. Here, the precursor molecules and the particles concentrations have to be adjusted to obtain well-defined discrete hollow spheres and not a porous solid. They have been especially used for the synthesis of metal oxide capsules such as SiO_2, TiO_2 or even mixed structures of different oxides obtained through sol-gel reaction.[22–25] These hollow spheres present specific properties which make them appropriated for their use as catalysts, optoelectronic devices, and drug delivery systems. Recently, particles with sharp edges, sharp corners, or rough surfaces have attracted more attention than spheres, because it was demonstrated by Mahmoud *et al*. that these particles are more efficient as catalysts than hollow spheres due to their shape (see Figure 7).

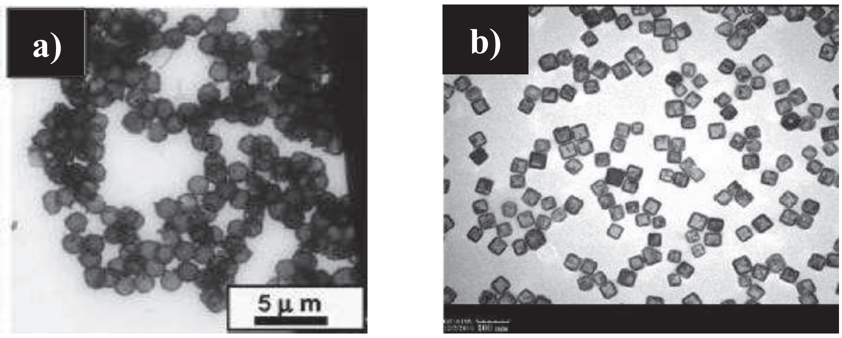

Figure 7. a) SEM image of hollow titania spheres[23], and b) TEM image of gold-palladium hollow cubes.[26]

This method is quite powerful to create hollow nanoparticles, but it requires first the synthesis of the same amount of nanoparticles used as templates. In consequence, for the synthesis of hollow spheres in particular, soft templates will be generally preferred.

I.2.1.2. Mesoscopic structures

These structures refer to materials organized at a higher length scales (mesoscopic scale) such as zeolites or filaments.

Zeolites are alumino-silicate structures formed by tetrahedras of (AlO_4) and (SiO_4) containing water with the general formula: [27,28]

$[(M^1,M^2_{1/2}]. AlO_2.ySiO_2.zH_2O$ where M^1 = Li, Na, K, etc and M^2 = Mg, Ca, Sr, Ba, etc.

Zeolites pores and other “molecular sieves” like aluminophosphates or gallophosphates, are arranged periodically within the structure with a pore size which varies from 3 to 10 Å. Their specific porosity confers them a very high specific surface area and very well-defined micropores, and their hydrothermal resistance resulting from their crystalline walls, made some zeolites to be commercialized as adsorbents, catalysts, or ions exchange media. They are also used as templates to create microporous structures in order to increase the specific surface area of nanoparticles (see Figure 8.a).[29–31] Indeed, the specific surface area is one of the most important parameter when it comes to catalysis, drug loading or photovoltaic applications among others. In particular, zeolite seeds have been used in combination with spherical particles in order to create porous capsules presenting a zeolite morphology.[32]

In this category, we can also notice that preformed filaments or fibers are used in order to obtain 1D mesoscopic structure. These 1D-structures are also quite important in the field because, as for zeolites, their specific surface area is very high due to the surface over volume ratio, and they can be also used when anisotropic properties are required (see Figure 8.b)).[33]

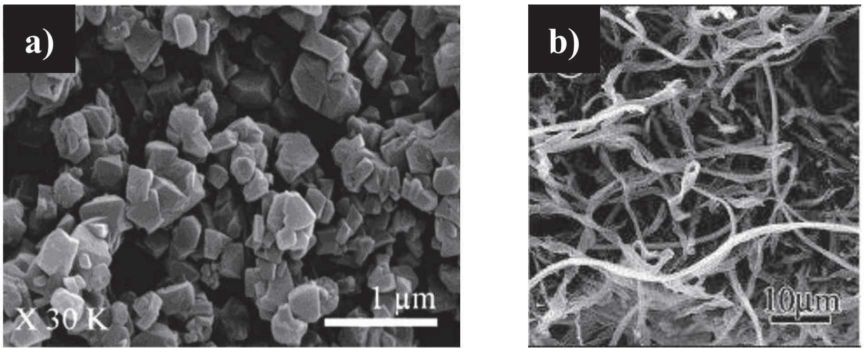

Figure 8. a) SEM image of carbon structure synthesized using zeolites as template, and b) TEM image of Al_2O_3 fibers made from cotton fibers as bio-template.[31,33]

In conclusion we observe that the hard template technique is quite reliable to create particles with different shapes and properties, or porous materials. However, because they require the synthesis of sacrificial nanoparticles prior to their own synthesis, soft templates are often preferred to synthesize these structures. In the following part, we will explain what soft templates are and how they can be used to create nanoparticles in a one step process. The synthesis of 3D mesoporous and macroporous structures will be discussed later on in part II.1.2.

I.2.2. « Soft templating » as chemical reactors

I.2.2.1. Emulsions

- Basic notions: physical-chemistry of complex fluids bi-phasic systems

In the literature, we can find two categories of bi-phasic system composed of two non-miscible phases: foams (air-liquid foam) and emulsions (bi-liquid foam). Foams and emulsions are ternary systems which are composed of an aqueous phase (or polar phase), of amphiphilic molecules (or particles), and of a non-miscible phase in water (air in the case of foams and an oily phase in the case of emulsions).[34] In order to create a bi-phasic system from these non-miscible phases, it is necessary to add energy into the system, which is generally a mechanical energy. During the vigorous mixing, interface will be created and optimized between the two non-miscible phases, where the minor phase will be dispersed as droplets within the major one (continuous). The amphiphilic molecules (or particles) will act in this case as the interface stabilizer. Here we will present more especially the case where the interface stabilizers are surfactants.

The cohesion of a liquid is due to molecular attractive forces such as Van der Waals forces and hydrogen bonds. In consequence, in order to create an interface between two non-miscible phases like an aqueous phase and an oily phase, it is necessary to add energy into the system to break the attractive forces present in each phase. Moreover, in order to stabilize the interface created, it is necessary to add a component with affinity for both phases, which will act as a "buffer" and provide the cohesion of the bi-phasic system: surfactants molecules. These molecules will tend to lower the energy required to break intermolecular bonds per unit of surface created.

Surfactants molecules are amphiphilic molecules that contain a hydrophilic head and a hydrophobic tail. When introduced in an aqueous solution, they first remain at the surface with the hydrophilic head facing the water and the hydrophobic tail exposed to air (with air behaving like a hydrophobic medium). As their concentration increases, these molecules will agglomerate in solution, forming spherical structures, known as micelles, made of a hydrophobic tail core, surrounded by a hydrophilic head. The concentration at which the micelle forms is called the critical micelle concentration (CMC).[35] There are two types of emulsions depending on the nature of the continuous phase. "Direct" emulsions are made of droplets of oil in a continuous water media, and "reverse" emulsions are made of droplets of water in a continuous oily media (Figure 9). Although the interface is fairly easy to create, this system is thermodynamically metastable, the equilibrium state being a phase separation state. There are four principal mechanisms that lead to the progressive evolution of the system towards phase separation: Oswald ripening, flocculation, creaming (or sedimentation) and coalescence.[34] Ostwald ripening describes the process where the content of the smaller droplets will diffuse inside the content of bigger droplets through the continuous media. In this case, the higher pressure inside the smaller droplets (Laplace law) is the reason for this diffusion. A simple way to prevent this phenomenon is to choose two phases that are highly insoluble in order to avoid the diffusion of the droplets content within the continuous media, or to choose carefully the surfactant in order to decrease the surface energy.

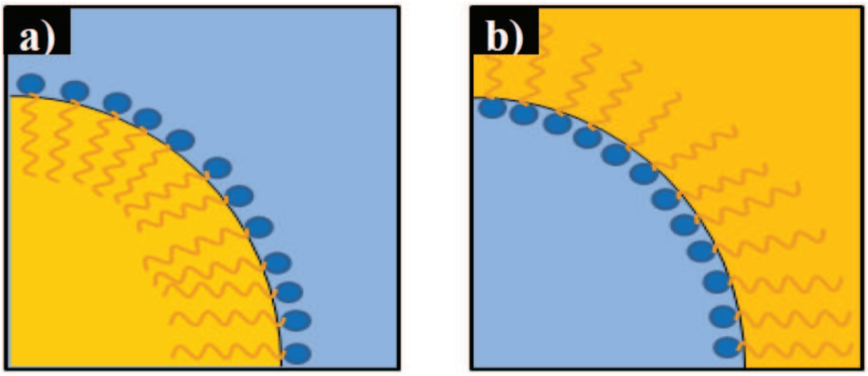

Figure 9. Schematic representation of a) a direct emulsion, and b) a reverse emulsion.

The flocculation process represents the agglomeration of the droplets into grapes as a result of attractive Van der Waals forces and Brownian movement. Creaming and sedimentation have for origin the gravity force. Due to the difference of density between the continuous phase and the droplets, if the droplets are denser than the continuous phase, they will be attracted towards the inferior part of the container (sedimentation), otherwise they will be attracted towards the superior part of the container (creaming). In order to avoid this evolution, the viscosity of the continuous phase can be increased in order to increase its resistance to the droplet movement. Also, if the system is maintained in permanent motion –shaked-, the forces that keep droplets in motion can overcome the gravity forces and prevent any sedimentation or creaming. Finally, the coalescence, which refers to the merging of two droplets as a result of the disappearance of the film that kept them separated, can destabilize an emulsion. This phenomenon is the worse because it is not reversible, but it can be reduced dramatically by choosing carefully the surfactant(s) that composed the interfacial film. Typically, the size of the droplets of an emulsion are comprised between 0.1 and 100 µm but it can go up to the millimeter under certain experimental conditions, especially when dealing with Pickering based emulsions.[36]

- Emulsions used for the synthesis of discrete particles

These emulsions have been used in particular for the one-step synthesis of hierarchically porous capsules, which makes them more attractive than hard sphere templates. In this context, Schacht *et al.* reported the synthesis of spherical capsules with a mesoporous shell filled with oil using a direct emulsion as template in 1996.[37] This concept has been developed later by using inverse emulsion[38] and has been recently improved in order to create capsules with several compartments.[39]

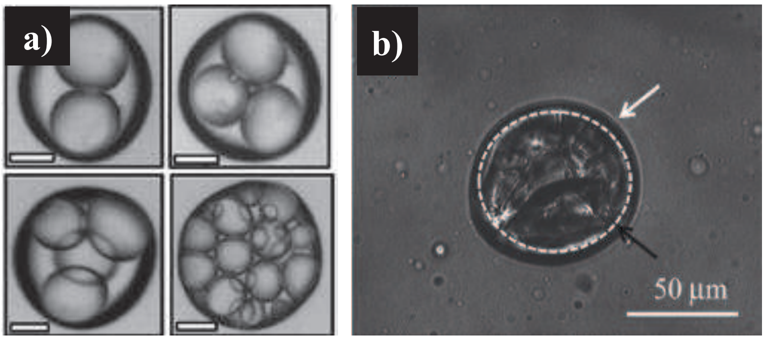

Figure 10. SEM images of multi-compartments capsules, a) polymer capsules (scale bar 40µm),[40] and b) Wax@Water@SiO2 capsules.[39]

These latest capsules have a great interest for the medical field and especially for multitherapy. As for the hard template method, a lot of different varieties of capsules where reported which can be used for catalysis and medical applications (Figure 10).[39,40]

I.2.2.2. Liquid crystals and Swollen Liquid Crystals (liquid-liquid interfaces)

Introducing surfactant in a solution above the CMC allows for the formation of micelles, but increasing further the concentration leads to gel-like ordered structures of this surfactant called lyotropic phases. They present specific long range organization and cubic, hexagonal, lamellar or sponge-like geometries (Figure 11).[41] These systems are called liquid crystals. Unlike the sponge-like phase, the cubic, the hexagonal and the lamellar phases present well-ordered high periodicity structures. However, the sponge-like structure still possesses a high periodicity with a characteristic feature dimension and a bilayer structure.

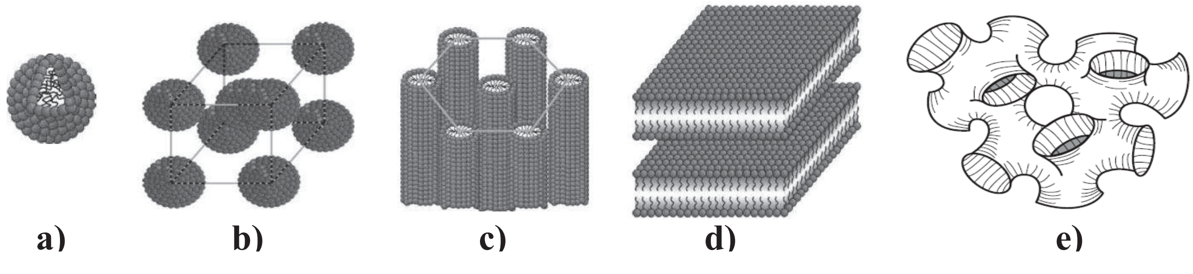

Figure 11. Schematic representation of a) a micelle of a direct emulsion, b) a cubic phase, c) a hexagonal phase, d) a lamellar phase, and e) a sponge phase.[41]

Micellar phases can be found for different surfactant concentrations. Direct micellar phase are generally observed at low concentration of surfactant. As the concentration in surfactant increases, the number of micelles will increase and they can possibly pack into a crystal structure with a cubic packing symmetry. As the surfactant concentration increases, the new surfactant molecules will be adapted by the micelles with a lengthening of these spherical micelles into rod-like micelles. Compared with spherical micelles, the rod-like objects have lost one degree of curvature. As surfactant concentration increases, the rod-like micelles will elongate more and pack according to a hexagonal symmetry, giving the so-called hexagonal phases. Adding more surfactant molecules will suppress the second degree of curvature, and surfactants will pack into bilayers with the hydrophilic head being exposed to water, as lamellar phases. These lamellar phases correspond to supermolecular aggregates of surfactant molecules, forming layers with large shape anisotropy. This latter structure is often placed right next to the sponge phase in the phase diagram, which can be described basically as a microstructure with a surfactant bilayer of multiply connected topology separating two solvent domains over macroscopic distances. Compared with lamellar phases that have no curvature degrees, sponge-like phases contain opposed curvatures, and are structured as minimum energy interfaces called giroïd surfaces. These liquid crystals (LC) are usually biphasic systems made of water and surfactants.

Swollen Liquid Crystals (SLCs) are a combination of microemulsions and liquid crystals. We can say that Swollen Liquid Crystals are to the Liquid Crystals what microemulsions are to micelles. As a result, and unlike binary LCs, SLC structures swell to a larger size by the addition of an oil phase that resides within the surfactant hydrophobic structures[42] (Figure 12). Moreover, another important difference is the addition of a cosurfactant, used as a wedge being intercalated between the surfactant molecules, that helps in defining the liquid crystal structure, making SLCs a quaternary system involving water, surfactant, oil, and cosurfactant.

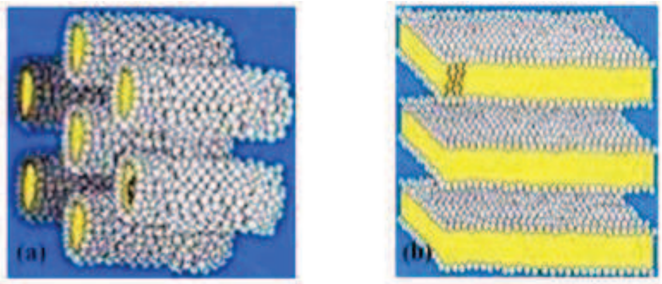

Figure 12. Swollen Liquid Crystal Phases (a) Hexagonal Phase, (b) Lamellar Phase.[43]

As mentioned above, the stability of the water-oil interface is insured by surfactant molecules, which are generally ionic and cosurfactant that helps to design the cylinder size. In this case, the repulsive forces between the ionic heads of the surfactant molecules in the structure walls must be taken into account for the stabilization of the structure.[44] For example, decreasing (resp. increasing) the radius curvature (resp. the cylinder diameter) of the SLCs, will contribute to increase the closeness of the ionic heads, hence the repulsive forces between them. It is therefore necessary to compensate this force by introducing new components that can shield this repulsive interaction, and stabilize the structure. Hence, we see that the design of the SLC will require a fine balance between the solvent swelling the cylinders (cyclohexane), the cosurfactant (1-pentanol) that helps to set the cylinder curvature radius, and an additive (a salt) that will screen the repulsive interactions between ionic surfactant heads, which result from a specific curvature radius. This last parameter has to be adjusted carefully because an excessive amount of salt can result in the molecules flocculation and so in the destabilization of the system.

In order to adjust the salt concentration of the solution, it has to be taken into consideration that it is not the salt concentration which matter but the ionic charge concentration.[44] The ionic strength is calculated according to the equation:

$$I = \frac{1}{2}\sum_{i=1}^{n} c_i z_i^2$$

where c_i is the molar concentration of ion i (mol/L), z_i is the charge number of that ion, and the sum is taken over all ions in the solution. It has been demonstrated that the nature of the salt does not have any impact on the SLCs, the only important parameter being the ionic force. Moreover, the nature of the surfactant molecules is in general not important as long as the concentration is adjusted in order to have a water-over-surfactant ratio of 40.[44] However, in strong acidic media, cationic surfactant like CTAB will be preferably used because anionic surfactants like SDS become protonated and lose their ionic characteristics. These structures have already been used as reactors to synthesize material with specific shapes such as Pt nanorods, zirconia needles, or polymers (Figure 13).[45,46] Recently, Lee *et. al.*[47] show the synthesis of PPy nanosheets in a hexagonal lyotropic phase using CTAB as surfactant, cyclohexane as the oil phase and 1-pentanol as co-surfactant. However, the hexagonal phase is really sensitive to the surfactant amount which makes it difficult to synthesize and, because of the viscosity of this phase, the polymerization reaction can take weeks if the solution is left at rest and unstirred.

In this section, we presented the different methods that allow for the synthesis of nanoparticles with and without the use of templates. In the next section, we will present the techniques that will allow us obtaining macroscopic structures with hierarchical architectures either in a one-step process (bottom-up approach), or in a two steps process where the nanoparticles are synthesized prior to their structuring at the macroscopic scale (nano-building block or nanotectonic approach).

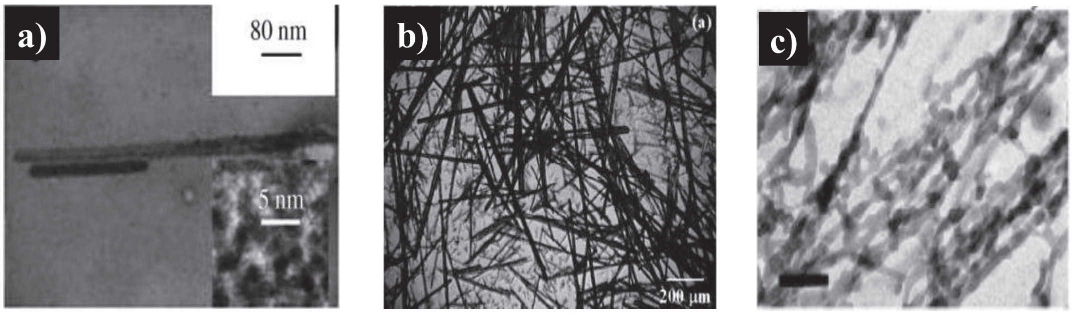

Figure 13. TEM images of a) Pt nanorods and c) polymer nanorods (scale bar: 100nm), and b) SEM image of Zirconia needles.[44–46]

II. Design of materials bearing specific architectures

II.1. Design of 3-D macroscopic structures

The synthesis of such 3D structures can be realized with the use of hard templates and soft templates as for discrete nanoparticles. This paragraph will present the most popular techniques used in the literature but it is not exhaustive due to the high diversity of the existing techniques.

II.1.1. Hard template

II.1.1.1. Natural and home-made macrostructures

As for discrete nanoparticles, macroscopic structures bearing hierarchical porosity can be synthesized using hard templates found in nature. This technique was first implemented by Mann *et al*. in 1997 who used a bacteria made of co-aligned filaments (*Bacillus Subtilis*) in order to obtain macroporous fibers made of silica (Figure 14.a)-b)).[48] Later on, other templates such as frustule diatom or Cuttlebone-Derived Organic Matrix were used to obtain architectures with a hierarchical porosity.[49,50] For all these systems, the principle is to impregnate the natural structure with the sol precursor of the material desired, and to trigger the sol-gel reaction. Although natural materials allow the synthesis of interesting structures, some applications require specific structures that cannot be synthesized by this method because of the lack of suitable templates in nature. That is why, in most cases tailor-made templates are employed, where rational design can be reached.

We can distinguish two main types of inorganic tailor-made templates: alumina templates and silica templates. They are commonly used as inorganic templates, which can be dissolved afterwards through HF or alkaline etching, if needed. Alumina templates are generally made from aluminum Anodisc® membranes made from anodized aluminum.[51] These small discs exhibit a very well define porosity with non-connecting straights pores aligned perpendicularly to the membrane surface. Therefore, these pores have been used as external templates in many syntheses of 1D objects (nanorods, nanotubes), with this template being removed after reaction by using a concentrated Sodium Hydroxide (NaOH) solution (Figure 14.c)).[52]

Silica templates are generally synthesized using soft-templates methods (see paragraph II.1.2), by surfactants or block copolymer templating (see paragraph II.1.1.2.), or by impregnation of a 3D arrangement of spherical particles (see paragraph II.2.2.).The variety of architectures, and facile removal with HF etching, makes silica a better mold than alumina templates. These structures have been mainly used for the synthesis of architectures presenting a hierarchical porosity.[53]

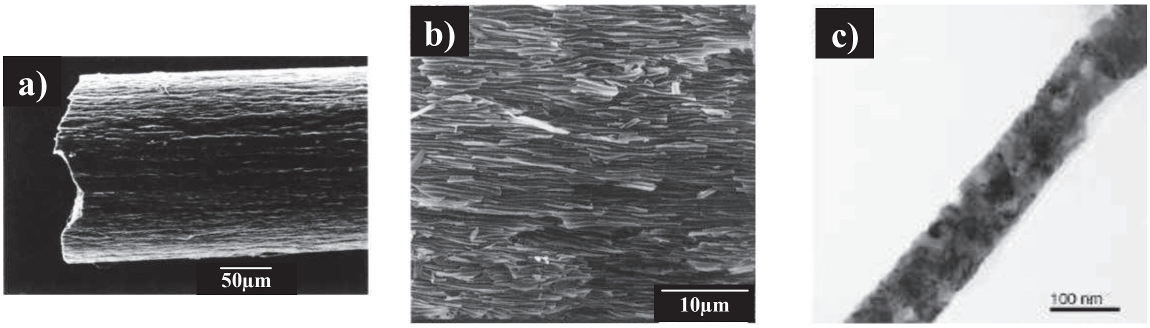

Figure 14. SEM images of a silica scaffold made using a Bacillus Subtilis as template a) exterior view, and b) cross-section of the fiber.[48] c) TEM image of an isolated CoPt nanowire obtain thanks to an alumina scaffold.[51]

This technique is quite powerful but, as for discrete particles, it involves the elimination of the template, which is not always straightforward and harmless for the new synthesized structure. That is why soft templates are generally preferred for such syntheses, where the removal of the template once the chemical reaction is finished, can be obtained through simple calcination treatment in air.

II.1.1.2. Block copolymers

As ionic surfactants, block copolymers present amphiphilic properties with the ability to form hexagonal, lamellar and sponge phases. The difference in templating, between ionic surfactants and copolymers, is the result of a broader family of copolymers, in nature, structure and size, that make them a more versatile group to achieve a larger domain of structures and pore size. Another advantage of block-copolymer, compared to ionic surfactant-based liquid crystals, is the rigid structure that results from their assembly, which allows the templating structure resisting the stress and strain resulting from the inorganic polycondensation reaction.

The first use of blockcopolymers as templates for mesoporous silica was reported by Bagshaw *et al.*[54] with Pluronic® 64L, and was expanded to other templates, inorganic materials, and structures. An example of a 3D wormhole mesoporous structure obtained with copolymers is displayed in Figure 15. Yang *et al.*[55] obtained numerous well-organized mesoporous structures of several oxides: TiO_2, ZrO_2, Al_2O_3, Nb_2O_5, Ta_2O_5, WO_3, HfO_2, SnO_2, and mixed oxides $SiAlO_{3.5}$, $SiTiO_4$, $ZrTiO_4$, Al_2TiO_5 and ZrW_2O_8. Later on, this technique was also combined with macroporous templates for the synthesis of alumina and silica monoliths presenting a hierarchical porosity.[56,57] For these materials, the block copolymer named "Pluronic®" was inserted into foams made of polyurethane in order to add some mesoporosity to the structure. This technique was later on largely explored for the structuring of the TiO_2 photoanode for Dye-Sensitized Solar Cells application. In the case of TiO_2 structuring, Pluronic® P123 is generally chosen as block copolymer and $TiCl_4$ as precursor of the titania framework. $TiCl_4$ in this case is attracted by the hydrophilic block of the co-polymer (ethylene oxide). The application of these mesoporous structure in DSSC was first reported by Kartini *et al.* in 2004,[58] and it exhibited a specific surface area around 150 $m^2.g^{-1}$with a mixed crystalline structure of rutile, anatase, and brookite. This process was improved later on by increasing the number of coated layers,[59–61] adjusting the sintering temperature,[62] and improving the coating method [63] (screen printing in place of dip coating). However, this templating method alone only gives cell photoefficiency around 5%. Until now, the best efficiencies (around 10%) are obtained for the cells where this templating method is combined with other techniques. These techniques are: the addition of additives (binders, surfactants) in the initial paste, the application of a $TiCl_4$ post treatment after the calcination process, and the addition of a scattering layer on top of the photoanode to ensure a better light trapping, among others.

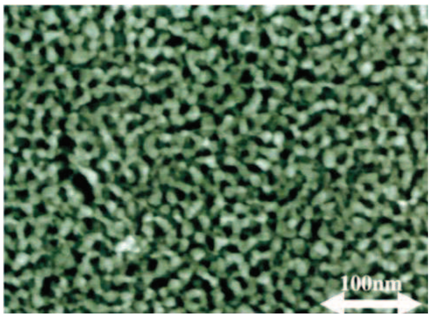

Figure 15. SEM image of a mesoporous structure synthesized with block copolymer templating.[59]

Unlike the hard template methods, which require an aggressive treatment for withdrawing the template, soft template techniques offer the advantage of mild conditions for the template removal, which prevent any post-synthesis degradation of the final material.

II.1.2. Soft template

As we can sense with the subtitle, "soft template" will make the use of molds coming from the fluid complex scientific domains where none external field will be applied dealing with extrusion, dip coating, spin coating and so forth.

II.1.2.1. Air-liquid foams

Macrostructures with hierarchical porosity can be obtained by using foams systems. The principle is the same than the use of emulsions as templates, but the biphasic liquid-liquid phase is now replaced by a biphasis liquid-gas phase. The first group working on this was G. L. Messing and coll. in 1990.[64] In this study, the foaming of the solution was induced by of Freon boiling, which was initially introduced at low temperature as a liquid. Once the foam had been created, the sol-gel reaction was triggered. It was only in 1999 that S.A. Bagshaw[65] synthesized hierarchically porous macrostructures resulting from foams, with the foam simply resulting from mechanical stirring of an aqueous solution containing non-ionic surfactants. Later on, other processes were used to form foams such as commercial foam spray,[66] that allowed for the combined injection of solution containing both the precursor of the sol-gel reaction along with the surfactant responsible for the creation of the foam, and the size of the pores was about 300µm. A promising method to form foams at room temperature was proposed by Livage in 2002[67] who used bubbling oxygen gas produced *in situ* through a viscous vanadium oxide gel in order to create vanadium oxide foams. The bubbling oxygen was created through the decomposition of H_2O_2 within the solution and the volume could reach up to 2.5L in less than 30min (Figure 16.a). The in-situ generation of gas was a promising concept for scale-up, but those foams demonstrated poor mechanical properties.

Finally, Carn *et al.* developed a technique that allowed controlling the pores size, pore shapes as well as the thickness and the length of the foam's Plateau border by introducing an insoluble gas in the inorganic sol coming through a sintered glass.[68] Varying the different parameters such as the diameter of the pores of the sintered glass and composition of the solution, monoliths architecture were prepared with a good shape control at all length scales (Figure 16.b)).

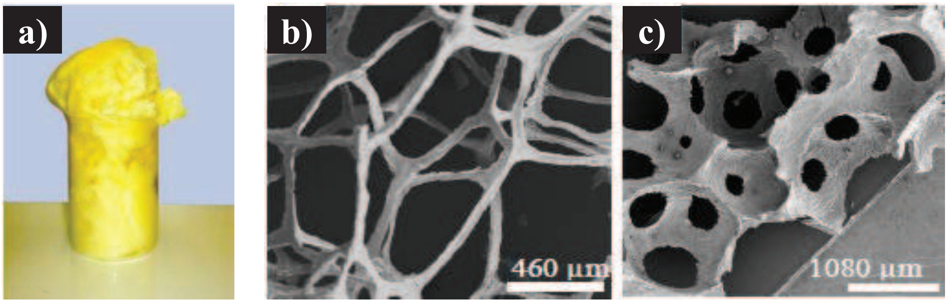

Figure 16. a) Picture of a Vanadium oxide foam obtain through the bubbling induced by H_2O_2 decomposition.[67] SEM images of inorganic foams synthesized by injection of an insoluble gas in inorganic sols: b) TiO_2 foam and c) SiO_2 foam. From F. Carn, Thesis of the Université Bordeaux 1, 2006.[69]

In parallel, the supercritical CO_2 foaming method was developed in the 1990's to synthesize polymeric microcellular foams.[70,71] The principle is the same that the one proposed by Livage *et al.* except that the foaming agent is the CO_2. It is inserted at the beginning of the experiment in its liquid state, under a pressure ranging between 50-300bars. Then, the pressure of the chamber is lowered after the polymerization was triggered which is responsible for the formation of CO_2 bubbles *in situ* leading to the formation of a porous structure. This method has been already adapted for a wide range of polymers (polyurethane, poly(methyl methacrylate), polystyrene)[72–74] and is even currently used in industry.

We have seen that this method presents a lot of advantages for the formation of monoliths with controlled pore size and geometry. However, these types of structures remain fragile, which limits their domain of application. In this context, emulsions are generally preferred for the synthesis of monoliths.

II.1.2.2. High Internal Phase Emulsion (HIPE)

It is possible to form macroscopic structures bearing macropores, mesopores and micropores from concentrated emulsions by combining/integrating different methods and processes. As presented in the section I.2.2., it is possible to form either micelles or liquid crystals with ternary system oil/water/surfactants which are used for the synthesis of discrete particles or mesostructured architectures. It was reported in parallel that High Internal Phase Emulsions commonly named HIPE, can be used to create macrostructures from emulsions.[75] These HIPE structures are obtained with microemulsions, when the volume fraction of the internal phase of the microemulsions becomes higher than 50% of the total volume. In this case, the micelles pack into a random compact arrangement of droplets of different size. If the continuous organic phase contains entities that can be polymerized, the whole structure can be frozen by polymerization, and a very open structure is obtained after water extraction.

Here, the interface between the aqueous and the non-miscible phase will act as a defect site for the system as it will represent a low energy zone minimizing the nucleation enthalpy.[76] If we introduce an organometallic precursor (metal alkoxide) in the organic phase, this precursor will start to react at the water/oil interface, the droplet being considered as a reservoir for the chemical reactor. In the case of a concentrated emulsion (HIPE), the reactors are close to each other and, as the inorganic framework resulting from the hydrolysis of the inorganic precursors will percolate and form a monolith structure. This method was used initially with polymers, by D. Barby *et al.* in 1982 for the synthesis of a macrocellular organic material with a hierarchical interconnected porosity named "polyHIPE".[77] This concept was later adapted to the sol-gel synthesis by A. Araya in 1989.[78] Since then, a lot of different types of HIPE were synthetized. The development of HIPE based on silica (called "SiHIPE") was developed by F. Carn *et al.* in 2004.[79] The macropores diameter of these structures, between 500 nm and 1 µm, was controlled by adjusting the volume fraction of the aqueous phase inside the droplet during the synthesis (Figure 17). Moreover, these structures exhibit a secondary porosity of 2-3 nm which confer them a high specific surface area.

As a result of their high surface area and their interconnected porosity, Si-HIPE are often used in combination with other materials for many applications. For example, they have been used as a simple support, which is functionalized with specific particles or molecules.[80,81] As an example, Brun *et al.*[1] functionalized Si-HIPE with Europium (III) ion, palladium, or even enzymes for applications in luminescence or heterogeneous catalysis (biodiesel synthesis). They synthesized also different frameworks from HIPE systems such as carbon, which was functionalized with $LiBH_4$ ions for hydrogen storage application.[82] It appears that HIPE structure is a powerful tool to create macroscopic architectures bearing a hierarchical porosity used for many purposes.[83] However, one drawback is that the inorganic materials resulting from this synthetic route, display low mechanical properties, and the whole architecture collapses even under moderate mechanical stress. Therefore, TiO_2 based poly-HIPE materials can hardly be used in current applications, and other routes have still to be explored to create more robust self-standing macrostructures.

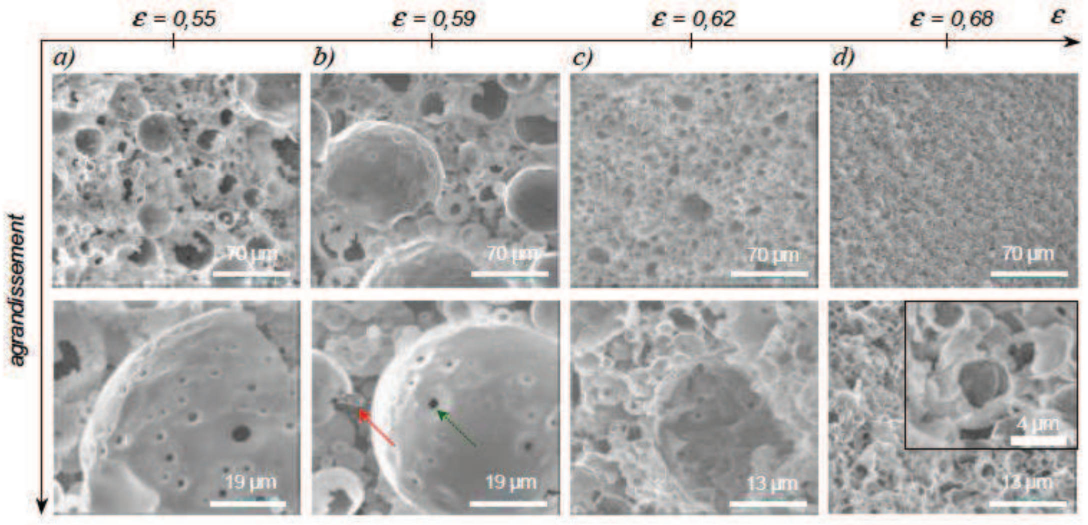

Figure 17. SEM pictures of « Si(HIPE)s » showing the influence of the oil volumic fraction on the porosity. The volumic fraction of the oil (dodecane) is respectively (a) 0,55 ; (b) 0,59 ; (c) 0,62; et (d) 0,68. From F. Carn, Thesis of the Université Bordeaux 1, 2006.[69]

In this section, we presented the synthesis pathways for 3D macrostructures. However, for many applications, thin films present many advantages due to their low thickness, an interesting feature when a high surface over volume ratio or a high light transmittance is required.

II.2. Design of 2-D macroscopic structures

In this section, we will present the different techniques used for the synthesis of thin films. The first part will focus on the most known techniques, and the second part will describe more especially the formation of films with optical/photonic property. This property is indeed interesting in many applications ranging from photonic to photovoltaic or even photocatalysis.

II.2.1. Major techniques to create a film

II.2.1.1. Evaporation (dip coating and drop casting)

Solvent evaporation is one of the most common techniques to obtain organized and structured films. At this stage, we have to distinguish two types of structurating mechanisms, with (i) films made from self-assembled pre-synthesized spherical particles, used generally as hard template, and (ii) films made from self-assembled micelles and inorganic precursors used as soft templates.

- Films structured with surfactant molecules

Mesostructured films made from a mixture of surfactant molecules and inorganic precursors, result from the organization of the matter induced by solvent evaporation, with the parallel self-assembly of surfactant as Liquid Crystals upon concentration increasing. As the solvent evaporates, the concentration of surfactant molecules inside the system increases, which has for consequence the organization of the surfactant molecules into mesophases ranging from micelles to hexagonal, lamellar or sponge mesophase. This method, called Evaporation Induced Self-Assembly (EISA) was introduced by Brinker *et al.* in 1999[84] and developed by Grosso *at al.* afterwards. They highlighted how the viscosity of the solution allowed them to adjust the evaporation kinetics, hence and the film structure and thickness. The thinnest films are obtained with a low viscosity solution when the surfactant concentration is below the CMC. In this case, only few seconds are necessary to evaporate the solvent and create a film. The EISA method is often combined with other methods such as dip-coating, Doctor-Blade, spin-coating or inkjet printing techniques. Here, these techniques only play the role of shaping techniques and they will be described in the following paragraphs.

- Films structured with spherical nanoparticles

In the case of pre-synthesized nanoparticles, with particles dispersed in solution, the film can be obtained through several deposition methods. Among them, we can distinguish the horizontal deposition (drop casting) and the vertical deposition (dip coating) (Figure 18.a)-b)). In this case, the technique used is not simply a shaping technique but its choice impacts also the coating processes, as explained below.

The drop casting method consists in the deposition of some droplets of a solution containing particles on a flat substrate. In this case, the solvent from the solution will evaporate and the particles concentration will locally increase near the edges of the droplet, which will magnify the attractive forces between the particles. This leads to the formation of a particles network and of a homogeneous film. This method has been especially developed by Denkov *et al.* for the formation of close packed structures of spherical particles.[85] Because this technique is based on the increase of particles concentration on the droplet borders, it can only be used with solutions where the particles diffusion kinetic is slower to the solvent evaporation kinetic.

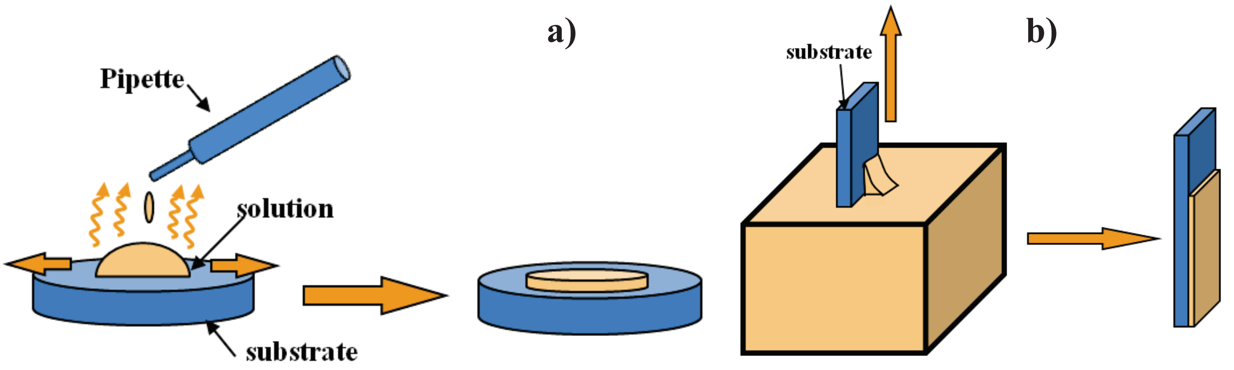

Figure 18. Representation of a) the drop casting process and b) the dip coating process.

With the dip-coating method, the solvent wets the substrate surface, leading to the formation of a meniscus. The solvent evaporation makes particles diffusing towards the meniscus, where they settle onto the substrate surface. In this case, the solvent evaporation kinetics should be higher than the particles deposition kinetics. This method has been widely used for the deposition of spherical particles arrangement since its development by Dimitrov *et al.*[86] and by Jiang *et al.*[87] Although, this method gives quite homogeneous films within the micrometer range (2-7 µm) due to the homogeneous dimension of the meniscus during the process, the thickness of the film can vary of about 10% due to the increase of the particles concentration with the time.[87]

In both cases, the affinity between the solvent and the particles, the particles concentration, the nature and the evaporation kinetic of the solvent, and the viscosity of the solution are key parameters to define the thickness and geometry of the film deposited.

II.2.1.2. Doctor Blade (tape casting)

Doctor blade (or tape casting) is one of the most widely used techniques for producing thin films on large surface areas. This technique aims to create a film of desired particles from a well-mixed slurry containing these particles along with other additives (such as binders, dispersants or plasticizers). In this technique, thickness spacers limit the area of the substrate where a film is created. The blade is positioned at one end of the substrate leaning on the spacers (Figure 19). Finally, the slurry is deposited in excess on the substrate – or in a mobile container linked to the blade - and the blade is put in movement relatively to the substrate. The movement is stopped when the blade reaches the other end of the substrate, once all the excess of slurry has been removed from the desired area. At the end of the process, the spacers are removed from the substrate and the edges of the films are cleaned to obtain a well-defined area.[88]

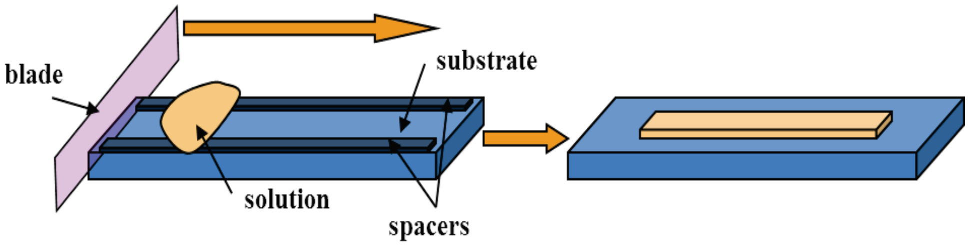

Figure 19. Representation of the Doctor blade method.

This technique was first developed in the 1940's by Howatt *et al.* in order to obtain thin sheets of piezoelectric materials and capacitors[89] and is now an accepted precision coating method. Several parameters will affect the thickness of the film: the speed of the blade, the thickness of the spacers, the solvent concentration and the viscosity of the slurry. Typically, the speed of the blade can operate up to several meters per minute and the thickness of the film varies from few microns to several hundred microns.[90]

II.2.1.3. Spin Coating

The spin coating process consists in the formation of a uniform film thanks to centrifuge forces. For this process, the substrate is held firmly on a rotating plate and spun at rather high speed. There are four major steps during the process: (i) the particle containing solution is poured onto the substrate; (ii) the spinning accelerates and the slurry is spread non-uniformly on the substrate, with the excess moving towards the edges; (iii) the excess of solution is wiped out from the substrate and only a uniform wet film remains; iv) the solvent evaporates with the air flux resulting from spinning, and a solid uniform film is obtained (Figure 20).

The key parameters that will influence the film thickness are the spinning speed, the solvent concentration within the initial solution and the viscosity of the solution. Typically, spin coater apparatus can rotate up to 10,000 rpm and the thickness of the films obtained can vary from 10 nm up to several tens of micrometers.[91]

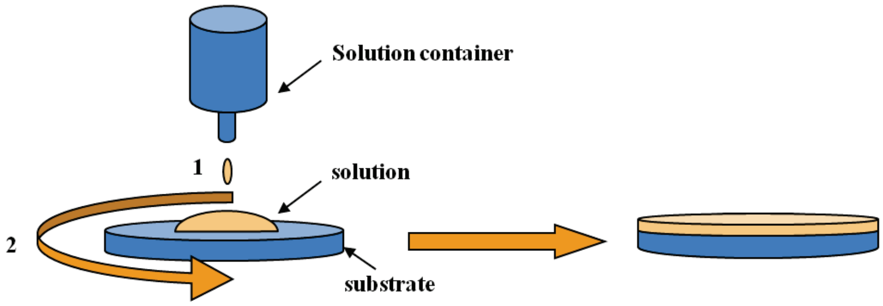

Figure 20. Scheme representing the spin-coating process.

II.2.1.4. Inkjet printing

Inkjet printing is a printing technique where there is no contact between the printing head and the substrate. In this process, small drops of the printing solution (few picoliters) are deposited onto the substrate by nozzles in order to form patterns (Figure 21). Historically, continuous inkjet technique (CIJ) was the first inkjet printing technology. The idea behind the process was not new at that time as it was patented by Lord Kelvin in 1867. In this technique, electrostatic forces are used to control the release of ink drops onto a sheet of paper. The first CIJ device was commercialized by Siemens in 1951, whereas the first inkjet printer was developed according to R.G. Sweet's experiments in the 1960's. However, in that process, the drop is deviated in order to form patterns, and this technology was further improved and Drop-On-Demand (DOD) systems were developed in 1977 by Siemens.[92] We can distinguish two main types of DOD printers where the difference resides in the energy which leads to the droplet formation: thermal and piezoelectric. In a thermal DOD, the ink is heated locally and a bubble is created as a result of solvent evaporation. This bubble leads to the ejection of the droplet. This method is limited to aqueous solvent and cannot be used with all polymers. With piezoelectric DOD, ink is contained into a piezoelectric material-based container that changes shape if an electric potential is applied, with the ejection of a droplet. This last technique is the most popular nowadays as it can be used with many solvents and for almost all types of particles.

However, in order to create an ink which fits an inkjet printing usage, the viscosity, the surface tension and the size of the particles within the solution have to be adjusted carefully to avoid any clogging or dripping of the ink in the nozzle. Typically, the dimensions of patterns for scientific applications are about few tens of microns width and few hundreds of nanometers thick. However, specific techniques and high resolution can decrease the width of the patterns to only few microns. [93,94]

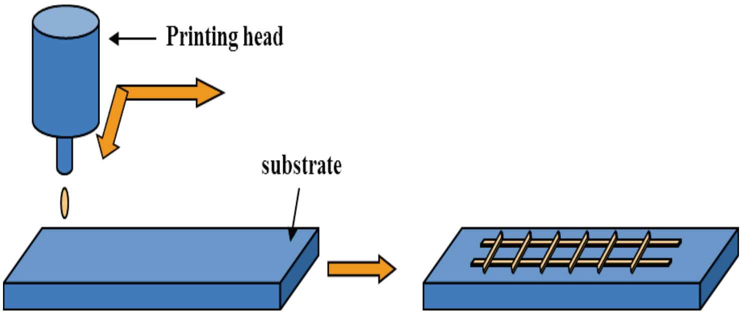

Figure 21. Representation of the ink-jet printing process.

In this part, some of the techniques commonly used to form a film have been presented. Depending on the thickness of the film desired, the film homogeneity importance and on the physical and chemical characteristics of the starting solution, some techniques will be preferred than others. When photonic properties are required for the final application, other techniques can be used. Some of these techniques are presented in the following paragraph.

II.2.2. Films with photonic or photoactive properties

For all the applications that require photoactive materials such as photoluminescence, photocatalysis, or photovoltaic, guiding the light through the bulk material is one the most important challenge. This is why a lot of efforts have been made on the synthesis of light trapping structures. Two major types of photonic structures were synthetized so far: the inverse opal structure [95–97] and the aligned nanowires structures[98–100] (Figure 18). In order to create a photonic effect, two parameters are necessary: the structure has to be well organized, and the dimensions of the pore where the light is trapped must follow the Bragg's law in order to obtain light internal scattering (which will act as a wave guide inside the structure).

The relation between the wavelength scattered and the size of the pore is given by the relation:[97]

$$\lambda = 1.633 \times \frac{d}{m} \times \sqrt{(f_1 \times n_1^2 + f_2 \times n_2^2)}$$

where, d is the cavities dimensions, m is the Bragg diffraction order, n_1 , n_2 , are the refractive index of the respective media and f_1 , f_2 the form factor of the cavities and interstices.

Although the light harvesting is increased in these structures, the studies reveal that the specific surface area inherent to this kind of structure is really low. In order to improve the materials properties, the next challenge will be to combine the high specific surface area of the mesoporous structures with the high harvesting properties of the organized structures.

II.2.2.1. Langmuir - Blodget technique

The Langmuir - Blodget technique is a derivative from the dip coating method. In this case, the films are obtained from amphiphilic particles. This method was first developed by Langmuir who studied the interfacial forces at liquid surfaces, and more especially, the behavior of amphiphilic particles at the water surface. He obtained the Nobel Prize for his work in 1932.[101] The film transfer onto a substrate was studied more in detail by Blodget in collaboration with Langmuir.[102,103]

Amphiphilic particles have the ability to float at the surface and with their hydrophilic part directed towards the water and their hydrophobic part directed towards the air. In order to have an arrangement of these particles in a crystal-like structure, the particles are compressed by a spacer placed at the surface. Once these particles are in a close-packed arrangement around the substrate, the substrate is pulled out of the container at the same time than the spacer moves towards the substrate, in order to keep the compression constant and, by doing so, maintaining the close-packed arrangement (Figure 22).

This –slow- method, known as nanospheres lithography, leads to the formation of homogeneous films presenting a well-ordered crystal arrangement, and it is mostly used for the formation of photonic structures.[104] Once the crystal-like structure is formed, the opal inverse structure of oxide materials can be synthesized either by using sol-gel processes, or by using other deposition techniques such as Chemical Vapor Deposition.

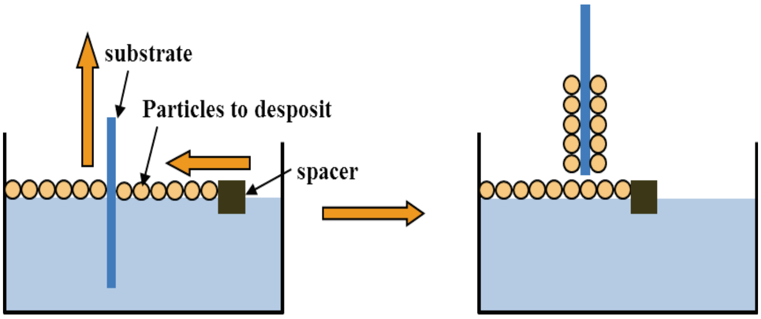

Figure 22. Scheme of the Langmuir-Blodgett technique.

This technique made possible the formation of multi-layers arrangement which can form photonic macrostructures (see Figure 23). It has attracted more and more interest lately as it is performed under mild conditions, it is cost effective and relatively easy to use.

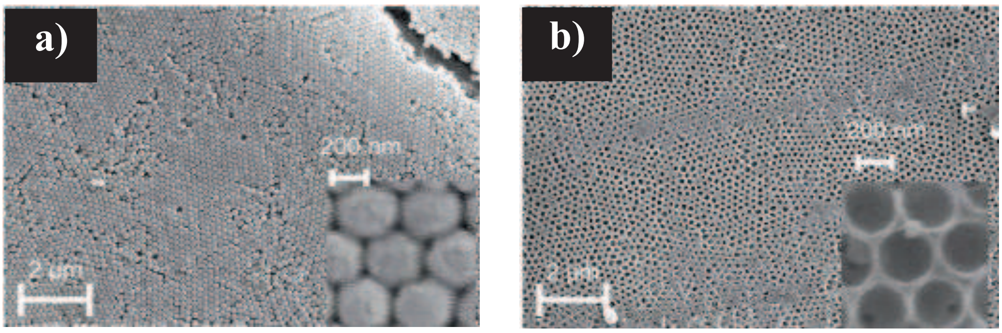

Figure 23. SEM images of a) an opal structure of silica spherical particles, and b) the inverse opal structure resulting from the deposition of a polymer and the removal of the silica template.[105]

II.2.2.2. *Chemical Vapor Deposition (CVD)*

Chemical Vapor Deposition[106] is a technique which allows synthesizing highly pure materials which can be designed for coatings, powders, fibers, and monolithic components. CVD is an old process developed first by Powell, Oxley, and Blocher in 1880's. At the beginning this technique was used for the production of incandescent lamps with filaments which strength was improved by an additional coating with carbon or metal.

In the CVD process, a solid coating is formed on a heated surface from a chemical reaction in the vapor phase. The materials formed can be synthesized using various chemical reactions, either used alone, or in combination, with thermal decomposition (pyrolysis) under specific atmosphere to favour reduction, hydrolysis, oxidation, carburization, and nitridation (Figure 24).

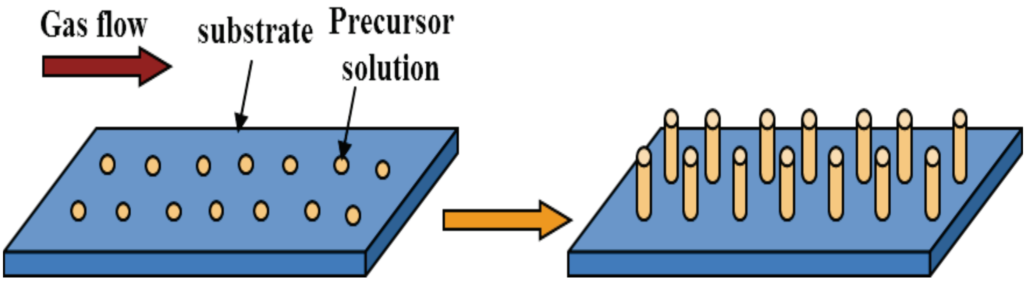

Figure 24. Scheme of the Chemical Vapor Deposition process.

CVD technique is a widely used technique as it can be used for the synthesis of most materials such as metals, oxides, carbides, nitrides, etc. Recently, this technique has been used in order to create photonic structures, either in combination with opal structures (formed by Langmuir-Blodget technique for example), or by spreading seed material droplets onto the substrate in order to create nanowires arrays. The alignment of the nanowires can also be improved by the use of a template to trigger their growth direction (Figure 25).[107]

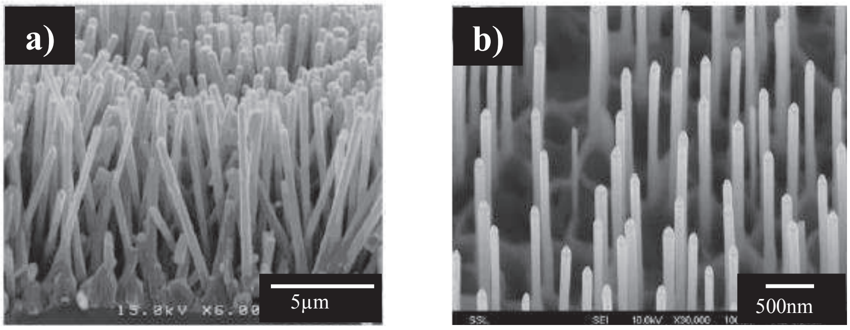

Figure 25. SEM images of (a) a side view[108] and (b) a top view of ZnO aligned nanowires structures.[107]

However, this technique works mostly in a batch mode, and reactors are usually quite expensive. This is why new techniques able to organize nanorods at high length scale for photonic application are still explored. This issue will be addressed in Chap.2 where we present the organization of ZnO nanorods within a macroscopic fiber.

In this part of the manuscript, we presented the techniques to create 2D macroscopic structures. In the next part, we will describe how to design 1-D macroscopic structures which are quite useful when high specific surface area and/or anisotropic properties are required.

II.3. Design of 1-D macroscopic structures (fibers)

This type of structures represents generally fibers. Fibers are very interesting structures as they are highly anisotropic, and present high specific surface area due to their high surface/volume ratio. They can possibly be assembled in woven mats. Manufacturing of very long organic fibers is a well-known technique, but the preparation of inorganic/organic composite or pure inorganic fibers, is more challenging. In this part, we will present the most popular techniques to generate such fibers. For all these techniques, the nanoparticles are first synthesized before their fiber structuring, the nanoparticles playing the role of nano-building blocks.

II.3.1. Electrospinning

Electrospinning is one of the most popular techniques to create polymer fibers because of its low cost and its easy process.[109] A polymer solution is extruded from a syringe through a needle (Figure 26), which is either positively or negatively charged with a high voltage power supply in order to create repulsive electrostatic forces. These forces overcome the solution surface tension, which will allow a continuous flow, and the charged extruded polymer, is collected on a plate, that is either neutrally, or oppositely charged. Between the extrusion and the collection process, the solvent evaporates and polymer fibers are collected.

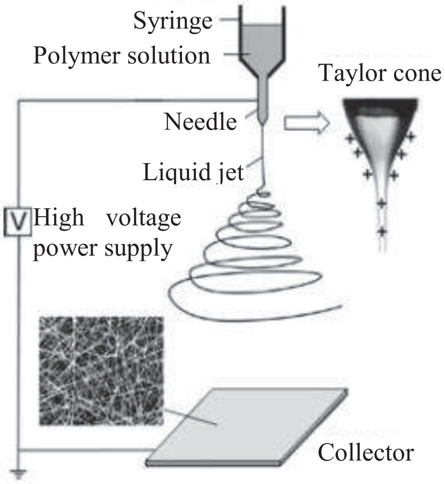

Figure 26. Schematic representation of the electrospinning process.[109]

This method was expanded to composite formulations with CNT or inorganic nanoparticles being added into the polymer solution. A large variety of different types of nanocomposite fibers were synthesized, such as TiO_2, ZnO, and carbon nanocomposite fibers. The polymer can be removed by thermal treatment afterwards, leading to purely inorganic fibers. TiO_2 electrospun fibers were tested in Dye Sensitized Solar Cells (DSSC), and a 6.2% photoefficiency was achieved.[110] The major issues with this technique is that the fibers are randomly oriented and that once the fibers are collected, their structure is fixed as they are difficult to handle (their diameter is in the range of few nanometers to few micrometers).

II.3.2. Melt-spinning

In this case, nanoparticles are mixed with a polymer, before the temperature of the resulting solution is increased to reduce its viscosity. The solution is extruded in air through a small circular needle, which cools down immediately, giving a stiffer fiber (Figure 27). A recent study reported the successful synthesis of TiO_2/polypropylene fibers via this technique, but not their application.[111] Although this technique can be used for a wide range of materials and fibers can be collected easily on winders, the complex structure of the extruder still makes the scale-up a difficult challenge, and electrospinning or extrusion process will be often preferred.

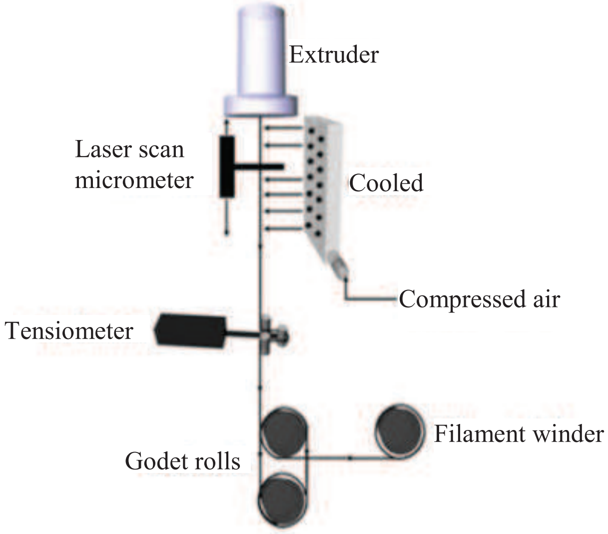

Figure 27. Schematic representation of a melt-spinning apparatus.[111]

II.3.3. Extrusion

II.3.3.1. Composite fibers prepared with the help of polymer coagulation

There are two different ways to extrude Polyvinyl Alcohol (PVA) based composite fibers. The first one is a process which was introduced by Vigolo *et al.* in 2000[112] for PVA/Carbon nanotubes (CNTs) fibers. This process consists in bridging the nanoparticles into a rotating bath containing the PVA solution. For this purpose, the surface of the CNTs is first functionalized using amphiphilic molecules which confer them a hydrophilic behavior and allow them to be dispersed in an aqueous solution. As the PVA chains are hydrophilic, when the CNTs are introduced in the beaker, the PVA chains are adsorbed onto their surface and act as a bridge between them (the PVA chains being connected to each other by hydrogen bonds). This principle was later adapted for the extrusion of Vanadium oxide (V_2O_5)/PVA composite fibers (Figure 28).[113] It was demonstrated that the extrusion flux allowed the particles to be aligned inside the fibers, which led to anisotropic properties and enhanced the mechanical properties.

The major drawbacks of this technique are that it can only be applied to nanoparticles with a very high aspect ratio and that the weight percentage of nanoparticles inside the fibers is generally low. In consequence, this method cannot be successfully applied if particles are either isotropic or anisotropic but with a moderate aspect ratio –as in our study-. For these particles, another method involving both polymer coagulation and reticulation was favoured.

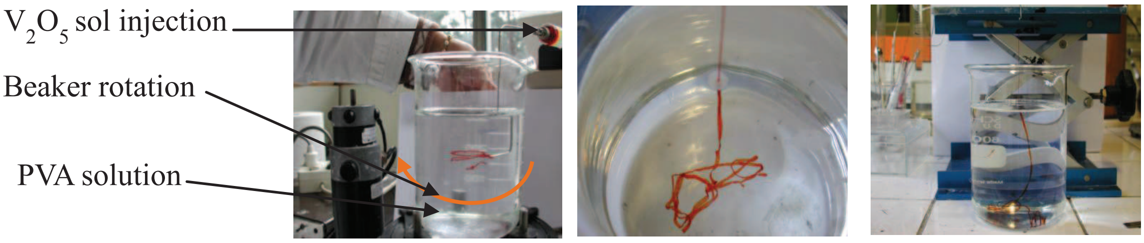

Figure 28. Extrusion system of V_2O_5/PVA composite fibers.[114]

II.3.3.2. Composite fibers prepared with the help of polymer dehydration/reticulation

For decades, PVA fibers were obtained through this process developed by Sakurada in 1985.[115] It was also adapted to the extrusion of PVA/CNT fibers,[116] with a CNTs dispersion being mixed with a PVA solution before being extruded into a concentrated solution of sodium sulfate (Na_2SO_4). The flocculation of the PVA chains results from the interaction between the Na^+ ions and the water molecules into the PVA chains, leading to a local dehydration of the PVA/CNT fibers (Figure 29).

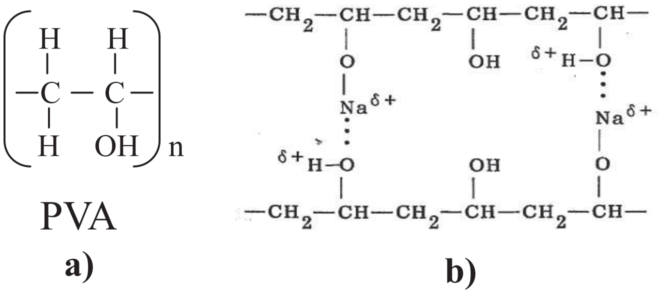

a) b)

Figure 29. Schematic representation of a) PVA molecule and b) of the salt-induced reticulation process.

The problem of this dehydration technique is that there is salt residues inside the fibers. That is why these fibers need to be washed after their formation in a solution which allows us to maintain the PVA floculation. A more detailed description of this method and on the resolution of the problems inherent to this method is discussed more in details from the Chapters II to IV.

In order to increase the fibers mechanical properties, it is possible to reticulate the PVA chains thanks to the addition of new components (glutaraldéhyde, borate ions). For example, borate ions were used as a reticulation agent by a japanese industry for the production of PVA fibers.[115] The reticulation mechanism is given Figure 30.

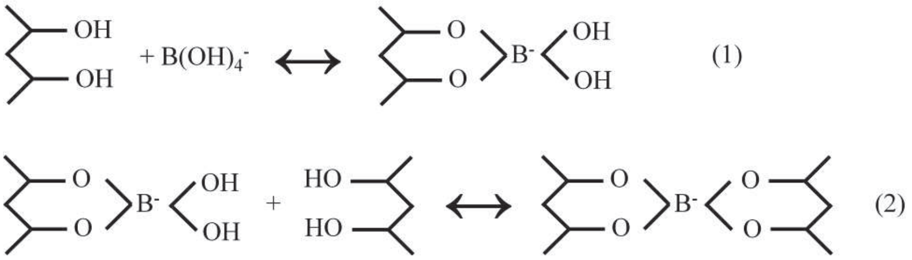

Figure 30. Reaction mechanism in two steps of the PVA chains reticulation using borate ions.

All these pathways were explored to generate 1-D, 2-D and 3-D macrostructures bearing hierarchical architectures, because specific and anisotropic properties were expected from these architectures, which we will discuss hereinafter, especially for optical and electrical properties.

III. Photoactive and conductor materials

In this PhD project we decided to focus more especially on photoactive (semiconductors) and conducting materials, and the following part describes how their macrostructure can influence their intrinsic properties.

In terms of electron transport properties, inorganic and organic materials can be divided in three main groups: conductors, semi-conductors and insulators. In all cases, the intrinsic nature of the material determines the category where it belongs. This is better described with its electronic band structure, and properties that can be easily deduced from, even though an accurate description requires the use of quantum physic equations, which is beyond our aim in this introduction.

The information presented in this section was extracted from the book of B. G. Yacobi *et al* published in 2004 where more detailed information can be found and where the theory of quantum physics is described.[117]

III.1. General considerations for atoms, electrons and energy bands

An atom is composed of a nucleus, considered as static in the structure due to its mass, and, of electrons which moves around the nucleus. Among the electrons, we can distinguish two types of electrons, the electrons highly stabilized by their proximity with the nucleus called core electrons, and the electrons less stabilized, and prone to interact with other species, called outer electrons or valence electrons. These valence electrons localized for solids in the Valence Band, are important in materials structure as they have the ability to interact with other neighbor atoms or can be relinquished upon excitation. It is the ability (or inability) of valence electrons to access easily –with a small energy gap - to empty electronic states (the Conduction Band for solids), that distinguishes conductors, semiconductors and insulators: (i) if the valence electrons do not need extra energy to become free carriers, the material will be classified as conductor, (ii) if they require a small amount of energy (some eV), the material will be classified as a semi-conductor, (iii) if the energy required is far too important, the material will be an insulator.

III.1.1. Inorganic materials

In the case of inorganic materials, a classic way to build the energy band diagram is to look at the crystalline structure and the relative position of the atoms within the material. For this approach, the valence electrons can be considered as moving in a periodic crystal potential V(r), which is periodic with the periodicity of the lattice. According to the *Schrödinger* equation and the *Kronig–Penney* model,[117] the electrons can only possess some discrete energy values when moving in a potential well. As a periodic crystal potential is a succession of potential well of the same energy, an electron moving in a crystal potential V(r) can only possess some discrete energy values. Moreover, as some energy levels are very close to each other, they can be regrouped within energy bands referred as *"allowed"* bands. In this configuration, some energy bands will be considered as "*allowed*" and some energy bands will be considered as "*forbidden*" for the movement of the electrons, the *"forbidden"* bands corresponding to bands where the energies are not solutions of the *Schrödinger* equation. In this configuration, the highest energy occupied band will be called the *valence band* and the lowest energy unoccupied band will be called the *conduction band*. The influence of the electrons distribution within these bands will be presented in the paragraph III.2.

III.1.2. Organic materials

In the case of organic materials, it is the chain structure and more especially the way the component will be bond "mostly covalently" and distributed which will help building the energy band diagram of the material. As we discussed earlier, electrons are moving around the nucleus at different energy levels and their behavior is then described as an electronic wave function. In this configuration, the electrons are considered to move freely on *atomic orbitals* (AO) which represent all the positions where the electrons can possibly be at a specific instant. When a solid is formed and the atoms will be placed next to each other, the electronic wave function of the atoms (atomic orbitals) will overlap generating molecular orbitals (MO). In this case, the new electronic waves functions generated will be approximated by a linear combination of the atomic wave function referred as *linear combination of atomic orbitals* (LCAO). As the wave functions can be either positives, or negatives, they can be either added both in-phase in a constructive way, or out-of-phase in a destructive way. In the first case, the combination of the AO forms a MO of less energy than the original AO which is stable and preferably filled of electrons, it is the **bonding** orbital. In the out-of-phase case, the combination of the AO forms a MO of higher energy than the original AO which is unstable and generally free of electrons, it is the **anti-bonding** orbital. Figure 31 present the dihydrogen case.[118]

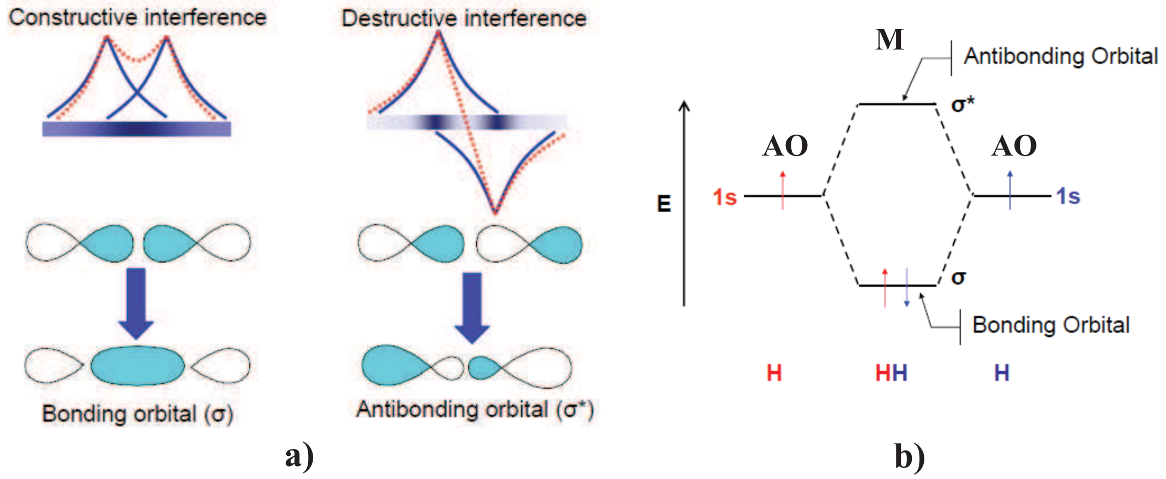

Figure 31. Schematic representation of the interactions happening when the atomic orbitals of two hydrogen atoms overlap: a) representation of the interferences for bonding and anti-bonding orbitals (the orbitals of the same colors possess the same phase (sign)), b) representation of the process in an energetic point of view.[119]

In the case of an atom bearing *N* valence electron with AOs of the same energy, *N* possible energy levels will result comprising *N*/2 bonding MO and *N*/2 anti-bonding MO. These energy levels will be regrouped in energy bands similarly to inorganic compounds. The highest energy band filled of electrons (bonding energy levels) is similar to the valence band in inorganic materials and is called the Highest Occupied Molecular Orbital (HOMO). On the other hand, the lowest energy band unoccupied by electrons (anti-bonding energy levels) is similar to the conduction band for inorganic materials and is called the Lowest Unoccupied Molecular Orbital (LUMO). These two bands constitute the *allowed* band for the electrons, and the band in between (if it exists) constitutes the *forbidden band* for the electrons.

Here, we described the basics for the building of the energy band diagram of organic materials. Now, we will explain how this band diagram will be used to determine the intrinsic properties of inorganic and organic materials.

III.2. Energy band diagram and materials properties

As we discussed previously, a material possess a valence band (HOMO) and a conduction band (LUMO). If a band is fully unoccupied, it does not contribute to the electrical conductivity of the material because it does not contain any electrons. In the contrary, fully occupied bands cannot contribute to the electrical conductivity because all the levels will be occupied which prevents any electrons from gaining energy within the band when an electric field is applied. From this observation, we can conclude that only the partially filled bands can contribute to the electrical conductivity of the material. In the case of conductors, there are two possibilities: either the valence band is partially filled which ensure the conductivity of the material, or there is an overlap between the valence band and the conduction band which allow the passage of the electrons from one band to another without any problems. In the case of semiconductors and insulators, there is a gap (a forbidden band) in between the occupied valence band and the unoccupied conduction band. The width of this gap will make the distinction between semiconductors and insulators. A fairly small gap will be characteristic of a semiconductor material whereas a very wide gap will be characteristic of insulator materials (Figure 32). Basically, a material will be considered as semiconductor if the gap energy (Eg) between the valence and the conduction band is lower than 3.5eV and as an insulator above.

Among these categories, semiconductor materials are particularly interesting because their properties can be influenced by exterior stimuli such as light and pressure. Indeed, if a light source bearing the same energy than the band gap energy (Eg) of the semiconductor is projected on the material, an electron from the valence band of the material will be excited and transferred to the conduction band which will create an electron-hole pair within the material. This electron-hole pair can be used in different ways for different applications such as photoluminescence, photocatalysis and photovoltaic. The use of these electron-hole pairs will be more developed in the following chapters. In this project we decided to focus more especially on nanoparticles of zinc oxide (ZnO) and titanium dioxide (TiO_2). These materials posses a band gap energy between 3.2 and 3.4 eV which means that they are wide band gap semiconductors which will absorb in the domain of Ultra-Violet (UV) light. Thanks to their electronic properties, these materials are particularly interesting for applications where protection from UV light is needed such as sunscreen cream but also for photoluminescence, photocatalysis and photovoltaic application.

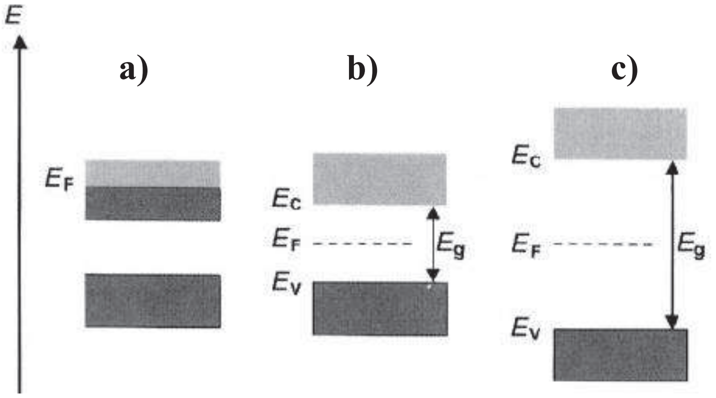

Figure 32. Energy band diagram representation for a) conductor materials, b) semi-conductors materials and c) insulator materials.[117]

In conclusion to this part, we can say that the intrinsic material structure is mainly directing its physical properties. These properties can be predicted by building the energy band diagram of the materials which will give us the information on its electrical and optical properties. In consequence, the analysis of the band diagram is essential to determine for which application a material can be used and how it can be combined with other materials.

IV. Conclusion

In this chapter we have presented the different methods to synthesize and shape materials from the nanoscale to the macroscale. We described first, how the particles shape and size can be controlled by adjusting the experimental conditions. More specifically, we detailed how the choice of the precursor (metallic cation with its ligands), the pH of the solution, the solvent nature, the temperature and the precursor concentration could affect them. A fine adjustment of these parameters allows obtaining materials with the desired crystalline structure. Also, the introduction of shape controllers or templates within the reaction media can help shaping the particles, which is of great importance for the synthesis of anisotropic particles. In our case, both shape controllers and soft templates (Swollen Liquid Crystals) are used for this purpose.

Then, using these nanoparticles as nano-building blocks, we have detailed the methods allowing designing the material macrostructure architecture along with its mesostructure. The methods used for the design of 3D, 2D and 1D architectures were presented. Due to their simplicity, their low cost process, and their possible application in industry, we chose to focus more on extrusion process using a coagulation bath for 1D structures (fibers), and on Doctor Blade and drop casting technique for 2D structures (films).

Finally, we have demonstrated how the intrinsic structure such as crystalline structure or arrangement of polymer chain could influence their optical and electrical properties. All these concepts are related to each others as the nanoparticles crystalline/chain structure can be tuned by the experimental conditions of the particles synthesis (part I). Moreover, the shaping of the material meso/macrostructure into hierarchical architectures and the design of their porosity (part II) can also affect the intrinsic physical properties.

V. PhD objectives

In this PhD project, we have intended to synthesize new materials by combining these strategies in order to improve the materials properties for each application. In a first step, we have combined the anisotropic photoluminescence properties of zinc oxide (ZnO) nanorods particles with the extrusion process in order to obtain macroscopic fibers bearing anisotropic properties. In a second step, we have synthesized macroscopic fibers of titanium dioxide (TiO_2) for photocatalysis application. Here the fibers geometry was used in order to create a synergy between the pollutant gas flow and the fibers without inducing a loss of charge within the reactor. In a third step, the TiO_2 fibers extrusion starting solution and process were improved in order to generate fibers with higher photocatalytic efficiencies with a semi-industrial process. Finally, anisotropic conductive polymer particles (PPy) were synthesized in order to generate organic electrodes presenting higher conductivity than the one using isotropic particles.

Chapter 2:
ZnO/PVA Macroscopic Fibers Bearing Anisotropic Photonic Properties

In Nature, we can observe that specific organization of nanoparticles at various length scales can have a strong impact on the material resulting properties. For example, it is the case of nacre where the organization of flat-like sheets of calcium carbonate in a layered arrangement confers to the material specific properties. This arrangement in nacre is especially responsible for optical properties, iridescence, and for high mechanical properties, the resistance of nacre being one thousand times higher to the one of simple calcium carbonate powder.[1] From this observation, organizing anisotropic nanoparticles inside macroscopic structures is a recent challenge which opens new perspectives for various application domains. The power of "soft chemistry" when combined with complex fluids has allowed to obtain macroscopic fibers of carbon nanotubes and vanadium oxide ribbons which has been used mainly for their mechanical, electrical, optical and sensor properties.

In this context, this Chapter will be dedicated towards the synthesis of Zinc Oxide (ZnO) nanorods/ Polyvinyl alcohol (PVA) macroscopic fibers studied for their photoluminescence properties. In a first step, the fibers will be obtained by extrusion process and their composition will be determined. Then, the fibers will be stretched at different elongation percentage in order to determine the influence of this stretching on the nanorods alignment inside the fibers. The influence of the protocol used to stretch the fibers will be also studied at this stage. Finally, the fibers will be tested for their mechanical and their photoluminescence properties where we will emphasize the influence of the nanorods alignment inside the fibers on these properties.

I. General concept and objectives

I.1. ZnO structure

In this part we will describe briefly the ZnO structure. More details can be found in the book of Klingshirn *et al.*[2]. The electronic structure of Zinc is $(1s)^2(2s)^2(2p)^6(3s)^2(3p)^6(3d)^{10}(4s)^2$ which means that Zinc possesses two valence electrons on its 4s orbital. The Oxygen electron configuration is $(1s)^2(2s)^2(2p)^4$, and so, it possesses six valence electrons on its outer shell. However, among them, only two electrons on the 2p orbitals can create bonds with other elements, as the four others are lone pair electrons. In consequence, the bonds in ZnO crystal lattice involve a sp^3 hybridization of the electron states, leading to four equivalent orbitals, directed in tetrahedral geometry. As discussed in the Chap. 1 section II.1.2., the bonding orbitals constitute the valence band, and the conduction band originates from its antibonding counterpart.

The Zinc tetrahedral coordination determines the ZnO crystal structure where every Zinc atom is surrounded by four oxygen ions. In this configuration, the bulk structure has a bi-layer structure constituted by a zinc layer and an oxygen layer, resulting from the arrangement of the neighboring tetrahedrons. Zinc oxide can present two main types of structures: a cubic zinc blende structure (Figure 1.a.) or a hexagonal wurtzite structure (Figure 1.b.) depending on the stacking sequence of the bi-layers. The zinc-blende structure corresponds to an arrangement of two interpenetrating face-centered cubic lattices which have been displaced by ¼ of the body diagonal axis. It belongs to the $F\bar{4}3m$ space group. The hexagonal wurtzite lattice is a uniaxial lattice. Its main axis, referred as c-axis, is directed along one of the tetrahedral binding orbitals. The **a** and **b** vectors of the lattice are perpendicular to the c-axis, have equal length, and include an angle of 120°. The wurtzite primitive cells comprise two ZnO units, each one comprising two pairs of ions. This structure belongs to the $P6_3mc$ space group. ZnO crystallizes with great preference in the wurtzite structure which will be the most common structure synthesized. At ambient conditions, the ZnO wurtzite has the lattice constants $a = b = 0.3249$ nm and $c=0.52042$nm with a specific mass density of $d = 5.675$ g.cm^{-3}.

Due to the great difference in their electronegativity, the Zn-O bond presents a strong degree of polarity. Indeed, the oxygen present the second highest electronegativity value among all chemical elements (3.44 on the Pauling scale) after fluorine, and Zinc possesses a low electronegativity value (1.65 on the Pauling scale). As a result, the ZnO structure elements could be almost considered as ionized Zn^{2+} and O^{2-}. Besides, in consequence of this high bond polarity, the wurtzite structure is favored during the synthesis compared to the zinc blende structure which occurs preferentially for tetrahedrally oriented bonds with lower polarity like GaAs. This last structure can be obtained for ZnO only if it was grown on a zinc-blende type substrate like GaAs (100) with a ZnS buffer. Moreover, the polar character of these bonds is responsible for a small deviation of the structure geometry compared to the ideal wurtzite geometry. Indeed, the tetrahedrons are slightly distorted with a difference in the angle between the c-axis towards the other bonds (α) of 0.01° and an axis length ratio which is 2% below the ideal wurtzite ratio value. The deviations observed in ZnO structure are the highest of all the wurtzite structures identified so far. Due to its specific structure ZnO and its high polarity, present a great interest for its property such as piezoelectric, thermal, and optical properties. In this project, we decided to focus on its optical properties, especially photoluminescence which are anisotropic due to its high polarity.

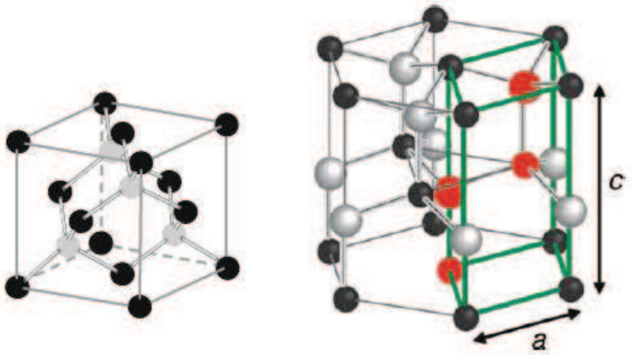

Figure 1. The cubic zinc-blende-type lattice (**a**), and hexagonal wurtzite-type lattice (**b**). In the wurtzite lattice, the atoms of the molecular base unit (2x ZnO) are marked by *red* full circles and the primitive unit cell by *green* lines.[2]

I.2. ZnO photoluminescence properties

I.2.1. Photoluminescence

Photoluminescence is a non-destructive technique employed for the analysis of materials structure, more especially to detect the presence of defects within the materials structure.[3] As discussed in paragraph III of Chap.1, the electrons can only possess energy values within the *"allowed"* energy bands when moving in a crystal lattice structure. In a semiconductor, the highest allowed occupied band (valence band) and the lowest allowed occupied band (conduction band) are separated by a *"forbidden"* energy band, the width of this latter band being called the band gap energy (E_g). According to this structure, in order to excite an electron from the valence to the conduction band, it is needed to transfer a minimum energy to the electron, at least equal to E_g. During a photoluminescence (PL) experiment, the electrons are excited through optical excitation resulting in the creation of electron-hole pairs called excitons. These excitons will then deactivate either radiatively or non-radiatively. The exciton lifetime depends on the crystal lattice, the nature and concentration of impurities, and other defects present in the structure. The principal interest of PL resides in the deactivation through a radiative process as it can be detected and measured easily. There are five main transitions that can be observed during a PL experiment (Figure 2).

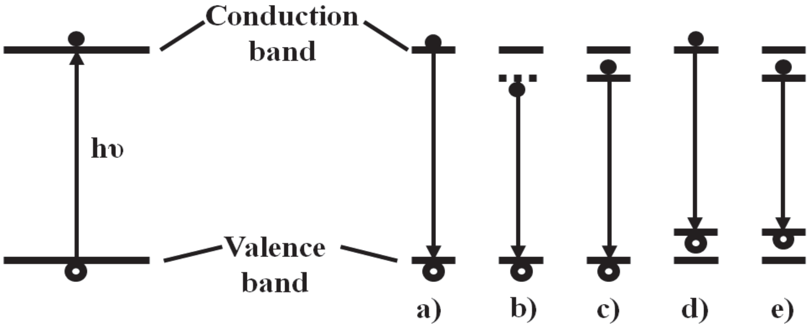

Figure 2. Excitation process of an electron (left side) and the most commons deactivation processes associated a) band-to-band recombination, b) free excitons recombination, c) exciton bound to donor recombination, d) free electron to acceptor recombination, and e) donor to acceptor recombination.[3]

The first transition represented is generally observed for materials with small effective mass with large electron orbital radii. It corresponds to a simple band-to band recombination and lead to the emission of a photon possessing the same energy than the band gap of the material. The second process corresponds to free excitons recombination. The energy of the photon emitted is lower than E_g because of the coulombic attraction existing between the electron-hole pair. The third process represents the case where the exciton will be bound to a shallow donor during its excitation and will then recombine with the hole. The fourth case corresponds to the situation where the free electron generated by the excitation will recombine with an acceptor. In both cases, the energy value of the photon will be lower than E_g and will be determined by the nature of the acceptor and the donor. Finally, in the case where there are both an acceptor and a donor specie inside the structure, we can have a last transition corresponding to an acceptor-donor transition.

I.2.2. Photoluminescence in ZnO

From the previous section, it can be deduced that the PL spectrum will display several peaks, positioned at energies inferior or equal to Eg depending on the type of radiative transition that the electron will undergo. So far, numerous studies were performed on ZnO structures to index the PL spectrum peaks and to determine their origin, but this last point is still controversial. In Figure 3 we can find a summary of the different defects that have been identified with their respective energy shift compared to the conduction band. From these values, the peaks observed on a low temperature PL spectrum can be indexed, from which the photon energy resulting from the different transitions can be deduced.

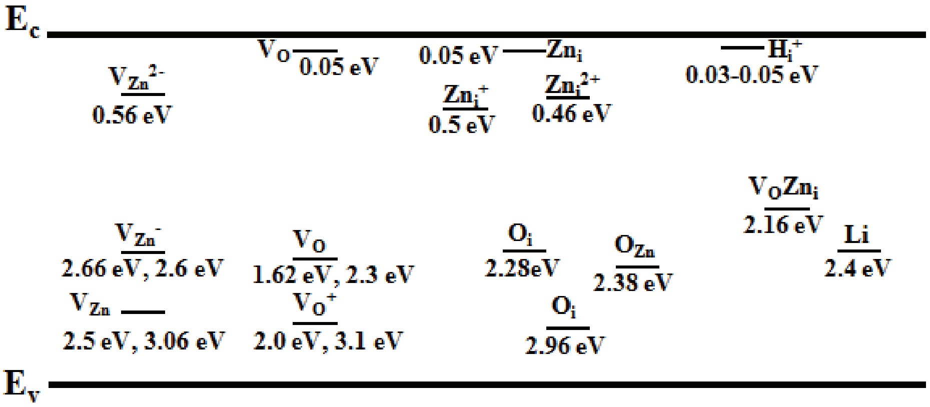

Figure 3. Calculated energy levels of different defects in ZnO from different studies in the literature.[4] All the levels are referred to the conduction-band minimum energy (Ec). V_{Zn}, V_{Zn}^-, V_{Zn}^{2-} denote neutral, singly charged, and doubly charged zinc vacancy, respectively. Zn_i, Zn_i^+ and Zn_i^{2+} indicate neutral, singly charged and doubly charged zinc interstitial respectively. V_O denotes neutral oxygen vacancy while V_O^+ and V_O^{2+} denote singly charged and doubly charged oxygen vacancy. H_i^+ and O_i represent single charged hydrogen and oxygen interstitial, respectively. O_{Zn} indicates antisite oxygen and V_OZn_i corresponds to a complex of oxygen vacancy and zinc interstitial. Li corresponds to impurities linked to the presence of Li ions into the structure.

However, there are significant differences between PL spectra recorded at low temperature (LT) and PL spectra recorded at room temperature (RT). As discussed previously, the excitons generated during a PL experiment can be either free excitons, or can be bound to donor or acceptor specie during the excitation and deactivation processes. If the free-exciton binding energy with the donor and acceptor species is too small, the excitons are thermally dissociated from their centers at RT and, in this case, the peaks corresponding to their presence are no longer observed at RT. For this reason, some transitions peaks present at LT disappear at RT. Moreover, the PL peaks of the transitions still occurring at RT become broader due to vibronic processes and are shifted to lower energies.[5] In our study, we investigated the behavior of our macroscopic fibers at RT in order to assess the quality of the ZnO crystals. In this case, the PL spectrum presents one sharp peak positioned between 373 and 390 nm corresponding to near band edge (NBE) emission correlated to an exciton-exciton collision process, and one broad peak in the green part of the visible spectrum correlated to deep level defects in the structure.[6] Moreover, in some cases the peak of the NBE emission presents a shoulder around 390 nm.[7] The origin of this last peak is still controversial in the literature. So far, this peak has been attributed to first LO phonon replica of free excitons, free-to-neutral acceptor transition involving stacking faults, surface excitons, and, excitons bound to neutral acceptors.[7–10] Recently, several studies have ruled out some of these hypotheses and this peak is predominantly attributed to surface defects leading to free excitons - neutral acceptor transitions.[7,8,11,12] It was also demonstrated that even though it is not possible to extract a value for the impurity level from PL experiment, the ratio between the NBE peak and the green emission peak (due to deep level defects) constitute a good indication on the quality of the crystal. In our case, as we desired nanorods with few structural defects, it was needed to obtain the smallest green emission peak. The results and discussion of the photoluminescence of the ZnO/PVA macroscopic fibers are presented in section III.3.

I.3. Organization of ZnO nanorods in macroscopic fibers objective

The development of biomimetic routes to reproduce structure and properties of nacre (optical and mechanical) has lead to the synthesis of several organic-inorganic hybrid generated using inorganic particles with very high aspect ratio in order to obtain specific properties. More especially, the association of micro-extrusion and gelling mechanisms, allowed Vigolo *et al* [13] to achieve the preparation of Carbon nanotubes/ Polyvinyl Alcohol (CNTs/PVA) fibers in 2000. Thanks to a post-synthesis stretching of the fibers above the PVA glass transition, it was possible to improve the alignment of the CNTs along the fiber main axis.[14] These fibers were mostly studied for their mechanical, electrical and thermal properties. In particular, it has been demonstrated that by improving the alignment of the CNTs along the fiber main axis, it was possible to improve these three properties.[14,15] Later on, our research group synthesized vanadium oxide (V_2O_5)/PVA macroscopic composite fibers for their optical and sensor properties.[16–19] This study showed that V_2O_5/PVA composite fibers present enhanced anisotropic birefringence and sensor sensitivity due to a collective alignment of the nanoribbons along the fiber main axis depending on the nanoparticles alignment. This alignment was adjusting thanks to the shear rate during the extrusion process.

In this chapter, we decided to investigate a new type of fibers, which contain ZnO nanorods as the inorganic part. We aimed at checking if the alignment of a population of ZnO nanorods within the fiber would create a synergetic response among the nanorods to produce anisotropic properties independently of any physical contact between them. As ZnO possesses a much lower aspect ratio than CNTs or V_2O_5 ribbons, it was necessary to use another coagulation method than previously reported, during the extrusion process. The initial extrusion shear rate was chosen according to that required for a maximum of alignment of the V_2O_5 ribbons inside the fibers. The alignment of the ZnO particles were improved by a post-synthesis stretching of the hybrid fibers above the PVA glass transition at T=85°C. We report hereinafter the influence of this stretching/alignment on the fibers properties.

Zinc oxide is a wide direct band gap semiconductor with a band gap of 3.37 eV and high exciton binding energy (60 meV). This last energy is larger than the thermal energy at room temperature,[20] which make Zinc Oxide a good candidate for photovoltaic, ultra-violet nano-optoelectronic devices and lasers operating at room temperature.[21] Considering the morphology of ZnO, a tremendous amount of nanostructures have been obtained ranging from nanowires,[22] nanorods,[23] nanobelts,[24] nanotubes,[25] aligned nanonails,[26] and so forth. Due to their higher aspect ratio and their easy process, we decided to focus on the nanorods nanostructure. Properties of ZnO regarding the absorption and emission properties are well-known,[27–29] but it is interesting to check if the expected emission polarization predicted from modeling,[30] can be observed for ZnO anisotropic structures. As measurements on a single nanorod are difficult,[31] being able to align a whole population of ZnO nanorods along a single axis, is a better way to evaluate the macroscopic effect of collective alignment. As a result, beyond the specific interest of validating anisotropic properties provided by shape anisotropy at the nano-scale, actual functionality can result from a magnification of this local property by providing the correct synergy among a collection of nanoparticles through preferential orientation, and true applications can result from this magnification if the design and processing of these synergistic nanostructures is easy.

II. System studied and experimental protocol

II.1. ZnO nanorods syntheses

The synthesis of ZnO nanorods was inspired from Zhu *et al.*[32] Typically, 0.95 g of $ZnCl_2$ and 0.75ml of $N_2H_4.H_2O$ were added to 160ml of distilled water under stirring. A slurry-like white precipitate was formed. Once the solution became homogeneous, it was transferred into an autoclave and was maintained at 200°C for 24h. The zinc oxide sol weight fraction was determined through dry extracts and adjusted at 2.8% (pH=7). As shown in Figure 4.a., the ZnO particles present a significant anisotropic shape with an aspect ratio, length/diameter, of around 20. This shape ratio would formally rank these particles among the "nanowire" nomenclature, but we think that the "nanorod" terminology remains more appropriate and descriptive.

II.2. ZnO/PVA co-extrusion process

The final solution was prepared by adding 1.2g of solid polyvinylalcohol (PVA) into 10 mL of the 2.8% ZnO solution under stirring at 90°C for 1h. The molecular weight of PVA was chosen high enough to ensure good mechanical properties of the fiber (Mw= 120 000). The ZnO/PVA solution is injected with the nanoparticles into a rotating beaker containing the gelling agent, that is, a saturated aqueous solution of Na_2SO_4 (Figure 4.b.). The dehydration mechanism was presented in Chap.1, part II.3.3.2.

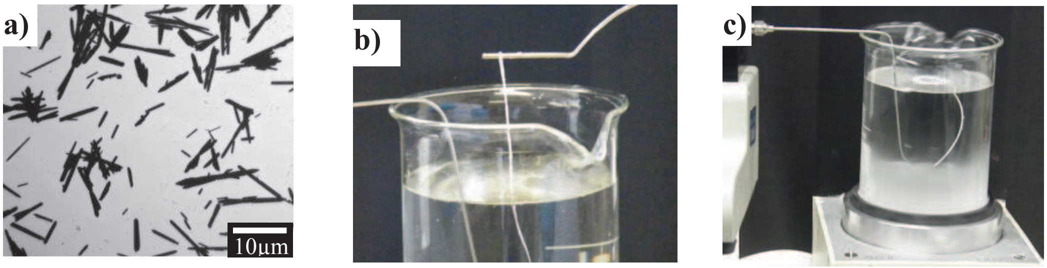

Figure 4. Overall synthetic path. a) as-synthesized TEM picture of ZnO particles b) typical extrusion where the PVA/ZnO hybrid sol is injected through a syringe needle into a rotating beaker containing a Na_2SO_4 saturated water solution. c) as-synthesized hybrid fibers extracted by hand from the beaker.

The extrusion was maintained tangential to the rotation axis of the beaker in order to promote a pseudo-coaxial flux at the external part of the syringe hole. The diameter of the spinneret is around 1mm. The beaker containing the salt solution was kept at constant rotation of 25 rpm, while the solution containing the PVA/ZnO dispersion was extruded out of the syringe at a constant flux of 40 ml.h^{-1}. Upon the completion of the extrusion process, the ZnO/PVA fibers were meticulously taken out of the beaker by hand (Figure 4.c.) and allowed to dry in air (ambient conditions). Finally, the fibers were washed once in water to remove the excess of salt.

II.3. ZnO fibers extension process

Stretch under load of the fibers was performed in a chamber equipped with a system allowing controlling the temperature inside it coupled with a ZWICK/ROELL Z2.5 apparatus (Figure 5). In order to avoid the fiber to slide during the process, it is first glued to a paper frame with cyanoacrylate glue before its insertion between the jaw of the traction apparatus, the length of the frame being fixed at 25 mm. Before the stretching of the fibers, the temperature of the chamber was brought to 85°C in order to be above the PVA glass transition. The fiber was then stretched at a constant traction speed of 1 mm/min (4% of the initial length) till it reached the desired elongation percentage. The fiber is then cooled down at room temperature still maintained by the traction system to avoid any further deformation.

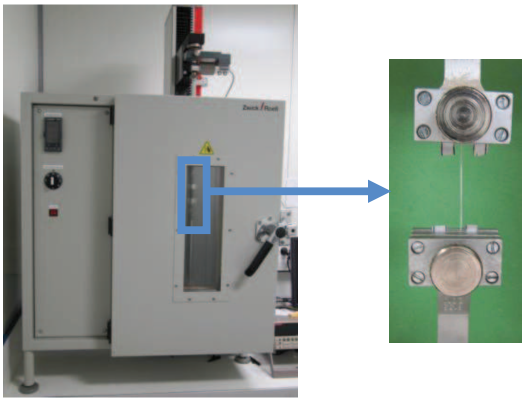

Figure 5. Picture of the system used for the stretching of the fibers. The picture on the left represents the whole system (thermal chamber and traction apparatus) and the picture on the right is a zoom on the elements serving for the fiber traction.

III. Characterization of the fibers

III.1. Characterization of the fibers structure

III.1.1. Composition of the fibers

From the combination of both TGA (water content determination≈1.5%) and elemental analyses (Table I), the weight percentage of ZnO was estimated at 35%w, and the following fibers stoichiometry is proposed: $(ZnO)_1(VA)_{2.2}(Na_2SO_4)_{0.35}.0.2H_2O$. Considering the proposed composition we notice that a significant amount of sodium sulfate remains trapped in the composite fibers, despite severe washing, as evidence below with XRD investigations. This salt is embedded within the PVA matrix as a result of its polymerization.

The diameter of a fiber was about 300µm. By considering that the nanorods were perfectly aligned and that they were forming lines parallel to the fiber main axis, we could evaluate that the average distance between two nanorods ($d_{correlation}$) was comprised between 2.5 and 3 µm.

Table I. Elemental analysis obtained by coupling laser ablation with plasma torch and mass spectroscopy (ICP-MS).

Element	C	Zn	Na
wt% (exp.)	23.3	28.4	6.6

III.1.2. Structural analyses

The crystalline structure of the ZnO particles was characterized by XRD (Figure 6.b.). The ZnO nanorods present the hexagonal ZnO Wurtzite (space group $P6_3mc$) structure with lattice constants a= 3.25(2) Å and c = 5.21(2) Å, in good agreement with the expected values (JCPDS 76–0704). The XRD pattern of the composite fibers (Figure 6.d.) was compared with that of PVA (Figure 6.a.) and Na_2SO_4 (Figure 6.c.). The diffractogram confirms the combination of ZnO and PVA, with the sodium sulfate embedded in the fiber.

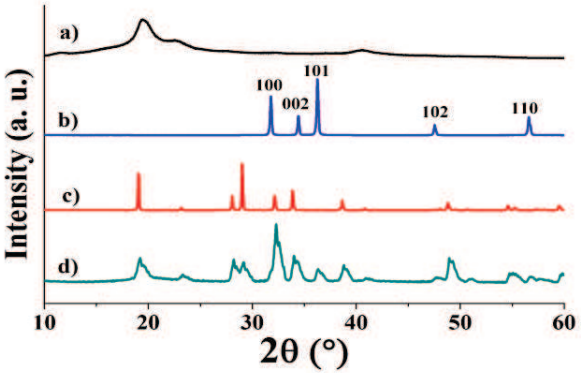

Figure 6. X-ray diffraction patterns of a) PVA, b) ZnO, c) Na_2SO_4 salt and d) composite PVA/ZnO fibers.

The crystalline structure of the ZnO particles was further investigated by Raman scattering to evaluate the level of crystallinity and concomitantly that of defects (Figure 7). The Raman spectrum is characteristic of pure and well-crystallized hexagonal wurtzite:[33,34] The absence of contribution around 578-583 cm^{-1} (A_{1L} and E_{1L} modes) reveals that the punctual defects such as interstitial zinc cations or oxygen vacancies, if present, are only residual in the ZnO lattice.[35] Compared with the ZnO particle alone, the Raman spectra of the composite fibers show a slight blue shift (<2cm^{-1}) of the peak at 438 cm^{-1}, corresponding to the E_{2H} mode which we ascribe to a minor stress induced by the PVA matrix confinement onto the ZnO nanocrystals when the fiber is stretched out.

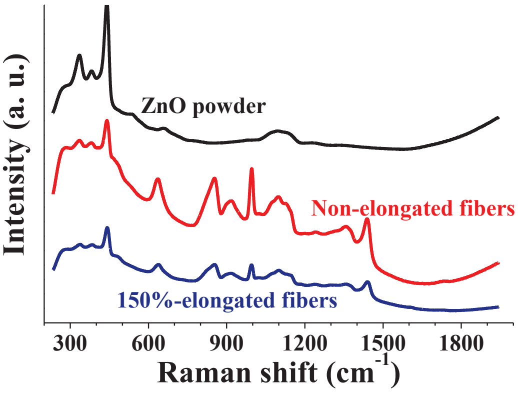

Figure 7. Raman spectra of the ZnO nanorods (black), non-elongated PVA/ZnO fibers (red) and 150% - elongated PVA/ZnO fibers (blue) excited by 785 nm line.

III.1.3. Analysis of the nanorods alignment inside the fibers

III.1.3.1. Experimental set up

Studies of the ZnO particles alignment inside the fiber were performed with a homemade X-ray scattering apparatus equipped with a microfocus copper rotating anode X-ray source (Rigaku MicroMax-007 HF) combined with multi-layers optics and a 3-pinholes collimation, the sample holder being mounted on a X-Y stage. Individual fibers were vertically placed on off-centered supports, with the fiber main axis perpendicular to the X-ray beam. The scattering signal was collected on a 2-dimensional detector (Image plate from Mar Research). In the present work, the sample-detector distance was fixed to 103 mm in order to record in parallel the Bragg reflections over a 0-40 degree 2-theta angular range. Silver behenate was used as a reference.

III.1.3.2. Analysis procedure

The anisotropic angular distribution of ZnO crystals in the fibers was quantified by integrating first the radial intensity of the (001) diffraction line, and report this intensity as a function of the [(-100) - (+80)] degree angular orientation on the 2D detector, zero being located at the position of the maximum intensity. This analysis was applied to fibers prepared under various stretching constraints, and the quantification of the anisotropy was achieved by fitting the previous angular-dependent intensities with a Lorentzian function, the anisotropy factor being further reported as the full width at half maximum (FWHM). It results that a higher anisotropy will appear with a narrower distribution of the diffracted intensity on the 2D detector, hence a small FWHM. Therefore, this value represents the angular distribution of the particles axes around the fiber axis and allows for quantifying the particles orientation inside the fiber.

III.1.3.3. Nanorods alignement versus elongation percentage

SEM observation (Figure 8) confirms that the fiber stretching promotes a better alignment of the ZnO particles along the fiber main axis. Without the fiber post-stretching, a spontaneous but limited pre-alignment of the ZnO particles exists (Figure 8.a.,b.), as a result of the co-axial flux shaping extrusion, but this alignment remains limited. Applying tensile stress to the fiber above the PVA T_g and cooling it down under stress, drastically increases this alignment (Figure 8.c.,d.), as confirmed by XRD and Wide Angle X-ray Scattering (WAXS) analyses, presented in the following paragraphs. If we consider that the nanorods are perfectly aligned, the distance between two nanorods ($d_{correlation}$) has been estimated between 2.5 and 3 µm.

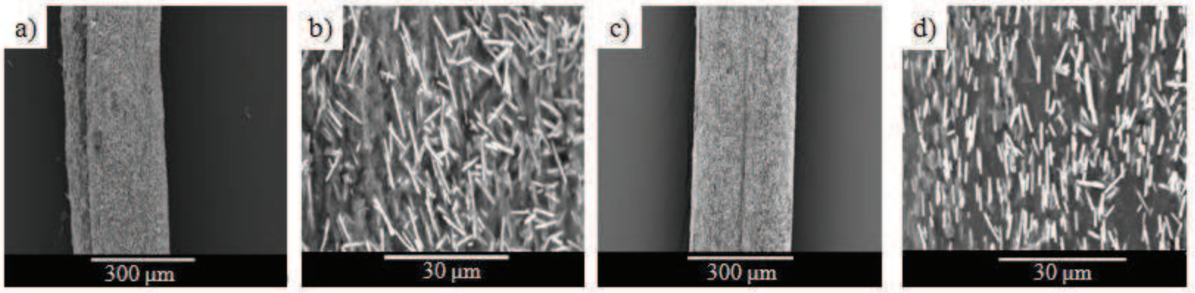

Figure 8. SEM images of a non-elongated fibers (a, b) and of a 150%-elongated fiber (c, d).

The experimental geometry was set in order to detect reflections up to (2Θ = 40°), that is, an angular range containing the three main reflections of the wurtzite structure: (00l), (002), and (101) (Figure 9) (additional reflections due to the Na_2SO_3 salt are also observed). This pattern was collected with a 50%-elongated fiber and the angular distribution of the scattered intensity gives access to quantitative information on the angular distribution of the main axis of the ZnO nanorods.

This diffraction pattern reveals the anisotropic distribution of the intensity corresponding to the (00l), (002), and (101) planes. With a fiber vertically placed and perpendicular to the X-ray beam, the maximum of intensity is centered on the coronal and sagittal planes for the (100) and (002) reflections, respectively. As for the diffraction assigned to (101), it is distributed over four spots at π/4 of the coronal and sagittal planes (Figure 9).

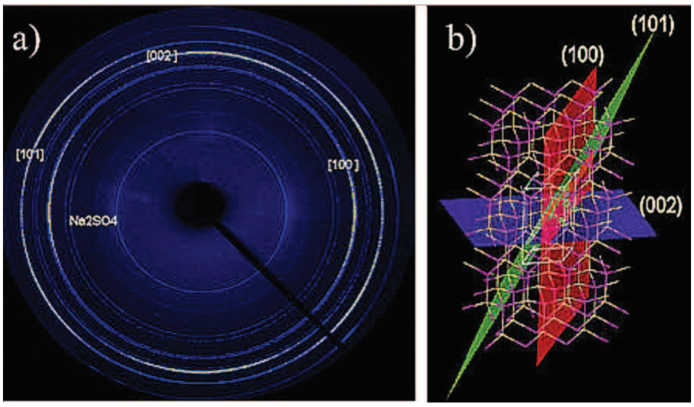

Figure 9. a) 2D X-Ray pattern of a partially elongated fiber. The fiber axis is vertical. b) unit cell of the wurtzite (space group P63mc) with the visualization of the crystallographic planes of interest.

We selected the (100) reflection line to quantify the angular distribution χ of the diffracted intensity I= f(χ). As illustrated with the two examples reported in Figure 10 a. and b., for non-elongated and 150% elongated fibers, respectively, the intensity as function of the angular distribution, is narrower for the elongated fiber than for the non-elongated one, as a result of a better alignment among the ZnO nanorods.

III.1.3.4. One step fibers stretching

In a first study, we decided to stretch the fiber in one step according to the protocol described in section II.3. For this protocol, the fiber was maintained tense by the jaw of the apparatus before its stretching but no forces were applied on it. Figure 10.c. presents the evolution of FWHM/2 versus the elongation percentage of the fibers. As already observed on SEM images, the ZnO particles are already partially aligned by the extrusion process with an average angle of ±31° with respect to the fiber axis. This alignment is improved by a factor 2 upon fiber stretching with a limit reached for 100%- elongated-fibers. Above 100% extension the ZnO wires mean orientation within the fibers is no more improved. This result was confirmed with similar analyses carried out on several set of fibers. Finally, the nanorods present a mean orientation angle of 18° with respect to the main fiber axis.

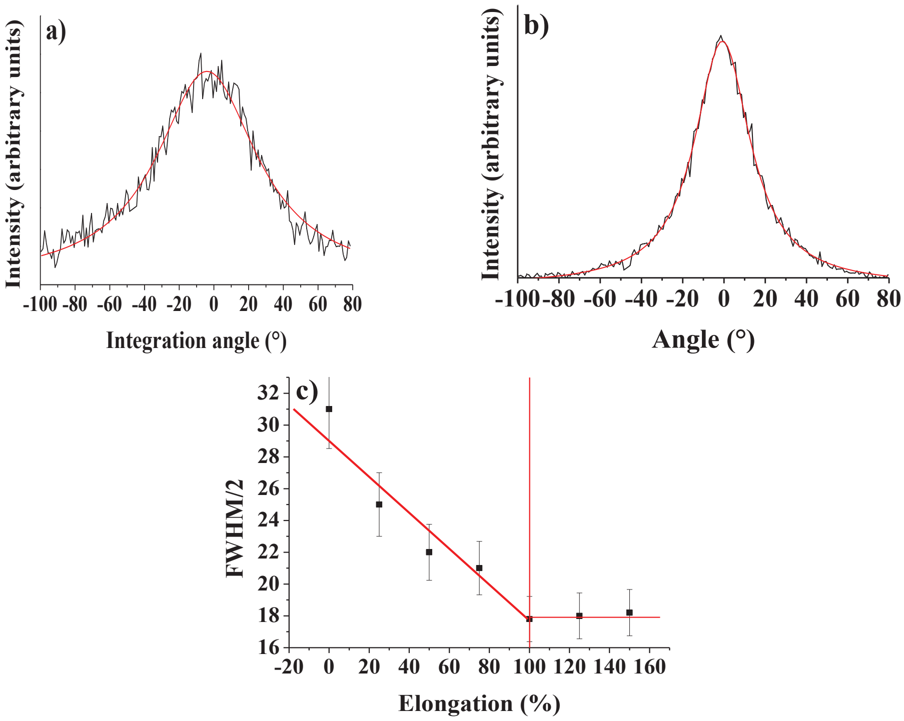

Figure 10. (a,b) Curves representing the Lorentzian integration of the light intensity on the circle corresponding to the (100) diffraction and their fitting, (a) non-elongated fibers, (b) 150%-elongated fiber; (c) presents the FWHM/2 evolution of the fitted peaks, as a function of the stretching percentage.

III.1.3.5. Multi- steps based fiber stretching

In a second study, we investigated if the nanorods alignment inside the fibers could be improved by using different stretching protocols. Especially, we were wondering if pre-stretching the fiber at room temperature before its elongation at T=85°C, which would result in applying a stress on the ZnO nanorods, would help aligning the nanorods along the fiber main axis. The force value associated to the fiber pre-stretching at room temperature was determined by performing mechanical tests. In the following, the force needed to reach the plastic domain of the fiber, or the force needed to break it when no plastic behavior is observed, is referred as F_p. We postulated that in order to generate enough stress on the nanorods to observe significant results, the force that we have to apply on the fiber during its pre-stretching should be above 35% F_p. Also, in order to avoid generating too many defects and cracks within the fibers during its pre-stretching, we decided to apply a force below 80% F_p. Mechanical tests performed on ten fibers with different F_p values, showed that at in order to respect the condition $0.35F_p < F < 0.8F_p$ for all the fibers, the force applied should be around 1.4N. This value will be referred in the following as F_0. From this result, we designed two set of experiments.

For the first set of experiments, the fibers were successively submitted to a force F_0, heated above the PVA glass transition, elongated till their elongation was worth 25% L_0 (L_0 being the initial length of the fiber) and cooled down. The process was then repeated to reach successively a total elongation value of 50%, 75%, 100%, 125% and 150% of L_0. For the second set of experiments, the same protocol was followed except that this time, the elongation step was 50% instead of 25%. This means that the elongation of the fibers was worth successively 50%, 100% and 150% of L_0.

In order to check the influence of the stretching protocol on the alignment of the nanorods inside the fibers, we performed WAXS analyses. The results are presented in Figure 11. We can observe that the evolution of the mean orientation angle of the nanorods regarding the main axis of the fiber follows the same trend for all the stretching protocols. In all cases we can observe a decrease of the mean orientation angle value when the fibers elongation is varying from 0% to 100%. As for the first study, 100% elongation is a threshold for the new protocols, and the minimum mean orientation angle value is quite similar for all the protocols (around 16°).

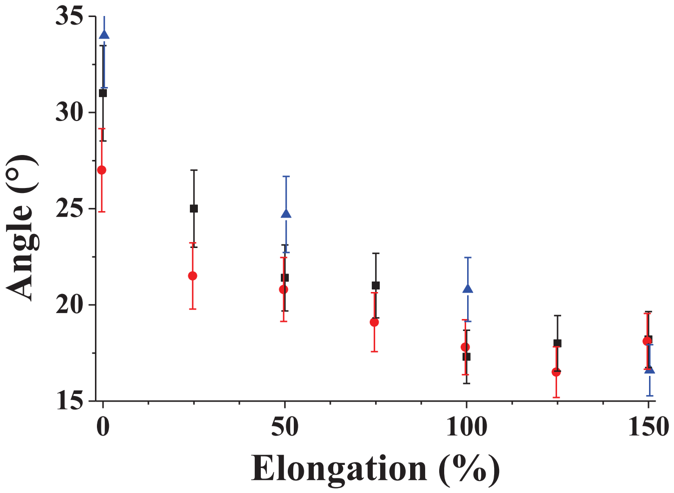

Figure 11. FWHM/2 evolution of the fitted peaks obtained through WAXS analyses as a function of the stretching percentage: ■ fibers stretched according to the protocol described in section II.3., ● fibers stretched according to the first protocol described in this paragraph (25% step), ▲ fibers stretched according to the second protocol described in this paragraph (50% step).

In conclusion, we can deduce from these results that the stretching protocol does not influence the alignment of the nanorods inside the fibers. For the following experiments, we stretched the fibers according to the protocol described in section II.3., which is more convenient to perform than the two protocols described in this paragraph.

III.2. Fibers mechanical properties

Tests were carried out with fibers prepared with different pre-stretching at 85°C. For each pre-stretching percentage, these tests were carried out on several sets of fibers and the average values of the Young Modulus and of the tensile strength at break are presented in Table II. The stress applied on the fibers corresponds to the force applied on the fiber normalized by the area of its section. As illustrated in Figure 12, that displays the different tensile stress curves as a function of the fiber elongation of representative samples, non-extended fibers exhibit only an elastic behavior with a reversible elongation up to 2% before rupture. As the fiber is pre-stretched at 50% L_0 at 85°C, its mechanical properties are modified with an additional plastic response that allows for an additional 7% non-reversible elongation. Extension of the pre-stretching to 100% increases the tensile strength resistance since the elastic limit is reached for a higher stress (50 MPa instead of 25 MPa for the non-extended fiber). Finally, higher pre-extension (150%) has a negative impact on the stress/strain curve, probably as a result of a too extensive fiber extension that degrades the PVA matrix cohesion.

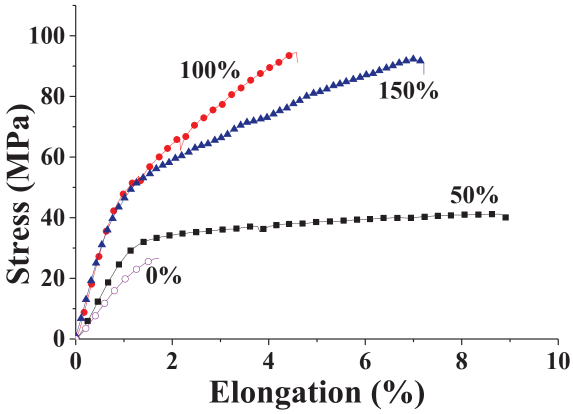

Figure 12. Mechanical tests on fibers pre-elongated at several percentages: ○ not extended, ■ 50%, ● 100%, ▶ 150%.

These tests along with the macroscopic behavior as illustrated in Figure 12, illustrate the synergy between the two components (PVA, ZnO): (i) PVA provides the organic flexibility to the inorganic part and confines the ZnO nanorods within a compressive matrix, as revealed by the Raman analysis, and (ii) the ZnO nanorods provide an additional resistance via their intrinsic mechanical strength and the collective resistance resulting from their preferential alignment along the PVA fiber main axis. An additional proof of the constriction of the PVA matrix around the ZnO nanorods, as a result of the pre-extension, is the increasing of the nanocomposite fiber stiffness marked by an important improvement of the Young Modulus (Table II).

In the elastic regime, at low strain, the tensile Young modulus varies from 2 to 6 GPa as the fiber pre-extension goes from 0 to 100% extension, which corresponds to the range of values obtained for similar composite fibers, prepared either with carbon nanotubes[13] or V_2O_5.[16] Here again, increasing the fiber extension beyond 100% has a negative impact on the Young Modulus. From these results, we deduce that the better the nanorods are aligned along the fiber main axis, the better the mechanical properties are.

Table II. Mechanical properties of fibers stretched at different percentages (average value calculated on several sets of fibers, values have been normalized to the fiber section)

Elongation %	Young Modulus (GPa)	Tensile strength (MPa)
0	2.0	39.6
50	3.2	43.4
100	6.0	79.9
150	5.2	79.2

III.3. Fibers photonic properties

Photoluminescence measurements were performed at room temperature using the fourth harmonic (266 nm) of a Brilliant (Quantel) Q-switched Nd:YAG laser as the excitation source. The laser pulse frequency was 5 Hz, the laser diameter 2 mm, and the pulse duration around 4-6 nanosec. Fluorescence was detected with a StellarNet EPP2000-UV-VIS spectrometer.

We conducted photonic analyses on ZnO fibers since ZnO photoluminescence significantly varies depending on the quality of the crystals and the presence and nature of defects (oxygen vacancies, interstitial zinc cations, etc…). The control of defects is indeed of paramount importance in applications that exploit the wide range of optoelectronic properties. Photonic properties of ZnO are well known, and we focused our analysis on the influence of both the intrinsic ZnO particle anisotropy and collective alignment onto the optical properties. Therefore, the optical measurements were designed in order to see how both dimensionality and alignment of nanorods along the fiber main axis, influence the photonic properties. Measurements were carried out first in two configurations: (top) laser beam perpendicular, that is, at an angle of 90º, to the fiber main axis (Electrical field parallel to the plane of the fiber main axis), and (bottom) laser beam parallel, that is, at an angle of 0°, to the fiber main axis (Electrical field perpendicular to the fiber main axis), (see Scheme 1). These two configurations were used to measure the photoluminescence resulting from the anisotropic absorption for non-stretched (Scheme 1.a.) and stretched (Scheme 1.b.) fibers.

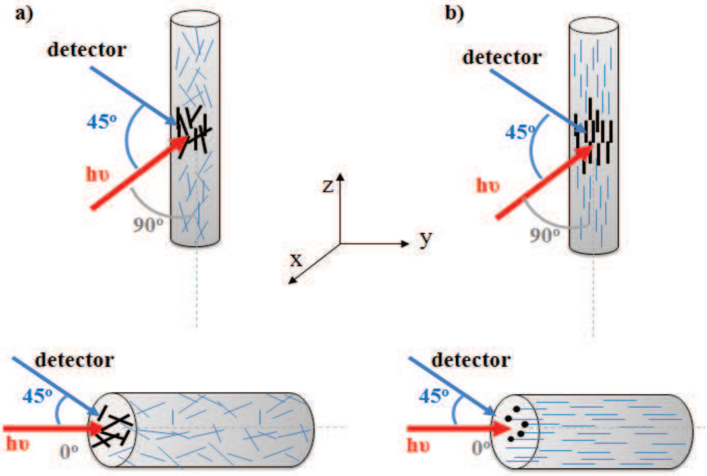

Scheme 1. Schematic representation of PL measurements on non-stretched (a) and stretched (b) ZnO fibers. The excitation beam strikes perpendicularly to the ZnO fiber (angle of 90°, configuration top) and parallel to the ZnO fiber (angle of 0°, configuration bottom), and detector is place at an angle of 45° between the laser and the main axes of the fibers.

III.3.1. Photoluminescence: light absorption

Figure 13.a. displays the photoluminescence (PL) spectra obtained for the non-stretched fibers with the laser oriented at 90° or 0° of the fiber main axis. Their photoluminescence is compared with that of ZnO particles alone. The PL spectrum of ZnO particles is dominated by a sharp and strong peak at around 388 nm (3.27eV) in the UV region. This emission corresponds to the near band edge emission (NBE) of highly pure wurtzite ZnO crystals, and it arises from the recombination of the free excitons through an exciton–exciton collision process. This band presents a shoulder at lower energies (lambda > 390 nm), which it is usually assigned to optical transitions involving free electrons and neutral-acceptor levels (see part I.2.2.). The contribution of each of both signals was obtained by deconvolution of the spectra (see Table III). No other signals in the green visible region (450-600 nm) associated to defects or impurities were detected.[36–38] This profile in the PL spectrum confirms that the ZnO structure is highly crystalline with no structural defects, in agreement with SEM, WAXS and XRD results.

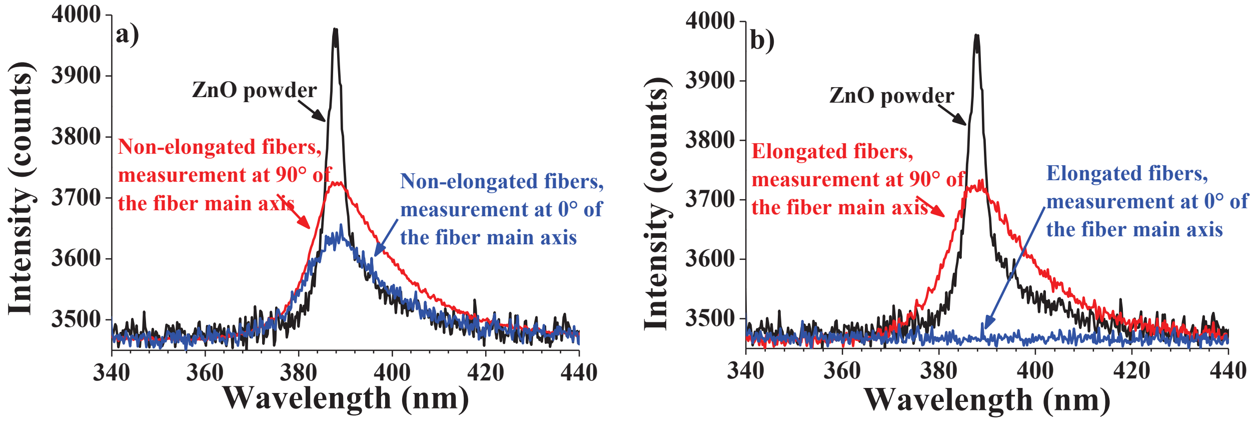

Figure 13. PL spectra of non-stretched and stretched ZnO fibers measured upon excitation beam oriented at 90º (in red, configuration a, Scheme 1) and 0º (in black, configuration b, Scheme 1). The grey curve corresponds to the PL spectrum of pure ZnO nanorods (reference).

The luminescence spectra of the nanocomposites ZnO/PVA fibers display similar, but broader, profiles as for the ZnO particles alone. This broadening results from the surface interactions between the free electrons on the ZnO surface and the polymer matrix. For non-stretched fibers, a similar response is observed for both the longitudinal and transversal measurements.

Table III. Contribution of each signal (mean peak at ~380 nm and the shoulder at ~390 nm) to the total emission spectra in different samples. The 380 nm peak corresponding to the recombination of free excitons through an exciton–exciton collision process and the ~390 nm peak to optical transitions involving free electrons and neutral-acceptor levels.

Sample	% (380 nm)	% (390 nm)
ZnO nanorods	63	37
ZnO/PVA fiber (non-stretched)	48	52
ZnO/PVA fiber (150% stretched)	51	49

This isotropic response illustrates the poor alignment of ZnO nanorods after the fiber extrusion if the post-extrusion stretching is not applied. On the contrary (Figure 13.b.), responses of stretched fibers display huge differences: the intense UV emission detected when the laser beam is perpendicular to the fiber main axis (90°) is almost suppressed when the measurement is conducted with the laser beam parallel to the fiber main axis (0º). This difference can result only from the alignment of ZnO nanorods within the composite fiber, and their resulting orientation with the incident beam. If the propagation vector $\vec{k}$ of the incident light is normal to the fiber and concomitantly to the aligned ZnO nanorods main axis, then the light wave, polarized with its electric field $\vec{E}$ (perpendicular to $\vec{k}$) parallel to the axis of the fiber will give an optimal interaction with the absorption transition dipole of ZnO ($\vec{\mu}_{ZnO}$), and $\vec{E}.\ \vec{\mu}_{ZnO}$ will be maximal. If the propagation vector $\vec{k}$ of the incident light is parallel to the main axis of the fiber, then $\vec{E}.\vec{\mu}_{ZnO}$ is almost equal to zero, and almost no PL will be detected.[30,39]

III.3.2. Photoluminescence: light emission

In addition to enhanced photoluminescence,[39] it is expected that spatially aligned 1D ZnO nanostructures can exhibit polarized emission,[30] or photonic confinement.[40,41] The size scale for reaching quantum confinement and waveguiding phenomena is close to the average Bohr radius for excitons in ZnO, and this value has not yet been attained in the synthesis of single-ZnO crystalline wires. We determined if the preferential orientation of ZnO nanorods inside the polymer provided some of these particular photonic effects as a result of their collective response. The small diameter of the fibers (~300 µm) prevented us from recording the PL emission as a function of several angles with our current system. Therefore, we positioned the detector at two positions (Scheme 1), toward the side of the fiber, at 90° of the laser (position 1), or toward the cross-section of the fiber at 90° of the laser (position 2).

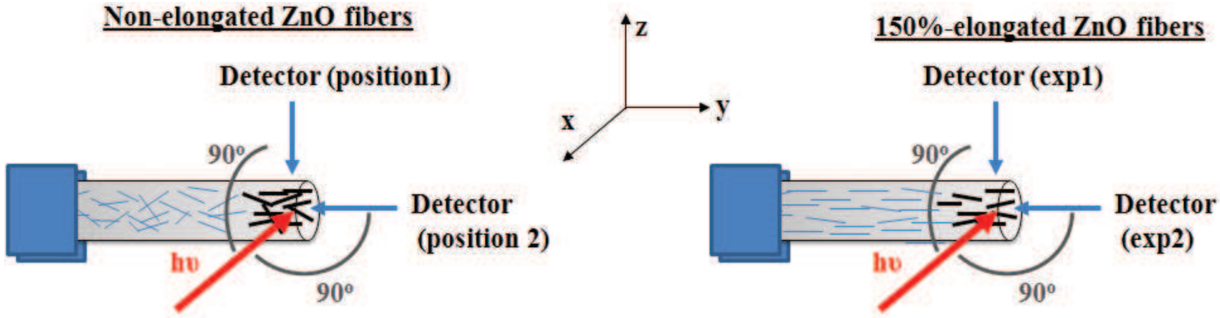

Scheme 2. Schematic representation of PL measurements on non- stretched (left) and stretched (right) ZnO fibers. The excitation beam strikes perpendicularly to the ZnO fiber (angle of 90°) and the detector is positioned in two perpendicular directions to the incident laser.

The laser beam was polarized with the electric field parallel to the main axis of the fiber in order to assure an optimal interaction with the absorption dipole of ZnO. The measurements have been conducted with identical experimental conditions, and special care was taken to ensure that no reflected incident beam was hitting the detector. The spectra were finally normalized in order to compare the intensity of the signals. Figure 14 shows the emission spectra registered for the composite fibers without (a) or with (b) elongation.

As PL emission is isotropic, its angular dependence mostly depends on the surface of emission in a given direction. Hence, the emission is enhanced perpendicularly to the main axis of the nanorods, because the surface of emission is larger, compared to the cross-section of the fiber. It is also expected that the collective alignment of ZnO nanorods in the PVA fibers, should give an anisotropic angular emission with two major angles of emission: perpendicular to the fiber, since the surface of emission of the ZnO nanorods is larger, and along the fiber main axis, as a result of the anisotropy of alignment of the ZnO nanorods. The comparisons between the PL spectra upon polarized light excitation for the non-stretched and stretched fibers, show indeed that the intensity of the emission by non-stretched fibers, is more homogeneously distributed than for the stretched ones. For example, the emission perpendicular to the fiber (detector in position **1**) is enhanced with the stretched fiber (Figure 14.b.), compared to the non-stretched one (Figure 14.a.). More important, the non-stretched fiber does not emit any PL along the main axis of the fiber (detector in position **2**) (Figure 14.b.) whereas the stretched one (Figure 14.a.) demonstrates a clear PL emission.

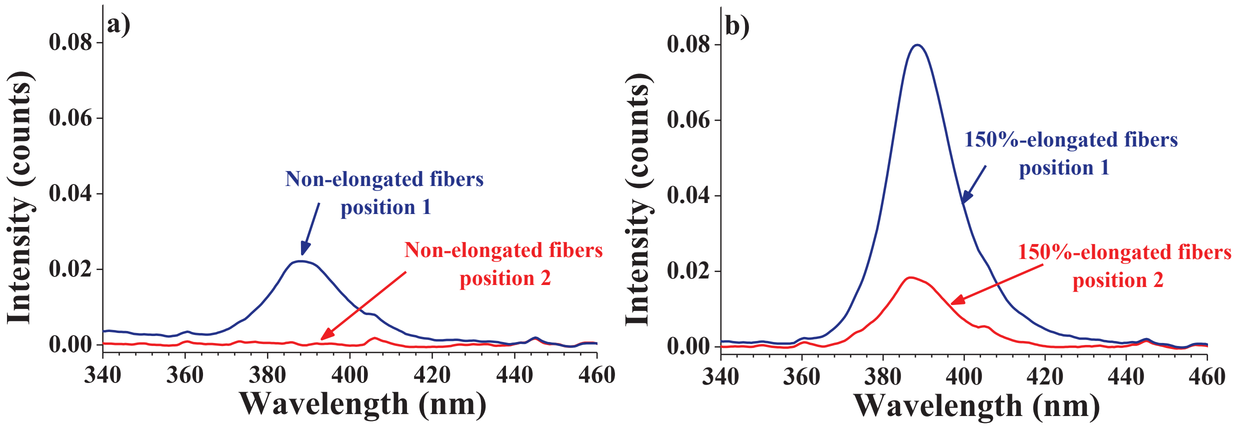

Figure 14. PL spectra of non-stretched and stretched ZnO fibers obtained with polarized excitation beam, and detection according to the setup of Scheme 2 (detector position 1 in blue, and detector position 2 in red).

Tests to detect photonic confinement and an actual waveguide phenomenon were not conclusive with our experimental system setup: the presence of flat and parallel end faces on the nanowires is a requirement for the optical feedback in a resonant cavity, and this feature is very difficult to reach when nanorods are interacting with a polymer host matrix. However, our measurements demonstrate that the parallel alignment of ZnO nanorods along the PVA fiber main axis allows the nanorods to act collectively as an antenna with polarized optical emission. This particular alignment provides preferences in the PL emission directions, which should be enhanced by a still higher alignment of nanorods within the PVA matrix.

Conclusion

Composite macroscopic fibers made of ZnO nanorods embedded into PVA matrix have been synthesized through extrusion-based co-axial flux nanoparticles alignment, with a modified process, compared with previous studies.[43] Unlike other works where the very high aspect ratio of particles allowed for an easy alignment during the fiber extrusion, the correct alignment of the ZnO particles could be achieved only with a specific post-synthesis fiber stretch process under hot mechanical traction above the polymer glass transition temperature. The as-synthesized fibers have been thoroughly characterized at the macro-, meso and microscopic length scales. According to the XRD pattern, ZnO corresponds well with hexagonal ZnO Wurtzite-type (space group $P6_3mc$) with lattice constants a= 3.25 Å and c = 5.21Å. Raman spectroscopy has revealed that the ZnO particles exhibit a high crystallinity, and no significant defects associated to the extrusion process were observed. A small blue-shift of less than 2 cm^{-1} was detected for the elongated ZnO fibers, which reveals that the fiber extension process improves the interaction between the polymer matrix and particles, and creates locally some surface stress in the ZnO structure. At the mesoscopic length scale, the ZnO nanorods are partially pre-aligned by the extrusion process itself with an average angle of 31 degrees, but this alignment is not high enough to emphasize anisotropic properties. Improvement of this alignment through the applied hot mechanical traction step allowed us to confine the mean alignment of nanorods within a 18° angle value at 100% elongation, above which ZnO wires main orientation within the fibers remains constant. Considering these fibers mechanical properties we have found that the longitudinal Young's modulus can be increased from 2 to 6 GPa. When photonic properties are addressed, intense near band edge (NBE) emission with no green emission in the PL spectrum confirmed that the ZnO particles are highly crystalline with no structural defects. In the case of non-elongated fibers, an isotropic response was observed in the longitudinal and transversal measurements. On the contrary, for elongated fibers, the intense UV emission detected when the ZnO nanorods are aligned perpendicular to the laser beam is almost suppressed when the measurement is conducted at an angle of 0º, depicting thereby anisotropic photonic properties. Similar anisotropy was observed regarding the angular dependence of the photoluminescence emission.

Chapter 3:
Photocatalytic TiO_2 Macroscopic Fibers Obtained Through Integrative Chemistry

Titanium dioxide (TiO_2) is a typical n-type semiconductor which has been widely used in industry due to its unique and various properties such as its anti-bacterial property, its stability (chemical resistance to acidic media), its super hydrophilic behavior under radiation, its electronic, magnetic, electrochemical, and photocatalytic properties. This material is found in applications such as photovoltaic cells with Dye-Sensitized solar Cells, sensors, self-cleaning coatings, cosmetics (UV protection), painting, and air and water depollution (heterogeneous catalysis).

This chapter describes our investigation on TiO_2 photocatalytic property used for air depollution, because. TiO_2 is well-known for successfully eliminating pollutants in gas or liquids. Nanostructured TiO_2 exhibits enhanced photocatalytic activity compared to conventional bulk materials because of its high surface area to mass ratio, which makes it one of the most intensively researched substances in the past decade. In this PhD project, we have been attached to provide an additional structure with the synthesis of 1D macroscopic structures (fibers) composed of pure TiO_2. We studied the influence of the fibers structural parameters on the photocatalytic properties, the structural parameters being adjusted by varying the formulation. In a first step, the fibers were generated and their composition was determined. Then, their structural parameters were investigated (porosity, roughness). Finally, these parameters were related to the photocatalytic performance of these fibers for air depollution.[1]

I. General principle and objectives

I.1. TiO_2 structure

The electronic structure of Titanium is $(1s)^2(2s)^2(2p)^6(3s)^2(3p)^6(3d)^2(4s)^2$ which means that it possesses four valence electrons, two on its 3d orbital, and two on its 4s orbital. Oxygen, with a $(1s)^2(2s)^2(2p)^4$ electron configuration, possesses six valence electrons on its outer shell, but, only two electrons on the 2p orbitals can create bonds with other elements as the four others belong to lone pair electrons. As it needs only two electrons to fill its orbitals and because it is more electronegative than the Titanium, the Oxygen will have the tendency to attract electrons whereas Titanium will have the tendency to give electrons. The determination of the valence band and the conduction band is quite complex as it results of the overlap of the Oxygen 2p and the Titanium 3d and 4s orbitals with the formation of bonding and anti-bonding orbitals (see Chap. 1 section II.1.2). However, in this configuration, the valence band can be described as the oxygen 2p orbital in character whereas the conduction band can be described as the Titanium 3d and 4s orbitals in character.

With this electronic structure, titanium dioxide can form three major crystalline phases: Rutile, Anatase and Brookite (Figure 1).[2]

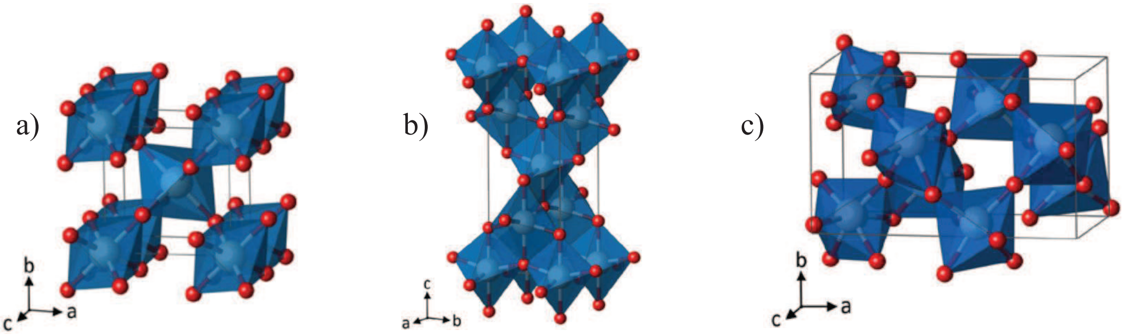

Figure 1. TiO_2 crystalline phase representation a) Rutile, b) Anatase, and c) Brookite. The oxygen atoms are represented in red, whereas the titanium atom is represented in white.[2]

The Anatase and Rutile phases possess a tetragonal network and Brookite is rhombohedral. The Rutile phase is an arrangement of octahedra which are composed of six oxygen atoms on their corner and one titanium atom at their center.[3] [2] In this structure, each oxygen atom is bound to three titanium atoms, and each titanium atom is bound to six oxygen atoms. The Rutile phase belongs to the $P4_2/mnm$ space group with the lattice constants a = b = 4.594 Å and c = 2.959 Å. The Anatase phase is similar to the Rutile phase, except that its structure is more distorted.

Compared to the Rutile phase, the Anatase phase possesses two Ti-O bonds that are much longer than the other four and the O-Ti-O bond deviates from an angle of 90°. It belongs to the $I4_1/amd$ space group, with the lattice constants a = b = 3.783 Å and c = 9.514 Å. Brookite has an orthorhombic cell. The Brookite crystalline structure is also composed of TiO_6 octahedra with interatomic distances and O– Ti–O bond angles in the same range as those of Rutile and Anatase, but with a broader distribution due to the structure distortion: the six Ti–O bonds possess different lengths ranging from 1.87 to 2.04 Å, and the twelve O–Ti–O bond angles are also all different ranging from 77° to 105°.[4]

Due to their respective structure, each TiO_2 crystalline phase presents specific properties, which will make them suitable for different domains of application. For example, due to its high refractive index and thermodynamic stability, Rutile is used in white coatings and paints (high-grade, corrosion-protective), plastics, rubber, leather, paper, or sun-block lotion. Due to its electronic structure, Anatase has excellent optical properties (light absorption) and it is mostly used as an optical coating or as a photocatalyst. Brookite has no true application until now.[3] In our project, we were then interested in synthesizing TiO_2 nanoparticles with the Anatase structure as it is the most efficient for photocatalysis application. It has been reported that Anatase is preferentially synthesized as nanoparticles with small crystallites size (below 30nm).[5–7] It has also been demonstrated that the shape of the particles could influence their properties, which was illustrated by looking at its influence on the performances of Dye-Sensitized Solar Cells.[8] In the part II.1.2, we demonstrate how it is possible to change the experimental conditions of a single procedure in order to obtain the Anatase phase rather than Rutile.

I.2. Photocatalysis

I.2.1. General concept

A catalyst is a component that allows accelerating a thermodynamically favored reaction with low kinetics, and which is entirely regenerated at the end of the chemical reaction. Heterogeneous catalysis involves a solid phase interacting with either gaseous or liquid compounds, and photocatalysis is a reaction where the catalyst is activated by light. Photocatalysis uses mostly semiconductors, among them titanium dioxide (TiO_2) is a major actor in heterogeneous catalysis as it is abundant, cheap, non-toxic, and stable. Moreover, its band gap energy and the position of the first excited electron states confer the suitable energy to perform various reactions such as the water photo-electrolysis, or oxidation of organic pollutants. However, as TiO_2 absorbs only Ultra-Violet (UV) light, it is mostly used in combination with an external UV light source for application such as air depollution.

The equations representing the chemical reaction that occurs during the photocatalysis process and the major conclusions presented in this paragraph are extracted from the reviews of Berger *et al.*[9], Fujishima *et al.*[10] and Hoffmann *et al.*[11] The reaction path leading to the pollutants degradation starts with the photon-induced generation of electron-hole excitons within the TiO_2 structure (E.1).

$$TiO_2 + h\nu \rightarrow e^-_{free} + h^+_{free} \qquad \text{(E.1.)}$$

These excitons can relax through three mechanisms that compete with each other as a function of the experimental environment (Figure 2): the exciton can simply recombine within the bulk releasing heat (step b), they can be trapped at the surface in defect sites (step a, c, and d), or they can react with molecules adsorbed onto the material surface. Once the electrons and holes are trapped at the material surface, they can react with acceptor (step d) or donor molecules (step c), respectively, or recombine at surface trapping sites (step a).[10]

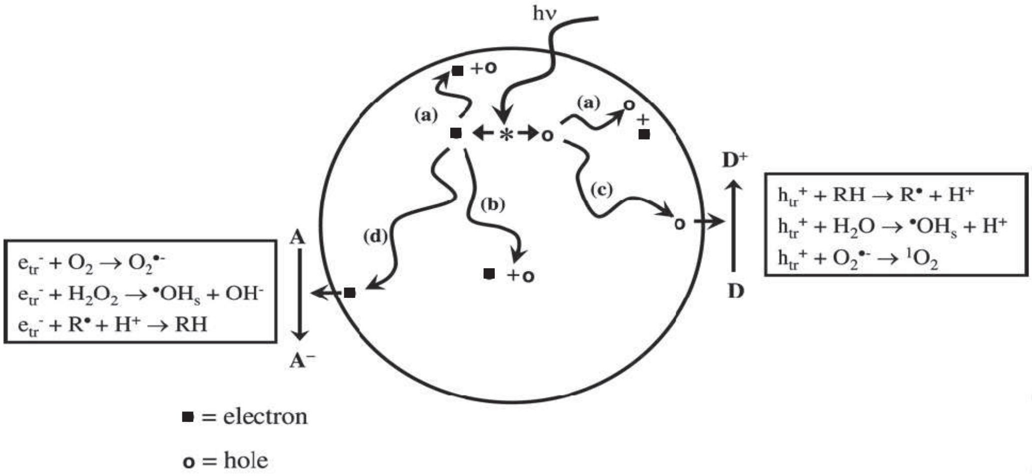

Figure 2. Schematic representation of the possible processes which can happen after the excitons have been generated a) excitons trapped at the surface, b) recombination of the excitons in the bulk, c) reaction between a hole and a donor specie, and d) reaction between an electron and an acceptor specie.[10]

The experimental conditions such as the temperature, the light source and the relative humidity can favor one process towards the others, which is also controlled by the material purity and nanostructure. For TiO_2, the excitons tend to react mostly with oxygen and water. Therefore, photocatalysis has to be conducted in a controlled atmosphere where humidity can be regulated.

I.2.2. Air depollution

I.2.2.1. General case

Excitons generated by the photons within the titania structure, can reach the surface of crystals and react with adsorbed molecules, either directly with the pollutant, or with other molecules and creating free radicals that will then react with the pollutant. When they react with water and oxygen molecules present in the surrounding air, new species bearing high reactivity towards the pollutant are created, the most common being $OH^\bullet$ and $O_2^{\bullet -}$. The reactions leading to their creation are:

$$h^+ + H_2O_{ads} \rightarrow OH^\bullet{}_{surface} + H^+ \qquad \text{E.2.}$$

$$e^- + O_{2\,ads} \rightarrow O_2^{\bullet -}{}_{surface} \qquad \text{E.3.}$$

$$e^- + O_{2\,ads} + H^+ \rightarrow HO_{2\,surface}^{\bullet} \leftrightarrow O_{2\,surface}^{\bullet -} + H^+ \qquad \text{E.4.}$$

The reaction between water molecules and holes (E.2.) leads to the creation of new hydroxyl groups at the surface, which makes the TiO_2 super-hydrophilic. Moreover, it leads to the release of H^+ species, which can be involved in new reactions. However, as this reaction consumes holes, it is in competition with the reactions involving direct interactions between holes and pollutant. In consequence, these last reactions can only occur once the surface is saturated in $OH^\bullet$ groups. The other reactions depicted (E.3. and E.4.) leads to the formation of O^{2-}. This last specie has been demonstrated to be less active than $OH^\bullet$ or h^+ in oxidation reaction with the pollutant, but can lead to the formation of more reactive oxygenated species (E.5. to E.8.). The reaction pathway leading to the formation of these species plays an important role in air depollution as the hydroxyl groups created are no more adsorbed on the surface and can react in all the experimental volume.

The determination of the predominant process leading to the oxidation of the pollutant is still controversial: formation of the $OH^\bullet$ radical has been postulated to be the predominant process species for a long time, but according to the review of Fujishima *et al.*[10], h^+ plays also an important role depending on the experimental conditions. Indeed, in some conditions, one of these two processes can be inhibited whereas in other cases, they are both active. In this context, the predominant process has to be determined for each experiment.

$$O_2^{\bullet-} + O_2^{\bullet-} + 2H^+ \rightarrow H_2O_2 + O_2 \qquad \text{E.5.}$$

$$H_2O_2 + e^- \rightarrow OH^\bullet + OH^- \qquad \text{E.6.}$$

$$H_2O_2 + O_2^{\bullet-} \rightarrow OH^\bullet + OH^- + O_2 \qquad \text{E.7.}$$

$$H_2O_2 + h\upsilon \rightarrow 2\, OH^\bullet \qquad \text{E.8.}$$

I.2.2.2. Acetone degradation

The aim of photocatalysis is to fully degrade a pollutant until the only resulting products are carbon dioxide (CO_2) and water,[12] with the pollutant being “mineralized” if the full degradation is observed. However, it happens that the photocatalysis reaction creates intermediary or secondary pollutants called by-products, creating a cascade of additional reactions until these by-products are mineralized in their turn.

In this project, we decided to use acetone as the pollutant because it is a common indoor pollutant generated by daily products such as cleaning and cosmetic products. During the acetone degradation, the major by-products created are formaldehyde, acetaldehyde, formic acid, and acetic acid. As the two latter ones are in equilibrium with their basic form adsorbed at the surface, they are not identified in the gaseous phase. In consequence, only the formaldehyde and the acetaldehyde can be detected during photocatalysis, which makes them the best probes to measure the photocatalytic activity of TiO_2. The photocatalytic properties of titanium oxides are well known, but photocatalysis depends also on the kinectics of reaction, and increasing the contact time between pollutants and TiO_2 is a way to improve overall the process, without changing the intrinsic properties of the material itself. Therefore, one of the objectives of this study was to increase this time by controlling the structural parameters of the fibers.

I.3. Organization of TiO_2 in macroscopic fibers and objectives

Recent studies show that TiO_2 photocatalytic ability was enhanced by preparing various morphologies of nanostructured TiO_2 including nanoparticles, nanofibers, nanostructured films or coatings, and nanotubes.[13–28] Numbers of recent works reported especially the fabrication of one-dimensional (1D) TiO_2 photocatalyst.[29–31] Indeed, the large surface-to-volume ratio, the enhanced adsorption of various reactants, and the favorable morphology for enhancing a longer reactant-catalyst contact, are expected to improve, overall, the properties of these materials.[32] Among the techniques developed for the fabrication of 1D TiO_2 nanostructures, electrospinning offers several advantages like simplicity, process controllability, low production-cost, and scalability for producing industrial quantities.[33–36] However, one penalty inherent to the electrospinning technique is that native fibers are randomly dispersed during the synthesis step, resulting in a direct loss of unidirectionality at the macroscopic scale. It is expected that enhanced photocatalytic performances could result from synergy between the catalyst 1D hierarchical structure, and optimized unidirectional gas flux. Design of such a hierarchical anisotropy can be addressed through an Integrative Chemistry pathway, which allows for multiscale material processing.[37–41] Material organization at the nanoscale can be controlled by structure-directing agents and soft chemistry processes, whereas organization at the micrometric scale can be successfully achieved by extrusion of organic-inorganic 1D nanocomposite fibers, as shown for the design and production of carbon nanotubes,[42] and vanadium oxide macroscopic composite fibers.[43–47] We studied in this report, how the specific 1D shape design, and orientation, of TiO_2 at different scales, can actually influence the photocatalytic properties, as a function of an unidirectional gas flow. Therefore, three types of titanium nanoparticles (nanorods & isotropic) were synthesized, extruded as nanocomposite fibers, and processed as to evaluate the influence of fiber orientation on the photocatalytic degradation and mineralization of acetone.

II. Studied system and experimental protocol

As the same characterization techniques are used in this chapter and in the following chapter, all the characterization technique protocols are described in the Annex 3.1. in order to avoid repetitions.

II.1. TiO_2 nanoparticles syntheses

II.1.1. TiO_2 nanorods

The synthesis of TiO_2 nanorods was inspired from Sugimoto et al.[48] Typically, 20.7 mL of titanium isopropoxide were mixed with 20.1 mL of triethanolamine under stirring, and the resulting solution was shared in three and poured into closed flasks. Each flask was completed with deionized water till 30 mL, followed by the addition of 1.4 mL of ethylenediamine. Finally, deionized water was added under stirring till 100 mL, and a first aging leading to a gel formation was carried out by leaving the closed flasks at 100°C for 24 h in an oven. The resulting solution was poured into Teflon-lined autoclaves for a second aging step at 140°C for 72 h to nucleate and grow titania particles. Suspensions were cooled down through the autoclaves inertia. Final suspensions were successively centrifuged at 17,000 rpm for 25 min, and washed with the following liquids: deionized water; HNO_3 3M; deionized water; ethanol; NaOH 1M; deionized water; HNO_3 3M; deionized water.

II.1.2. TiO_2 spherical particles

In a first experiment, 5 mL of a 37 wt% HCl solution were first added to 50 mL of a 15%w TTAB (tetradecyltrimethylammonium bromide) solution in a beaker. 6.4 mL of titanium isopropoxide was then slowly added under stirring, and the solution was left at room temperature. A slurry-like white precipitate was formed after several hours, which was recovered after full evaporation. The resulting powder was washed several times with deionized water until no foaming resulting from the remaining surfactant was observed. Another synthetic path was developed using 50 mL of a 15 wt% solution of a nonylphenol-EO_{10} nonionic surfactant (Tergitol™ NP-10) in place of TTAB, all synthesis parameters remaining the same.

The crystalline structure of the powder obtained was analyzed with a thermally-assisted X-ray diffraction (XRD) (Annex 3.1.I). The chamber is thermally controlled which allows performing the experiment at different temperature, the range selected being 25-900°C.

As displayed in Figure 3.A., through this synthetic pathway, the Rutile phase is the only crystalline phase be observed between 25°C and 900°C. However (see part I.1), the Rutile structure is not as effective in photocatalysis as Anatase. And the first synthetic pathway was modified to allow for the formation of Anatase. There are five parameters (part I.1.1.2) that can be adjusted to favour one specific structure: the organometallic precursor and its concentration, pH, temperature, and solvent. Therefore, in a second step we kept all parameters constant, except for the pH that was modified and increased up to 1.8 with addition of ammonia before addition of the titanium isopropoxide. This method was applied with both surfactant additives (TTAB or Tergitol™ NP-10). With this method, the Anatase phase is obtained at 25°C and remains up to 600°C (Figure 3.B.). In consequence, this synthetic pathway was used to synthesize the TiO_2 nanoparticles that were used in all the experiments described in this chapter.

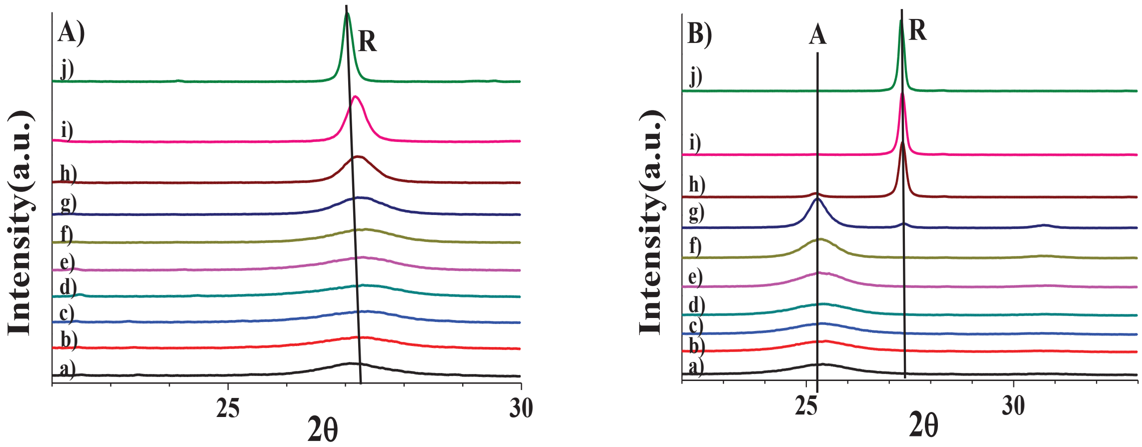

Figure 3. X-rays diffraction patterns of (A) 4-TERG-TiO_2 powder synthesized at pH=0, (B) 4-TERG-TiO_2 powder synthesized at pH=1.8, at a temperature of 25°C (a), 100°C (b), 200°C (c), 300°C (d), 400°C (e), 500°C (f), 600°C (g), 700°C (h), 800°C (i) and 900°C (j). A: Anatase; R: Rutile.

II.2. TiO_2/PVA co-extrusion process

First, the concentration of the aqueous suspensions of TiO_2, obtained in part II.1.1. and in part II.1.2., was adjusted at 2.5 wt% for titania nanorods, and at 4 wt% and 10.5 wt% for spherical particles prepared with Tergitol or TTAB (verified with dry extracts). The variation in the TiO_2 concentration aimed at modifying the structural parameters of the final fibers. Solid PVA was then added into the solution under stirring at 90°C in a proportion of 1.2 g of PVA for 10 mL of solution. This solution was kept under stirring for 1 hour until the PVA was fully dissolved and then cooled down at room temperature. The fibers were generated by needle injection (spinneret diameter of 1mm) of the PVA/TiO_2 sols into a rotating bath (25 rpm) containing a saturated salt solution of Na_2SO_4 at 45°C (Figure 4) to induce the coagulation of the PVA chains, via a salt effect. This mechanism, which minimizes the electrostatic repulsion, has been already employed for the spinning of neat PVA fibers.[49] The gelation mechanism was presented in Chap.1, part II.3.3.2. The extrusion speed was set at 40 $mL.h^{-1}$, and the flux was maintained tangential to the rotation axis of the beaker in order to promote a pseudo-coaxial flux at the external part of the syringe hole. Upon the completion of the extrusion process, the TiO_2/PVA fibers were meticulously taken out of the beaker by hand and allowed to dry in air. Finally, the fibers were washed once in water to remove the excess of salt.

Anisotropic particles alignment during extrusion, is limited because their shape factor is not large enough, and the PVA chains do not adsorb strongly onto TiO_2 nanoparticles, as required to induce bridging coagulation.[50] The absence of spontaneous coagulation allowed us to directly mix TiO_2 particles and PVA through homogeneous dispersions, where PVA is used as a porogen agent that will create inter-particle void spaces upon calcination. Both surfactants (TTAB and Tergitol NP-10) used during the isotropic nanoparticles synthesis play the role of dispersant in a first place, responsible for another level of porosity within the final fiber.

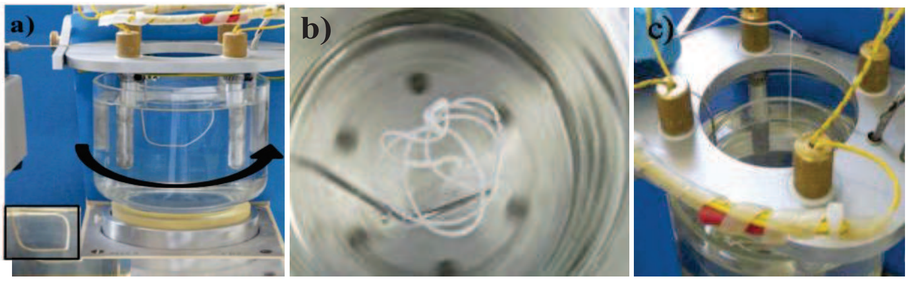

Figure 4. Pictures of TiO_2 fibers generation through extrusion process (a) Extrusion process, bottom embedded figure focused on the needle out-flow (b) view from above once extrusion has been performed, (c) fiber manual extraction from the beaker. The yellow arrow indicates the rotational beaker.

II.3. TiO_2 fibers sintering

The as-synthesized fibers were then sintered under air at 450°C for 6 hours in order to remove the organic part while promoting crystallization. Overall, five different inorganic fibers were prepared and labeled hereafter X-Y-TiO_2 where X concerns the weight % of particles in the sol, and Y the nature of surfactant (Y is replaced by "RODS" for the fibers containing TiO_2 nanorods). Thereby, we report in the following the comparison among several fibers, named as: 2.5-RODS-TiO_2, 4-TTAB-TiO_2, 10.5-TTAB-TiO_2, 4-TERG-TiO_2 and 10.5-TERG-TiO_2.

III. Characterization of the fibers

III.1. Characterization of the fibers structure

III.1.1. Fibers composition

The as-synthesized nanocomposite macroscopic fibers are made of TiO_2 nanoparticles, PVA, and some remaining sodium salt with some degree of hydration. The element composition of fibers was evaluated trough C, Ti, and Na elemental analyses combined with Thermo-Gravimetry Analysis (TGA, under air, 2°C/min), and their stoichiometry is given in Table 1. The elemental analyses were obtained by coupling laser ablation with plasma torch and mass spectroscopy.

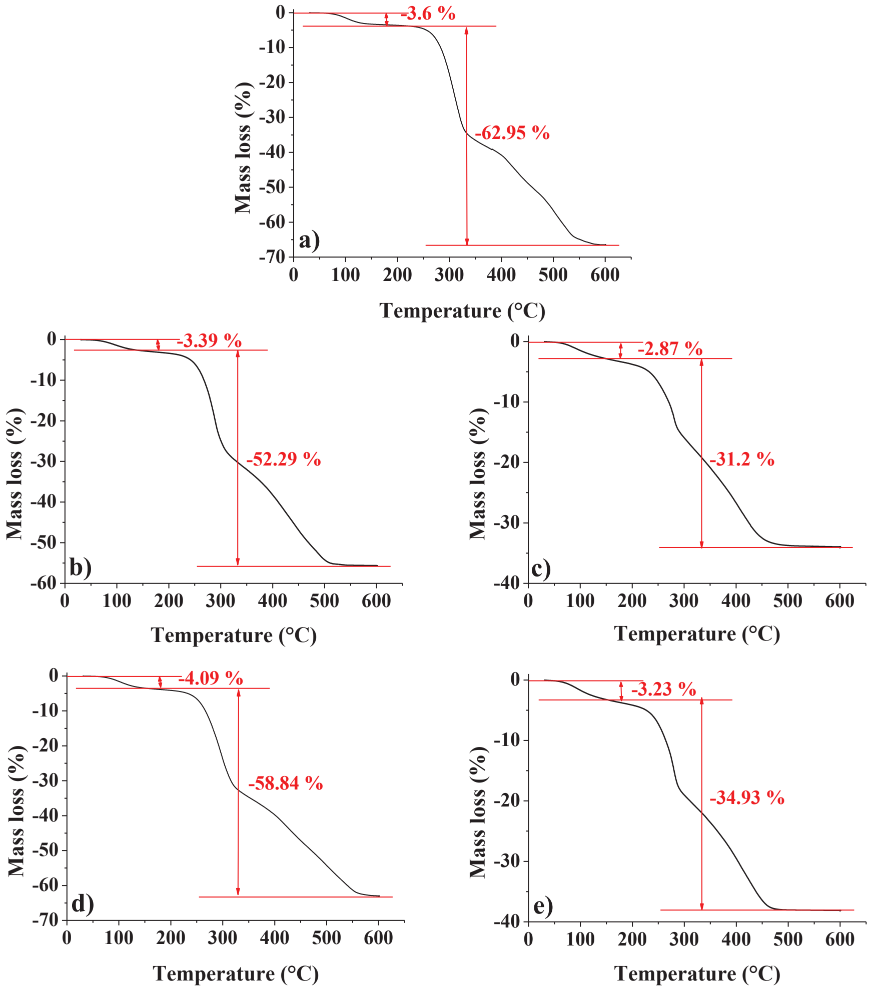

Figure 5. TGA curves of (a) 2.5-RODS-TiO_2, (b) 4-TTAB-TiO_2, (c) type 10.5-TTAB-TiO_2, (d) 4-TERG-TiO_2, and (e) 10.5-TERG-TiO_2 fibers, the mass loss between 0 and 200°C corresponding to the water content.

Table 1. Elemental analyses of TiO_2 fibers obtained by coupling laser ablation with plasma torch and mass spectroscopy (ICP-MS), and their resulting stoichiometry.

Fibers	% weight				Stoichiometry	%w TiO_2
	C	Ti	Na	H_2O		
2.5-RODS-TiO_2	35.5	9.4	5.1	3.6	$(TiO_2)_1(PVA)_{9.8}(Na_2SO_4)_{0.8}.1.3H_2O$	12
4-TTAB-TiO_2	24.2	11.4	8.2	3.4	$(TiO_2)_1(PVA)_6(Na_2SO_4)_{1.1}.1.2H_2O$	15
10.5-TTAB-TiO_2	17.4	18.4	10.7	2.9	$(TiO_2)_1(PVA)_{2.7}(Na_2SO_4)_{0.85}.0.65H_2O$	24
4-TERG-TiO_2	31.7	11.2	4.6	4.1	$(TiO_2)_1(PVA)_{7.5}(Na_2SO_4)_{0.68}.1.5H_2O$	15
10.5-TERG-TiO_2	18	18	9.9	3.2	$(TiO_2)_1(PVA)_{2.7}(Na_2SO_4)_{0.76}.0.7H_2O$	25

III.1.2. Surface composition

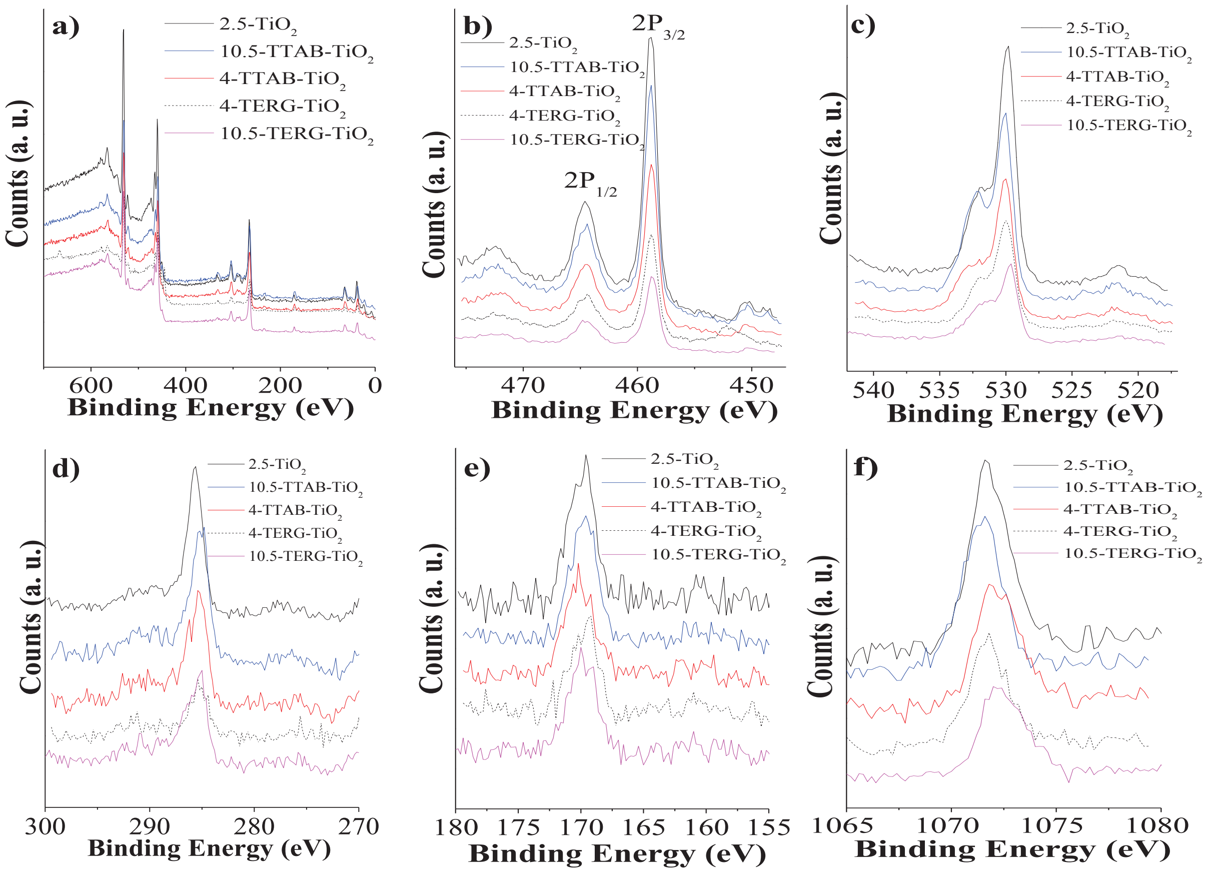

Figure 6. XPS spectra of the TiO_2 macroscopic fibers. (a) Survey spectra in the range 0-700 eV, (b) spectra focused on the Ti-2p region, (c) spectra focused on the O-1s region, (d) spectra focused on the C-1s region, (e) spectra focused on the S-1s region, (f) spectra focused on the Na-1s region. We can notice that the Na-1s spectrum is out of the range of the Figure 6.a. survey.

We ran XPS studies to probe the chemical composition of the different fibers. Indeed, it is important to check if the 450°C thermal treatment applied to the fibers could allow us to get rid of all carbon residues, for a better photocatalytic effect, because XRD (Figure 3) demonstrated that the temperature cannot be increased limitless without inducing the Anatase-to-Rutile transformation, another major drawback since Rutile is less effective than Anatase for photocatalysis. The qualitative results of first XPS experiments are displayed in Figure 6. Survey spectra were taken (Figure 6.a.) and the presence of Titanium (Ti^{4+}), Oxygen (carboxyl groups), Sulfur (sulfate groups), Carbon and Sodium was evidenced. The atomic distribution through the fiber thickness was also measured by coupling XPS with Ar-ion sputtering technique (Figure 7).

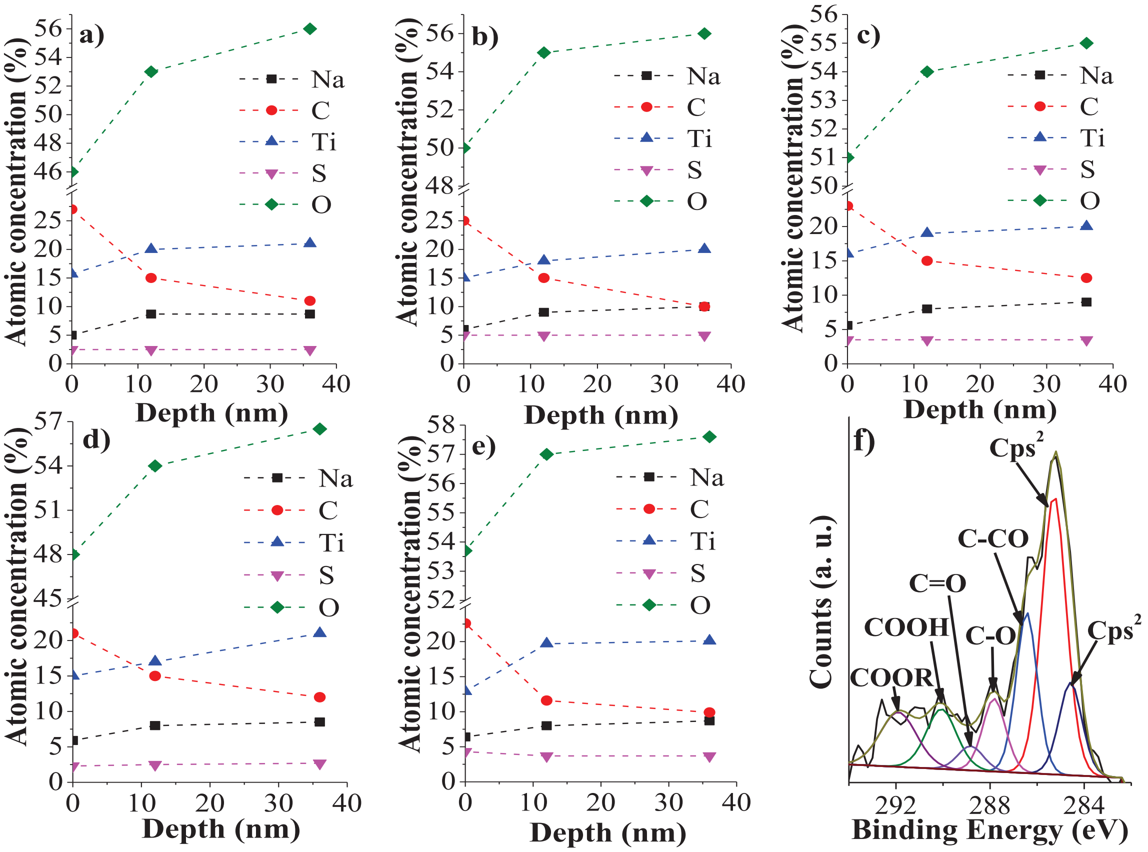

Figure 7. Surface relative atomic concentration of the calcined fibers extracted from X-ray photoelectron spectrum (XPS), summed to 100% relative (a) 2.5-RODS-TiO_2, (b) 4-TTAB-TiO_2, (c) 10.5-TTAB-TiO_2, (d) 4-TERG-TiO_2, (e) 10.5-TERG-TiO_2 fibers, and (f) example of deconvolution spectra for the C1s peak obtained for the 10.5-TTAB-TiO_2 fiber (pass energy 40 eV).

The evolution of the atomic composition (summed to 100%) as a function of the fiber depth (Figure 7.a.-e.) demonstrates that the fiber composition varies within a first surface shell, namely from the fiber surface down to 12 nm, and in the sub-surface region of the fiber from to 12 nm down to 40 nm. The carbon concentration is high (25%) at the surface and decreases down to 10-15% at 12 nm from the surface, followed by a steady reduction to 10-12% atomic percentage at 40 nm from the surface. C1s peaks (Figure 7.f.) demonstrate that carbonate and other carboxyl groups are present at the fiber surface. This excess in Carbon concentration should result from Carbon residues still remaining after the thermal treatment at 450°C. Automatically, as the Carbon concentration decreases from the outer to the inner surface, all the other relative atoms concentration are increasing, except for Sulfur and Sodium, depicting a constant atomic concentration profile. This evolution reflects a homogeneous distribution of the TiO_2 phase within the fiber, whereas the constant rate of Sulfur and Sodium, which is artificially increased by the Carbon concentration reduction, means that the actual concentration in sodium sulfate is higher at the surface of the fibers. As the fibers contain a significant amount of carbon at their surface, they will be treated with UV light prior to the photocatalysis experiment in order to eliminate these carbon residues. As the salt could also impact the fibers photocatalytic behavior, it is needed to find a way to wash the fibers more efficiently. This was achieved by using a semi-industrial process which is presented in Chap. 4, part II.

III.1.3. Structural analyses

Once these hybrid fibers have been synthesized we applied thermal treatment to both promote TiO_2 nanoparticles crystallization and create inter-particle void space. As said within the experimental section, the TiO_2 nanorods synthesis provides immediately the TiO_2 Anatase allotropic form (Figure 8.E.) and calcinations result only on creating inter-particles void space though PVA calcination. Concerning the other syntheses using TTAB and Tergitol, we employed thermally-assisted X-ray diffraction (XRD) to assess the evolution of the crystalline structure during thermal treatment (Figure 8.A.-B.).

The spectra present organic diffraction peaks at room temperature vanishing when the temperature reached 400°C. We can notice that broad peak representative of the [101] Anatase Miller indices at room temperature cannot be distinguished on the TTAB-TiO_2 fibers diffractogramm. When the temperature of the thermal treatment increases, the Anatase monophasic form peak becomes sharper from 100°C to 600°C. We can also notice a shoulder aside the Anatase [101] diffraction, disappearing at 700°C in both cases. This diffraction peak is certainly due to sodium sulfate (present within the starting composite fibers), which is probably oxidized at high temperature (Table 1). This hypothesis was validated by XRD pattern of the dried powder used to generate the starting TTAB-TiO_2 and TERG-TiO_2 sols where the as-discussed above-shoulder is absent from the full set of diffractogramms (Figure 8.C-D).

Above 600°C, and up to 900°C, the allotropic transformation from Anatase to Rutile occurs leading for both TTAB-TiO_2 and TERG-TiO_2 inorganic fibers to a biphasic Rutile/Anatase material. As the TP-XRD-experiments were monitored at 2°C per minute, we kept this ramp value for treating the fibers at 450°C (2°C.min^{-1} heating rate) during 6 hours, in order to fully calcine the organic counterpart of the starting composite fibers, while promoting monophasic

Anatase crystallization. The crystallites size of the particles inside the calcined fibers was evaluated using the Debye-Scherrer formula: $D = k\lambda/(H.\cos(\theta))$, with D the crystallites diameter, k the shape factor ($k = 0,9$), λ the incident light wavelength ($\lambda_{CuK\alpha 1} = 1,5406$ Å), H the full width at half maximum of the peak, and θ the Bragg angle. The crystallites size of the spherical particles was about 6 nm and the crystallites size of the nanorods was about 11x20 nm.

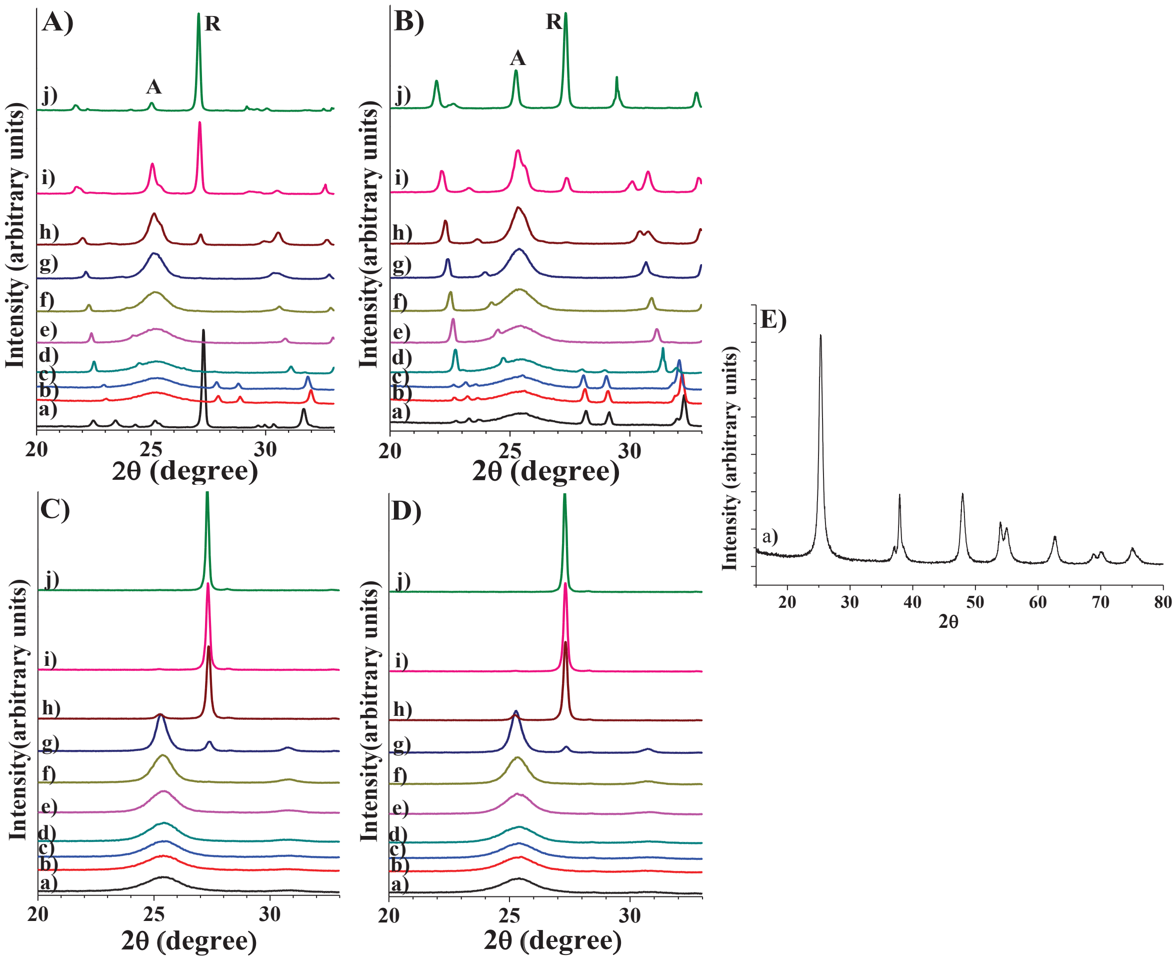

Figure 8. X-rays diffraction patterns at different temperatures. (A) 4-TTAB-TiO_2 fibers, (B) 4-TERG-TiO_2 fibers, (C) 4-TTAB-TiO_2 powder, (D) 4-TERG-TiO_2 powder, (E) 2.5-RODS-TiO_2 powder, at 25°C (a), 100°C (b), 200°C (c), 300°C (d), 400°C (e), 500°C (f), 600°C (g), 700°C (h), 800°C (i) and 900°C (j). A: Anatase; R: Rutile.[51,52]

III.1.4. Fibers porosity

SEM analyses (Annex.3.1.II) allowed us to visualize the distribution of particles and pores after this thermal treatment (Figure 9). We observe that the diameter of the fibers varies with the initial concentration of the inorganic phase in the extruded sol. When the concentration in TiO_2

increases from 2.5 wt% (Figure 9.a.) to 4 wt% (Figure 9.c.-e.), then 10.5 wt% (Figure 9.g.-i.), the diameters increase as well from 230 µm (Figure 9.a.), to 500 µm (Figure 9.c.-e.), and finally 700 µm (Figure 9.g.-i.), respectively. This evolution is the result of the variation in the sol viscosity, resulting from the particles concentration, which balances the shear applied over the extruded jet. Regarding the 2.5-RODS-TiO_2 fiber, the final diameter can be also relevant to a shape effect from the needle-like TiO_2 particles, as already reported for vanadium oxide macroscopic fiber diameter.[44] However, it appears (Figure 9.b.) that the TiO_2 needles are randomly positioned within the fiber core, which precludes a similar shear-thinning effect. A close observation of the fiber surface (Figure 9.b,d.,f.,h.,j.) reveals also the interparticle porosity, that ranks within the mesoporosity range (above 2 nm),according to the IUPAC nomenclature.[53]

The porosity was studied by nitrogen physisorption measurements (Annex.3.1.III) on calcined fibers (Figure 10.a.-e.). All curves exhibit a rather straight adsorption curve, which can be described as a mix of type II-IV isotherms, along with a broad pore size distribution in the mesoporous range. Almost hysteresis is observed. The lack of steep adsorption at $P/P_0 < 0.05$, indicates that the fibers do not bear microporosity. It is finally noteworthy that the nitrogen isotherm of the 2.5-RODS-TiO_2 fibers differs slightly from the others at high P/P_0 values (above 0.9), and that the hysteresis is still small but more pronounced than for the other samples. We explain this feature as a result of the aggregation of anisotropic particles in bunches that can contribute to define some bottle-neck porosity.

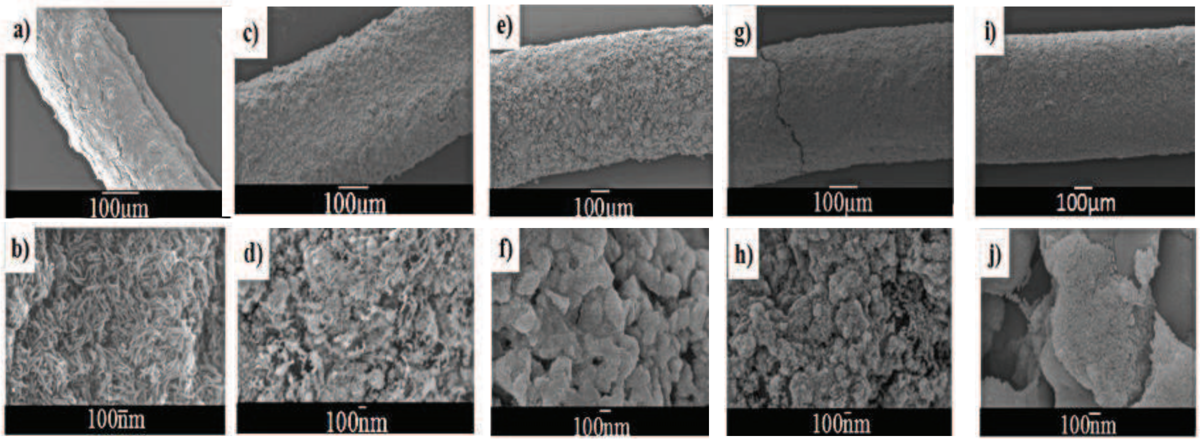

Figure 9. SEM images of the different thermally treated TiO_2 fibers: 2.5-RODS-TiO_2 fiber (a) and (b), 4-TTAB-TiO_2 fiber (c) and (d), 10.5-TTAB-TiO_2 fiber (e) and (f), 4-TERG-TiO_2 fiber (g) and (h) and 10.5-TERG-TiO_2 fiber (i) and (j).

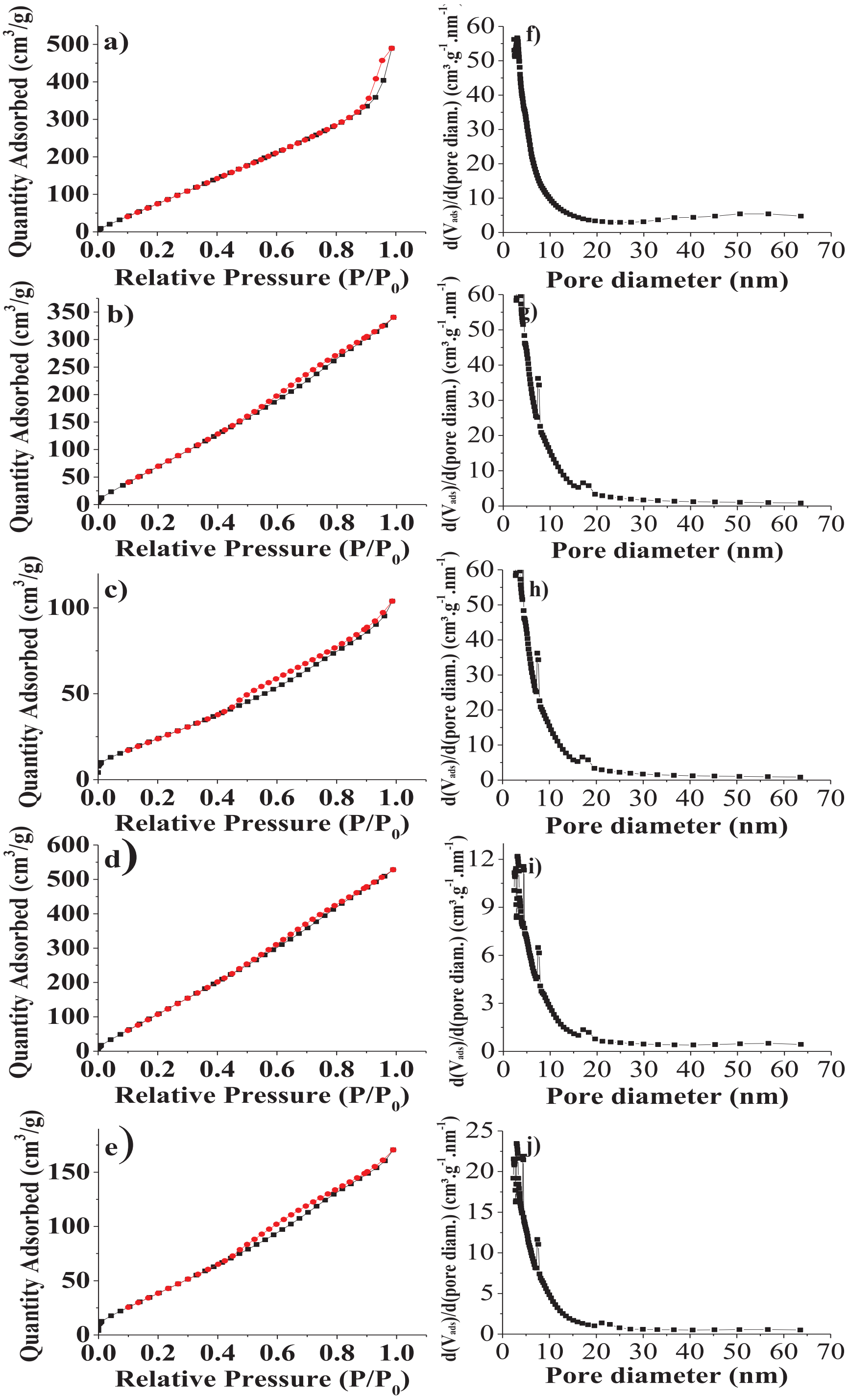

Figure 10. Nitrogen physi-sorption experiments. ■ Adsorption curves, ●desorption curves. (a) 2.5-RODS-TiO_2, (b) 4-TTAB-TiO_2, (c) 10.5-TTAB-TiO_2, (d) 4-TERG-TiO_2, (e) 10.5-TERG-TiO_2 fibers. Pore sizes distribution deduced from nitrogen adsorption curves (f) 2.5-RODS-TiO_2 fibers, (g) 4-TTAB-TiO_2, (h) 10.5-TTAB-TiO_2, (i) 4-TERG-TiO_2, and (j) 10.5-TERG-TiO_2 fibers.

We explain this feature as a result of the aggregation of anisotropic particles in bunches that can contribute to define some bottle-neck porosity. The pore size distribution (Figure 10.h.-j.), calculated with the BJH equation from the desorption curves, indicates that the pore size ranges between 6 nm and 15 nm.[53] The specific surfaces area of the titanium dioxide fibers are displayed in Table 2. All surface areas are relevant to mesoporosity. The specific areas are ranging from 100 to 700 $m^2.g^{-1}$. The lower surface areas are obtained with the fibers synthesized with the higher titanium oxide weight fraction (10.5 wt%). We assumed that the high values of the specific surface areas was due to the high amount of pores on the fibers surface (very high total pore volume), which was generated thanks to this specific synthetic pathway.

Table 2. Specific surface area of the calcined TiO_2 fibers obtained through Nitrogen physi-sorption experiments. * BJH determined from the desorption curves.

Fibers	BET surface $m^2.g^{-1}$	BJH surface* $m^2.g^{-1}$	Total Pore Volume $mL.g^{-1}$	Ds (surface roughness)
2.5-RODS-TiO_2	520	450	0.76	2.37
4-TTAB-TiO_2	430	412	0.53	2.3
10.5-TTAB-TiO_2	106	120	0.16	2
4-TERG-TiO_2	700	652	0.82	2.31
10.5-TERG-TiO_2	190	214	0.26	2.1

III.1.5. Surface roughness

The surface roughness of these materials can be an important factor in photocatalysis, for an optimized interaction between the pollutants and the catalyst. It was evaluated from the determination of the Fractal surface Dimension (Ds), which can be deduced from the nitrogen isotherm adsorption curves (Figure 11 The calculations allowing the determination of the fractal dimension are presented in Annex 3.1.III. Ds must vary between 2 (flat surface) and 3. Any value higher than 2 describes an increasing surface roughness.

We see in Table 2 that Ds becomes closer to 2, as the TiO_2 content increases. This is especially true for 10.5-TTAB-TiO_2 which presents a flat surface (Ds = 2). We assume that increasing the percentage of inorganic mater within the starting sol favors the stacking of the titania particles during the drying process, and increases the efficiency of sintering during the thermal treatment, which results in both lower porosity and surface roughness.

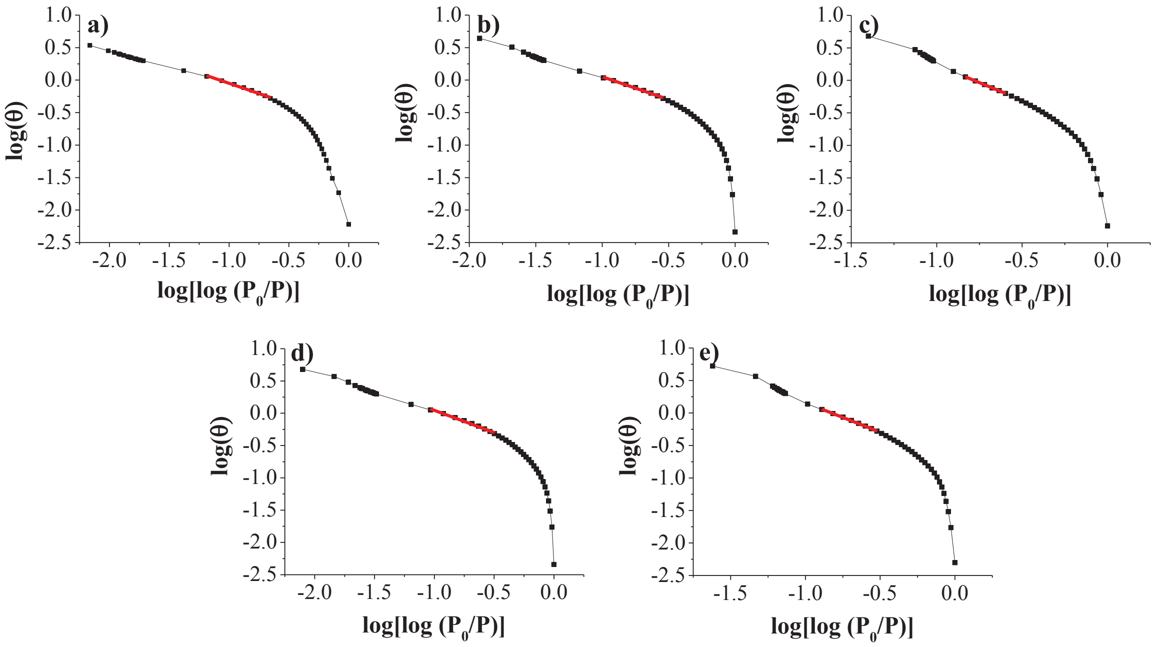

Figure 11. Surface fractal analysis of a) 2.5-RODS-TiO_2, b) 4-TTAB-TiO_2, c) 10.5-TTAB-TiO_2, d) 4-TERG-TiO_2, e) 10.5-TERG-TiO_2 fibers obtained from the adsorption curve of the isotherm.

III.2. Optical properties and band gap

Light penetration was modeled with the Kubelka–Munk model that describes the light penetration in porous media (F(R)) with only two parameters: an absorption coefficient of the porous solid, k, and an isotropic particle size-dependent scattering coefficient, s (which both have units of cm^{-1}).[54]

We performed DRUV experiment in order to determine the energy band gap of our fibers, which corresponds to the energy where the fibers absorb a maximum of photons. This parameter is important to determine the type of UV lamps that are used for the photocatalytic experiment. The DRUV spectra of the calcined fibers are shown in Figure 12.a. The calcined fibers were also grounded and sieved through a 90µm mesh in order to obtain a higher contribution from the bulk of fibers, compared with the surface signal collected from the fibers themselves (Figure 12.b.). The spectra of these powders display a similar absorption edge with a mean value of 3.1eV± 2%, for all the fibers. Such a bandgap is smaller than the often-reported 3.2 eV for anatase, but are still consistent.[55] We concluded that the crystalline structure and the intrinsic optical properties of the TiO_2 is not significantly affected by the starting solution concentration in TiO_2 nanoparticles.

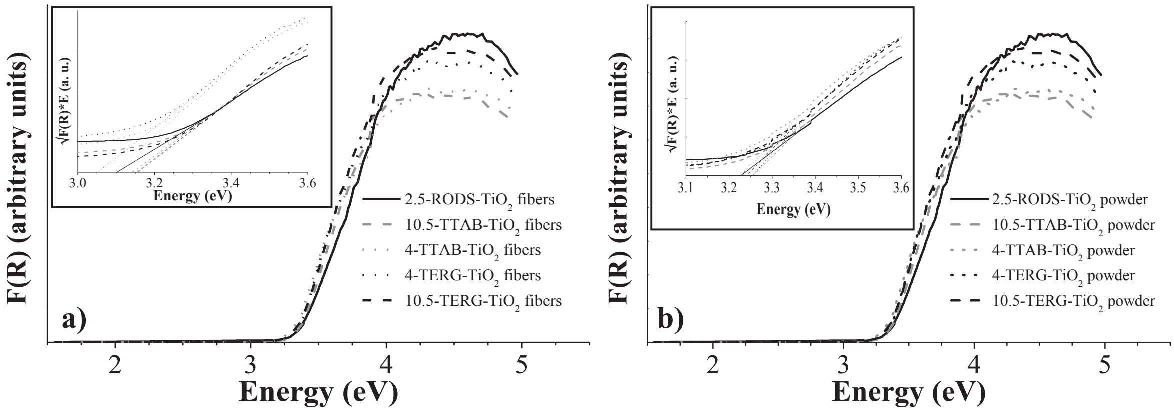

Figure 12. Diffuse reflectance UV spectra of (a) the calcined fibers, (b) the grounded and 90 μm sifted powdered fibers.

III.3. Photocatalytic properties

III.3.1. Experimental set up and modelisation

Photocatalytic mineralization of gaseous acetone was carried out in a specially designed batch reactor (Scheme 1), based on a PTFE circulating loop where a photoreactor 1 was inserted. Acetone was chosen as a test for Volatile Organic Compound (VOC) decomposition, because its photocatalytic mineralization is well documented.[56–58] The photocatalytic experiment protocol is described in Annex.3.1.V. Photocatalytic activity of our samples was compared with Quartzel® PCO from Saint-Gobain Quartz and a commercial nanocrystalline anatase (P25 from Evonik), under strictly identical conditions (reactor, lamps, flow-rate, % RH, initial acetone concentration). The ratio of remaining acetone are given per gram of photocatalytic media, even though it is known that Quartzel® fibers are made of quartz fibers coated with TiO_2 (composition of the commercial product unknown, fiber diameters 9 μm, specific surface area 120 $m^2.g^{-1}$).

The detailed photocatalytic experiment protocol is presented in Annex.3.1.V. The relative humidity was adjusted to 15 % , the flow-rate of the circulation pump was 3.3 L. min^{-1}, corresponding to a 0.7 m. s^{-1} velocity of the gas on the photocatalytic media for reactors 1. The device leaks were determined by introducing acetone and monitoring its concentration along with the CO_2 concentration in the dark for 20 hours, and their contribution were further subtracted. The equations used for the calculation of the acetone degradation and the mineralization yield are presented in Annex.3.1.V.

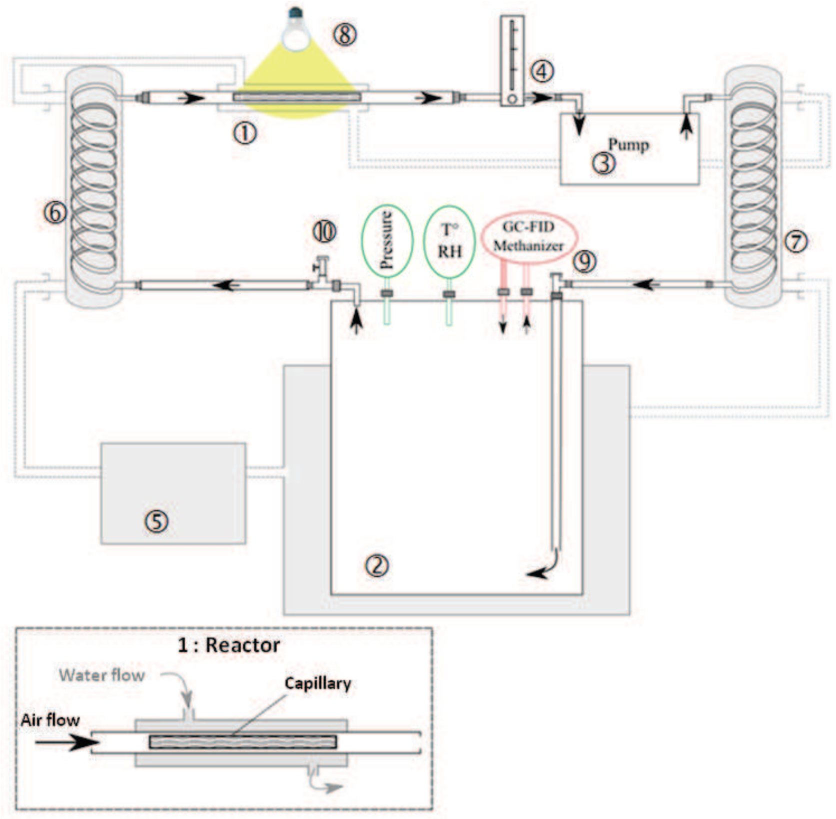

1- Reactor
2- 17 L tank
3- Pump
4- Flow meter
5- Water bath
6&7- Cooling columns
8- Light Source
9- Synthetic air entry
10- Synthetic air exit

Scheme 1. Photocatalytic circulating batch reactors designed for gas-solid reactions.

III.3.2. Fibers photocatalytic performance

We probed the influence at different scales (1D micrometric fibers, isotropic or needle-like particles, surface roughness) of the hierarchical architecture of TiO_2 materials onto their photocatalytic performances. The cylindrical reactor containing a pyrex canister was designed to test the fibers with a parallel flow gas. In a first step the photocatalytic device and the reaction conditions were settled with commercial TiO_2 fibers (Quartzel® PCO, Saint-Gobain Quartz) in the same configuration. The performances of the TiO_2 fibers were then compared to those of this commercial material under identical conditions. Complementary comparison was made using the 90µm powder from the 10.5-TERG-TiO_2 fibers. This powder was deposited as a slurry on the pyrex canister in the reactor (11.8mg of the grounded fibers). The results are given in % acetone degradation *per gram of media* on one hand, and in % of mineralization of the acetone during the experiment on the other hand. Mineralization percentage is defined as the number of moles of CO_2 evolved per mole of degraded acetone (Figure 13). Evolution *vs* time of the acetone degradation and the associated mineralization rate are presented in Figure 13.a.-b. The fibers present photocatalytic properties as they degraded and mineralized acetone (Figure 13) when settled in the reactor. The commercial material has a higher degradation rate, which is not surprising since our fibers are too thick to allow a high light penetration.

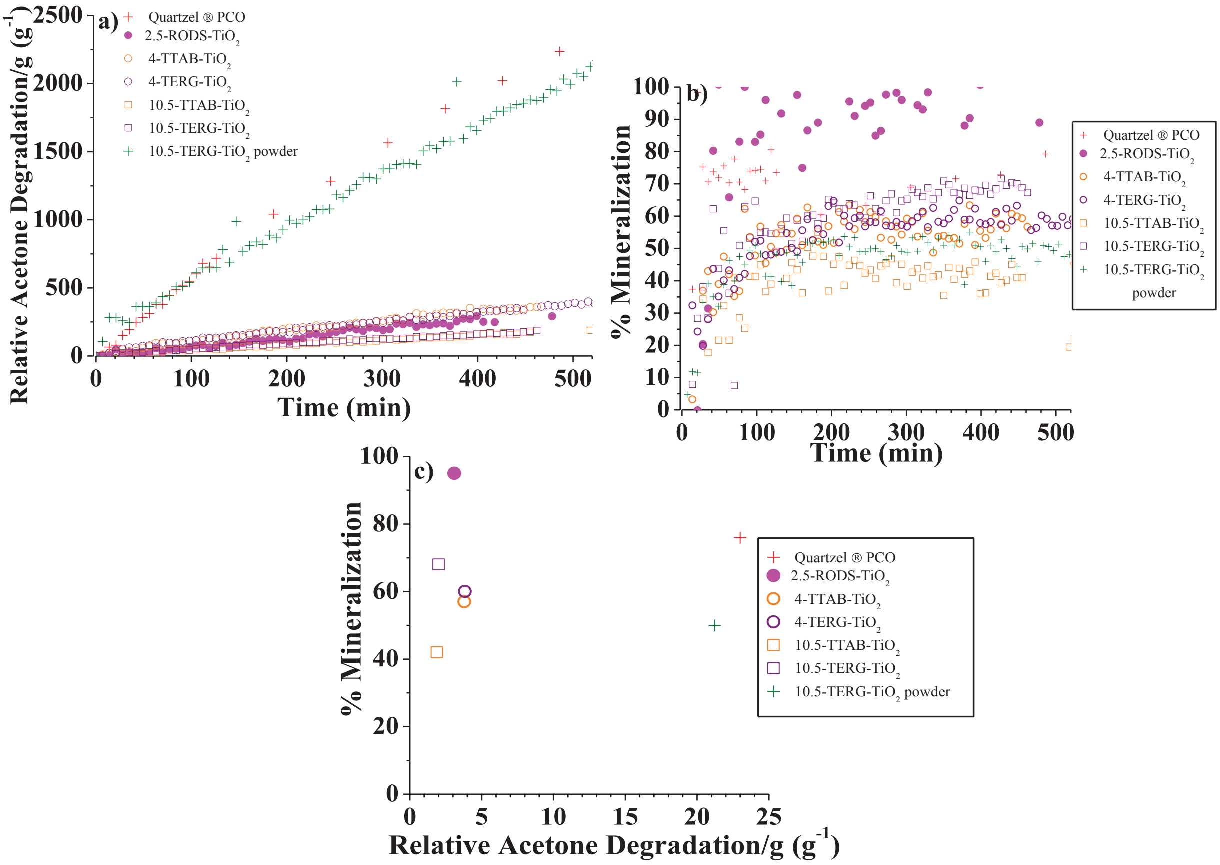

Figure 13. a) Evolution vs time of acetone degradation b) Evolution vs time of mineralization rate c) Comparison between the final acetone degradation percentage and the final mineralization percentage of the five types of fibers, the powdered 10.5-TERG-TiO_2 fibers, and the Quartzel ® under irradiation of acetone at 366 nm (RH 15 %, temperature 22 ± 2 °C, initial acetone concentration 45 ppmv, air flow rate 3.3 L minute^{-1}).

Nevertheless, we observe that our fibers exhibit a similar or higher mineralization rate when dealing with anisotropic particles (full degradation of acetone into CO_2) than those of the commercial products (Figure 13.c.). We noted also that the 10.5-TTAB-TiO_2 fibers, with the lowest surface roughness (Ds = 2) exhibit the lowest percentage of mineralization and the lowest acetone degradation per gram of media. The 2.5-RODS-TiO_2 fibers were found to be the most efficient in term of mineralization percentage (95%). However, as their surface roughness is also higher than the ones of the other fibers, it is difficult to conclude on the better mineralization of the anisotropic nanoparticles compared to the isotropic ones. The surfactant used for the TiO_2 nanoparticles synthesis does not seem to have a significant influence on the acetone degradation per gram of media, as the results are similar in both cases. However, TERG-TiO_2 fibers seem to have slightly higher performances for both the acetone degradation and the mineralization. These results confirm that the initial size of fibers (several hundreds of microns) do not allow for a complete access of light to titania, but the higher level of mineralization supports the concept of a higher residence time for the acetone by-products leading to a high percentage of degradation.

Moreover, the loss of efficiency with the 10.5-TTAB-TiO_2 and the 10.5-TERG-TiO_2 fibers compared to the 4-TTAB-TiO_2 and the 4-TERG-TiO_2 fibers can be assigned to the lack of surface roughness, compared with other materials. Also, the diameter of the fibers was too large and the UV light could only penetrate in the shell of the fibers, which let the center of the fiber inactive for photocatalysis reaction. As the performances were evaluated per gram of media, we assumed that the large diameter of the fibers was also a factor responsible for the low performances of our fibers compared to the commercial product. This factor was checked by comparing the 10.5-TERG-TiO_2 fibers (degradation: 2 %, mineralization: 68%) with the same fibers crushed and sieved at 90µm powder (11.8 mg deposited onto the walls of the canister). The results obtained with the crushed fibers (degradation: 21.23%; mineralization: 50 %) demonstrate that the degradation was improved by the surface effect that allowed for a better irradiation, but the mineralization is reduced due to the disappearance of the fiber shape factor that allowed for a higher residence time. We could deduce from this result that reducing the diameter of the fiber could help improving their performances. No by-product was detected within the sensitivity of the analytical device (0.1 ppmv), while high but not complete mineralization was achieved. We assume that any by-product, if formed, was adsorbed on the reactor walls.

Conclusion

PVA/TiO_2 macroscopic fibers can be prepared through original integration between sol-gel chemistry, extrusion process and salt-induced flocculation. Upon calcination at 450°C in air, stable macroscopic fibers made of Anatase nanoparticles, are generated. Although fragile, these mineral fibers can be manipulated and keep their structural integrity even after catalytic tests under gas flow. The thermal treatment allows for creating some mesoporosity by burning the original PVA matrix and residual surfactants molecules trapped in the TiO_2 structure, but XPS experiments reveal that there are still salt and carbon residues present after calcination both on the TiO_2 fiber surface and in a sub-surface level, down to 40 nm. Photocatalytic efficiency was demonstrated at the gas-solid interface with lower degradation rate, but a higher mineralization percentage that the commercial Quartzel® fibers thanks to their optimized structure. It was obvious that the overall size of our materials cannot allow them to compete -at this stage- with optimized commercial catalysts. This study allowed us anyway to understand the influence of structural factors on taylor-made materials (fiber shape and surface roughness), which will be used in the future to optimize their photocatalytic efficiency. Unfortunately, we could not conclude clearly on the influence of the nanoparticles shape on the photocatalytic performances, and it would be interesting to test them again when the fiber generation process will be fully controlled. Nevertheless, according to these results, particles synthesized with Tergitol NP-10 seem to give slightly higher result than the ones synthesized with TTAB. In our future work, this surfactant will be then used for TiO_2 syntheses. Also, we have identified two main penalties that need to be considered for optimizing the as-synthesized fiber photocatalytic properties. First, it will be important to minimize the amount of carbon and salt content while maintaining the Anatase phase during the thermal treatment. The second main issue is to optimize the light access into the fiber core by reducing the fibers diameter. Even though these materials exhibit a high surface area (up to 700 $m^2.g^{-1}$), the light access is limited by natural screening. Finally, as we demonstrate that surface roughness has an impact on the acetone degradation, increasing this surface roughness could help in increasing the photocatalytic performances of the fibers.

Annex

Annex 3.1: characterization techniques and protocols

I. X-ray diffractometry

The crystalline structure of the powder obtained was analyzed with a thermally-assisted X-ray diffraction (XRD). The equipment used is a PANalytical X'pert MDP diffractometer with a Bragg–Brentano θ–θ geometry diffractometer, equipped with a back graphite monochromator and an Anton Paar HTK16 chamber (Cu-Kα X-ray, $\lambda = 1.54$ Å, 40 kV working voltage, 50 mA working intensity).

II. Scanning electron microscopy

Scanning Electron Microscopy (SEM) observations were performed on a 6700F JEOL apparatus which is a high resolution model equipped with a cold cathode field emission gun. Working voltage was set up at 10 kV or 5 kV.

III. Nitrogen adsorption/desorption method and roughness calculation

Specific surface areas and pore characteristics at the mesoscale were measured using nitrogen adsorption method with a Micromeritics ASAP 2010. The samples were outgassed at 150°C under vacuum for 12 h before the measurement.

The surface roughness was evaluated from the determination of the Fractal surface Dimension (Ds), which can be deduced from the nitrogen isotherm adsorption curves. Ds was calculated according to the procedure described previously.[59] The experimental adsorption isotherm data are replotted according to:

$$\log(\theta) = \log(K) - \nu \log(\log[P_0/P])$$

where $\nu = 3 - Ds$, θ is the relative adsorption calculated by normalizing the curve with the highest adsorption value, K is a constant and Ds is the surface fractal dimension that we are looking for.

Ds is deduced from the slope of the line, and it must vary between 2 (flat surface) and 3. Any value higher than 2 describes an increasing surface roughness. The adsorption range to be used for this analysis has to be taken within the partial pressure range $0.05 < P/P_0 < 0.3$ and limited below the Kelvin condensation step that corresponds to the pore filling.[60]

IV. Diffuse reflectance UV-vis (DRUV)

The diffuse reflectance UV-vis spectra (DRUV) were measured in steps of 1 nm with a Perkin-Elmer 860 Spectrophotometer equipped with a 15 cm diameter-integrating sphere bearing the holder in the bottom horizontal position. The instrument was calibrated with a certified Spectralon white standard (Labsphere, North Sutton, USA). Light absorption in porous media was modeled with only two parameters according to the Kubelka–Munk: an absorption coefficient, k, and an isotropic scattering coefficient, s (which both have units of cm^{-1}).[54]

V. Photocatalytic experiment protocol and modelisation

The gas circuit consisted of a thermo-regulated pyrex reservoir tank 2 (17 L) connected to a Kel-F circulating pump 3, the flow-rate of which may be controlled by a flow-meter 4. In order to limit gas heating, thermo-regulated columns 6 and 7 were inserted at the pump outlet and inlet. The reservoir tank was equipped with a manometer and a temperature/hygrometry probe in order to record the circulating gas temperature and relative humidity all along the experiment. Thermoregulation of the whole device was made through the water-bath 5. The gas was automatically and periodically sampled through a 10 $L.min^{-1}$ pump to a Varian 3800 GC equipped with a FID detector (for Volatile Organic Compound (VOC) monitoring) and a methanizer for CO_2 detection. A cylindrical photoreactor 1 was used in the experiment and. was composed of a thermoregulated pyrex column where a pyrex canister (inner diameter 10 mm) containing the photocatalytic fibers was slipped. Four fluorescent tubes (Philips TLD8W) with emission maximum at 366 nm were set upon the photoreactor 1.

For all the experiments, the same procedure was followed: once the reactor containing the photocatalytic media was settled in the device, synthetic air was introduced and the relative humidity was adjusted to 15 % by injecting the required amount of water through a septum on top of the tank. The flow-rate of the circulation pump was 3.3 $L. min^{-1}$, corresponding to a 0.7 $m. s^{-1}$ velocity of the gas on the photocatalytic media for reactors 1. The temperature of the circulating gas was 22 ± 2 °C. The photocatalytic media were first irradiated for 20 hours without acetone under these conditions in order to activate them and determine the possible evolution of adsorbed VOCs or CO_2. No peak appeared on the chromatograph during this step, but slow CO_2 increase was noticed due to the leaks in the device and possibly to the photocatalytic degradation of residual organic materials contained within the fiber. The lamps were then switched off. Then 45 ppmv (2µL) of acetone was injected in the tank through the septum.

The acetone adsorption step on the media was followed by GC. When the gaseous acetone concentration was stable, the lamps were switched on (time 0). Acetone and CO_2 concentration was monitored every 7 min by automatic sampling on the GC-FID-methanizer.

Modelisation

The device tightness was determined by introducing acetone and monitoring its concentration in the dark for 20 hours. During the photocatalytic experiments, the linear decrease in the dark (no more than 20 %) was taken into account, and its contribution was further subtracted. For the determination of the mineralization yields (evolution of CO_2), the linear increase from 30 ppmv to 170 ppmv over 20 hours in the dark (leaks) was deduced from the CO_2 evolution during the photocatalytic experiment. The acetone and CO_2 leaks are fitted by linear curves, their slopes being referred in the following as k_1 and k_2 respectively.

In order to calculate the % of acetone degradation, we considered that the reference value of acetone, $[\mathrm{Acetone}]_{\mathrm{ref}}$, was equal to the initial concentration of acetone minus the leaks intrinsic to the system.

$$[\mathrm{Acetone}]_{\mathrm{ref}} = [\mathrm{Acetone}]_{\mathrm{t=0}} - \mathrm{k}_1 \times \mathrm{t}$$

In consequence, the acetone degradation percentage can be expressed as:

$$\%\ \mathbf{Degradation} = \left(\mathbf{1} - \frac{[\mathbf{Acetone}]_{\mathbf{t}}}{[\mathbf{Acetone}]_{\mathbf{ref}}}\right)$$

For the calculation of the mineralization rate, the same adjustments were made. We then considered that the acetone concentration which was degraded by the photocatalysis experiment corresponded to:

$$[\mathrm{Acetone}]_{\mathrm{degraded}} = [\mathrm{Acetone}]_{\mathrm{ref}} - [\mathrm{Acetone}]_{\mathrm{t}}$$

In the CO_2 case, we defined that the CO_2 concentration generated by the mineralization of the acetone itself was equal to:

$$[\mathrm{CO}_2]_{\mathrm{produced}} = [\mathrm{CO}_2]_{\mathrm{t}} - ([\mathrm{CO}_2]_{\mathrm{t=0}} + \mathrm{k}_2 \times \mathrm{t})$$

Finally, we obtained that the mineralization rate was given by the equation:

$$\%\ \mathbf{Mineralization} = \frac{[\mathbf{CO_2}]_{\mathbf{produced}}}{\mathbf{3} \times [\mathbf{Acetone}]_{\mathbf{degraded}}}$$

Chapter 4:

Advanced nanotextured TiO_2 fibers bearing enhanced photocatalytic properties

In the previous chapter, we demonstrated how it is possible to generate titanium dioxide/ polyvinyl alcohol (TiO_2/PVA) macroscopic fibers through extrusion. These fibers were made of isotropic or anisotropic TiO_2 nanoparticles. It was demonstrated that after calcination, these TiO_2 fibers present interesting photocatalytic properties, with the surface roughness being a key parameter for the acetone degradation. However, due to their large diameter (around 400µm), their acetone degradation rate per gram of media could not be compared with the commercial product (Quartzel PCO fibers) as light cannot penetrate deep in the fibers structure. In the literature, the catalytic behavior of vanadium oxide fibers has been improved by the insertion of latex particles allowing the formation of macropores after the calcination step.[1] In consequence, two possible routes leading to the improvement of the fibers photocatalytic performances were explored: the reduction of the fibers diameter, and the increase of their roughness (macroporosity).

In the first part of this chapter, a new type of fiber is investigated, which was generated by using a syringe with a smaller diameter (600µm instead of 1mm). Latex particles were inserted into the TiO_2/PVA solution with the aim of adding another type of macroporosity inside the final fiber structure in order to increase the surface roughness. The influence of the latex particles sizes and concentrations is also illustrated for this process.

In the literature, PVA fibers and carbon nanotubes/PVA fibers have been generated by a continuous spinning process using a static coagulation bath.[2,3] However, adapting this process to composite fibers made of isotropic particles presents a real challenge as the particles here act as defect in the fibers instead of acting as a mechanical adjuvant. Therefore, in a second part, we present the adaptation of this spinning process to our fibers, which allows for the generation of several hundred meter long fibers. Here, the continuous spinning process uses a spinneret with a diameter about 300µm (smaller than before) and a static coagulation bath.

I. Enhancement of the fibers photocatalytic properties: triggered topology and smaller fibers diameter

I.1. Studied system and experimental protocol

I.1.1. Particles syntheses

Monodisperse Polystyrene (PS) dispersions were prepared by emulsion polymerization according to the process described by Zhang *et al.*[4] Latex particles presenting diameters of 130 nm and 260 nm were synthesized for this study.

The TiO_2 nanoparticles were synthesized according to the process described in our previous work.[5] Typically, 5 mL of an HCl solution was first added to a 50 mL nonylphenol-EO_{10} nonionic surfactant (Tergitol NP-10) 15wt% solution. The pH of the solution was then increased up to 1.8 by addition of an ammonia solution. Titanium isopropoxide was then slowly added under stirring (6.4mL), and the solution was left at room temperature. A slurry-like white precipitate was formed after several hours, which was recovered after full evaporation. The resulting powder was washed several times with deionized water until no foaming resulting from the remaining surfactant was observed.

I.1.2. TiO_2/PVA/Latex fibers co-extrusion process

First, aqueous suspensions of TiO_2 nanoparticles were prepared from the dry extracts in order to obtain 4 wt% TiO_2 in the final solution. Solid PVA was then added into this solution under stirring at 90°C in a proportion of 0.12 g of PVA per mL of solution. This solution was kept under stirring for 1 hour until the PVA was fully dissolved and then cooled down at 60°C. When the solution reached 60°C, the latex particles were incorporated in the solution maintained under stirring. In order to ensure the homogeneity of the solution, the solution was then cooled down at room temperature and agitated with a vortex mixer. The fibers were then generated by needle injection (spinneret diameter of 600 µm) of these PVA/TiO_2/latex sols into a rotating bath (25 rpm) containing a saturated salt solution of Na_2SO_4 at 45°C. The extrusion speed was set at 40 $mL.h^{-1}$, and the flux was maintained tangential to the rotation axis of the beaker. Upon the completion of the extrusion process, the TiO_2/PVA/latex fibers were meticulously taken out of the beaker by hand and allowed to dry in air. Finally, the fibers were washed once in water to remove the excess of salt.

I.1.3. TiO_2 fibers sintering and labels

The as-synthesized fibers were then sintered at 450°C for 6 hours in order to remove the organic part while promoting crystallization. Overall, seven different inorganic fibers were prepared and labeled hereafter X-Y-TiO_2 where X denotes the diameter of the latex nanoparticles, and Y the latex particles weight percentage in the sol. Thereby, we report in the following the comparison among several fibers, named as: TiO_2, 130-10-TiO_2, 130-30-TiO_2, 130-60-TiO_2, 260-10-TiO_2, 260-30-TiO_2, and 260-60-TiO_2. The results were compared to our first results, where the fibers where extruded through a bigger needle (1mm diameter) without latex in the starting solution. More specifically, it was compared to the 4-TERG-TiO_2 fibers, which will be referenced in this chapter as "TiO_2 ref".[5]

I.2. Characterization of the fibers structure

I.2.1. Structural analyses

The TiO_2/PVA/latex sols can be extruded as composite PVA/TiO_2/latex macroscopic fibers (Figure 1). As for the fibers synthesized in the previous chapter, the absence of coagulation allowed us to directly mix TiO_2 particles with latex particles and PVA through homogeneous dispersion. Here, both the PVA and the latex particles are used as porogen agents. Once these hybrid fibers had been synthesized we applied thermal treatment to promote TiO_2 nanoparticles crystallization and sinter the materials while calcinating the organic counterpart.

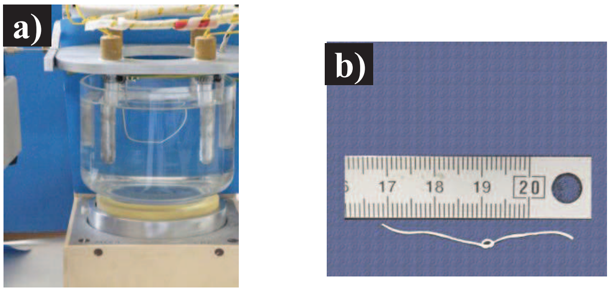

Figure 1. Pictures of TiO_2 fibers generation through extrusion process (a) extrusion process (b) view of a knotted fiber to highlight its mechanical resistance.

We recorded the X-rays diffraction (XRD) patterns (experimental protocol in Annex.3.1.I) in order to see if the introduction of latex particles could disturb the formation of the crystalline phase of TiO_2 (Figure 2). The XRD patterns were similar for all types of fibers. The fibers are mainly composed of Anatase phase with a trace of Brookite, together with sharp peaks being related to Na_2SO_4. As a result, it appears that the presence of latex particles during the calcination step does not have any influence on the final crystalline structures of the fibers, for any size and concentration.

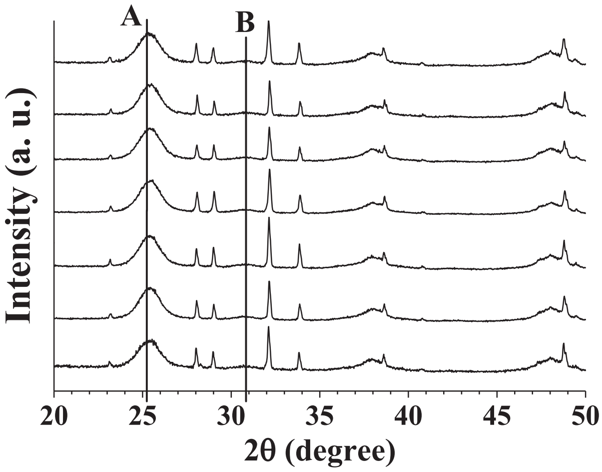

Figure 2. X-rays diffraction patterns of the fibers after calcination (a) TiO_2, (b) 130-10-TiO_2, (c) 130-30-TiO_2, (d) 130-60-TiO_2, (e) 260-10-TiO_2, (f) 260-30-TiO_2, (g) 260-60-TiO_2, and (h) of the salt used for the coagulation of the PVA (Na_2SO_4). A: Anatase, B: Brookite.

I.2.2. Fibers topology

The topology is defined as the texture of the fiber surface at high length scale (several hundred of nanometers). SEM analyses (protocol in Annex 3.1.II) allowed vizualizing the distribution of particles and macropores after this thermal treatment (Figure 3). We observe clearly that the introduction of latex particles within the fibers helps nanostructuring them as the surface of the 130-60-TiO_2 (Figure 3.d.) fiber presents macroporosity which is not observed for the TiO_2 fiber (Figure 3.b.). Moreover, the diameter of the fibers varies from the simple to double. Indeed, when the amount of organic mold increases the final fiber diameters decrease drastically, with values ranging from 100 to 200 µm (Figure 3).

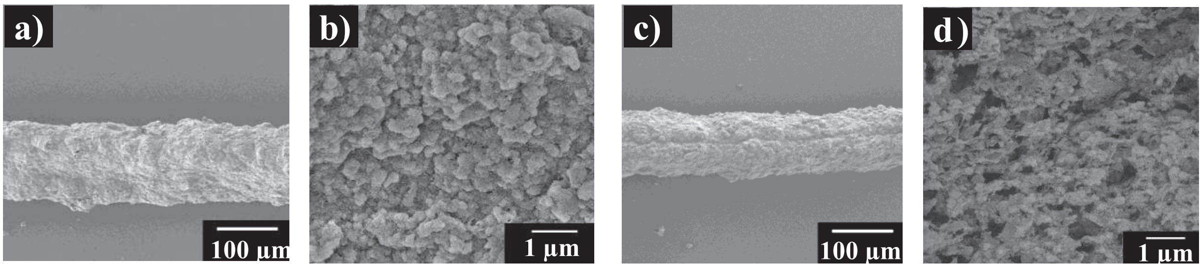

Figure 3. SEM pictures of a TiO_2 fiber (a) and (b), and of a 130-60-TiO_2 fiber (c) and (d).

I.2.3. Fibers porosity and roughness

The porosity was studied by nitrogen physisorption measurements (experimental protocol in Annex.3.1.III) on calcined fibers (Figure 4).

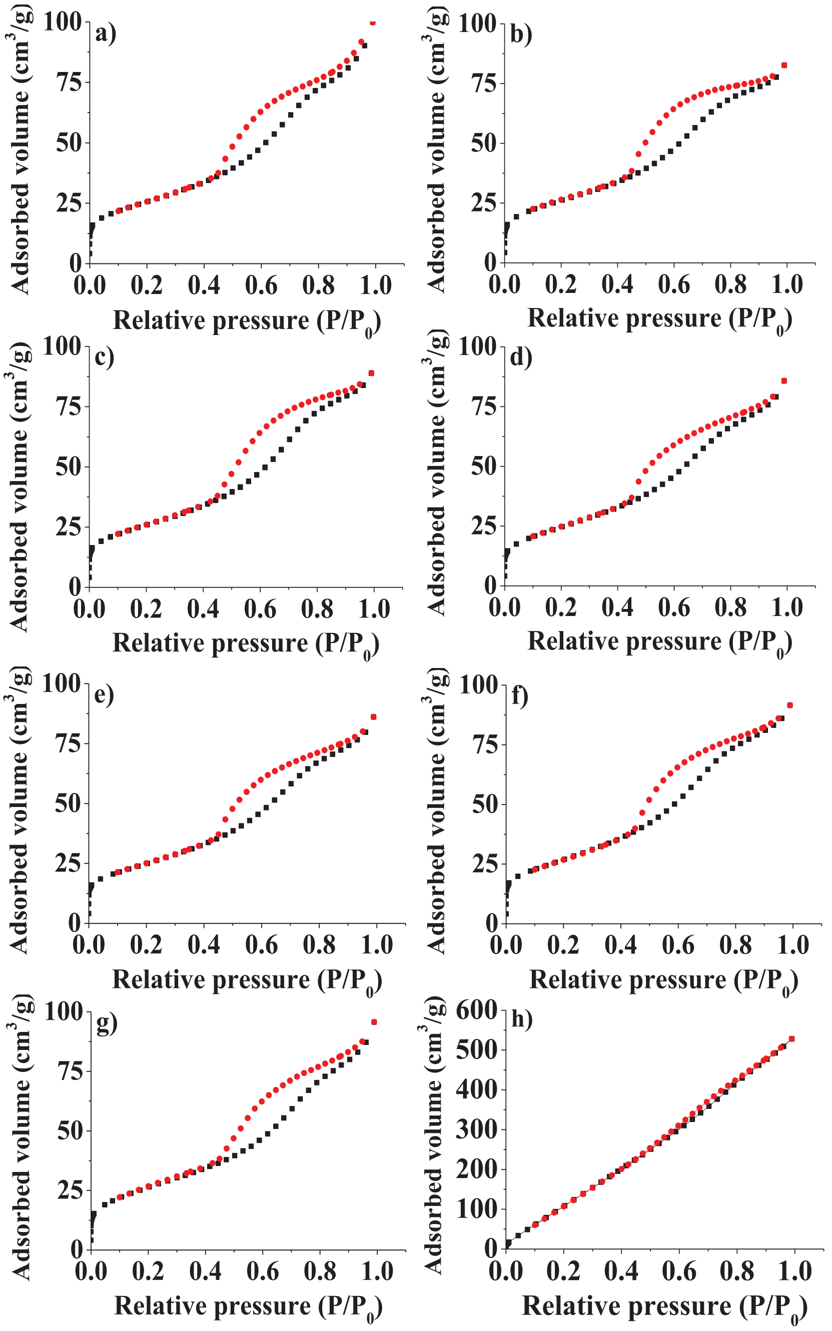

Figure 4. Nitrogen physi-sorption experiments. ■ Adsorption curves, ●desorption curves. (a) TiO_2, (b) 130-10-TiO_2, (c) 130-30-TiO_2, (d) 130-60-TiO_2, (e) 260-10-TiO_2, (f) 260-30-TiO_2, (g) 260-60-TiO_2, and (h) TiO_2 ref fibers which is the fiber of reference from previous work.[5]

All the materials exhibit a rather straight adsorption curve, which can be described as a type IV isotherm, with a pore size distribution within the mesoporous range. The hysteresis observed is larger for the new synthesized fibers compared to the reference fibers (Chap.3),[5] indicating some rather opened bottle-neck porous structure, which can be related to the templated imprints of the latex particles within the fibers. The steep adsorption at $P/P_0 < 0.05$ reveals also some microporosity. The pore-size distribution, calculated with the Barret–Joyner–Halenda (BJH) equation from the desorption curves, indicates that the pore sizes are between 5 and 10 nm rather than 6 nm and 15 nm for the reference (Figure 5).[6]

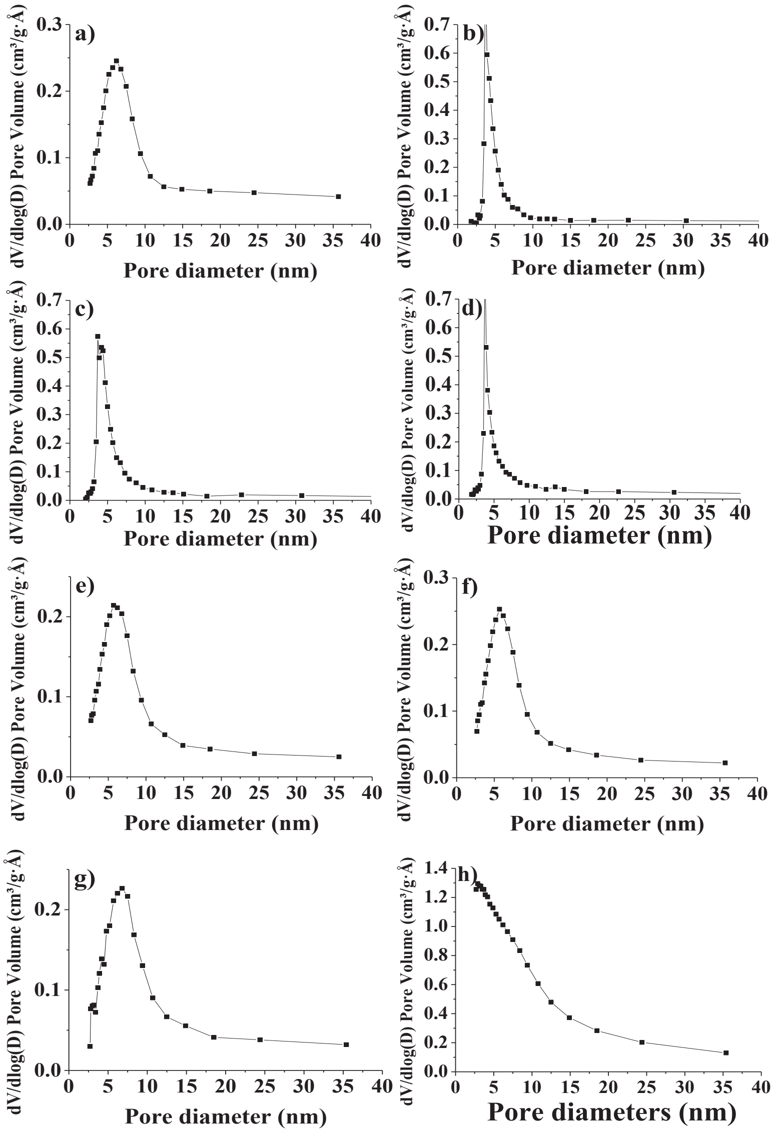

Figure 5. Pore sizes distribution of (a) TiO_2, (b) 130-10-TiO_2, (c) 130-30-TiO_2, (d) 130-60-TiO_2, (e) 260-10-TiO_2, (f) 260-30-TiO_2, (g) 260-60-TiO_2, and (h) TiO_2 ref fibers.

The specific surface areas of the TiO_2 fibers are displayed in Table 1. All surface areas were in agreement with a pronounced mesoporosity. However, as for the pores size, the specific areas of the new fibers decreases compared to the reference fibers from 700 $m^2.g^{-1}$ to about 95 $m^2.g^{-1}$. Decreasing the diameter of the fibers from 450µm (Chap.3)[5] to 150µm for the new fiber batches (containing latex or not) address thus a strong impact over the specific surface area. This phenomenon can be explained by an exalted sintering process due to a smaller temperature gradient within the fibers bearing the smaller diameters. In parallel, we analyzed the surface roughness of these materials, as this feature can be an important factor in photocatalysis for an optimized interaction between the pollutants and the catalyst (figure in Annex 4.1).[5]

The material roughness is defined in the literature as the ratio of the external surface area over the area of the geometrical envelope of the particles.[6] As the topology, it corresponds to the texture of the material surface, but at a smaller length scale. It was evaluated from the determination of the Fractal surface Dimension (Ds), which can be deduced from the nitrogen isotherm adsorption curves (calculation detailed in Annex.3.1.III). The Ds values obtained for the different sets of fibers are summarized in Table 1. For reminder, it must vary between 2 (flat surface) and 3, any value higher than 2 describing an increasing in the surface roughness.[7] *D*s was about 2.5 for the new fibers (with or without latex templates) which is significantly higher than the fibers of the previous study (Ds=2.3).[5] Although the new fibers present a similar roughness value (around 2.5), the topology of the fibers templated by latex particles is different from the TiO_2 fibers one (Figure 3), which is expected to affect their photocatalytic behavior, as the air convection flux is sensitive to the surface topology.

Table 1. Specific surface areas, total pore volume and surface roughness of the calcined TiO_2 fibers obtained through nitrogen physisorption experiments. *TiO_2 ref, refers to the reference 5.

Fibers	BET surface $m^2.g^{-1}$	BJH surface* $m^2.g^{-1}$	Total Pore Volume $mL.g^{-1}$	Ds (surface roughness)
TiO_2	91	110	0.16	2.54
130-10-TiO_2	92	110	0.13	2.53
130-30-TiO_2	92	110	0.14	2.55
130-60-TiO_2	88	107	0.14	2.5
260-10-TiO_2	89	106	0.14	2.54
260-30-TiO_2	96	116	0.15	2.52
260-60-TiO_2	95	112	0.15	2.5
TiO_2 ref	700	652	0.82	2.31

The optical properties (band-gap) of the fibers were also investigated and the results were similar for all the types of the fibers (see Annex 4.2).

I.3. Photocatalytic properties

I.3.1. Experimental set up and models

Photocatalytic mineralization of gaseous acetone was carried out in a specially designed batch reactor described in Chap.3 (part III.3.1, Scheme 1). In a first step, the photocatalytic device and the reaction conditions were settled with commercial TiO_2 fibers (Quartzel PCO, Saint-Gobain Quartz) in the same configuration (canister and reactor). These commercial photocatalytic media is made of quartz fibers coated with TiO_2 (exact composition unknown, fibers diameter 9µm, specific surface 120 $m^2.g^{-1}$). The performances of our TiO_2 fibers were compared to those of this commercial material under identical conditions (flow rate, RH and temperature). A first test carried out in the dark allowed us to determine that over this time, the leaks can be modeled by a linear curve. The slopes of the acetone and CO_2 leaks being evaluated at -0.024 $ppmV.min^{-1}$ and 0.115 $ppmV.min^{-1}$, respectively. As in Chap.3, the equations leading to the calculation of the % of acetone degradation and the % of mineralization were modified in order to take into account the leaks intrinsic to the system (Annex 3.1.V). According to these results, the reactions kinetics (k) were investigated by plotting the curve corresponding to both an order 0 and an order 1 reaction models. The calculations of the acetone degradation kinetics, taking into account the leaks, are presented in Annex 4.3.

The photocatalytic behavior of the fibers was tested by introducing 24.8 mg of Quartzel®, and 19.3 to 50.4 mg of laboratory-made fibers, in the canister reactor. The mass used for all types of fibers is given in Table 2.

Table 2. Mass of calcined TiO_2 fibers inserted in the reactor for the photocatalytic experiments.

Fibers	TiO_2	130-10-TiO_2	130-30-TiO_2	130-60-TiO_2	260-10-TiO_2	260-30-TiO_2	260-60-TiO_2	TiO_2 ref	Quartzel
Mass (mg)	43.1	23.9	20.2	22.3	44.8	34.7	19.3	50.4	24.8

I.3.2. Fibers photocatalytic properties

We compared the curves plotted using the equations of order 0 and order 1 reactions for the sample labeled "TiO_2", adjusted for taking into account the leaks of the apparatus (see equations in Annex 4.3). These curves are displayed in Figure 6, and the linear shape of the curve in Figure 6.b. indicates clearly that the reaction follows an order 1 reaction kinetics.

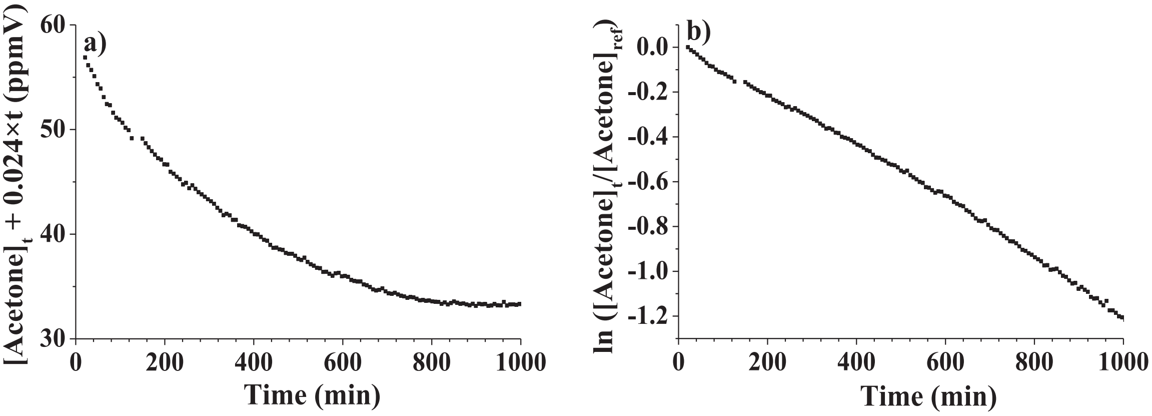

Figure 6. Comparison between the curves representing the TiO_2 fibers data plotted according to the equation, of a) an order 0 reaction and b) an order 1 reaction.

The curves representing the order 1 model for all types of fibers are displayed in Annex 4.4 and the values are summed up in Figure 7.b. Typical curves of acetone concentration against time are compared Figure 7.a. The first-order kinetic constants, k, calculated from the acetone degradation rate per gram of media, are given Figure 7.b. (fitting of the curves in Annex 4.4). A very positive result is the much higher efficiency of these new fibers relative to our previous fibers (TiO_2 ref) bearing a lower roughness with a larger diameter.[5]

These results show that the specific surface area is not the crucial parameter under these conditions as the reference fibers present a much higher specific surface area ($TiO_{2ref,}$ 700 $m^2.g^{-1}$)[5] compared to that of the latex-based ones (88-95 $m^2.g^{-1}$). This results is consistent with our previous work where we could observe that even though the specific surface area of the 4-TERG-TiO_2 (700 $m^2.g^{-1}$) was much higher than the one of 4-TTAB-TiO_2 (430 $m^2.g^{-1}$), the reaction kinetics were similar (Chap.3).[5] This phenomenon is certainly due to the experimental conditions as the photocatalytic tests are performed under uni-axial flux with a velocity of 0.7 $m.s^{-1}$ where, in such hydrodynamic condition the internal mesoscopic voids are certainly not completely involved in the photocatalysis reaction.

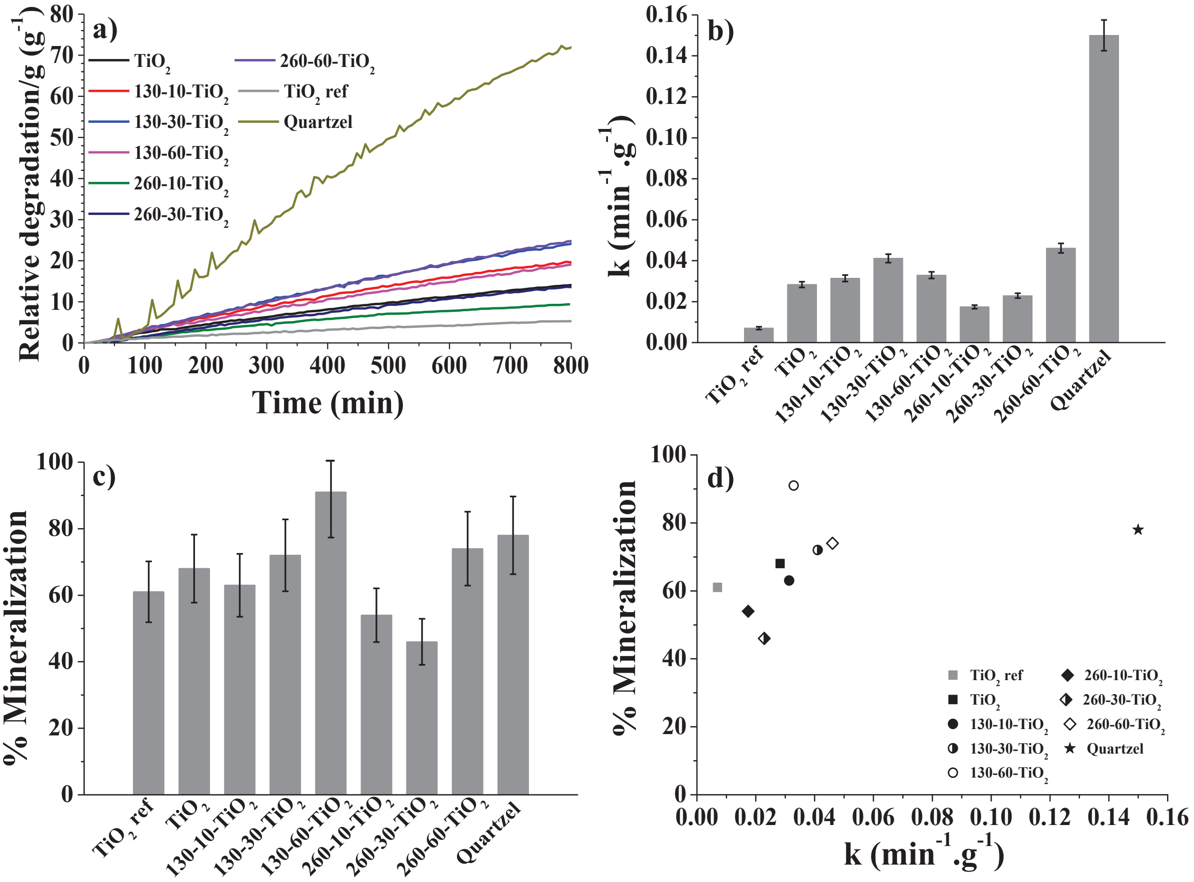

Figure 7. Results for the photocatalytic properties of the fibers: a) % acetone degradation/g of media against time; b) calculated first-order rate constants of acetone degradation; c) % mineralization between 200-400 minutes d) comparison between acetone degradation kinetics relative to % mineralization for the nine types of fibers under irradiation of gaseous acetone at 366 nm (RH 15 %, initial acetone concentration 50 ppmV, air flow rate 3.3 $L.min^{-1}$).

In the previous study we demonstrate that the roughness was a key parameter as we observed that the higher the roughness, the higher the reaction kinetics.[5] If we just look at the fibers which are not templated by the latex particles (TiO_2 ref and TiO_2 fibers), we can see that the higher reaction kinetics of the new fibers compared to the previous one confirms the influence of the roughness on the acetone degradation, since the roughness of the new fibers without latex particles templates (Ds=2.5) is much higher than the previous one (Ds=2.3). Also we do not have to forget that the UV penetration depth can be at maximum about few micrometers while the fiber diameters are about several hundred micrometers, thus only a thin shell of the fiber is UV activated. In consequence, the higher reaction kinetics of the new fibers, given per gram of media, also results from the diminution of the fibers diameter. We can conclude that the overall increase of the reaction kinetics between TiO_2 ref (0.007 $min^{-1}.g^{-1}$) and TiO_2 fibers (0.028 $min^{-1}.g^{-}1$) results from the combination of an increase of the surface roughness and a decrease of the fibers diameter.

By comparing the TiO_2 fibers with and without latex prepared under these new conditions, it may be concluded that latex beads, used as sacrificial templates, induced an improvement of the efficiency for the fibers templated by 130 nm latex particles, but not for the one templated by 260 nm ones, except the 260-60-TiO_2 sample. Regarding the 260 nm latex-based TiO_2 fibers, we observed that the increase in latex content increased the photocatalytic efficiency of the fibers (Figure 7.b.). It also appeared that, for a given latex content, the fibers templated by 130 nm latex particles performed better than the 260 nm fibers (except for the 130-60-TiO_2 sample). Generally, this difference in reaction kinetics can be attributed to a difference in the fibers surface topology, which leads to a better light penetration within the structure and to a turbulent-induced air flux behavior at their surface, which favors acetone degradation reaction. This result is important as it shows that the surface topology is also a parameter to take into account when it comes to photocatalytic performances.

Taking into account the higher diameter of the TiO_{2ref} fibers (350nm),[5] it was thus confirmed that for the thickest fibers, light penetration was not optimized and that smaller diameter fibers were more efficient. Moreover, the surface roughness is confirmed to influence the acetone degradation reaction kinetics. Finally, the topology appears to be also an important parameter for the optimization of the acetone degradation kinetics.

The mineralization percentage was calculated between 200-400 minutes of irradiation (Figure 7.c.) and was found to be stable in this range taking into account CO_2 leaks from outside the reactor, which induces a consequent error on the calculated values. The mineralization percentage varies from 46 (260-30-TiO_2) to 91 % (130-60-TiO_2), but most of the fibers present a similar mineralization percentage around 70%.

The 260-10-TiO_2 and 260-30-TiO_2 fibers present lower mineralization values than the majority of the fibers, in agreement with the acetone degradation kinetics results. From this result, we can deduce that insertion of voids created by large latex particles in small proportion does not allow creating a surface topology (roughness) high enough for optimizing the mineralization reaction (short residence time of acetone on the fibers surface). However, by increasing their concentration (260-60-TiO_2) it is possible to optimize the surface roughness for a better residence time (more turbulent hydrodynamic flux character) and thus a better mineralization rate.

The 130-60-TiO_2 fibers present a higher mineralization rate than the majority of the fibers. From this result, we can conclude that the surface topology created by small latex particles at high concentration (succession of small pores inside the structure) permit also increasing the time of residence of the acetone onto the TiO_2 fibers surface and thereby mineralization process.

I.4. Intermediary conclusion

In this study we have employed the extrusion process to promote the morphosynthesis of hybrid titania-based macroscopic fibers. Within the starting sols we have varied both the diameters of the latex nanoparticles in use as well as their concentration. Upon a thermal treatment in air we obtained the Anatase phase with residual Brookite, while the latex calcination allowed promoting tunable voids. In comparison with previous published works,and in line with our previous conclusions (Chap.3), we have demonstrated that the fibers roughness, diameter size, and topology are indeed important parameters involved both in acetone degradation and mineralization processes, for uni-axial air flux heterogeneous catalysis. The catalysts roughness and topology are thus features that should be added into the list of the key parameters (particles sizes, crystalline character, surface area) involved within the air-photocatalysis efficiency. The increase of the fibers roughness along with the decrease of their diameter, allowed multiplying the fibers efficiency toward acetone degradation by 4 compared to our previous results.[5] Moreover, by changing the surface topology of the final fibers by the insertion of macroscopic voids the acetone degradation kinetics was multiplied by 1.64, which represents a total multiplication of the reaction kinetics by 6.5 compared to our previous study. Despite this increase of efficiency the rough fibers generated in this study are still less active than the commercial Quartzel Titania-based photocatalyst, being 3 times less efficient relative to acetone degradation rate while offering the approximate same mineralization capabilities for the best fibers. The first penalty of the fibers synthesized in this work is still their diameter, which does not allow optimizing the quantity of matter in interaction with the UV light penetration depth, as most of the fiber still remains inactive. As all the catalytic efficiencies toward both acetone degradation and associated mineralization are normalized per gram of media, this issue is of crucial importance. The second main issue is of technology, when regarding the extrusion process in use. This configuration, well calibrated for lab experiments, does not allow for higher scale industrial production. Hence, our next goal was to cancel the two above mentioned penalties at once by minimizing the fiber diameter as low as possible while offering a technological process able to address high scale industrial production.

II. Towards a continuous spinning process

In our laboratory, a technological process offering a semi-industrial scalable production has been developed for the spinning of carbon nanotubes (CNTs)/PVA macroscopic fibers. The fibers obtained with this process had a diameter comprised between 15 and 60µm depending on the spinning conditions.[3] These diameters are much smaller than the ones obtained with the process used in the previous study, which gave 150µm diameter fibers (see part I). Due to their high anisotropy and their mechanical strength, the CNTs within the CNTs/PVA fiber reinforce its mechanical strength during the process which allows stretching the fiber during the process by a factor 5.6. We report in the following how this process was adapted, for the first time, to the spinning of PVA/TiO_2 fibers. It was primarily done by adjusting the solution formulation and the experimental conditions. Unlike CNTs and V_2O_5 ribbons, TiO_2 nanoparticles behave more as a defect than a reinforcement of the fiber. Hence, the spinning conditions had to be adapted to avoid the fiber breakage. Moreover, with the latex particles acting also as a defect, a further adaptation was needed when inserting them in the starting solution. Finally, as the spinneret diameter is about 300µm with this process (twice lower than in part I), the rheology of the solution was adapted to allow a continuous flow of the fiber while maintaining its cohesion.

II.1. Studied system and experimental protocol

II.1.1. Solution preparation

The adjustment of the solution formulation is crucial for the semi-industrial spinning process. As the spinneret diameter was significantly lower than in part I (twice smaller), the viscosity of the solution used previously, containing 10wt% PVA and 4wt% TiO_2, was found to be far too high to allow the continuous extrusion of a fiber with this process. Since the viscosity of the solution is mainly due to the PVA, it was necessary to lower its concentration within the starting solution. However, as the reticulated PVA chains ensure the fiber cohesion, and as the TiO_2 particles act as a defect within the fiber, the PVA concentration as to be high enough to avoid any breakage.

To respect both criteria, we decided to use a starting solution composed of 4wt% TiO_2 and 6wt% of PVA. The previous study (see part I) showed that the fibers containing 260nm diameter latex particles in the proportion of 60wt% compared to TiO_2 present the best photocatalytic performances. As a result, we chose to investigate both the behavior of a starting solution without any latex particles, and of a starting solution containing 260nm diameter latex particles in the proportion of 60wt% compared to TiO_2. In the following, these fibers will be referred to as TiO_2-indus and TiO_2-latex-indus, respectively. The TiO_2 particles were synthesized according to the procedure described in part I.1.1., and we used PVA with a high molecular weight to maximize the mechanical strength of the fiber (Mw=195kg.mol^{-1} hydrolyzed at 99%).

TiO_2-indus starting solution. This solution was prepared by mixing 10g of an 8wt% TiO_2 nanoparticles aqueous dispersion with 10g of a 12wt% PVA aqueous solution at a temperature of 80°C.

TiO_2-latex-indus starting solution. First, 7.56g of a 10.6wt% TiO_2 nanoparticles aqueous dispersion was heated up at 90°C, and 0.42g of solid PVA was added under stirring and let to dissolve for one hour. Then, 6.5g of a 12wt% PVA aqueous solution was poured into the solution along with 0.030g of distilled water. Once the solution became homogeneous, it was cooled down at 50°C where 5.22g of a 9.2wt% latex aqueous dispersion (260nm diameter) was added. The homogeneity of the final solution was obtained through agitation using a vortex mixer.

II.1.2. Experimental set up

The fibers spinning was performed using the apparatus describe in Figure 8. It is composed of a syringe pump, a coagulation bath, a washing bath, a drying part, and a rotating winder. The role of each element is developed in the paragraphs below.

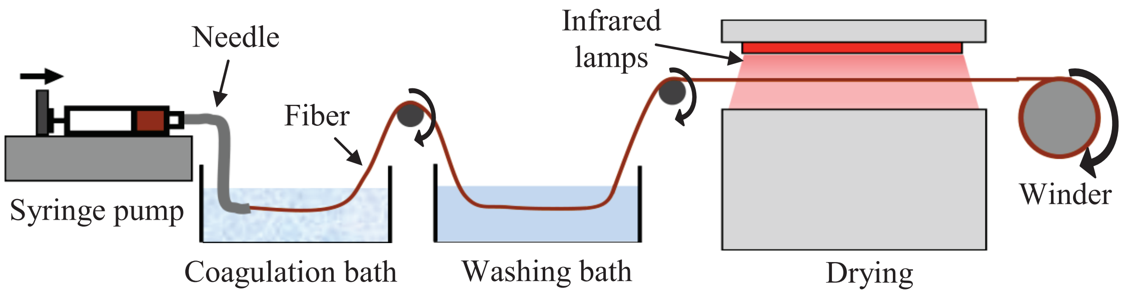

Figure 8. Schematic representation of the spinning process.

II.1.2.1. The syringe pump

The syringe pump (Figure 9) was used to inject the solution in the coagulation bath at a constant rate set at 6mL/h. As the spinneret diameter was about 300µm, the calculated linear injection speed was about 1.4m/min.

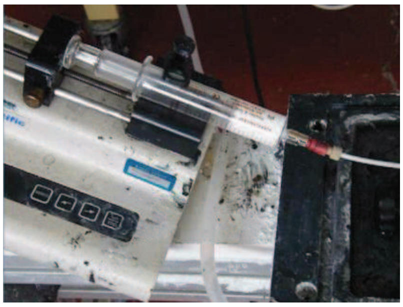

Figure 9. Picture of the syringe pump used for the injection of the starting solution in the coagulation bath.

II.1.2.2. Coagulation bath

The coagulation bath (Figure 10) was a saturated solution in sodium sulfate (Na_2SO_4 at 320g.L^{-1}) maintained at 40°C, which is the temperature where Na_2SO_4 reaches its maximum of solubility in water. When the solution was extruded from the syringe needle, it coagulated instantly to form a solid filament. The minimum residence time of the fibers within the coagulation bath was fixed at 30 seconds (s) to reinforce the mechanical stability before extraction.

Figure 10. Pictures of the coagulation bath (saturated salt solution of Na_2SO_4 at 320g.L^{-1}), (left) the injection of the solution into the bath, (right) the exit of the solid fiber out of the bath.

II.1.2.3. Washing bath

The washing bath aimed at removing all the salt residues present in the fibers after the coagulation process (Figure 11). As the PVA is soluble in water, the washing bath could not be composed only by water, otherwise, the humid fiber would stretch too much and end up by breaking. Empirically, it was demonstrated that the addition of sodium tetraborate inside the washing bath allows overcoming this problem as it allows the reticulation of the PVA chains (see Chap.1).[8] In our study, the concentration in sodium tetraborate was set at 0.1 mol.L^{-1} and the minimum residence time was 1 minute.

Figure 11. Picture of the fiber passing through the washing bath (aqueous solution containing sodium tetraborate at 0.1 mol.L^{-1}.

II.1.2.4. Fibers drying

The fiber was dried with the helps of two infrared lamps, at a temperature set at 75°C. The fiber was first carried under these lamps with a roller conveyor belt coated with Teflon (Figure 12). Once the fiber reached the end of the drying stage, it was tensed and suspended above the conveyor belt in order to avoid a flattening of the fiber at its exit from the washing bath.

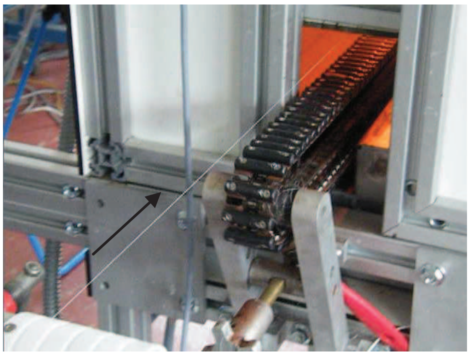

Figure 12. Picture of the fiber entering in the drying apparatus.

II.1.2.5. Fibers winding

The fiber obtained was collected on a winder rotating at a minimum speed of 3.2m.min^{-1} (Figure 13). As the injection speed is about 1.4m.min^{-1}, the minimal stretching factor of the fiber during the all process is 2.3. With this process, it was possible to collect several hundred meter TiO_2 fibers continuously. As demonstrated with the CNTs/PVA fibers, the fibers still contain salt at the end of this process and a second washing of these fibers was necessary to totally remove it.[8]

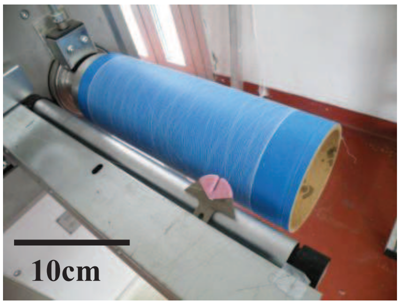

Figure 13. Picture of the fiber winding

II.1.2.6. The second washing bath

The second washing step proceeded through an unwinding of the fiber, passing through a water bath, followed by a second drying step and a new winding. It has been demonstrated for the CNTs/PVA fibers that this second washing steps allowed to remove all the salt contained in the fiber.[8] During this step, the TiO_2/PVA fiber was not stretched because it was too fragile and it would have broken.

II.1.2.7. Sintering process

Finally, the as-synthesized fibers were sintered at 450°C for 6 hours in order to remove the organic part while promoting crystallization. Overall, two different types of inorganic fibers were prepared by this process: TiO_2-indus fibers generated from a solution without latex particles, and TiO_2-latex-indus fibers, generated from a solution containing 260nm diameter latex particles (60wt% relative to TiO_2). At the end of the process, the fibers diameter was ranging between 40 and 47µm, which is about 3 times smaller than the fibers presented in part I (Figure 3).The results were compared to our first results, especially to the 4-TERG-TiO_2 fibers referenced in this part as “TiO_2 ref”, and to the TiO_2 fibers and 260-60-TiO_2 fibers presented in part I.

II.2. Characterization of the fibers structure

II.2.1. Structural analyses

We studied X-rays patterns (experimental protocol in Annex 3.1.I) in order to see if the new fibers processing and the additional decrease of the fibers diameters influenced the crystalline phase of TiO_2 (Figure 14). The X-rays patterns of the fibers generating with the semi-industrial process, templated or not by latex particles, are similar. The new fibers are mainly composed of Anatase phase (85-90%), with some Brookite (10-15%). The amount of Brookite is significantly higher than the fibers studied in part I, which all presented the same X-rays pattern (Figure 14.c.). Besides, XRD patterns confirm that all the salt has been removed from the fibers after the two washing steps. From these results, we conclude that both the fiber diameter and the presence of salt residues inside the fibers could have an influence on the crystalline phase obtained after calcination. As our goal is to obtain the pure Anatase phase alone, further studies should explore how changes in the sintering parameters (temperature and time) could help to reduce the amount of Brookite.

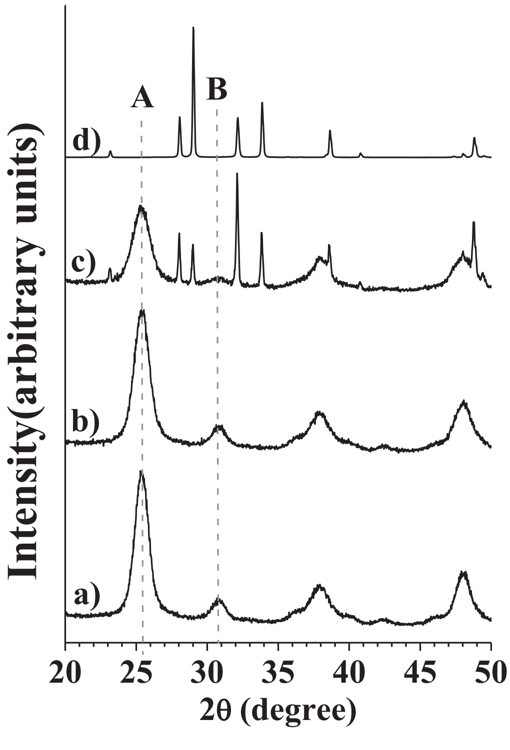

Figure 14. X-rays diffraction patterns of the fibers after calcination at 450°C for 6h (a) TiO_2-indus, (b) TiO_2-latex-indus, (c) TiO_2, and (d) of the salt used for the coagulation of the PVA (Na_2SO_4). A: Anatase, B: Brookite.

II.2.2. Fibers topology

SEM analyses (experimental protocol in Annex 3.1.II) allowed us visualizing the fibers topology resulting from this new process (Figure 15). Overall the fibers present a flattened shape with a width ranging from 40 to 47 µm and a thickness ranging from 10 to 17µm. Their topology is clearly different from those observed so far (Chap.3 and Chap 4, part I). Indeed, for both types of fibers, the topology looks like a "tree trunk" at the macroscopic scale meaning that the fibers present large and deep striation at the surface oriented along the fibers main axis. As the fiber is stretched and the PVA chains are aligned during the process, we assumed that these ridges result from the alignment PVA chains before calcination. An analysis of the fibers cross section (Figure 15.c. and e.), reveals that the TiO_2-latex-indus fibers present enhanced bulk porosity compared to TiO_2-indus fibers, which results in an increase of their width and thickness. As the photocatalysis reaction takes place in priority at the surface, this should not impact the photocatalytic performances.

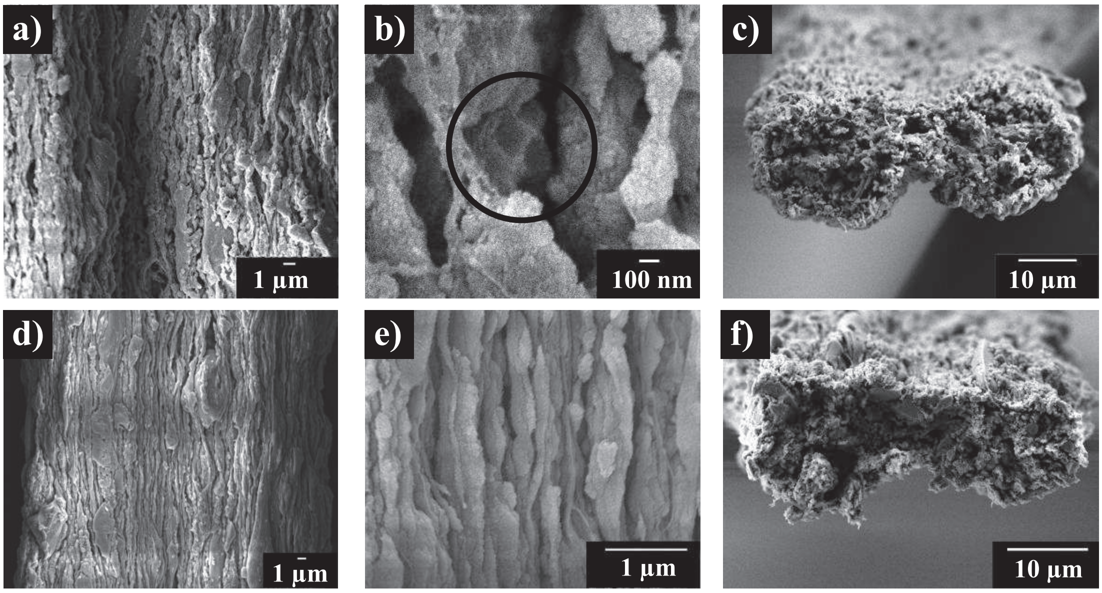

Figure 15. SEM images of (a-c) a TiO_2-latex-indus fiber, and (d-f) a TiO_2-indus fiber.

We observed that the surface topology is almost not affected by the insertion of latex particles in the starting solution (voids template), as the overall topology of the TiO_2-latex-indus fibers is similar to the one of TiO_2-indus fibers. Indeed, the presence of small latex particles before calcination only results in the creation of small imprints inside the macroscopic striation (Figure 15.b.), and not in the creation of new macroscopic voids as it was the case for the fibers studied in part I. From this result, we deduce that the surface macroporosity created by the PVA chains overcome the one created by the latex particles. Moreover, we observe that the striation at the TiO_2-latex-indus fibers surface is more distorted than the TiO_2-indus fibers one, which means that the latex particles act as a defect and prevent a perfect alignment of the PVA chains. As we performed photocatalytic tests using an uni-axial air flux along the fibers main axis, this could have an impact on their photocatalytic performances.

II.2.3. Fibers porosity and roughness

Specific surface areas and pore characteristics at the mesoscale were measured using nitrogen adsorption method (Figure 16, experimental protocol in Annex 3.1.III). All the materials exhibit an adsorption curve representative of a type IV isotherm, and a pore size distribution within the mesoporous range. The hysteresis observed is significant for the new synthesized fibers as it was for the fibers in part I. The presence of steep adsorption at $P/P_0 < 0.05$ showed that the fibers were also microporous.

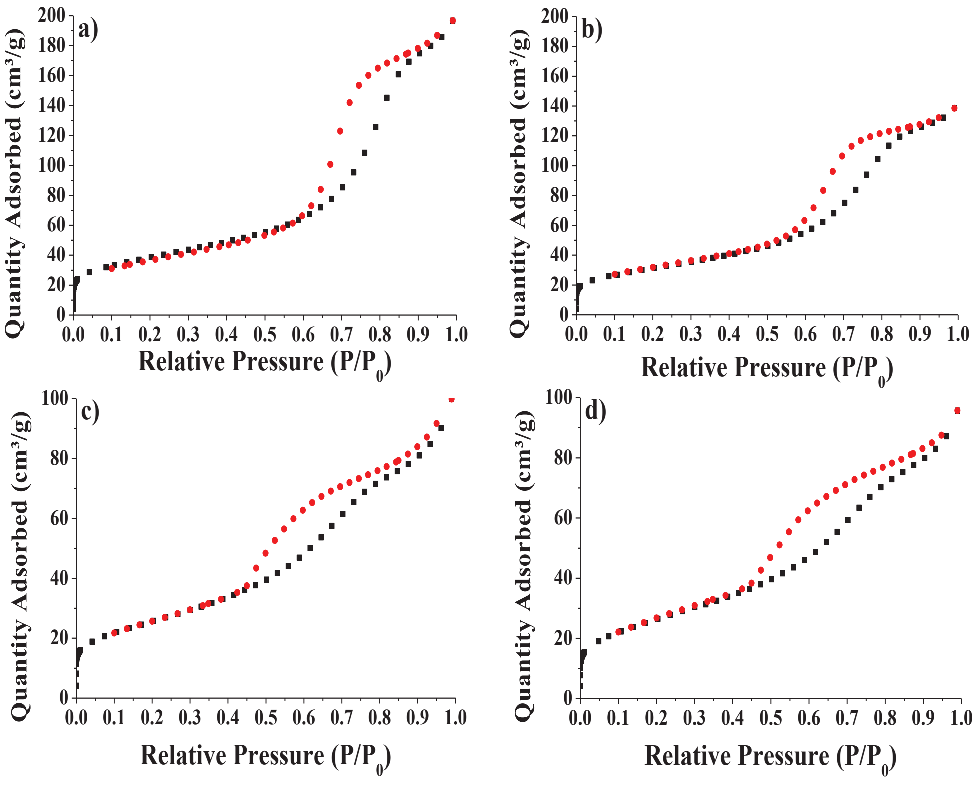

Figure 16. Nitrogen physi-sorption experiments. ■ Adsorption curves, ●desorption curves. (a) TiO_2-indus, (b) TiO_2-latex-indus, (c) TiO_2, and (d) 260-60- TiO_2 fibers.

The BET specific surface areas of the TiO_2 fibers are displayed in Table 3. All surface areas were in agreement with a pronounced mesoporosity. The specific areas of the new fibers increases compared to the fibers presented in part.I from about 95 $m^2.g^{-1}$ to about 120 $m^2.g^{-1}$. This phenomenon is explained by the absence of salt within the fiber. Indeed, for a given porous structure, as salt crystals are not porous, their presence at the surface artificially decreases the value of the BET specific surface area calculated per gram of media. Moreover, the new macroporosity induced by the PVA chains can also be responsible of a higher specific surface area as it opens some internal porosity that allows the nitrogen to penetrate deeper in the bulk.

Table 3. Specific surface areas, total pore volume and surface roughness of the as-synthesized TiO_2 fibers obtained through nitrogen physisorption experiments.

Fibers	BET surface $m^2.g^{-1}$	BJH surface* $m^2.g^{-1}$	Total Pore Volume $mL.g^{-1}$	Ds (surface roughness)
TiO_2-indus	136	166	0.31	2.56
TiO_2-latex-indus	110	132	0.22	2.55
TiO_2 fibers	91	110	0.16	2.54
260-60-TiO_2 fibers	95	112	0.15	2.5
TiO_2 ref	700	652	0.82	2.31

The pore-size distribution, calculated with the Barret–Joyner–Halenda (BJH) equation from the desorption curves, indicates that the pore size distribution is ranging between 6 and18 nm rather than 5 and 10 nm for the fibers presented in part.I (Figure 17).[6] The new process leads to an increase in pore size along with an increase of the total pore volume.

In parallel, we analyzed the surface roughness of these materials, as this feature can be an important factor in photocatalysis for an optimized interaction between the pollutants and the catalyst (figure in Annex 4.5). Material roughness was evaluated from the determination of the Fractal surface Dimension (Ds), which can be deduced from the nitrogen isotherm adsorption curves (experimental protocol in Annex 3.1.III). The values obtained for the different sets of fibers are summarized in Table 3. *D*s is about 2.55 for the new latex fibers which is within the same range than the fibers studied in part.I (Ds=2.5). This result shows that the new process allows generating fibers with a high surface roughness. Although the surface fractal dimensions are similar, as for the fibers studied in part.I, the difference of topology of these fibers can cause a difference in their photocatalytic performances.

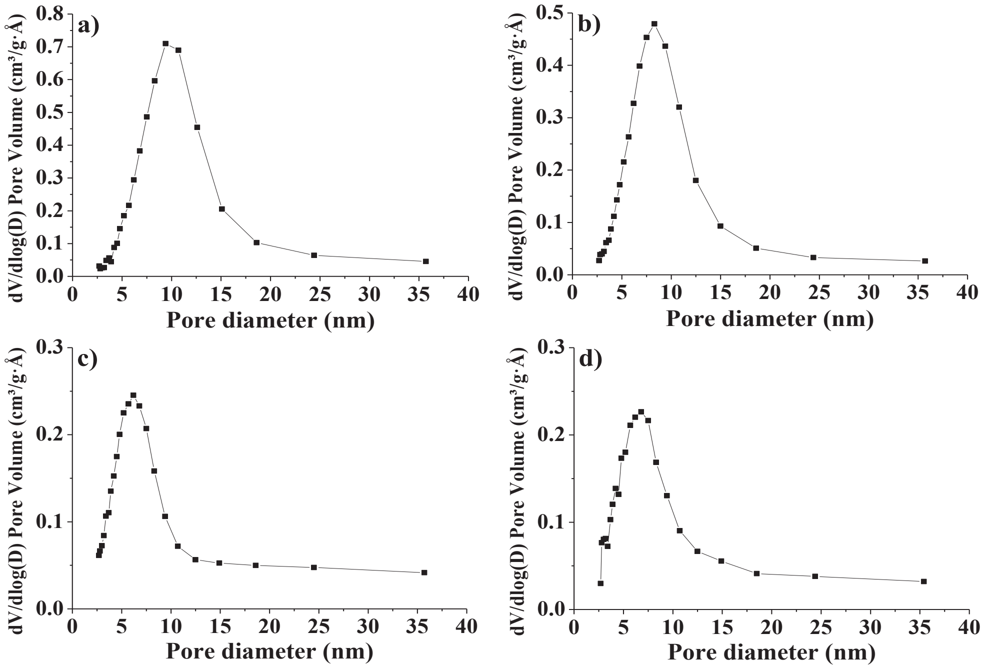

Figure 17. Pore sizes distribution of (a) TiO_2-indus, (b) TiO_2-latex-indus, (c) TiO_2, and (d) 260-60- TiO_2 fibers.

The optical properties (band-gap) of the fibers were also investigated and, as in part I.3., the results were similar for all the types of the fibers and will not be developed here. The results can be found in Annex 4.6.

II.2.4. Photocatalytic properties

Typical curves of acetone concentration against time are compared Figure 18.a. The first-order kinetic constants normalized by the fibers mass, k, are given Figure 18.b. (fitting of the curves in Annex 4.7). A very positive result is that the efficiency of these new fibers was multiplied in average by a factor 3 relative to the fibers synthesized in part.I. More importantly, the fibers generated present reaction kinetic values that are in the same order of magnitude than the Quartzel PCO from the company Saint-Gobain (commercial product), which makes them competitive in a commercial point of view.

As demonstrated in part.I, the specific surface area of the fibers does not influence their photocatalytic performances under the experimental conditions applied in our study. In consequence, the higher efficiency cannot be attributed to the higher specific surface area of the new fibers (about 120 $m^2.g^{-1}$) compared to the fibers presented in part.I (88-95 $m^2.g^{-1}$).

Also, both previous studies (Chap.3 and part.I) underlined that the parameters that influence the fibers photocatalytic properties are their roughness, their diameter size, and their surface topology. However, in this study, the roughness of the two types of new fibers is similar (Ds=2.55), and close to those of the fibers presented in part I (Ds=2.5-2.55). In consequence, this parameter is not responsible for the increase in the fibers photocatalytic performance when using this new continuous spinning process.

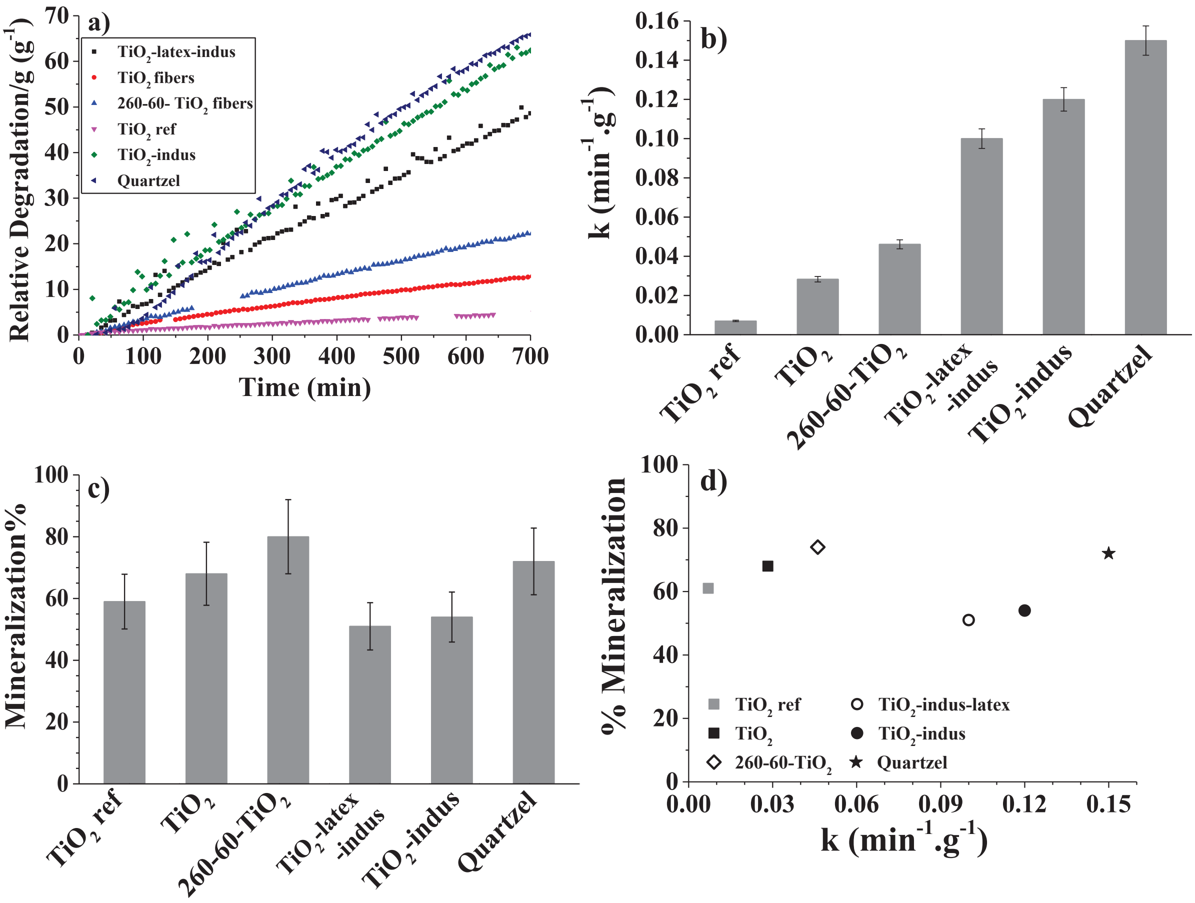

Figure 18. Results for the photocatalytic properties of the fibers: a) % acetone degradation/g of media against time; b) pseudo-first-order rate constants of acetone degradation calculated from the degradation rate by gram of media; c) % mineralization between 200-400 minutes d) comparison between acetone degradation %/g media relative to % mineralization for the four types of fibers, the reference fibers, and Quartzel® fibers under irradiation of gaseous acetone at 366 nm (RH 15 %, temperature 22 ± 2 °C, initial acetone concentration 50 ppmV, air flow rate 3.3 L minute^{-1}).

As the diameter of the new fibers has been divided by at least three compared to the fibers studied in part I, we can assign the dramatic increase in the photocatalytic performance to this parameter. Moreover, as described in part II.2.1, the topology of the new fibers ("tree trunk") is drastically different from the ones observed so far. We can then conclude that the overall increase in the reaction kinetics between the fibers presented in part I. (0.037 $min^{-1}.g^{-1}$ in average) and the fibers produced by this new semi-industrial continuous process (0.1 $min^{-1}.g^{-}1$ in average) results from the combination of a decrease of the fibers diameter and a modification of their surface topology.

By comparing the TiO_2-indus fibers with the TiO_2-latex-indus fibers, it is concluded that latex beads, used as sacrificial templates, do not provide any improvement of the photocatalytic performances (Figure 18.b). On the contrary, TiO_2-latex-indus fibers seem to be slightly less efficient than TiO_2-indus ones. As their diameter sizes are in the same order of magnitude, this difference in reaction kinetics can be attributed to a difference in the fibers surface topology. Indeed, as described in part II, latex particles prevent PVA chains alignment, which caused the distortion of the fiber striation. In this case, we think that the air-flux is disturbed and does not penetrate as efficiently in the fiber as in the case of the TiO_2-indus fibers, that presents a well-aligned striation along the fiber main axis (Figure 15.).

The insertion of latex particles in the starting solution as voids template is then useless for the fibers generated with this semi-industrial process. Improvement of the photocatalytic efficiency of fibers generated with this semi-industrial process is then the result of two key parameters: fibers diameter and surface topology.

As in part I, the mineralization percentage was calculated between 200-400 minutes of irradiation (Figure 18.c.) and was found to be stable in this range taking into account a significant error on the calculated values due to CO_2 leaks from outside the reactor. The mineralization percentage is varying from 51 (TiO_2-latex-indus) to 80 % (260-60-TiO_2), where two groups can be identified.

The group presenting the lowest mineralization rate is composed of the TiO_2 ref fibers, and the fibers generated by the semi industrial process with a mineralization rate around 55%. The group presenting the higher mineralization rate, around 72%, is composed of the fibers generated through the process presented in part I and of the Quartzel PCO fibers. From this result, we can deduce that despite the high acetone degradation rate, the topology of the new fibers is not fully yet optimized for acetone mineralization. The residence time (linked to the mineralization rate) is then lower for the fiber topology with striation than for the fiber topology without striation, the residence time being even higher when the surface is cluttered of a succession of pores. We hypothesized that the turbulent hydrodynamic flux character created by the pores was responsible for the increase of the residence time.

II.3. Intermediary conclusion

In this study we used a new semi industrial spinning process for the generation of macroscopic TiO_2 fibers. Upon a thermal treatment in air we obtained the Anatase phase of TiO_2 (85-90%) with some Brookite (10-15%). This new process allowed us to significantly decrease the fibers diameter, and to modify drastically their topology, which are both important parameters involved both toward acetone degradation and mineralization processes, for uni-axial air flux heterogeneous catalysis. We demonstrated that the diminution of the fiber diameter combined with this new topology made of striation, rather than a succession of pores, present enhanced properties for the acetone degradation but are not optimized for the mineralization rate. Indeed, we assumed that the striation allows a better penetration of the air flux within the fibers but that the residence time is lowered due to a diminution of the turbulent hydrodynamic flux character. Here, the insertion of latex particles as template in the starting solution is useless as they do not create supplementary macroscopic voids within the structure (the striation induced already a macroscopic porosity about several hundred of nanometers). Moreover, it seems even to be a penalty as it prevents the correct alignment of the PVA chains during the spinning process, which causes a distortion of the striation, resulting in a lower air flux penetration within the fiber structure. Overall, the new fibers are in average 3 times more efficient than the fibers presented in part.I, but present a smaller mineralization rate (15% lower than the fibers in part I.).

Thanks to this increase in efficiency, the fibers generated *via* this semi industrial process present acetone degradation kinetics which are in the same order of magnitude than the one of the commercial Quartzel Titania-based photocatalyst, with a mineralization rate is about 10-15% lower. These fibers are a good Proof of Concept to demonstrate further their competitiveness from a commercial point of view. However, some improvements need to be achieved. Among them, the mineralization rate and the mechanical strength after calcination remain strong penalties for their use for commercial application. One pathway to solve both penalties at once would be to weave the fibers as a piece of textile. Indeed, it would enhance the mechanical properties, and the fibers perpendicular to the air flux will enhance the turbulent hydrodynamic flux character leading to an increase of the mineralization rate.

Conclusion

In this chapter, we demonstrated that the fiber diameter is a crucial parameter for the improvement of photocatalytic efficiency, as it governs the gas over solid surface interaction. Also, besides the particles size, crystalline character, and specific surface area, the catalysts roughness and topology are features of importance for the air-photocatalysis efficiency. More specifically, topologies conferring a high penetration of the air flux within the fibers structure, like striation, are optimized for the acetone degradation but not necessarily for its mineralization rate. Optimizing the fibers diameter along with their topology using a semi-industrial process, it has been possible to multiply the acetone degradation kinetics by 3 compared to the fibers presented in part I, which constitute overall a multiplication by a factor 17 compared to our first study (Chap.3).[5] This dramatic improvement makes these fibers at the edge of being competitive with the commercial product (Quartzel). However, the mineralization rate has to be optimized, which can be achieved by inducing a turbulent hydrodynamic flux character within the catalyst structure. This was achieved on the fibers in part I. when the topology was composed of a succession of pores.

From these results, it appears clearly that the fibers generated through the semi-industrial process are the best candidate for photocatalytic application. However, some improvements are needed for their industrial development, like the enhancement of their mechanical properties and of their mineralization rate. For these two purposes, their weaving could be an interesting solution as the fibers crossing will lead to an enhancement of the mechanical properties and the fibers perpendicular to the air flux could induce a turbulent hydrodynamic flux character. Moreover, one of the major drawbacks of air depollution by TiO_2 induced photocatalysis is that the TiO_2 is only sensitive to light presenting a wavelength within the UV range. In consequence, another perspective could be to make them sensitive to visible light. As our fibers are composed of pure TiO_2, this purpose could be achieved by doping with other materials such as platinum or gold nanoparticles.

Annex

Annex 4.1: Fibers surface fractal analysis (part.I)

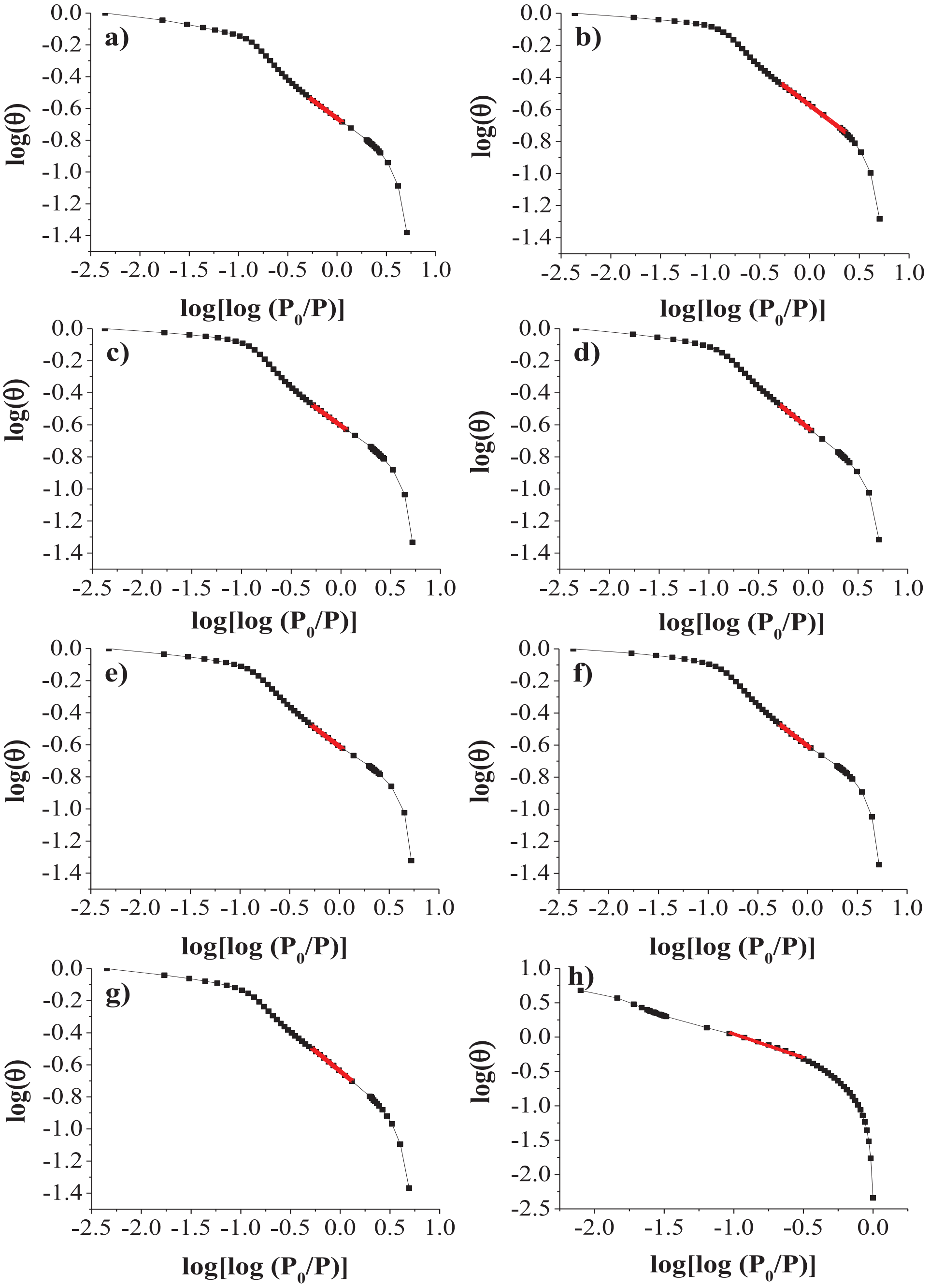

Surface fractal analysis of (a) TiO_2, (b) 130-10-TiO_2, (c) 130-30-TiO_2, (d) 130-60-TiO_2, (e) 260-10-TiO_2, (f) 260-30-TiO_2, (g) 260-60-TiO_2, and (h) TiO_2 ref fibers obtained from the adsorption curve of the isotherm.

Annex 4.2: Fibers optical properties (part.I)

The diffuse reflectance UV spectra (DRUV, see figure below) in Kubelka–Munk unit *F*(R) were typical of the spectrum of titanium dioxide. A more accurate determination of the indirect bandgap of the Anatase TiO_2 fibers by plotting $\sqrt{F(R)*E}$ *vs* energy indicated a mean value of 3.06eV± 0.05 (see table below), for all the fibers and a slight deviation to 3.15 eV for the 260-60-TiO_2 sample. Such a bandgap is smaller than the often-reported 3.2 eV for Anatase, but are still consistent.[9] We concluded that the crystalline structure and the intrinsic optical properties of the TiO_2 is not significantly modified by the insertion of latex particles within the fibers.

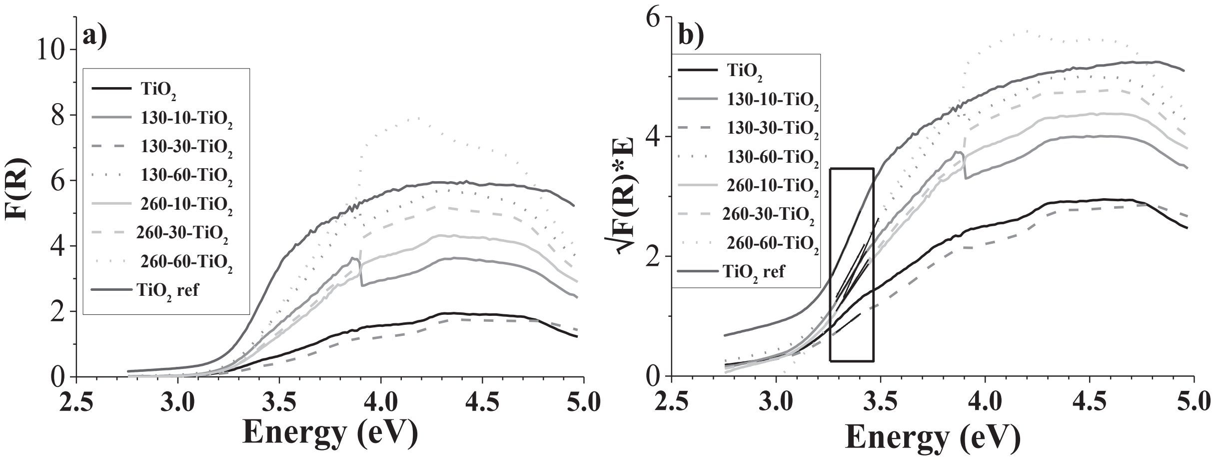

Diffuse reflectance UV spectra of the as-prepared fibers (a). The figure b) is the representation of the √(F(R)*E) *vs* Energy which allow the determination of the band gap value. This value is given by the intersection with the X axis of the linear part of the curve circled in figure b).

Table: Energy of the band gap of the as-synthesized TiO_2 fibers obtained through DRUV experiments and crystallite size of the Anatase deduced from X-rays patterns (Figure 2).

Fibers	Band Gap energy (eV)
TiO_2	3.01
130-10-TiO_2	3.07
130-30-TiO_2	3.02
130-60-TiO_2	3.08
260-10-TiO_2	3.08
260-30-TiO_2	3.09
260-60-TiO_2	3.15
TiO_2 ref	3.05

Annex 4.3: Equation used to determine the acetone degradation kinetics taking into account the apparatus leaks

In the following, we consider that the acetone leaks can be represented as a linear curve over the time, the slope of this curve being referred as k_1.

When there are not any leaks, the equation representing the curve an order 0 reaction is:

$$[\mathrm{Acetone}]_t = [\mathrm{Acetone}]_{t=0} - k\,t \qquad (1)$$

In consequence with leaks, we will have:

$$[\mathrm{Acetone}]_t + k_1 \times t = [\mathrm{Acetone}]_{t=0} - k\,t \qquad (2)$$

When there are not any leaks, an order 1 reaction curve follows the equation:

$$\ln\left(\frac{[\mathrm{Acetone}]_t}{[\mathrm{Acetone}]_{t=0}}\right) = -\,k\,t \qquad (3)$$

With leaks we will then have:

$$\ln\left(\frac{[\mathrm{Acetone}]_t}{[\mathrm{Acetone}]_{\mathrm{ref}}}\right) = -\,k\,t \qquad (4)$$

with $$[\mathrm{Acetone}]_{\mathrm{ref}} = [\mathrm{Acetone}]_0 - k_1 \text{ x } t \qquad (5)$$

In consequence, if by plotting "$[\mathrm{Acetone}]_t + k_1$ x t" *vs* "t", or "$\ln\left(\frac{[\mathrm{Acetone}]_t}{[\mathrm{Acetone}]_{\mathrm{ref}}}\right)$" *vs* "t", we obtain a straight line, the reaction is of order 0 or of order 1 respectively, the slope of the line representing then the reaction kinetics value in $\mathrm{ppm.min^{-1}}$ or in $\mathrm{min^{-1}}$ respectively.

Annexe 4.4: Fibers acetone degradation reaction kinetics (part.I)

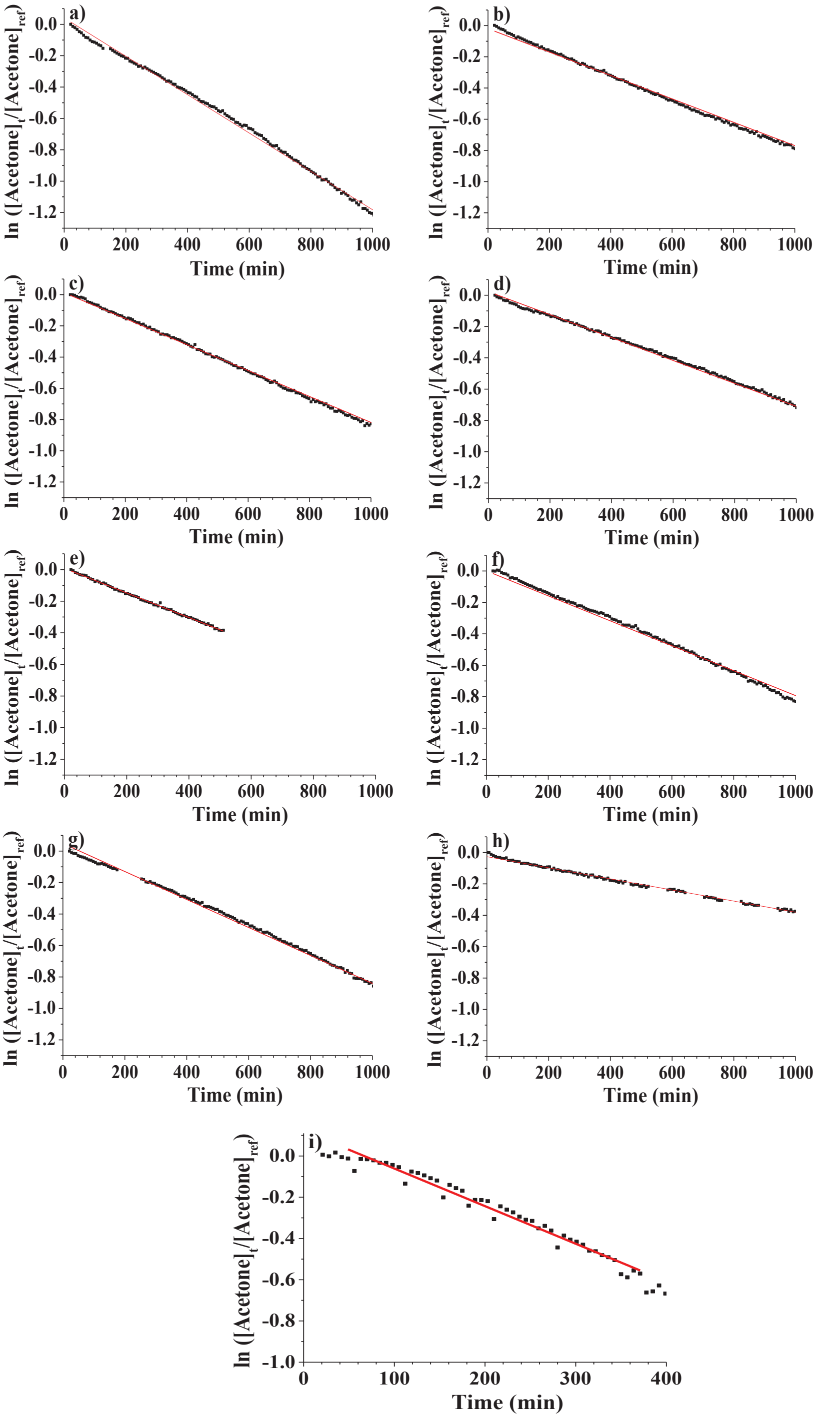

Kinetics reactions obtained through photocatalytic experiments following an order 1 reaction (a) TiO_2, (b) 130-10-TiO_2, (c) 130-30-TiO_2, (d) 130-60-TiO_2, (e) 260-10-TiO_2, (f) 260-30-TiO_2, (g) 260-60-TiO_2, (h) TiO_2 ref fibers, and (i) commercial Quartzel.

Annex 4.5: Fibers surface fractal analysis (part.II)

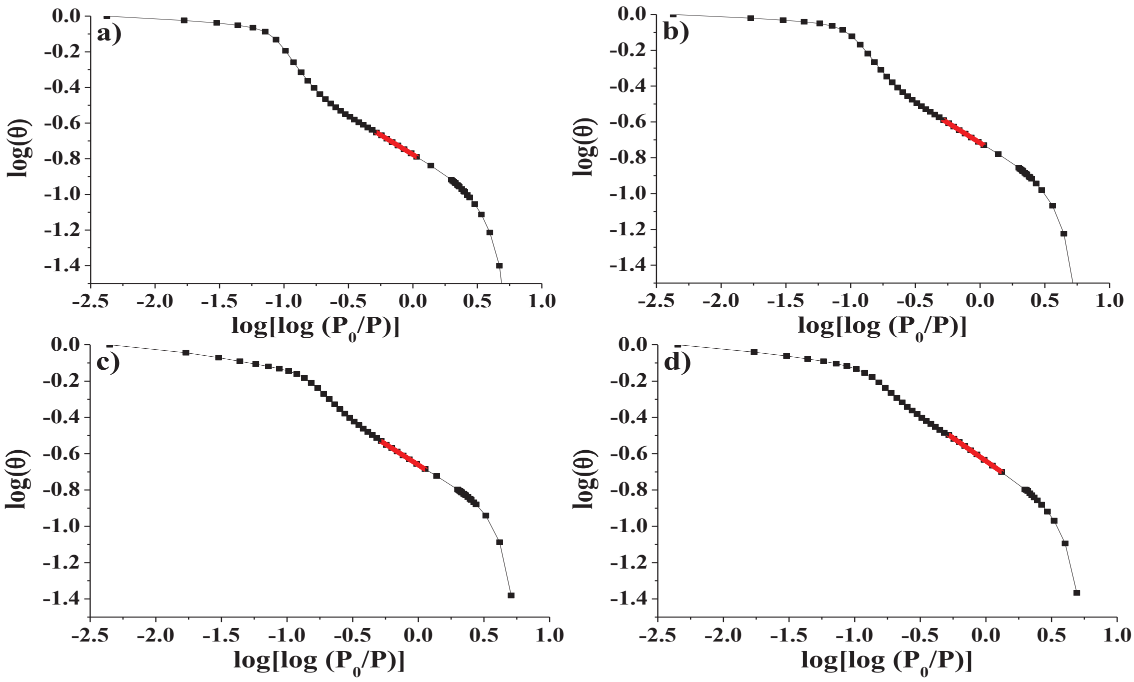

Surface fractal analysis of (a) TiO_2-indus, (b) TiO_2-latex-indus, (c) TiO_2, and (d) 260-60- TiO_2 fibers obtained from the adsorption curve of the isotherm.

Annex 4.6: Fibers optical properties (part II)

The diffuse reflectance UV spectra (DRUV, see figure below) in Kubelka–Munk unit F(R) are typical of the spectrum of titanium dioxide. A more accurate determination of the indirect bandgap of the Anatase TiO_2 fibers by plotting $\sqrt{F(R)*E}$ *vs* energy indicated a mean value of 3.08eV$\pm$ 2% which is consistent with the results in part I (see table below).

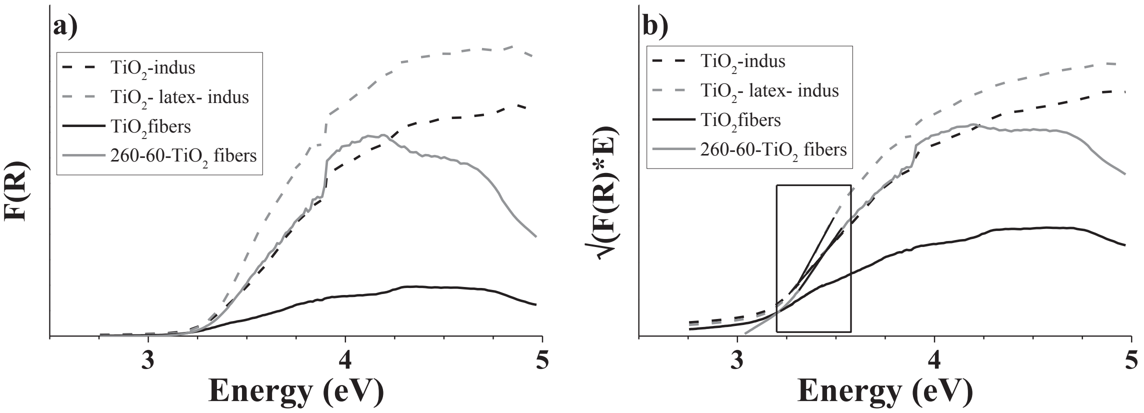

Diffuse reflectance UV spectra of the as-prepared fibers (a). The figure b) is the representation of the √(F(R)*E) *vs* Energy which allows the determination of the band gap value. This value is given by the intersection with the X axis of the linear part of the curve circled in the figure b).

Table: Energy of the band gap of the TiO_2 fibers obtained through DRUV experiments.

Fibers	Band Gap energy (eV)
TiO_2	3.01
260-60-TiO_2	3.15
TiO_2-indus	3.08
TiO_2-latex-indus	3.16

Annex 4.7: Fibers acetone degradation reaction kinetics (part II)

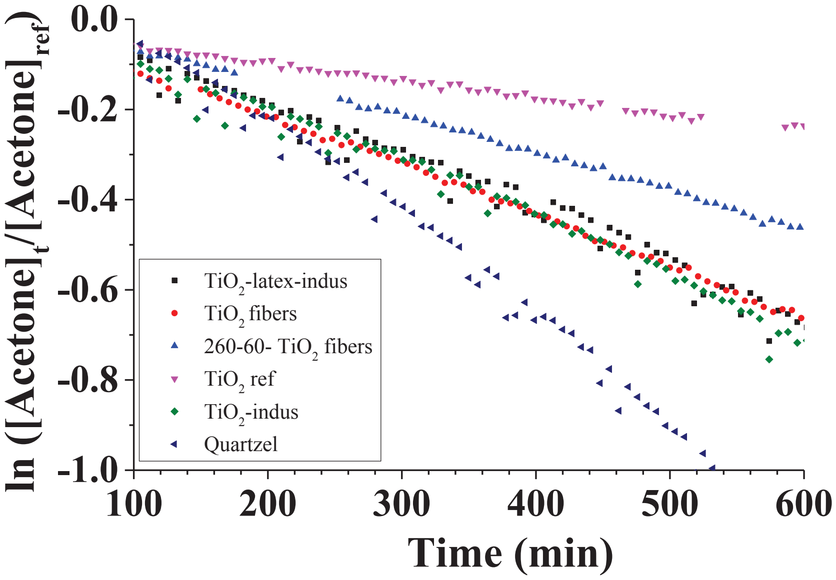

Kinetics reactions obtained through photocatalytic experiments following an order 1 reaction

Chapter 5:

Synthesis of Nanosheets and Nanorods of Polypyrrole for Conducting Thin Films Application

As demonstrated in many studies, anisotropic nanoparticles present many advantages when it comes to conductivity properties, these later being also anisotropic. Moreover, the arrangement of such nanoparticles at higher length scales allows to transpose this specificity, as demonstrated with the alignment of carbon nanotubes inside macroscopic fibers.[1] Among the different material families, organic materials seem to be promising candidates for new electronic devices due to their appealing characteristics such as an easily tunable bandgap, a high mechanical flexibility, and a high biocompatibility.[2] Besides, their processing can be achieved both at low cost and quite easily. For instance, inexpensive techniques such as spin-coating, inkjet printing, or spray coating are employed. Another asset of organic compounds is their chemical structure, which can be triggered easily through synthesis, giving numerous different structures. So far, most of the researches focused on synthesizing 1D structures of conducting polymer particles for electronic applications (nanorods, nanotubes, nanofibers). For the present project, our goal was to prepare 2D structures, which could be used in Dye Sensitized Solar Cells (DSSC), by starting from the synthesis of nanosheets of a conducting polymer, the Polypyrrole (PPy).

Swollen Liquid Crystals (SLCs) were chosen as nano-reactors for the synthesis of these nanosheets of polypyrrole, from the polymerization of pyrrole dissolved in the aqueous phase. The first part of this chapter is then dedicated to the study of the SLCs, more especially to the study of the domain of stability of the different SLCs phases according to their chemical composition. In the second part, we discuss the influence of the monomer polymerization degree over the final structure of the PPy nanoparticles, when confined within SLCs.

I. General concept and objectives

I.1. Synthesis of polypyrrole

Polypyrrole (PPy) is a polymer that has lately attracted a lot of attention due to its conductive and sensor properties. As for both these domains of research, the use of anisotropic objects allows improving the overall material performances, intensive research has been conducted on this type of synthesis. Until now, 1D structures such as nanorods, nanofibers, and nanotubes have been obtained through hard templating, soft templating, seeding, and interfacial reaction, the first two techniques being the most popular. [3–6]

Porous inorganic structures, presenting well-defined hexagonal arrangement of channels, and nano-fibers remain the most common hard templates used for the synthesis of 1D PPy structures.[7] Material growth in porous membranes is a quite common process which was pioneered by Martin.[8] It consists of three simple steps: 1) filling of the membrane pores with a monomer solution, 2) inducing the polymerization reaction within the pores, and 3) removing the template in order to retrieve the polymer. In recent years, Anodisc™ alumina membranes containing anodically etched pores has been the most common porous materials used, this material presenting pore size that can be as small as 5 nm. Also, vanadium oxide ribbons and carbon nanotubes were shown to be a suitable hard template for PPy nanofibers synthesis, where the polymerization reaction occurs at the template surface.[6]

Surfactant self-assembly and reverse microemulsions were also used for the formation of PPy 1D structures. In the case of surfactant-based synthetic routes, it was demonstrated that only synthetic pathways involving cationic surfactant with long carbon chains such as cetyltrimethylammonium bromide (CTAB) lead to the formation of PPy nanofibers. Recently, W/O reverse microemulsions were investigated as a dynamic templating system in order to produce PPy nanotubes. For this type of synthesis, $FeCl_3$ is dissolved into the aqueous core of the reverse microemulsion, which helps forming rod/tube-shaped structures.[2]

Only few 2D PPy structures were reported in literature and, generally, these nanoplates are aggregated and form 3D structures at the micrometer range.[9–11] Almost all the studies reporting the formation of PPy thin films involve electro-polymerization. The formation of smooth PPy thin films using pre-synthesized 2D structures (nanosheets) was first reported by Lee & al.[12] In this study, Swollen Liquid Crystals (SLCs) presenting hexagonal arrangements were used as soft template, with the pyrrole being added into the aqueous continuous phase, and polymerization induced by chemical catalysis. However, the drawback of this method is the polymerization reaction kinetics, which is about several weeks. Besides, no study has been conducted so far with non-hexagonal SLCs. Therefore, the present study tried to address two successful goals: increase our knowledge on these SLCs by identifying a single parameter that would allow us to switch from one mesophase to the other, and see if the synthesis in other geometries than the hexagonal one could help to speed up the reaction and/or prepare other types of nanostructured PPy.

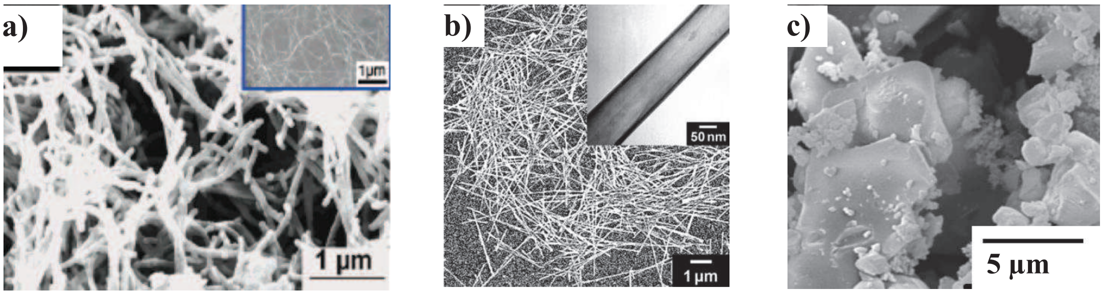

Figure 1. TEM images of PPy a) nanofibers,[6] b) nanotubes,[13] and c) nanoplates[14] obtained by templating methods.

I.2. Physical-chemistry of Swollen Liquid Crystals

Swollen liquid crystals are composed of a water phase, an oil phase, surfactant molecules, co-surfactant molecules and salt. In order to be able to assess the phase diagram of this quaternary system, it is fundamental to understand the physical-chemistry phenomena involved. More specifically, it is important to understand how the interfaces and the surfactant radius of curvature will be affected when varying the phase composition. For this purpose, three theories have been proposed. More details about these methods can be found in the book written by Cosgrove et al.[15]

Two of these theories are based on the nature of the surfactant. One of them, introduced by Israelachvili et al.,[16] is based on the geometrical characteristic of the surfactant molecule. In this case, the preferred radius of curvature between an oily and an aqueous phase is determined by: the minimal area of the head group (a_0), the volume of the hydrophilic tail (v), and the maximum extended chain length of the tail (lc). With this concept, if $a_0 > v/lc$, the water will be the continuous phase of the emulsion, if $a_0 < v/lc$, then the oil will be the continuous phase, and if $a_0 \approx v/lc$, a planar interface will be obtained between the two phases.

Another well-known theory introduced by Griffin et al.[17] is based on the chemical structure of surfactant molecules: the hydrophilic–lipophilic balance (HLB) theory. In this case, the radius of curvature will be determined by calculating the relative proportions of hydrophilic and hydrophobic groups within the molecule. With this theory, Griffin proposed a general formula for non-ionic alkyl polyglycol ethers compounds. Later on, Davies[18] proposed a new general formula to calculate the HLB of a surfactant using constants assigned to hydrophilic (H) and hydrophobic (L) groups. If we call n_H and n_L the number of these groups per surfactant molecule, the HLB can be defined as:

$$HLB = [(n_H \times H) - (n_L \times L)] + 7$$

For lamellar structures, i.e. zero curvature, it was shown that HLB=10.[19] Then oil will be the continuous phase if HLB<10, and water will be the continuous phase otherwise.

From these two theories, we can conclude that the nature of the surfactant molecules (chemical composition and geometry) is a key parameter to adjust the radius of curvature of an interface. However, other parameters, which are not taken into account in these theories, can be adjusted to change the radius of curvature.

Another theory, more complete as it takes all the interactions into account, was proposed by Winsor[20] to account the influence of amphiphiles and solvents on interfacial curvature: the "R ratio" method. In this concept, three different regions are identified: a water region (W), an oil region (O) and an amphiphilic region with surfactant molecules (C). At the interface, these three regions coexist which lead them to interact between each other. In this model, the film stability and its radius of curvature can be determined when all the cohesive interactions are known. These cohesive interactions are presented in Figure 2 where the cohesive energy between a molecule x and a molecule y is defined as A_{xy}, A_{xy} being positive when the interaction between the molecules is attractive. For surfactant–oil and surfactant–water interactions A_{xy} can be considered to be composed of two additive contributions:

$$A_{xy} = A_{Lxy} + A_{Hxy}$$

where A_{Lxy} quantifies interaction between non-polar portions of the two molecules (typically London dispersion forces) and A_{Hxy} represents polar interactions, especially hydrogen bonding or Coulombic interactions. In this case, A_{Hco} (polar interaction between surfactant and oil phase) and A_{Lcw} (non-polar interaction between surfactant and water phase) are generally very small values and can be ignored. The cohesive energy A_{Lco} evidently promotes miscibility of the surfactant molecules with the oil region, and A_{Hcw} with water. On the other hand, A_{oo} and A_{LL} oppose miscibility with oil, while A_{ww} and A_{HH} oppose miscibility with water. From this information, the R ratio will be defined as:

$$R = \frac{A_{Lco} - A_{oo} - A_{LL}}{A_{Hcw} - A_{ww} - A_{HH}} \qquad (1)$$

In brief, the R ratio can be defined as the ratio between the interactions favoring the oil phase as the continuous phase over the interactions favoring the water phase as the continuous phase. Thus, if R>1, the oil phase becomes the continuous phase, if R<1 the water phase becomes the continuous phase, and if R=1, the interface is balanced which consist in a planar interface. In this case, we can see clearly that by varying the interactions energies, it is possible to modify the radius of curvature of the system. If we consider that the nature of the oily and the water phases are not changed, A_{LL}, A_{Lco}, and A_{HH} can be modified by changing the nature of the surfactant or by adding another one in the mixture (co-surfactant). Morevover A_{HH} can also be modified by adding salt into the water phase when dealing with ionic surfactants. Now that we have identified which parameters can be modified to adjust the radius of curvature, we will explain how we used them in our project and for which purposes.

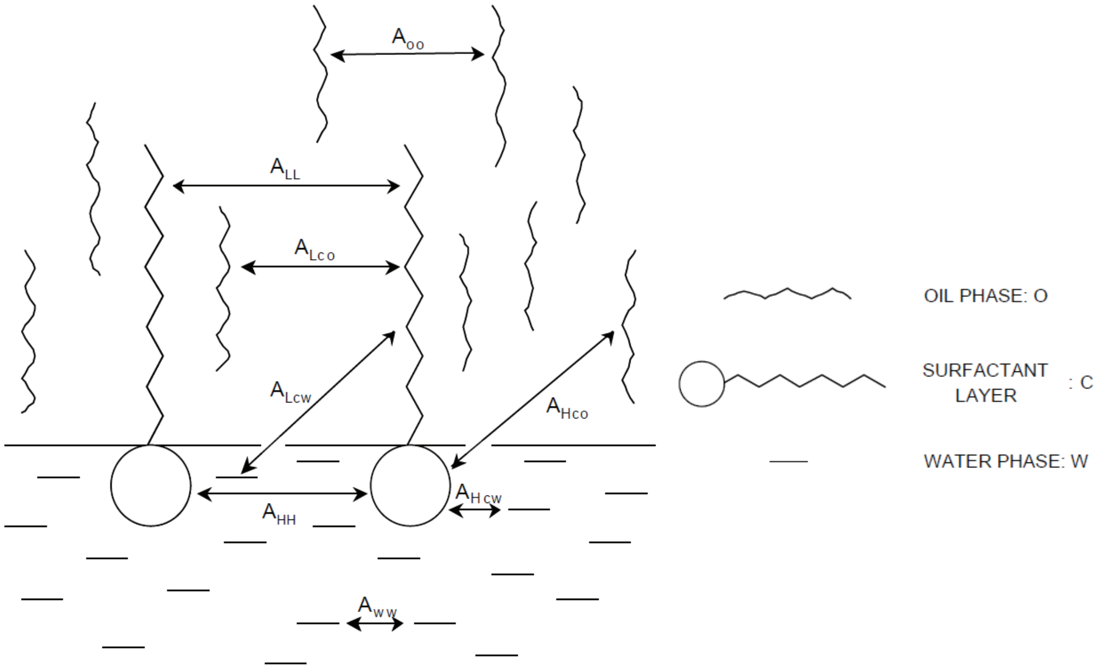

Figure 2. Schematical representation of the cohesive energies present at the interfacial region of an oil–surfactant–water system.[20]

I.3. Synthesis of Polypyrrole nanosheets and objectives

When it comes to the syntheses of hierarchically porous materials or anisotropic objects, systems relevant to soft matter have become an important actor in material structuring. The role of quaternary ammonium surfactants as template for the formation of mesoporous silica, was first demonstrated by Kresge *et al.*[21,22] Attard *et al.* used direct nonionic surfactant-based binary hexagonal liquid crystals (LC) to synthesize porous materials and porous metal films by direct Liquid Crystal Templating (LCT).[23–26] This LCT method was further expanded to giant direct hexagonal mesophases made of a quaternary system (water, surfactant, cosurfactant and oil) called Swollen Liquid Crystals (SLC).[27] Compared to binary LC, the hydrophobic part of SLC can swell as a result of the addition of an oil phase within the hydrophobic surfactant structure. This swelling effect is stabilized by the addition of a co-surfactant (1-pentanol) along with that of a suitable amount of salt (NaCl, NaF, Na_2SO_4, etc) to adjust the repulsive electrostatic interaction between surfactant heads. Studies on the SLCs hexagonal phase demonstrated that well-defined hexagonal structures with cell parameters ranging from 3 to 30 nm can be obtained.[27]

Since these SLCs are dynamic systems, their stability results from a fine balance between components, and any uncontrolled change, resulting from their use as adaptive matrix for the synthesis of nanomaterials within, must take into account the influence of new additive on this stability, before and during the synthesis. The hexagonal phase of SLCs has already been used as a reactor to synthesize materials either in the aqueous or in the oil phase. The anisotropic confinement provided by the SLC led to nanomaterials with specific shapes such as Pt nanorods or nanoballs, zirconia needles, or polymeric nanowires.[28]

Polypyrrole has been studied for long because of its potential as organic electrode, the synthesis of this polymer in bulk giving spherical nanoparticles.[29–31] Lee *et al.*[32] reported that the SLCs hexagonal phase can be used for the formation of polypyrrole nanosheets when synthesized in the aqueous phase. As the Pyrrole is soluble in water, the polymerization reaction occured in between the cylinders of the SLCs hexagonal phase, which allowed the formation of PPy nanosheets (see Figure 3.c.). Compared with the nanoparticles, these polymer nanosheets could better self-assemble into continuous conducting films via a tile-like mechanism.

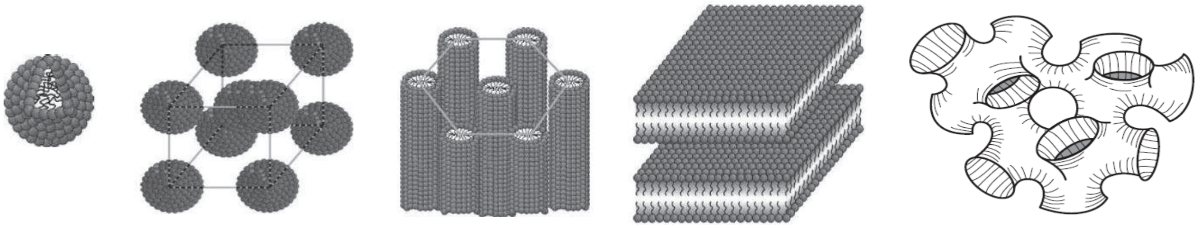

Figure 3: Schematic representation of a) a micelle of a direct emulsion, b) a cubic phase, c) a hexagonal phase, d) a lamellar phase, and e) a sponge phase.[33]

The hexagonal SLCs have demonstrated great success in the synthesis of numerous nanomaterials, but their use still presents two drawbacks: (i) the hexagonal phase is stable only in a narrow area of the phase diagram and it requires a fine adjustment of the co-surfactant, and (ii) it is very viscous, which limits the mixing of the SLCs phase containing the monomer and the one containing the catalyst, the reaction occurs then by diffusion and the reaction time can be extended to several weeks.

The structural study of these phases has remained focused on the domain of stability of the hexagonal phase until now, but the identification of other geometries could provide new developments regarding the use of these SLCs as nanoreactors.[27] Therefore, we investigated a partial phase diagram, based on the variation of two parameters (concentration in co-surfactant and salt) in order to identify other possible phases than the hexagonal and assess their domain of stability. The structural evolution of SLCs made of a mixture of cetyltrimethylammonium bromide (CTAB), water, cyclohexane, 1-pentanol and salt, is reported, with the identification of the different aggregate geometries within a partial phase diagram based on the amount of co-surfactant/CTAB for different concentrations in salt. Two salts, ammonium persulfate (AP), $(NH_4)_2S_2O_8$, or sodium fluoride (NaF), were selected for this study, with NaF being the salt used in previous reports, and AP being the catalyst used for the synthesis of PPy.[32] The possible influence of the nature of the salt was explored by comparing the phase diagram of the AP-based SLCs with similar structures prepared with NaF at 0.2M concentration.

The SLCs sponge phase appeared as a good candidate for the preparation of PPy nanosheets as: (i) it was demonstrated to possess a large domain of stability in the partial SLCs phase diagram (see part II), (ii) it is liquid, and the easy mixing of the two SLCs phases containing the monomer and the catalyst can ensure fast reaction kinetics, and (iii) its bi-layer organization is compatible with the formation of PPy nanosheets (see Figure 3.e.). The PPy polymerization in SLCs sponge phase was then investigated in part III.

II. Swollen Liquid Crystals phase diagram

II.1. Swollen Liquid Crystals preparation

In order to prepare the SLCs, we used cetyltrimethylammonium bromide (CTAB), cyclohexane, 1-pentanol, sodium fluoride (NaF), ammonium persulfate ($(NH_4)_2S_2O_8$), and hydrochloric acid (HCl). They were purchased from Aldrich and used as received without purification.

The preparation of the mesophases was slightly modified compared with the previously published method, where the co-surfactant was slowly added at the end of the synthesis until a transparent viscous phase was obtained.[28] The protocol followed for the SLCs preparation is described in Figure 4. Typically, the salt was dissolved in water at pH close to 0 at three different concentrations: 0.1M, 0.2M and 0.3M for NaF, and 0.05M, 0.1M and 0.15M for AP to keep the same equivalent ionic strength. Two grams of this solution were mixed with 1g of

CTAB and then placed in an ultrasound bath till a transparent homogeneous solution was obtained. Various pre-determined amounts of 1-pentanol (co-surfactant) were added, followed by the addition of cyclohexane (swelling agent) according to the equation:[34]

Mcyclo= 0.779*(Vwater/0.156) *(n.[salt]+0.104) (2) (n = valence of the salt)

The mixture was finally shaken with a vortex mixer until a homogeneous system is obtained, and stored for at least one week before analysis. In the following, samples are labelled NaF/M/R or AP/M/R, when prepared with NaF or AP, respectively, with M being the ions concentrations in solution (0.1; 0.2; 0.3) and R the pentanol/surfactant molar ratio. In the case of NaF, M is equal to the [NaF]. However, in the case of AP, the ions concentration is equal to the 2x[AP], this value will be referred to in the following as $[AP]_{ions}$. As the radius of curvature is influenced only by the ions concentration, this value will be the parameter that matters in the experiment. In consequence, the discussion will consider $[AP]_{ions}$ instead of [AP].

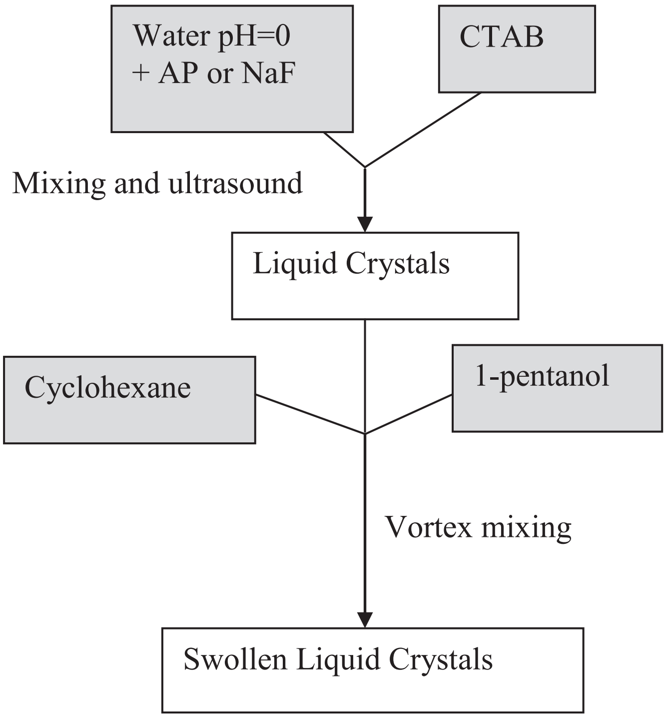

Figure 4. Experimental protocol for the SLCs preparation.

II.2. Macroscopic evolution

With the aim of providing the required information for the future synthesis of PPy in non-hexagonal SLCs, a partial phase diagram made with the AP catalyst used as a salt was studied first. This partial phase diagram was determined for three different AP ions concentrations (0.1, 0.2, 0.3 M). A 1-pentanol/CTAB molar ratio (R) between 0.2 and 2.2 was studied. For each salt ions concentration, the volume of cyclohexane was set constant and deduced from eq. (2). The macroscopic evolution of SLC (color, viscosity) containing a $[AP]_{ions}$ equal to 0.2M was followed according to the different values of 1-pentanol/ CTAB ratio, R, ranging from 0.4 to 1.8 (Figure 5).

The yellowish color of the SLCs is due to AP. Increasing the amount of 1-pentanol modifies both the turbidity and the viscosity of the SLCs, but no macroscopic phase separation was observed along the whole range, despite the high fraction of both water and cyclohexane. For R = 0.4, the SLCs is very viscous, almost solid-like, and turbid. By increasing R to 0.8 the SLCs present a still very viscous, but fully transparent phase that flows slowly. A slight addition of pentanol (R = 1.1) reduces drastically the viscosity while increasing the turbidity. At R=1.5, we observe that the phase is still turbid but it turns into a low viscosity fluid, and at R = 1.8, the phase has turned into a fully transparent fluid and perfectly stable over time (months). This final state of the SLCs, which can be achieved over a large range in 1-pentanol concentration, offers great opportunities as it is a perfect mixture of two non-miscible phases (water and cyclohexane) that are intimately interlocked.

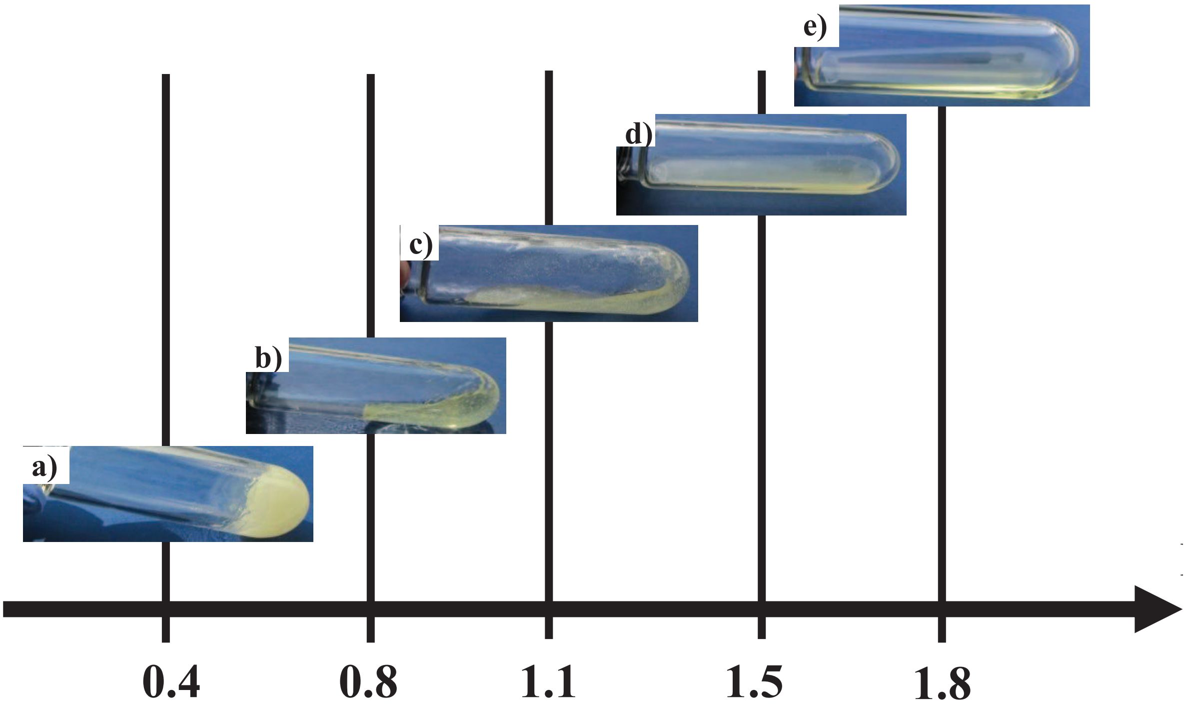

Figure 5. Images representing the evolution of the SLCs appearance depending on R at $[AP]_{ions}$=0.2M. Samples were prepared with 1.0g CTAB, 0.046g AP, 2.00g water (pH 2), 3.06g cyclohexane. The amount of added 1-pentanol was: (a) 0.097g, (b), 0.198g, (c), 0.264g, (d) 0.365g, and (e) 0.440g.

II.3. Structural evolution

II.3.1. Phase transition analysis (SAXS and cross-polarized optical microscopy)

In order to determine which phase corresponds to each appearance and their domain of stability, we performed SAXS analyses on the SLCs that we coupled with optical microscope analyses under polarized light. Indeed, the last analysis is needed to complete the first results obtained by SAXS analysis. The samples were first characterized by small angle X-ray scattering (SAXS) on a Nanostar (Bruker Co.), equipped with a copper anode (40kV, 35mA). The apparatus is equipped with two crossed Goebel mirrors in order to select the CuKα wavelength (0.154 nm) and produces a parallel beam, the final collimation being adjusted with a 3-pinhole setup (with a 300µm diameter for pinhole-2). SAXS patterns were acquired using a 22x22cm 2D gas detector HiStar from Bruker Co., positioned at a distance D of the sample. Silver behenate was used as a position reference. The scattering wave vector range used was 0.1 - 2.0 nm^{-1}. The mesophases were also observed under cross polarized light Leica DM2500P optical microscope equipped with a CCD FireWire Leica DFC420 camera. (Figure 7, see also Annex 5.3 for samples prepared with a 0.3M $[AP]_{ions}$).

The SAXS scattering patterns of the SLCs are shown in Figure 6 where we present the evolution of the patterns while increasing the amount of 1-pentanol (see also Annex 5.1). The presence of well-defined and most often sharp peaks is a specific feature of most of the observed patterns, revealing the presence of long-range ordered domains with repeating distances (deduced from the first-order peak location in reciprocal space) in the 10-40 nm range. From SAXS analyses, the positions of the peaks are also extracted, the ratios between their positions being presented in the Figure 10 that sums up the major results obtained with the different techniques.

A face-centred cubic phase (*Fm*3h*m* symmetry, A1) presents in theory 4 major peaks of diffraction at ratios of 1 (111), √(4/3) (200), √(8/3) (220), and √(11/3) (311). The cell parameter, a, represents the distance between the centres of two micelles, and is calculated from the first peak position with $a = (2\pi/q_1) \times \sqrt{3}$.[35] An hexagonal phase (H1) displays 4 major peaks of diffraction at ratios of 1, √3, 2, and √(7). The cell parameter, a, corresponds to the distance between the centres of two cylinders, and is calculated from the first peak position with $a = (2\pi/q_1) \times (2/\sqrt{3})$. A lamellar phase ($L_\alpha$) is represented by 3 major peaks of diffraction at ratios of 1, 2, and 3. The average size of the bi-layer (cell parameter) is calculated with $a = 2\pi/q_1$.

The images of the samples taken under cross-polarized light on the microscope are presented in Figure 7. In this figure, the images representing the samples at the lowest and the highest ratio of 1-pentanol were not included as they present an isotropic behavior (black image). A hexagonal phase is often characterized by either a smokey, or a mosaic bi-refringence texture. When observed by optical microscopy under cross-polarized light, a lamellar phase exhibits Malta-crosses.

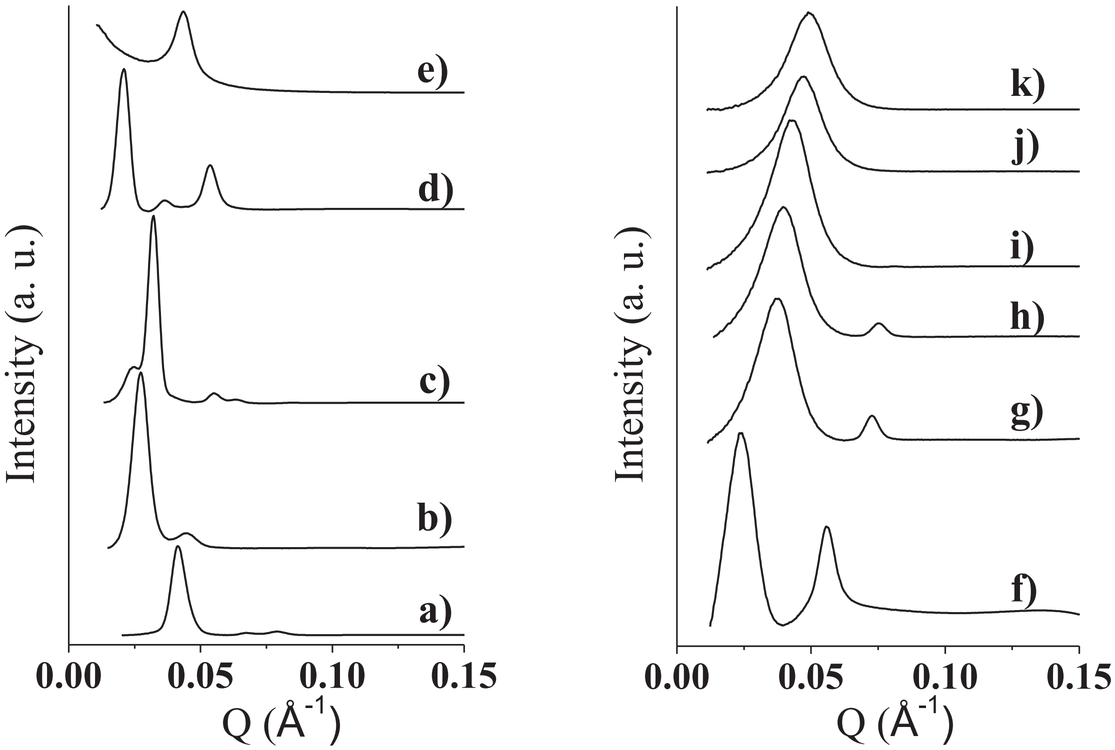

Figure 6. SAXS patterns evolution depending on the 1-pentanol over surfactant molar ratio (R) varying from 0.3 to 2.2 and AP salt ionic strength set at 0.2M: a) R=0.3, b) R=0.7, c) R=0.8, d) R=1, e) R=1.15, f) R=1.33, g) R=1.5, h) R=1.6, i) R=1.7, j) R=1.9, k) R=2.2.

The SAXS patterns of the SLC prepared with an increasing amount of co-surfactant suggests the presence of two types of structural modifications induced by 1-pentanol: continuous evolutions (while R increases from 0.3 to 0.7, or above 1.8 for instance), as well as structural transitions (*e.g.* occurring in the 0.8<R<1.0 or 1.33<R<1.7 range). Further investigation of these SAXS patterns was carried on by plotting a Porod representation ($I \times q^4 = f(q)$) to emphasize the high-q component of the signal (Annex 2). This representation reveals that scattering contributions significantly above the noise level exist at larger q, which can be assigned to the presence of well-defined shapes (*e.g.* spherical, cylindrical or platelet-like shapes) for the regularly stacked hydrophobic domains (cyclohexane + tail of the CTAB and 1-pentanol molecules). In the following paragraphs, the d-spacings is defined as $d=2\pi/q_i$ where q_i is the location in the reciprocal space of the ith peak.

At low R (R=0.3), the SAXS pattern presents a set of two major diffraction peaks whose positions are in the ratio 1:√(8/3) and the image of this sample on the microscope under cross-polarized light is totally black (Figure 10). From these results, we can deduce that this pattern corresponds to a face-centred cubic phase (A1). Due to the resolution of our equipment, we assume that the second peak is merged with the first peak and cannot be distinguished clearly. We can also conclude that the fcc structure is perfectly ordered at R = 0.3 (q1, q3, & q4 diffraction lines assigned and no birefringent textures observed) and it becomes progressively disturbed as R increases (only q1 and q2 with the good ratio, and birefringent textures observed at R=0.6 (Figure 7)). This structural disturbance goes along with an increase in the cell parameter, from 26 nm at R=0.3, to 40 nm at R=0.7.

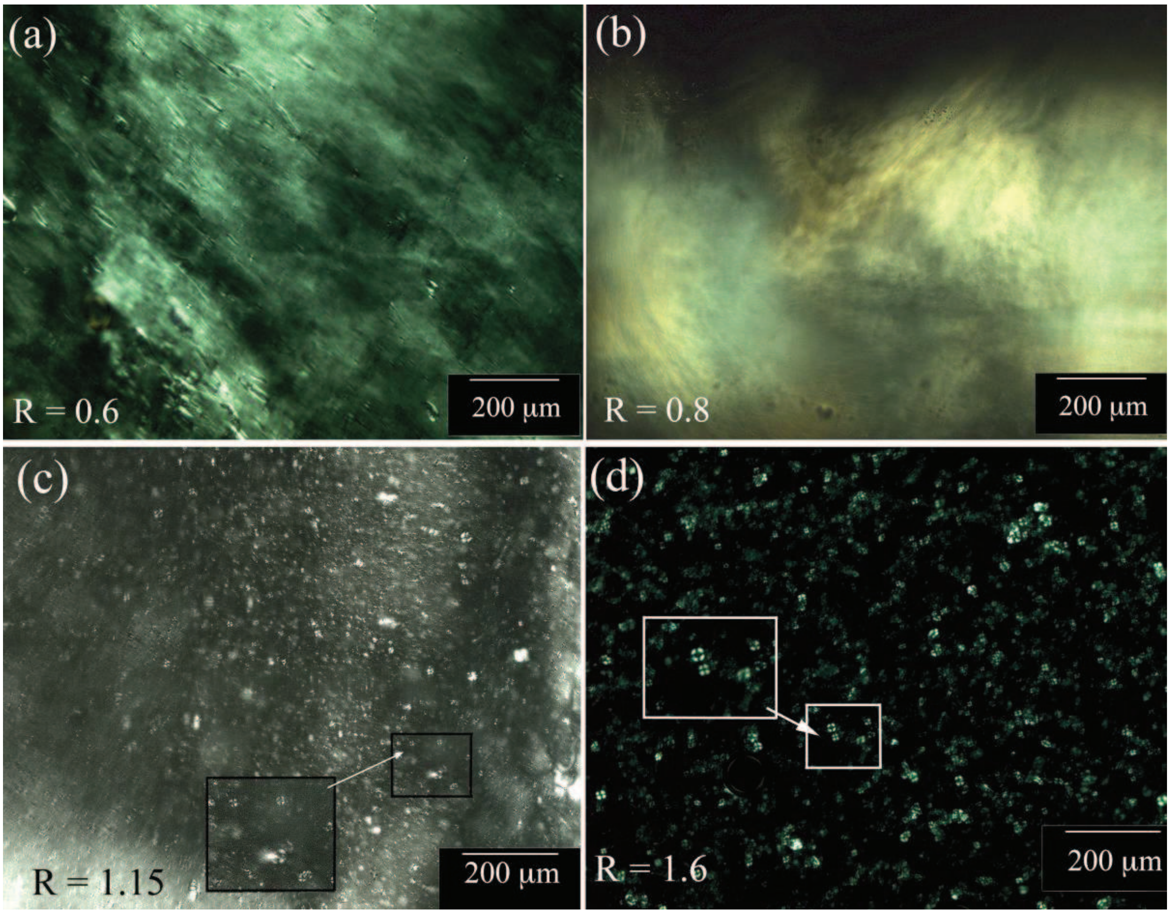

Figure 7. Optical microscopy under cross-polarized light of the SLCs made with AP (0.2M ionic strength): a) ill-ordered hexagonal phase (R=0.6), b) hexagonal phase (R=0.8), c) lamellar phase (R=1.15), d) mixed lamellar/sponge phase (R= 1.6). Samples were prepared with AP salt ionic strength set at 0.2M (1.0g CTAB, 0.046g AP, 2.00g water (pH 2), 3.06g cyclohexane).

If we increase R (0.8<R<1), the pattern exhibits a set of three diffraction peaks whose positions are in the ratio 1:√3:2, and we can observe a characteristic bi-refringence behaviour of an hexagonal phase on the image in Figure 7.b. and Figure 10. In consequence, we can deduce that it corresponds to a hexagonal phase (H1).[36] the cell parameter for this structure varies from 23 nm at R = 0.8 to 35 nm at R=1.0

At R=1.15, we observe a single narrow peak combined with an increase in the intensity at low q values. Moreover, the image of the sample in Figure 7.c. presents a bi-refringence behaviour with the presence of Malta crosses characteristic of a lamellar phase, more specifically of onions structure. The narrow peak indicates an anisotropic crystalline phase and the increase at low q indicates that there is a large distribution of the size of the mesophase. In order to see if there is the presence of a bilayer signal, we decided to use the Porod representation which consists in representing the spectra according to the equation: $f(q) = I \times q^4$.(Annex 2) In this representation, the presence of a “sinusoidal” signal at high q value will indicate the presence of the bilayer. As this sinusoid is observed on the SAXS pattern, we can conclude that the sample presents a bilayer structure. In consequence, even if the second peak of the lamellar phase at a ratio 1:2 is too small to be visible on the graph, we can deduce that we have here a L_α phase with a large distribution of distance between planes. The lamellar phase has a structural parameter around 15nm.

At higher R (1.3<R<1.7), the pattern exhibits a large peak at low q values and a narrow peak at higher q values, and the image in Figure 7.d. presents a bi-refringence behaviour with the presence of malt crosses. These features are typical of a mixed phase containing Lα plus an isotropic phase (the second peak of the Lα phase being too small to be visible on the graph). The isotropic phase nature, which could be a micro emulsion solution or a sponge phase among others, will be determined with the analysis of the pattern at highest R. Indeed, the patterns of the samples at the highest R present only a broad peak at low q values and so correspond to the pure isotropic phase. The key difference between a micro emulsion and a sponge phase is that, in a sponge phase, the local structure is similar to a lamellar phase and so possesses a bilayer structure. We plotted then the Porod representation of this pattern (Annexe 2) where we could observe the “sinusoidal” signal characteristic of the bilayer structure, more specifically the first half of a sinusoidal curve. From this result, we deduced that the broad peak in our case corresponds to a sponge phase (L3). In the mixed Lα + L3 phase, the Lα phase has a structural parameter *d* comprised between 16nm and 20nm, and the L3 phase has a *d* comprised between 8nm and 10nm. For the pure L3 phase, *d* is comprised between 13nm and 15nm. For each phase, the highest values of *d* correspond to the lowest R.

On the other hand, some samples located in between two domains exhibits patterns that are complicated to analyse due to the coexistence of several phases. In the following, we will name these phases “intermediary phase”.

In conclusion, we can see that for the lowest R, the SLCs exhibit an A1 phase. As we increase the 1-pentanol amount they will turn successively into a mixed A1 + H1 phase, a pure H1 phase, a pure Lα phase, a mixed Lα + L3 phase and finally a pure L3 phase.

II.3.2. Evolution of the structural parameter with R

The steady variation in characteristic stacking and domain sizes with R, was identified by plotting the evolution of the lattice parameter "a" (identified from Annex 5.2) with R (Figure 8). The labels a_C, a_H, a_L, a_Lmix, a_S, and a_hydrophobic represent respectively the lattice parameter of the cubic phase, the hexagonal phase, the lamellar phase, the lamellar phase part in the lamellar/sponge mixed phase, the sponge phase, and the size of the hydrophobic domains.

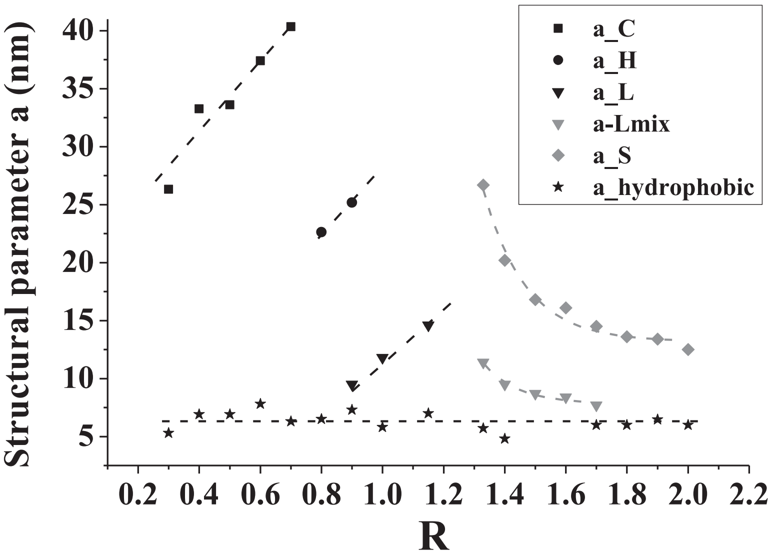

Figure 8. Evolution of the d-spacing deduced from the SAXS peak positions, as a function of the pentanol over surfactant molar ratio (R), and AP salt ionic strength set at 0.2M. a_C, a_H, a_L, a_Lmix, a_S, and a_hydrophobic representing respectively the lattice parameter of the cubic phase, the hexagonal phase, the lamellar phase, the lamellar phase part in the lamellar/sponge mixed phase, the sponge phase, and the size of the hydrophobic domains.

The diffraction peaks position evolves continuously with R. We can clearly observe two distinct trends for the lattice parameter, a, which are independent of the SLCs mesophase. A first trend is observed below R = 1.3 with an increase in the values of "a" with R (a_C: 26 to 40 nm; a_H: 22 to 26 nm; a_L: 9.5 to 14.6 nm). A second decreasing trend is observed above R = 1.3 (a_Lmix: 11.5 to 7.5 nm; a_S: 27 to 12 nm). Moreover, if we separately consider the regions where R<1.3 and R>1.3, we notice that the phase present after each phase transition possesses a lattice parameter smaller than the previous one. Also, the data points corresponding to the size of the hydrophobic domains, made of the two layers of CTAB alkyl chains and cyclohexane/1-pentanol contained within, remains close to 7 nm over the whole R range (a_hydrophobic is defined from the high q values component of the signal).

In conclusion, as a_hydrophobic remains constant, we can say that when R<1.3, the water domain of SLCs structure swell by the addition of 1-pentanol for a same mesophase, but becomes smaller in between two phases. When R>1.3, the apparition of the disordered sponge phase is responsible for an increase of the water domain size overall, which will then become smaller by further addition of 1-pentanol.

II.3.3. Freeze Fracture Transmission Electron Microscopy

The structure of the SLC phase was confirmed by Freeze Fracture Transmission Electron Microscopy (FF-TEM) with a TEM Hitachi H600 apparatus using a Tungsten filament operating at an accelerating voltage of 75 kV. Typically, one small drop of solution was either placed on a gold support, or in between two copper supports and then immersed quickly into liquid propane cooled down by liquid nitrogen. The samples were then transferred into the chamber of the freeze fracture apparatus (Leica BAF 060) and either cut with a blade (gold support), or fractured by pulling apart the two copper supports. A 4 nm layer of Platinum-Carbon and a 30 nm Carbon layer were sputtered. The replicas were cleaned, and deposited onto a copper grid (400 mesh), before being observed.

Figure 9 shows three representative structures of the whole series: for R=0.45 (Figure 9.a.), a network of small, nearly spherical objects arranged in a close packed structure is observed, which matches with the hypothesis of a cubic phase. For R=0.81 (Figure 9.b.), multi-facetted larger structures lead to the hypothesis of a hexagonal structure. Finally, the sample prepared with R=1.7 (Figure 9.c.) exhibits two different structures, with parallel lines (see arrow), and a worm like structure, which can be ascribed to the cross-section and surface of lamellar domains, respectively.

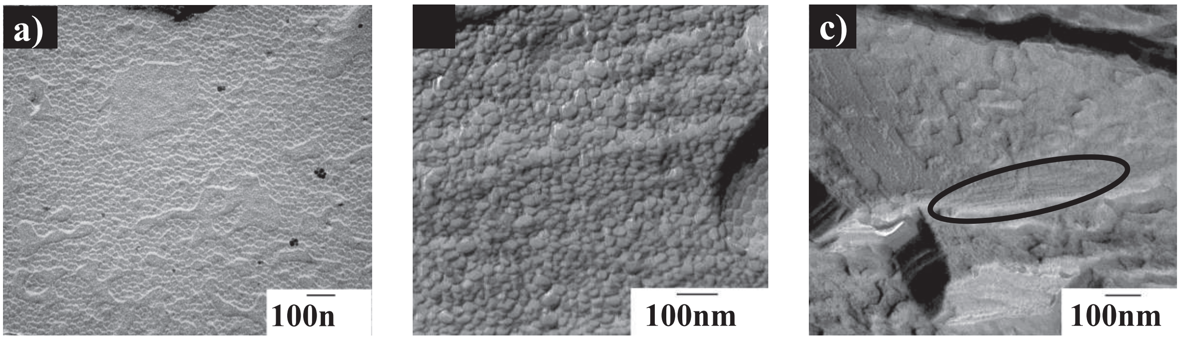

Figure 9. TEM images of SLCs replicas obtained by freeze fracture method: a) cubic phase (R=0.45), b) hexagonal phase (R=0.81), c) mixed lamellar/sponge phase (R=1.7). Samples were prepared with AP salt ionic strength set at 0.2M.

]

II.3.4. Phase diagram

Figure 10 displays the ratio values calculated for the SAXS peak positions of Figure 6. This figure summarizes also the information obtained with the different techniques used to characterize these mesophases which lead us to establish the partial phase diagram.

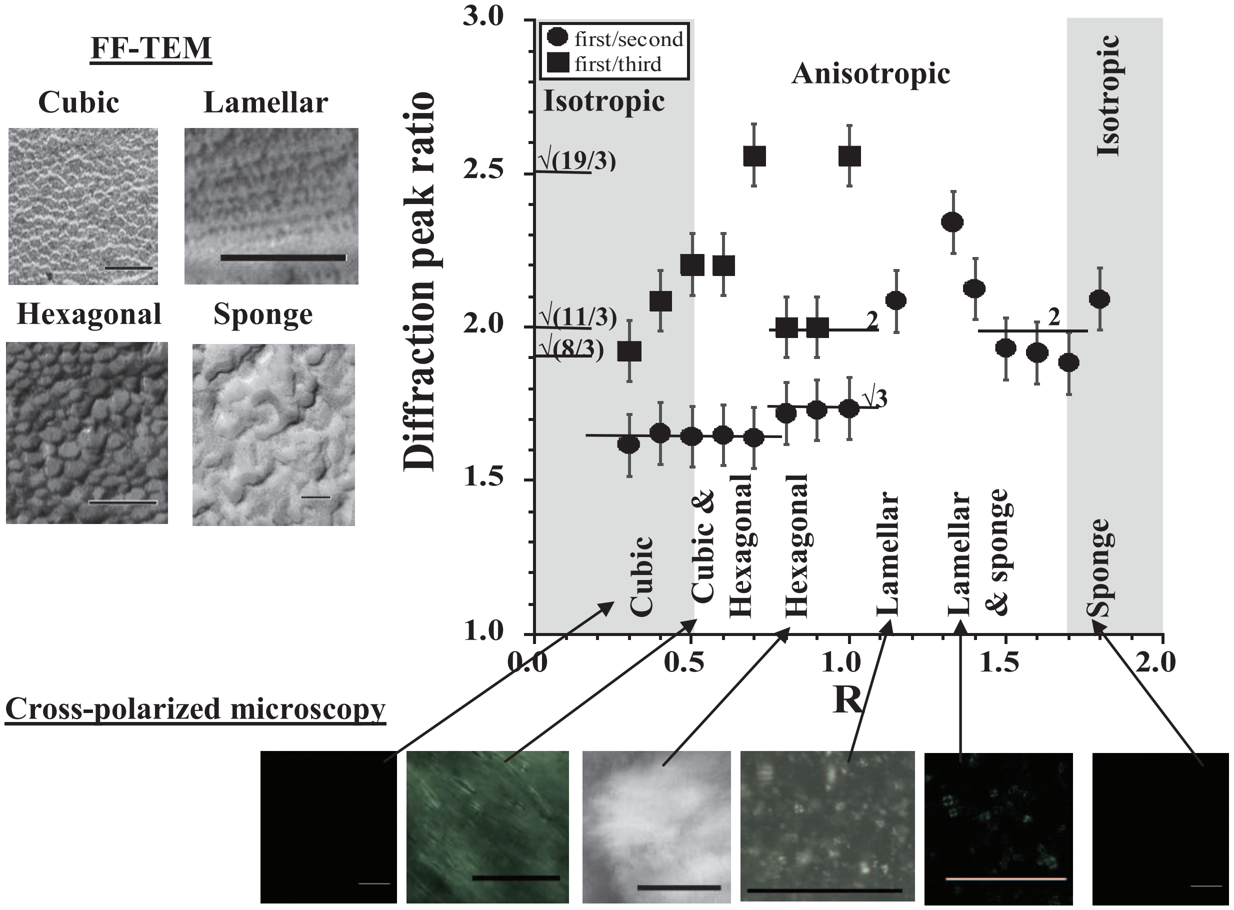

Figure 10. Summary of the informations collected, combined with the plot of the SAXS diffraction line ratio d_1/d_i calculated from peak positions in Figure 6. The gray areas correspond to the isotropic structure areas, and pictures of cryo-TEM (scale bar: 100nm) and polarized light microscopy (scale bar: 200µm) refer to Figure 7 and Figure 9, respectively.

The same analysis was carried out for other ionic strengths in AP, with a similar evolution being observed (Figure 11.a.). Variation in the ions concentration comes in parallel with a variation in the oil content (see eq.(2)), but none of them drastically modify the frontiers in phase transition: A1 → H1 → Lα → L3. Therefore, it can be concluded that the use of AP as a catalyst for the synthesis of polypyrrole, should keep the SLC structure untouched, if the initial concentration corresponds to an ionic concentration close to 0.3, corresponding to [AP]= 0,15M.

As the synthesis of polypyrrole involves the dissolution of the monomer in another SLC stabilized by a salt such as NaF, before mixing with an AP-containing SLC,[32] a parallel study with NaF used in place of AP confirms that the structural evolution as a function of the addition of pentanol, is similar to that observed with AP (Figure 11.b). As a result, it is expected that the synthesis of polypyrrole could be conducted in any of the structures of the pseudo phase diagram studied in this report.

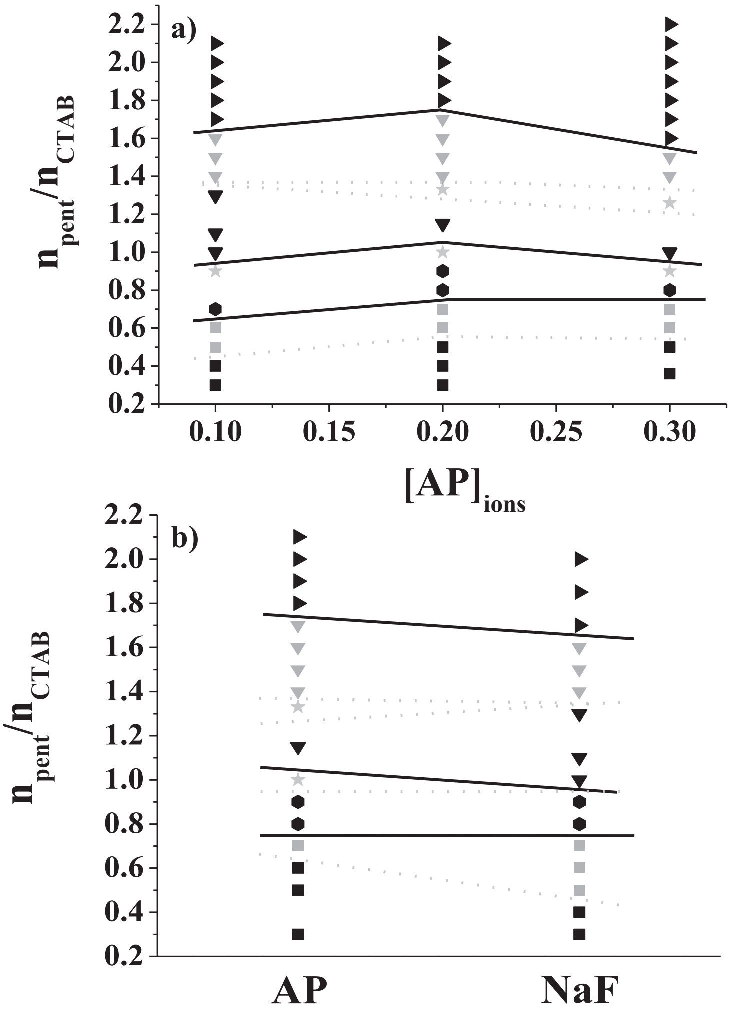

Figure 11. Evolution of the SLCs mesophase structure with R as a function of (a) the ammonium persulfate (AP), and (b) comparison between AP and NaF at 0.2M ions concentration: ■ cubic phase, ▨ mixed cubic/hexagonal phase, ⬢ hexagonal phase, ☆ "intermediary" phase, ▼ lamellar phase, ▽ mixed lamellar/sponge phase, and ▶ sponge phase.

II.4. Intermediary conclusion

CTAB/salted water/Cyclohexane/1-pentanol quaternary systems can form Swollen Liquid Crystals. In order to stabilize liquid crystalline phases, the amount of each component has to be carefully adjusted. We demonstrated in this report that at a fixed CTAB and oil/water ratio, the amount of 1-pentanol will determine the nature of the liquid crystalline phase. By increasing the amount of 1-pentanol, the crystalline phase will switch successively from cubic to hexagonal, to lamellar, and finally to sponge, with the apparition of mixed phases domains in between the pure phase domains. The salt concentration and the nature of it have only little influence on the size and the stability range of the phase domains.

As explained in the introduction, we want to use SLCs as nanoreactors for the polymerization reaction of the Pyrrole in order to obtain nanosheets. For this purpose, we need an anisotropic phase whose domain of stability will be wide enough to be able to resist to slight modification (variation in salt concentration and addition of Pyrrole). As the domain of stability of the lamellar phase is very narrow, this phase cannot be used in our application. As we explained in the introduction, the hexagonal phase is also not suitable due to its high viscosity, which increases dramatically the kinetics of reaction. Finally, the only phase matching our criteria is the sponge phase that possesses a wide domain of stability, a very low viscosity, and that possesses a local bi-layer structure which can direct the growth of the PPy in order to obtain nanosheets. In the next part we will then investigate the polymerization of the Pyrrole in sponge phase SLCs.

III. Polypyrrole syntheses

III.1. Experimental protocol

The protocol is basically the same as for the preparation of Swollen Liquid Crystals (SLCs) except that, pyrrole is added in the surfactant- and NaF-containing aqueous part of a SLCs, before the addition of cyclohexane and 1-pentanol. Pyrrole was purchased from Aldrich and was used without any purification process. For the synthesis of PPy, two different phases, one containing the Py (Phase A) and the other one containing the polymerization catalyst AP (Phase B), were prepared. The protocol followed for the preparation is described in Figure 12. Typically, the salt was dissolved in water at pH close to 0 at a concentration of 0.3M for NaF, and 0.15M for AP ($[AP]_{ions}$=0.3M). Two grams of this solution were mixed in warm water with 1g of CTAB and then placed in an ultrasound bath until a transparent homogeneous solution is obtained. At this stage, 0.033g of Pyrrole was added for the preparation of the Phase A. Then, around 4.05g of cyclohexane and around 0.45g of 1-pentanol were added into the mixture for both Phase A and Phase B. The mixture was finally shaken with a vortex mixer until a homogeneous system is obtained.

Phase B was slowly poured into Phase A, and the final mixture was gently stirred in order to ensure an optimal contact between the two phases, and left to react for one week before PPy extraction. For extraction, the SLC obtained after reaction was first mixed with

25mL of a water and ethanol solution (50:50), before being centrifuged at 4,000rpm for 10min. PPy settled at the bottom and the supernatant was removed. This step was repeated by adding 40mL of the washing solution, re-dispersing the PPy suspension for 10 min in an ultrasound bath, and centrifuged again at 4000rpm for 10min. Once again, the supernantant was removed. Finally, 10mL of a water solution at pH=2 was added to the precipitate, to protonate the PPy, and sonicated for 10 min. This final product used in the following is made of this aqueous PPy suspension.

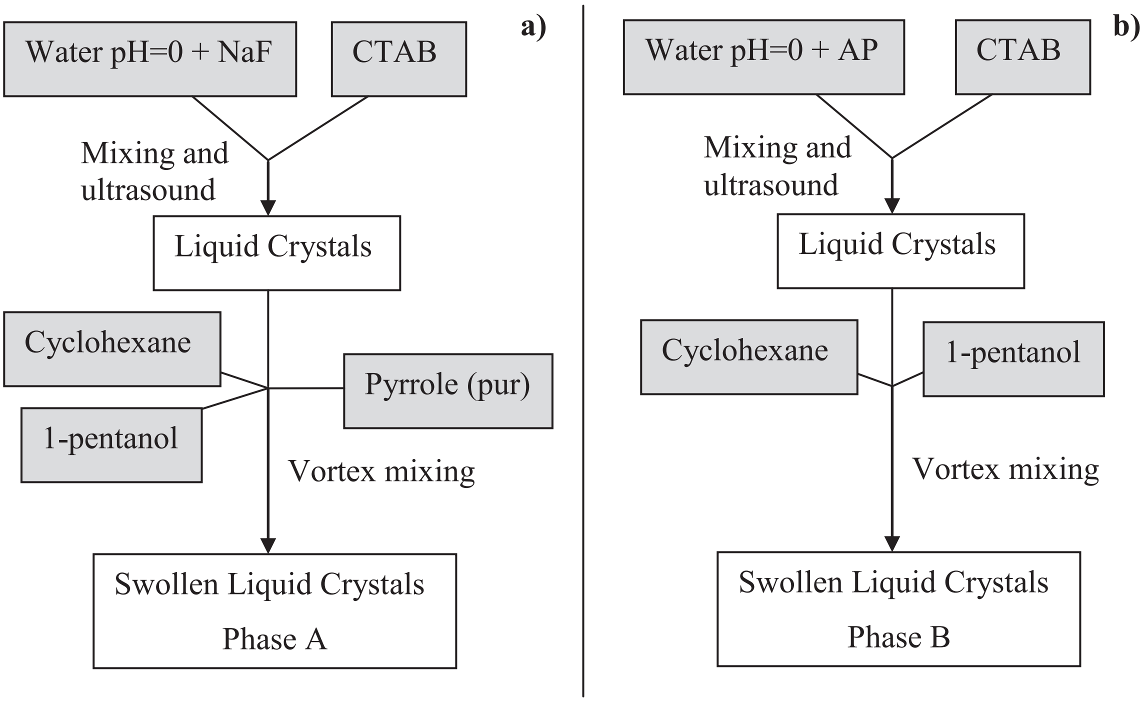

Figure 12. Experimental protocol for the preparation of the SLCs phases used for the polymerization reaction: a) the phase containing the monomer, and b) the phase containing the catalyst.

III.2. Preliminary results

III.2.1. Swollen Liquid Crystals stability

We investigated if the addition of Pyrrole within the SLCs structure leads to phase transitions. For this purpose, we performed SAXS analyses on sample prepared following the Phase A protocol, at different R ratio and we compared the results to the previous analysis (Figure 13).

We investigated samples with R = 0.5, 0.8, 1.45 and 1.8 as these values correspond to the middle of stability domains of the cubic, hexagonal, lamellar/sponge and sponge phases, respectively. As the stability domain of the lamellar phase is very narrow, we did not investigate this phase. From Figure 13, we observe that the insertion of Pyrrole within the structure does not modify the SLCs phase, and same structure as for the pure SLC, are obtained. In consequence, the phase diagram obtained in Part II can be used as reference for our study.

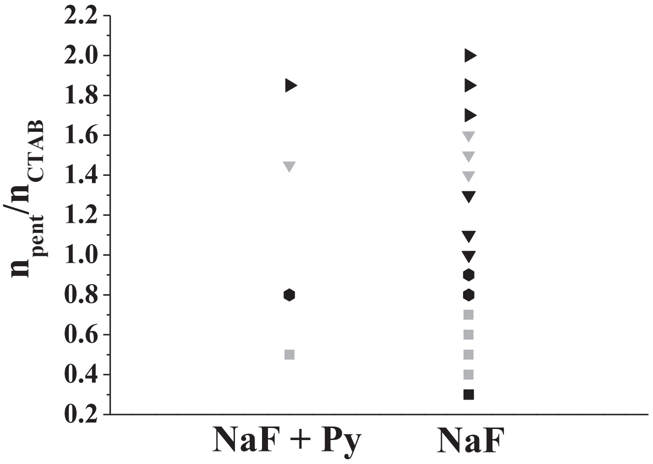

Figure 13. Comparaison of SLCs mesophase structure with R between the Phase A prepared with and without Pyrrole at [NaF]=0.2M: ■ cubic phase, ■ mixed cubic/hexagonal phase, ⬢ hexagonal phase, ▼ lamellar phase, ▼ mixed lamellar/sponge phase, and ▶ sponge phase.

III.2.2. Pyrrole polymerization

We carried out a first experiment to check that PPy nanosheets can be obtained by using SLCs sponge phase as a matrix for the polymerization reaction. Surprisingly, this first test showed different structures, depending on the age of pyrrole used (Figure 14). Indeed, an “aged” precursor (one year old opened flask) led to very opened and reticulated micrometric structures (Figure 14.b.) whereas the same experiment conducted with “fresh” precursor (new flask just received and opened before the reaction) led to dense monodispersed 100 nm nanoparticles (Figure 14.a.). With “fresh” Pyrrole, we obtained spherical PPy nanoparticles with a diameter about 100nm. However, with the “aged” Pyrrole monomer, we obtained larger particles within the micrometer range. In this case, we assumed that the Pyrrole already reacted in the bottle over the time and that the monomer was “pre-polymerized” before the experiment.

We notice that the structures obtained in the sponge phase are not lamellar as observed for synthesis in the hexagonal mesophase.[32] This can be explained by the difference of kinetics between the two reactions. As explained in part I, the hexagonal phase is very viscous, and the monomer polymerizes through the slow diffusion of pyrrole within the hexagonal phase containing the AP. Besides, the hexagonal phase being more rigid, applies a higher confinement effect, which reduces the particle growth along one axis. On the contrary, in the sponge phase, with “fresh” pyrrole, the diffusion kinetics is faster and the confinement matrix is more plastic, which allows a usual 3D nucleation and growth mechanism of spherical particles (Figure 14.c.). With the “aged” pyrrole, the existence of small chains of PPy before reaction, leads to polymerization between these oligomers, not between monomers, which results still in 3D objects, but with a more opened structure and larger size (Figure 14.d.). However, the formation of these 3D objects seems to be confined by the sponge-like structure, and their opened structure leads to 2D entities when coated on a substrate (Figure 14.b.).

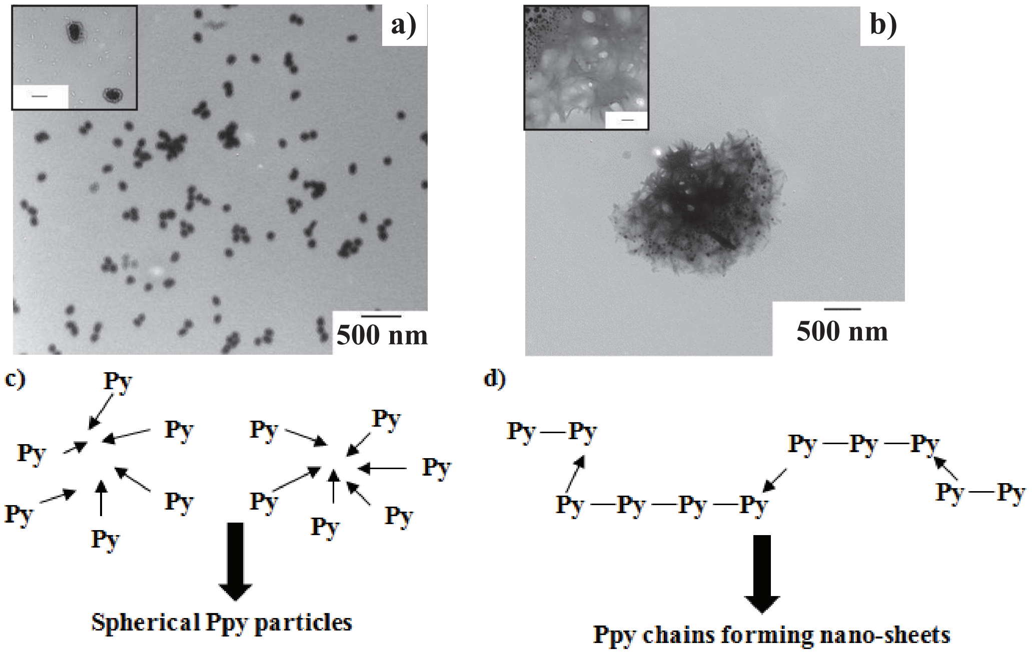

Figure 14. TEM images of PPy obtained through the polymerization reaction of the Py in SLCs sponge phase using a) a bottle opened right before the experiment b) a Py bottle opened for one year. The schemes c) and d) represent the proposed pathways for the low and the high purity cases, respectively.

From this preliminary experiment, we deduce that the high reaction kinetics due to the reaction in sponge phase (full polymerization in two days instead of several weeks), and higher plasticity of the phase, favors the formation of spherical objects during the polymerization reaction. However, it is still possible to obtain planar/anisotropic objects by using pre-polymerized PPy. We could not proceed further with these tests, but it would be interesting to perform a more detailed study on the relationship between the degree of polymerization of the starting oligomers and the morphology of the resulting PPy.

Conclusion

CTAB/salted water/Cyclohexane/1-pentanol quaternary systems form Swollen Liquid Crystals. In the first part of this report, we demonstrated that at a fixed CTAB and oil/water ratio, the amount of 1-pentanol determines the nature of the liquid crystalline phase. By increasing the amount of 1-pentanol, the crystalline phase switches successively from cubic to hexagonal, lamellar, and finally to sponge, with the existence of mixed phases domains in between the pure phase domains. The salt concentration and its nature have only a little influence on the size and the stability range of the phase domains. From this study, we also determined that due to its wide domain of stability and its bi-continuous structure, the sponge phase is a good candidate to replace the hexagonal phase for the PPy nanosheets polymerization.

However, in the second part, we demonstrated that the confinement applied by the sponge-like structure is not as drastic as that provided by the hexagonal phase, which results anyway in the synthesis of monodisperse 100 nm particles of PPy. We discovered inavertently that pre-polymerized PPy oligomers resulting from an aged chemical, gives opened nanostructures, which should be worth being studying by applying a more controlled way of this pre-polymerization.

Annex

Annex 5.1 : SAXS patterns

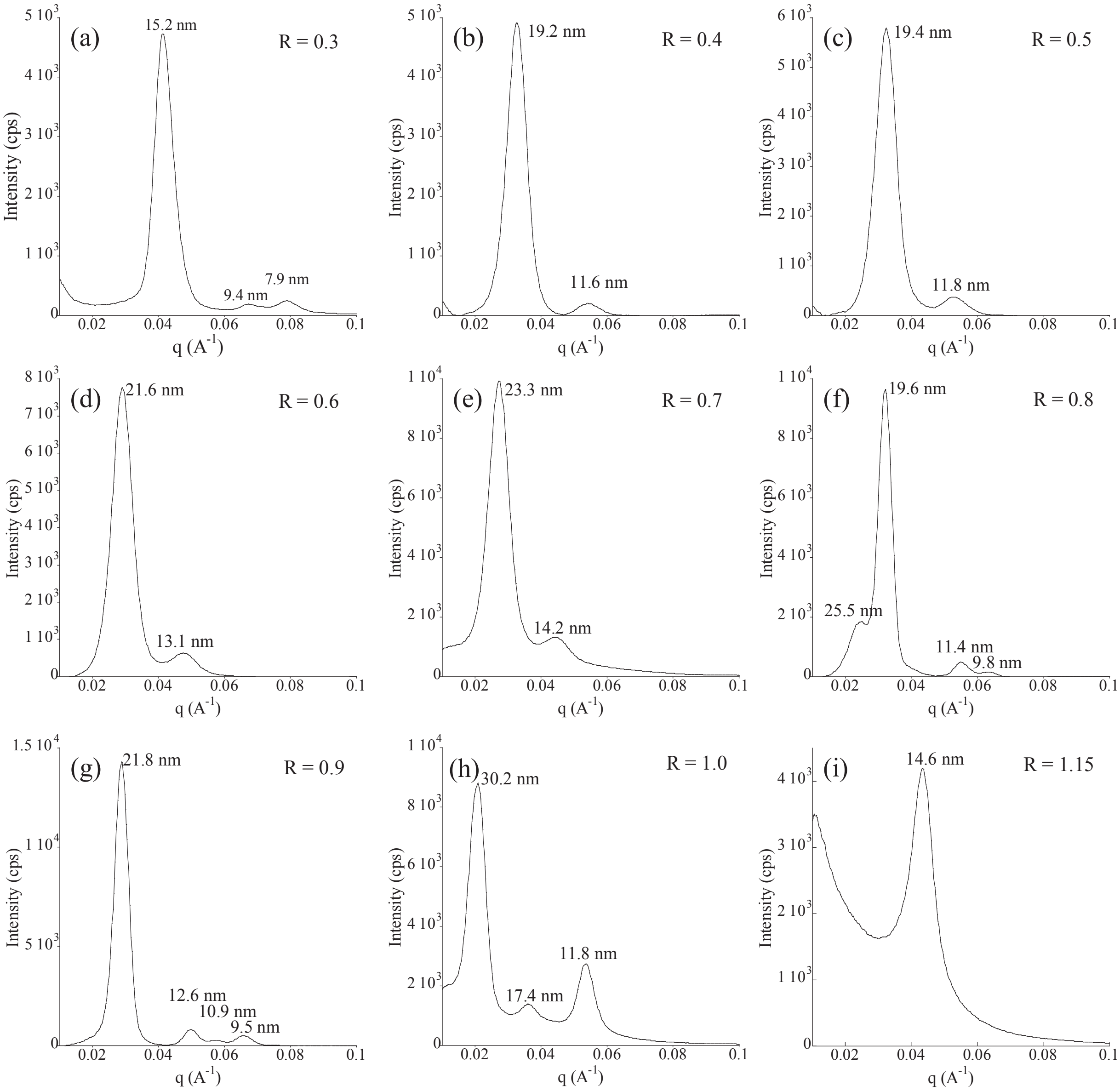

SAXS patterns evolution depending on the 1-pentanol over surfactant molar ratio (R) varying from 0.3 to 1.15, with $[AP]_{ions}$ set at 0.2M.

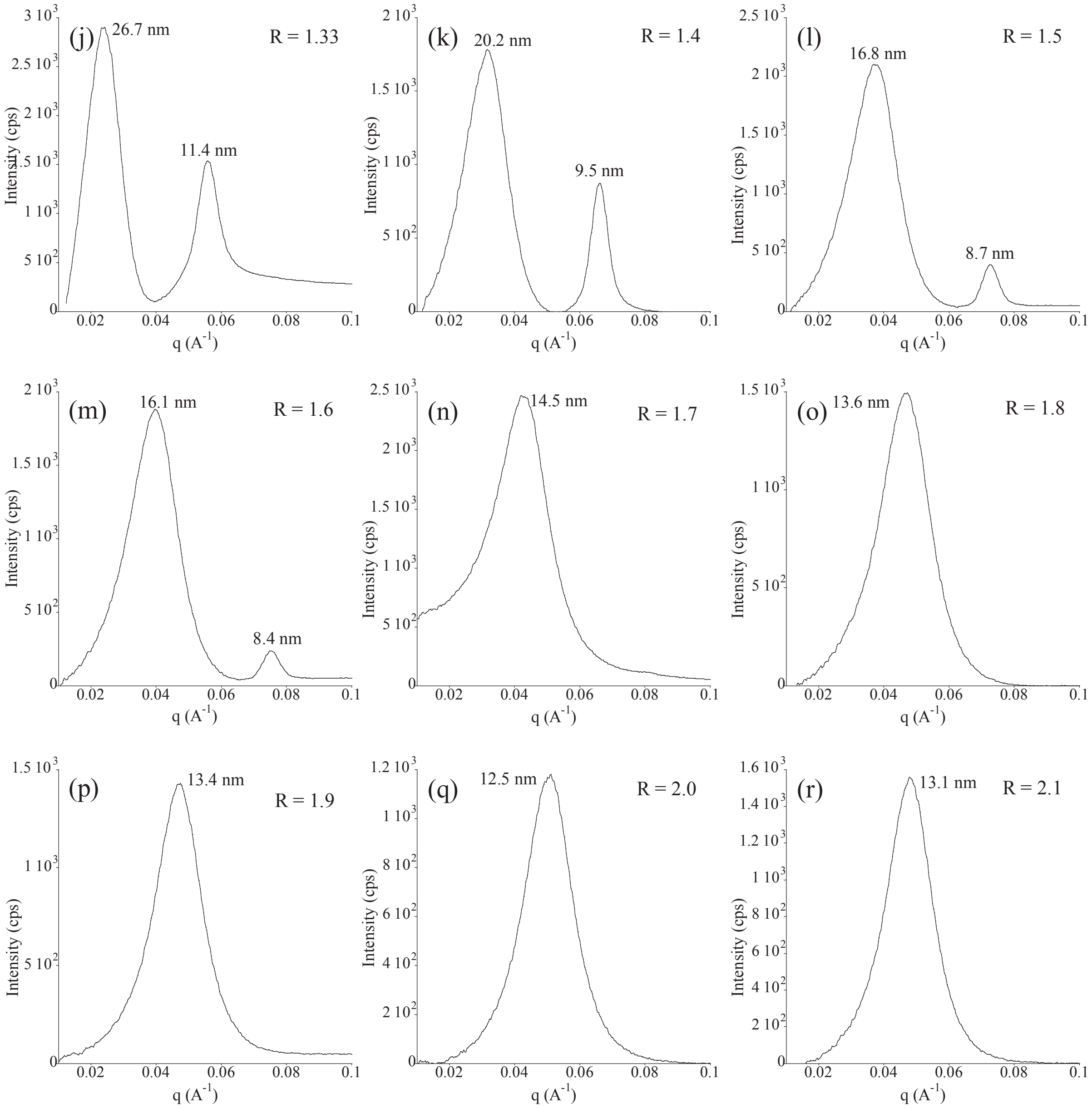

SAXS patterns evolution depending on the 1-pentanol over surfactant molar ratio (R) varying from 1.33 to 2.1, with $[AP]_{ions}$ set at 0.2M.

Annex 5.2: Porod representation of SAXS patterns

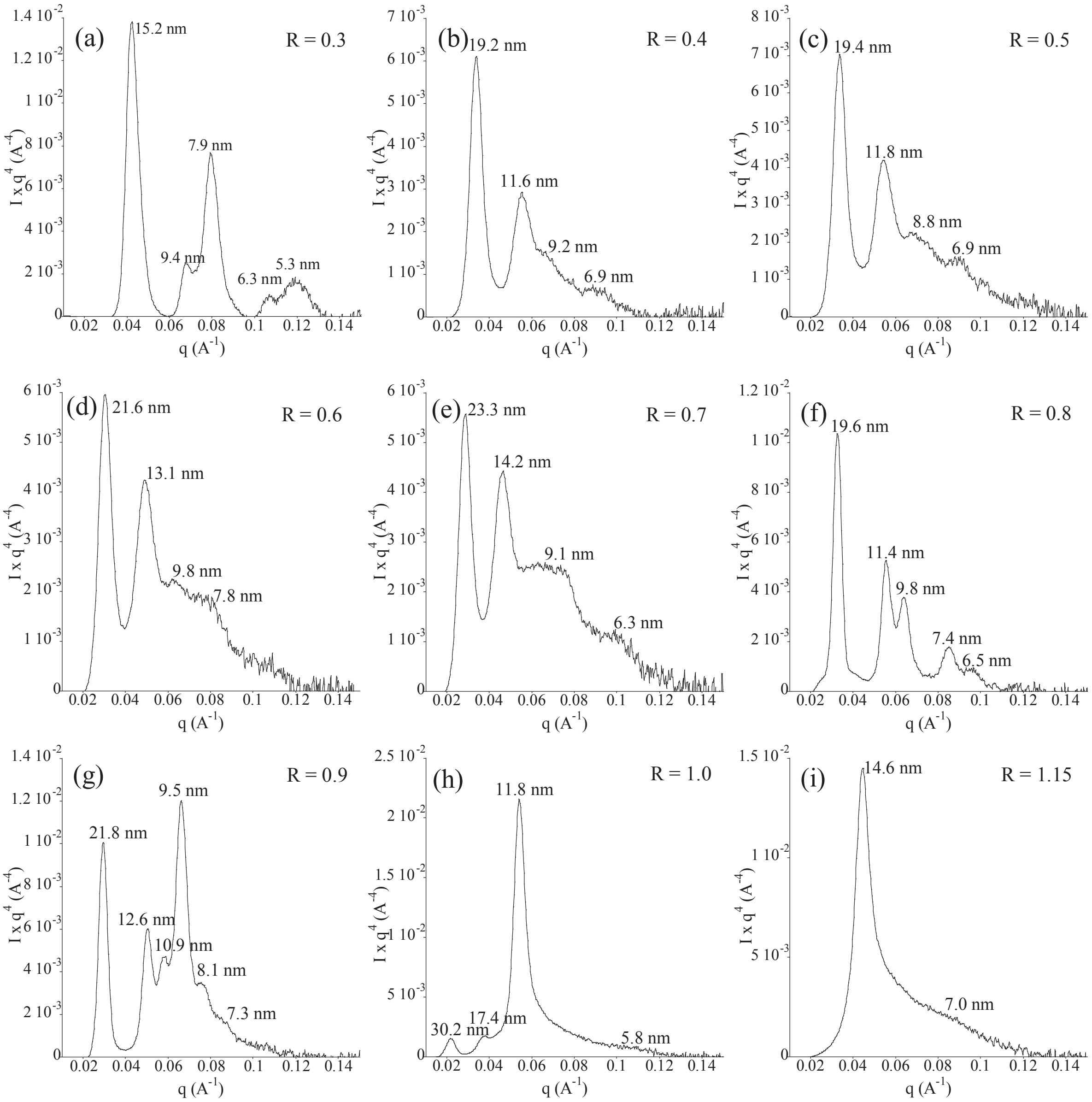

Porod representation of SAXS patterns evolution depending on the 1-pentanol over surfactant molar ratio (R) varying from 0.3 to 1.15, with $[AP]_{ions}$ set at 0.2M.

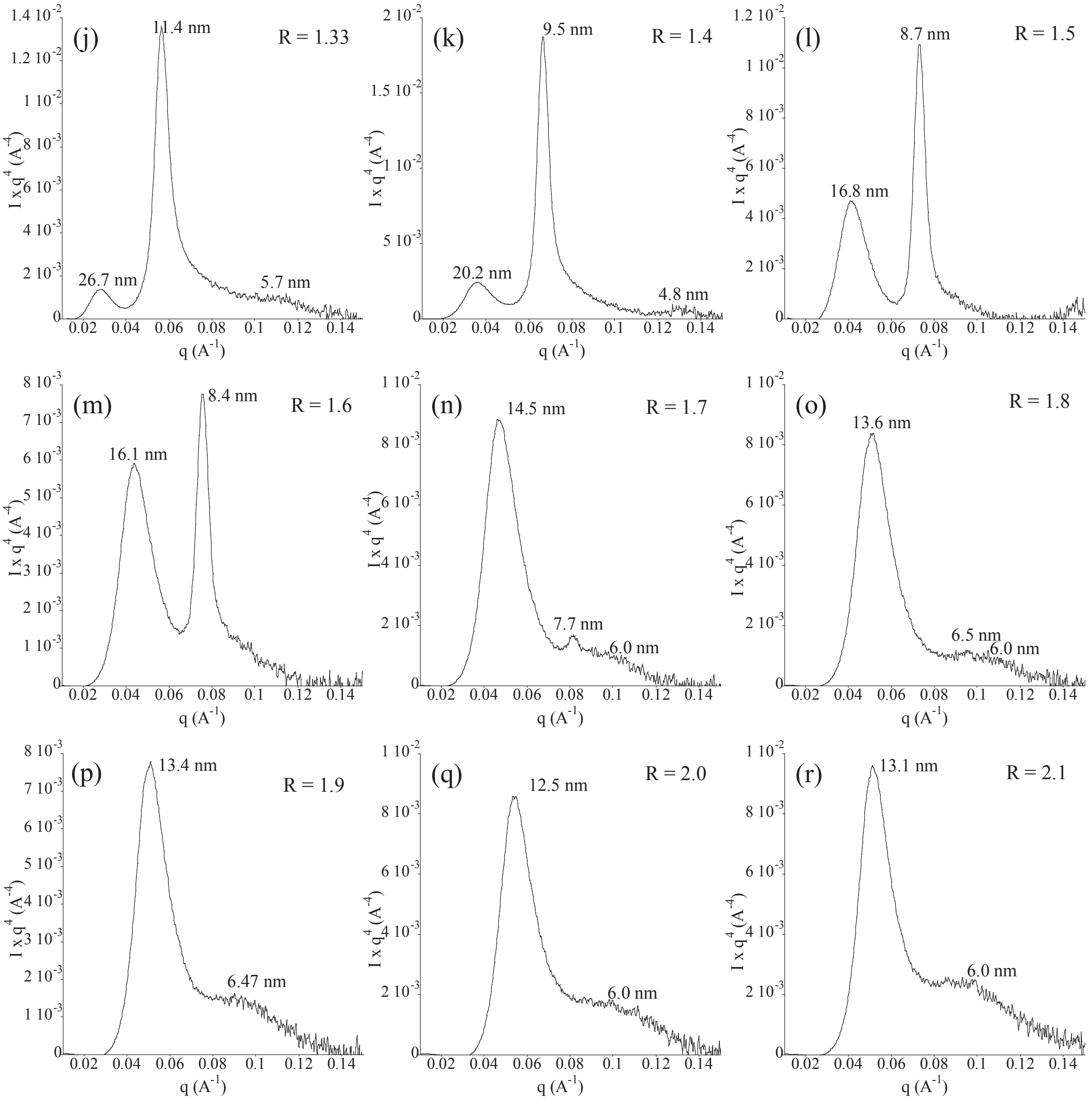

Porod representation of SAXS patterns evolution depending on the 1-pentanol over surfactant molar ratio (R) varying from 1.33 to 2.1, with $[AP]_{ions}$ set at 0.2M.

Annex 5.3: Optical microscopy under cross-polarized light

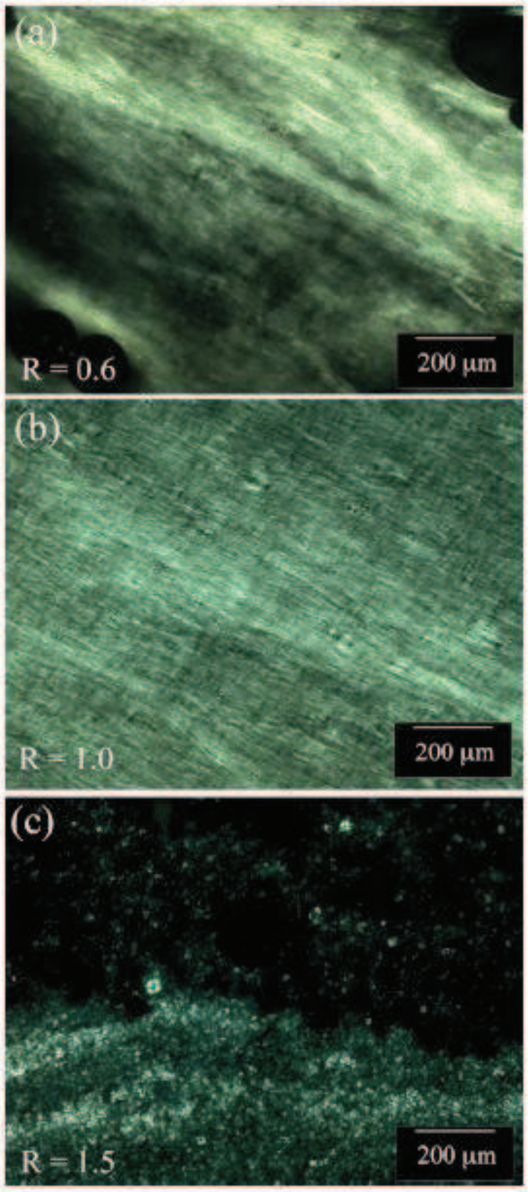

Optical microscopy under cross-polarized light of the SLCs made with $[AP]_{ions}$ = 0.3M: a) R=0.6, b) R=1.0, c) R=1.5.

General conclusion and perspectives

In this PhD project we synthesized functional materials using the transversal concept of *Integrative Chemistry*. For this purpose, we used the tools of the sol-gel and polymer chemistry, combined either with external macroscopic shaping modes such as extrusion, or intrinsic ones, such as swollen liquid crystals templates. The overall progression of this PhD project was iterative, where each new objective comprised a new parameter compared to the previous one. In this context, the first objective was to create an intrinsic interaction between the objects of a same material (photonic), the second one was to create an interaction between the objects of a material and its environment (photocatalysis), and the third one was to create an interaction between the material and the components of a whole system. The two first objectives are dedicated towards applications involving interactions between light and matter, and to their resulting benefits (photoluminescence, photocatalysis) and the third one toward conductive thin films application.

As it has been demonstrated that the material shape and architecture are as important as its composition, we first described the general context and the issues related to the synthesis of functional materials bearing hierarchical architectures. As we aimed to control the material architecture at all length scales, we presented first the strategies allowing controlling the shape of the particles at a nanoscopic and a microscropic length scale. These particles constituted in our study the nano-building block of our macroscopic material. Then, we discussed the existing shaping tools allowing the creation of mesoscopic and macroscopic architectures from these nano-building blocks.

As explained earlier, the first project aimed to create an interaction between the components of a same material. We decided to illustrate this concept by working on photoluminescent materials (zinc oxide (ZnO)) that we high scale organized in macroscopic fibers. For this project, we used the general "nano-manufacturing" concept based on integrative chemistry for the synthesis of ZnO/ polyvinyl alcohol (PVA) macroscopic fibers.[1] Here, thanks to the alignment of the ZnO nanorods, obtained by the post-synthesis stretching of the composite fiber, we obtained a synergy between the ZnO nanorods inside the macroscopic fiber. This synergy was responsible for the enhancement of the fibers mechanical properties. Also, we demonstrated that the alignment of a whole population of ZnO along the fibers main axis was responsible for an anisotropic photoluminescence behavior of the macroscopic fiber both in adsorption and emission. Until now, the only macroscopic structures bearing anisotropic photoluminescence properties existing are synthesized through more complex techniques, such as Chemical Vapor Deposition, for the formation of films composed of ZnO nanorods perpendicular to the substrate. The advantages of the process developed here are its low cost and the easy handling of these fibers after their synthesis. For example, we can imagine obtaining photoluminescent macroscopic films by weaving the fibers like an artificial grass. Also, thanks to their easy handling, the creation of new designs for switching devices can be investigated.

In a second project (third and fourth chapters), we introduced a new level of interaction, where the materials composing the fiber interacted with its environment (polluted air flux).

In the third chapter, we reported then the synthesis of titanium dioxide (TiO_2) macroscopic fibers bearing a hierarchical porosity, through an integrative multi-scale approach. First, we tested several syntheses of nanoparticles, one synthesis giving anisotropic TiO_2 nanoparticles, and two others giving isotropic particles where the surfactant used for the synthesis was changed. The type of surfactant used for the synthesis of the isotropic particles did not have any influence on the photocatalytic properties of the fibers. The only difference between the fibers generated using anisotropic or isotropic particles was the higher mineralization rate of the fibers containing anisotropic particles. However, as the structural parameters of the fibers were also different (surface roughness), it was difficult to conclude on the better mineralization of the anisotropic nanoparticles compared to the isotropic ones. On another hand, for the fibers generated with the isotropic particles, we studied the influence of their structural parameters on their photocatalytic properties, the structural parameters being adjusted by varying the formulation.[2] From these results, we demonstrated that the fibers presenting the highest surface roughness along with the smallest diameters gave the highest photocatalytic performances. Even though the performances could not compared with the commercial product (10 times less efficient than the commercial product), the main goal of this study was to explore how new synthetic paths – investigated in the third chapter – can help to improve the photocatalytic properties through a "*knowledge-based design of functional materials*" method, as defined by W. Jaegermann (TUD, Germany, personal communication) instead of a pure trial-and-error one. From this study, we learned that the proportion of TiO_2 compared to the PVA has to be limited to allow the generation of roughness and a reduction of the fiber diameter which appeared to be the two most important parameters in this study. As we could not conclude properly on the influence of the nanoparticles shape with this study, we decided to use isotropic particles for the improvement of the process as they are easier to synthesize.

With the clear identification of the meaningful parameters for photocatalysis application, we decided to investigate how to improve the processing methods for the generation of catalytic fibers, in order to increase the photocatalytic performances (Chapter 4). The first objective was to modify overall the fiber hierarchical shape by reducing their diameter, increasing the surface roughness and modifying their topology by inserting new macroscopic voids within the fiber structure. We decided then to investigate a new manufacturing protocol which involved a spinneret twice smaller than the one used in the previous study, and the addition of polymer beads inside the starting solution, in order to enhance both surface interaction and porosity. From this study, we showed that apart from the surface roughness and the fibers diameter, the surface topology is also of importance for enhancing the fibers photocatalytic properties. Despite a multiplication of the photocatalytic efficiency by 4, the fibers were still three times less efficient than the commercial product.

From these results, the next objective was to improve again the fibers efficiency while scaling up the spinning process. For this purpose, we adapted a semi-industrial process, which were already used for the synthesis of Carbon nanotubes/PVA fibers,[3] this process allowing reducing again the fibers diameter. We first demonstrated that it was possible to generate fibers of several hundred meters long continuously presenting a diameter 3 to 4 times lower that the ones generated in the first part of the Chapter 4. More importantly, these new fibers presented photocatalytic properties similar to the commercial product (Quartzel PCO from Saint-Gobain). Moreover, compared to the commercial product our fibers present the advantage to be exclusively composed of TiO_2, and are not supported by other media. However, as their mechanical resistance is quite low and that they are active only using Ultra-Violet (UV) light, it would be interesting to modify their composition to solve both problems. Also, the weaving of the fibers could solve the mechanical resistance problem.

The last step, which had from starting idea the multiscale integration of nanostructured functional materials within devices, was presented in the last chapter. This study was focused on the synthesis of polypyrrole (PPy) as it can be used both as electrolyte and as electrode. PPy was synthesized using Swollen Liquid Crystals (SLCs) as a nanoreactor used for the chemical polymerization of pyrrole.[4] First, the phase diagram of the SLCs was drawn, and it was concluded that the best candidate to perform the synthesis of PPy nanosheets was the sponge phase due to its bi-layer structure, its low viscosity, and its wide range of stability. Preliminary results showed that the pre-polymerization degree of the Pyrrole prior the catalyst insertion has an impact on the final PPy morphology. A more detailed analysis should be conducted to find the best pre-polymerization degree for the synthesis of PPy nanosheets. It could be interesting to test different techniques to obtain smooth thin films and to test them for their electrical properties. Also, in order to improve these properties, the PPy could be doped with carbon nanotubes. Finally, these films could be tested in DSSCs to compare their performances compared to the literature, and also in a new type of DSSCs where the liquid electrolyte could be replaced the PPy synthesized in this study.

Overall, this PhD project showed how the material architecture can influence its properties and more especially how it could induce an interaction either between the components of a same material, or between the material and its environment. In this project we have been attached to work on materials for sensing, air depollution, and flexible electrodes (photovoltaic) applications, which are all responding to an increasing economic, environmental and societal demand. In this context, we demonstrated how the *Integrative Chemistry* concept, which aims to bring together the tools from different disciplines, fosters the rational design of advanced functional materials.

References

Preface

(1) Mann, S.; Burkett, S. L.; Davis, S. A.; Fowler, C. E.; Mendelson, N. H.; Sims, S. D.; Walsh, D.; Whilton, N. T. *Chem. Mater.* **1997**, *9*, 2300–2310.

(2) Sanchez, C.; Arribart, H.; Guille, M. M. G. *Nat. Mater.* **2005**, *4*, 277–288.

(3) Backov, R. *Soft Matter* **2006**, *2*, 452.

(4) Whitesides, G. M.; Ismagilov, R. F. *Science (80-.).* **1999**, *284*, 89–92.

(5) Kinadjian, N.; Achard, M.; Julián-lópez, B.; Maugey, M.; Poulin, P.; Prouzet, E.; Backov, R. *Adv. Funct. Mater.* **2012**, *22*, 3994–4003.

(6) Kinadjian, N.; Le Bechec, M.; Pigot, T.; Dufour, F.; Durupthy, O.; Bentaleb, A.; Prouzet, E.; Lacombe, S.; Backov, R. *Eur. J. Inorg. Chem.* **2012**, 5350–5359.

(7) Kinadjian, N.; Nallet, F.; Ly, I.; Bentaleb, A.; Backov, R.; Prouzet, E. *J. Colloid Interface Sci.* **2013**, *submitted.*

Chapter 1

(1) Brun, N. *"Chimie intégrative pour la conception de matériaux poreux fonctionnels avancés et applications"*, Thèse, Université de Bordeaux 1, 2010.

(2) Leroy, C. *"Films mésoporeux de TiO_2 ou ZrO_2 dopés Eu^{III}"*, Thèse, Université de Bordeaux 1, 2009.

(3) Livage, J.; Sanchez, C.; Henry, M. *Prog. Solid St. Chem.* **1988**, *18*, 259–341.

(4) Livage, J. *Actual. Chim.* **1997**, 4–10.

(5) Brinker, C. J.; Scherer, G. W. *Sol-gel science : the physics and chemistry of sol-gel processing*; Academic Press: San Diego, 1990.

(6) Hench, L. L.; West, J. K. *Chem. Rev.* **1990**, *90*, 33–72.

(7) Jolivet, J. P. *De la solution à l'oxyde*; C.N.R.S. E.; E.D.P. Sciences: Paris, 1994.

(8) Zhao, Y.; Zhao, J.; Li, Y.; Ma, D.; Hou, S.; Li, L.; Hao, X.; Wang, Z. *Nanotechnology* **2011**, *22*, 115604.

(9) Sugimoto, T.; Okada, K.; Itoh, H. *J. Dispers. Sci. Technol.* **1998**, *19*, 143–161.

(10) Zeng, J.; Zheng, Y.; Rycenga, M.; Tao, J.; Li, Z.; Zhang, Q.; Zhu, Y.; Xia, Y. *J. Am. Chem. Soc.* **2010**, *132*, 8552–8553.

(11) Hu, H.; Deng, C.; Sun, M.; Zhang, K.; Yang, M. *Mater. Lett.* **2011**, *65*, 617–620.

(12) Chaudhari, N. S.; Bhirud, A. P.; Sonawane, R. S.; Nikam, L. K.; Warule, S. S.; Rane, V. H.; Kale, B. B. *Green Chem.* **2011**, *13*, 2500.

(13) Zhu, H.; Yang, D.; Zhang, H. *Inorg. Mater.* **2006**, *42*, 1210–1214.

(14) Rabenau, A. *Angew. Chemie Int. Ed. English* **1985**, *24*, 1026–1040.

(15) Szabó, M.; Pusztai, P.; Leino, A.-R.; Kordás, K.; Kónya, Z.; Kukovecz, Á. *J. Mol. Struct.* **2013**, *1044*, 99–103.

(16) Baghbanzadeh, M.; Carbone, L.; Cozzoli, P. D.; Kappe, C. O. *Angew. Chem. Int. Ed. Engl.* **2011**, *50*, 11312–11359.

(17) Dufour, F.; Cassaignon, S.; Durupthy, O.; Colbeau-Justin, C.; Chanéac, C. *Eur. J. Inorg. Chem.* **2012**, *2012*, 2707–2715.

(18) Hamedani, N. F.; Mahjoub, A. R.; Khodadadi, A. A.; Mortazavi, Y. *Sensors Actuators B Chem.* **2011**, *156*, 737–742.

(19) Kundu, S.; Peng, L.; Liang, H. *Inorg. Chem.* **2008**, *47*, 6344–6352.

(20) Hu, H.; Deng, C.; Yao, L. *Mater. Chem. Phys.* **2013**, *138*, 886–892.

(21) Banerjee, I.; Karmakar, S.; Kulkarni, N. V.; Nawale, A. B.; Mathe, V. L.; Das, A. K.; Bhoraskar, S. V. *J. Nanoparticle Res.* **2009**, *12*, 581–590.

(22) Li, L.; Ding, J.; Xue, J. *Chem. Mater.* **2009**, *21*, 3629–3637.

(23) Agrawal, M.; Pich, A.; Zafeiropoulos, N. E.; Stamm, M. *Colloid Polym. Sci.* **2008**, *286*, 593–601.

(24) Kimling, M. C.; Caruso, R. A. *J. Mater. Chem.* **2012**, *22*, 4073.

(25) Xu, Z.; Wang, Y. *J. Alloys Compd.* **2013**, *555*, 268–273.

(26) Mahmoud, M. A.; Narayanan, R.; El-Sayed, M. A. *Acc. Chem. Res.* **2013**, *46*, 1795–1805.

(27) Schwochow, F.; Puppe, L. *Angew. Chemie Int. Ed.* **1975**, *14*, 620–628.

(28) http://www.grace.com/EngineeredMaterials/MaterialSciences/Zeolites/ZeoliteStructure.aspx.

(29) Shao, G.; Yang, J.; Zhang, X.; Zhu, G.; Wang, J.; Liu, C. *Mater. Lett.* **2007**, *61*, 1443–1445.

(30) Sun, G.; Liu, Y.; Yang, J.; Wang, J. *J. Porous Mater.* **2010**, *18*, 465–473.

(31) Youn, H.-K.; Kim, J.; Chandrasekar, G.; Jin, H.; Ahn, W.-S. *Mater. Lett.* **2011**, *65*, 1772–1774.

(32) Valtchev, V.; Mintova, S. *Microporous Mesoporous Mater.* **2001**, *43*, 41–49.

(33) Fan, T.; Sun, B.; Gu, J.; Zhang, D.; Lau, L. W. M. *Scr. Mater.* **2005**, *53*, 893–897.

(34) Brochette, P. *Tech. l'Ingénieur* **1999**, *J 2150*.

(35) Israelachvili, J. N.; Mitchell, D. J.; Ninham, B. W. *J. Chem. Soc. Faraday Trans. II* **1976**, *72*, 1525–1568.

(36) Arditty, S.; Schmitt, V.; Giermanska-Kahn, J.; Leal-Calderon, F. *J. Colloid Interface Sci.* **2004**, *275*, 659–664.

(37) Schacht, S.; Huo, Q.; Voigt-Martin, I.; Stucky, G.; Schuth, F. *Science* **1996**, *273*, 768–771.

(38) Fornasieri, G.; Badaire, S.; Backov, R.; Mondain-Monval, O.; Zakri, C.; Poulin, P. *Adv. Mater.* **2004**, *16*, 1094–1097.

(39) Depardieu, M.; Nollet, M.; Destribats, M.; Schmitt, V.; Backov, R. *Part. Part. Syst. Charact.* **2013**, *30*, 185–192.

(40) Nie, Z.; Xu, S.; Seo, M.; Lewis, P. C.; Kumacheva, E. *J. Am. Chem. Soc.* **2005**, *127*, 8058–8063.

(41) Figueiredo Neto, A. M.; Salinas, S. *The Pysics of Lyotropic Liquid Crystals: Phase Transition and Structural properties*; Oxford University Press, Ed.; New York, 2005.

(42) Ramos, L.; Fabre, P. *Langmuir* **1997**, *13*, 682–686.

(43) http://en.wikipedia.org/wiki/Lyotropic_liquid_crystal.

(44) Pena dos Santos, E.; Tokumoto, M. S.; Surendran, G.; Remita, H.; Bourgaux, C.; Dieudonné, P.; Prouzet, E.; Ramos, L. *Langmuir* **2005**, *21*, 4362–4369.

(45) Surendran, G.; Apostolescu, G.; Tokumoto, M.; Prouzet, E.; Ramos, L.; Beaunier, P.; Kooyman, P. J.; Etcheberry, A.; Remita, H. *Small* **2005**, *10*, 964–967.

(46) Pena, E.; Santilli, C. V.; Pulcinelli, S. H.; Prouzet, E. **2004**, 4187–4192.

(47) Lee, D. U.; Pradhan, D.; Mouawia, R.; Oh, D. H.; Heinig, N. F.; Leung, K. T.; Prouzet, E. *Chem. Mater.* **2010**, *22*, 218–225.

(48) Davis, S. A.; Burkett, S. L.; Mendelson, N. H.; Mann, S. *Nature* **1997**, *385*, 420–423.

(49) Anderson, M. W.; Holmes, S. M.; Hanif, N.; Cundy, C. S. *Angew. Chem. Int. Ed. Engl.* **2000**, *39*, 2707–2710.

(50) Ogasawara, W.; Shenton, W.; Davis, S. A.; Mann, S. *Chem. Mater.* **2000**, *12*, 2835–2837.

(51) Dahmane, Y.; Cagnon, L.; Voiron, J.; Pairis, S.; Bacia, M.; Ortega, L.; Benbrahim, N.; Kadri, a. *J. Phys. D. Appl. Phys.* **2006**, *39*, 4523–4528.

(52) Gao, X.; Chen, J.; Yuan, C. *J. Power Sources* **2013**, *240*, 503–509.

(53) Rosen, J.; Hutchings, G. S.; Jiao, F. *J. Am. Chem. Soc.* **2013**, *135*, 4516–4521.

(54) Bagshaw, S. A.; Prouzet, E.; Pinnavaia, T. J.; Pinnavaiat, T. J. *Science* **1995**, *269*, 1242–1244.

(55) Yang, P.; Deng, T.; Zhao, D.; Feng, P.; Pine, D.; Chmelka, B.; Whitesides, G.; Stucky, G. *Science* **1998**, *282*, 2244–2246.

(56) Xue, C.; Wang, J.; Tu, B.; Zhao, D. *Chem. Mater.* **2010**, *22*, 494–503.

(57) Li, L.-L.; Duan, W.-T.; Yuan, Q.; Li, Z.-X.; Duan, H.-H.; Yan, C.-H. *Chem. Commun.* **2009**, 6174–6176.

(58) Kartini, I.; Menzies, D.; Blake, D.; Costa, C. D.; Meredith, P.; Riches, D.; Lu, G. Q. *J. Mater. Chem.* **2004**, *14*, 2917–2921.

(59) Zukalová, M.; Procházka, J.; Zukal, A.; Yum, J. H.; Kavan, L. *Inorganica Chim. Acta* **2008**, *361*, 656–662.

(60) Chi, B.; Zhao, L.; Li, J.; Pu, J.; Chen, Y.; Wu, C.; Jin, T. *J. Nanosci. Nanotechnol.* **2008**, *8*, 3877–3882.

(61) Dewalque, J.; Cloots, R.; Mathis, F.; Dubreuil, O.; Krins, N.; Henrist, C. *J. Mater. Chem.* **2011**, *21*, 7356.

(62) Dewalque, J.; Cloots, R.; Dubreuil, O.; Krins, N.; Vertruyen, B.; Henrist, C. *Thin Solid Films* **2012**, *520*, 5272–5276.

(63) Wei, M.; Konishi, Y.; Zhou, H.; Yanagida, M.; Sugihara, H.; Arakawa, H. *J. Mater. Chem.* **2006**, *16*, 1287.

(64) Wu, M.; Fujiu, T.; Messing, G. L. *J. Non. Cryst. Solids* **1990**, *121*, 407–412.

(65) Bagshaw, S. A. *Chem. Commun.* **1999**, 767–768.

(66) Suzuki, K.; Ikari, K.; Imai, H. *J. Mater. Chem.* **2003**, *13*, 1812.

(67) Livage, J. *Nature* **2002**, *416*, 702.

(68) Carn, F.; Steunou, N.; Livage, J.; Colin, A.; Backov, R. *Chem. Mater.* **2005**, *17*, 644–649.

(69) Carn, F. *"Intégration entre chimie douce et fluides complexes pour la genèse d ' architectures poreuses hiérarchisées : synthèses , caractérisations et application"*, Thèse, Université de Bordeaux 1, 2006.

(70) Cooper, A. I. *J. Mater. Chem.* **2000**, *10*, 207–234.

(71) Goel, S. K.; Beckman, E. J. *Polym. Eng. Sci.* **1994**, *34*, 1137–1147.

(72) Parks, K. L.; Beckman, E. J. *Polym. Eng. Sci.* **1996**, *36*, 2404–2416.

(73) Goel, S. K.; Beckman, E. J. *Polymer (Guildf).* **1993**, *34*, 1410–1417.

(74) Park, C. B.; Behravesh, A. H.; Venter, R. D. *Polym. Eng. Sci.* **1998**, *38*, 1812–1823.

(75) Lissant, K. J.; Mayhan, K. G. *J. Colloid Interface Sci.* **1973**, *42*, 201–208.

(76) Backov, R. *Actual. Chim.* **2013**, *373*.

(77) Barby, D.; Haq, Z. *"Low density porous cross-linked polymeric materials and their preparation and use as carriers for included liquids."* Patent n° 0060138, 1982.

(78) Araya, A. *"Hydrophobic, highly porous, three-dimensional inorganic structures."* Patent n° 4888309, 1989.

(79) Carn, F.; Colin, A.; Achard, M.-F.; Deleuze, H.; Saadi, Z.; Backov, R. *Adv. Mater.* **2004**, *16*, 140–144.

(80) Ungureanu, S.; Birot, M.; Laurent, G.; Babot, O.; Julia, B.; Achard, M.; Popa, M. I. *Chem. Mater.* **2007**, *19*, 5786–5796.

(81) Ungureanu, S.; Deleuze, H.; Sanchez, C.; Popa, M. I.; Backov, R. *Chem. Mater.* **2008**, *20*, 6494–6500.

(82) Brun, N.; Janot, R.; Sanchez, C.; Deleuze, H.; Gervais, C.; Morcrette, M.; Backov, R. *Energy Environ. Sci.* **2010**, *3*, 824.

(83) Brun, N.; Ungureanu, S.; Deleuze, H.; Backov, R. *Chem. Soc. Rev.* **2011**, *40*, 771–788.

(84) Brinker, C. J.; Lu, Y.; Sellinger, A.; Fan, H. *Adv. Mater.* **1999**, *11*, 579–585.

(85) Denkov, N.; Velev, O.; Kralchevsky, P. *Nature* **1993**, *361*, 26.

(86) Dimitrov, A. S.; Nagayama, K. *Langmuir* **1996**, *12*, 1303–1311.

(87) Jiang, P.; Bertone, J. F.; Hwang, K. S.; Colvin, V. L. *Chem. Mater.* **1999**, *11*, 2132–2140.

(88) http://link.springer.com/chapter/10.1007/978-0-387-88953-5_10.

(89) Howatt, G. N.; Breckenridge, R. G.; Brownlow, J. M. *J. Am. Ceram. Soc.* **1947**, *30*, 237–242.

(90) Hotza, D.; Greil, P. *Mater. Sci. Eng. A* **1995**, *202*, 206–217.

(91) Hall, D. B.; Underhill, P.; Torkelson, J. M. *Polym. Eng. Sci.* **1998**, *38*, 2039–2045.

(92) http://socrates.berkeley.edu/~scotch/innovation/inventing_injet.htm.

(93) http://www.sijtechnology.com/en/super_fine_inkjet/index.html#ac01.

(94) Kang, B.; Lee, W. H.; Cho, K. *ACS Appl. Mater. Interfaces* **2013**, *5*, 2302–2315.

(95) Du, J.; Lai, X.; Halpert, J. E.; Yang, Y.; Wang, D. *Sci. China Chem.* **2011**, *54*, 930–935.

(96) Kuo, C.-Y.; Lu, S.-Y. *Nanotechnology* **2008**, *19*, 095705.

(97) Seo, Y. G.; Woo, K.; Kim, J.; Lee, H.; Lee, W. *Adv. Funct. Mater.* **2011**, *21*, 3094–3103.

(98) Desai, U. V; Xu, C.; Wu, J.; Gao, D. *Nanotechnology* **2012**, *23*, 205401.

(99) Wu, J.-J.; Chen, G.-R.; Yang, H.-H.; Ku, C.-H.; Lai, J.-Y. *Appl. Phys. Lett.* **2007**, *90*, 213109.

(100) Ku, C.-H.; Wu, J.-J. *Appl. Phys. Lett.* **2007**, *91*, 093117.

(101) Langmuir, I. *J. Am. Chem. Soc.* **1917**, *39*.

---

(102) Blodgett, K. *J. Am. Chem. Soc.* **1934**.

(103) Blodgett, K. *J. Am. Chem. Soc.* **1935**, *57*, 1007–1022.

(104) Colson, P.; Henrist, C.; Cloots, R. *J. Nanomater.* **2013**, *2013*, 1–19.

(105) Griffete, N.; Frederich, H.; Maître, A.; Ravaine, S.; Chehimi, M. M.; Mangeney, C. *Langmuir* **2012**, *28*, 1005–1012.

(106) Pierson, H. O. *Handbook of Chemical Vapor Deposition (CVD)*; William Andrew, 1999.

(107) Mukherjee, B.; Varghese, B.; Zheng, M.; Karthik, K. R. G.; Mathews, N.; Mhaisalkar, S. G.; Tok, E. S.; Sow, C. H. *J. Cryst. Growth* **2012**, *346*, 32–39.

(108) Rajabi, M.; Dariani, R. S.; Iraji zad, a. *Mater. Sci. Semicond. Process.* **2013**, *16*, 171–178.

(109) Li, D.; Xia, Y. *Adv. Mater.* **2004**, *16*, 1151–1170.

(110) Jin, L.; Zhai, J.; Heng, L.; Wei, T.; Wen, L.; Jiang, L.; Zhao, X.; Zhang, X. *J. Photochem. Photobiol. C Photochem. Rev.* **2009**, *10*, 149–158.

(111) Chiu, C.-W.; Lin, C.-A.; Hong, P.-D. *J. Polym. Res.* **2010**, *18*, 367–372.

(112) Vigolo, B.; Pénicaud, A.; Coulon, C.; Sauder, C.; Pailler, R.; Journet, C.; Bernier, P.; Poulin, P. *Science* **2000**, *290*, 1331–1334.

(113) Biette, L.; Carn, F.; Maugey, M.; Achard, M.-F.; Maquet, J.; Steunou, N.; Livage, J.; Serier, H.; Backov, R. *Adv. Mater.* **2005**, *17*, 2970–2974.

(114) Serier, H.; Achard, M.-F.; Babot, O.; Steunou, N.; Maquet, J.; Livage, J.; Leroy, C. M.; Backov, R. *Adv. Funct. Mater.* **2006**, *16*, 1745–1753.

(115) Sakurada, I. *Polyvinyl Alcohol Fibres*; International Fiber Science and Technology, Ed.; M. Dekker.; New York, 1985; p. vol. 6.

(116) Mercader, C.; Denis-Lutard, V.; Jestin, S.; Maugey, M.; Derre, A.; Poulin, P. *J. Appl. Polym. Sci.* **2012**, *125*, 191–196.

(117) Yacobi, B. G. *Semiconductor Materials*; Kluwer Academic: New York, Boston, Dordrecht, London, Moscow, 2004.

(118) http://www.sparknotes.com/chemistry/bonding/molecularorbital/section1.rhtml.

(119) http://depts.washington.edu/chemcrs/bulkdisk/chem312A_sum05/handout_Transition_Metals_A.pdf.

Chapter 2

(1) Lopez, E.; Rousseau, M.; Bourrat, X. *Biofutur* **2008**, *291*, 53–56.

(2) Klingshirn, C.; Meyer, B.; Waag, A.; Axel, H.; Geurts, J. *Zinc Oxide*; Springer: Verlag Berlin Heildeberg, 2010.

(3) Smith, K. K. *Thin Solid Films* **1981**, *84*, 171–182.

(4) Willander, M.; Nur, O.; Sadaf, J. R.; Qadir, M. I.; Zaman, S.; Zainelabdin, A.; Bano, N.; Hussain, I. *Materials (Basel).* **2010**, *3*, 2643–2667.

(5) Dean, P. J. *Prog. Cryst. Growth Charact. Mater.* **1982**, *5*, 89–174.

(6) Djurisić, A. B.; Leung, Y. H. *Small* **2006**, *2*, 944–961.

(7) Fallert, J.; Hauschild, R.; Stelzl, F.; Urban, A.; Wissinger, M.; Zhou, H.; Klingshirn, C.; Kalt, H. *J. Appl. Phys.* **2007**, *101*, 073506.

(8) Zhang, Y. Z.; He, H. P.; Jin, Y. Z.; Zhao, B. H.; Ye, Z. Z.; Tang, H. P. *J. Appl. Phys.* **2008**, *104*, 103529.

(9) Schneider, L.; Zaitsev, S. V.; Bacher, G.; Jin, W.; Winterer, M. *J. Appl. Phys.* **2007**, *102*, 023524.

(10) Schirra, M.; Schneider, R.; Reiser, a.; Prinz, G. M.; Feneberg, M.; Biskupek, J.; Kaiser, U.; Krill, C. E.; Thonke, K.; Sauer, R. *Phys. Rev. B* **2008**, *77*, 125215.

(11) Janotti, A.; Van de Walle, C. G. *Reports Prog. Phys.* **2009**, *72*, 126501.

(12) He, H.; Yang, Q.; Liu, C.; Sun, L.; Ye, Z. *J. Phys. Chem. C* **2011**, *115*, 58–64.

(13) Vigolo, B.; Pénicaud, A.; Coulon, C.; Sauder, C.; Pailler, R.; Journet, C.; Bernier, P.; Poulin, P. *Science* **2000**, *290*, 1331–1334.

(14) Miaudet, P.; Badaire, S.; Maugey, M.; Derré, a; Pichot, V.; Launois, P.; Poulin, P.; Zakri, C. *Nano Lett.* **2005**, *5*, 2212–2215.

(15) Badaire, S.; Pichot, V.; Zakri, C.; Poulin, P.; Launois, P.; Vavro, J.; Guthy, C.; Chen, M.; Fischer, J. E. *J. Appl. Phys.* **2004**, *96*, 7509.

(16) Biette, L.; Carn, F.; Maugey, M.; Achard, M.-F.; Maquet, J.; Steunou, N.; Livage, J.; Serier, H.; Backov, R. *Adv. Mater.* **2005**, *17*, 2970–2974.

(17) Serier, H.; Achard, M.-F.; Babot, O.; Steunou, N.; Maquet, J.; Livage, J.; Leroy, C. M.; Backov, R. *Adv. Funct. Mater.* **2006**, *16*, 1745–1753.

(18) Dexmer, J.; Leroy, C. M.; Binet, L.; Heresanu, V.; Launois, P.; Steunou, N.; Coulon, C.; Maquet, J.; Brun, N.; Livage, J.; Backov, R. *Chem. Mater.* **2008**, *20*, 5541–5549.

(19) Leroy, M.; Achard, M.; Babot, O.; Steunou, N.; Masse, P.; Livage, J.; Binet, L.; Brun, N.; Backov, R. *Chem. Mater.* **2007**, *19*, 3988–3999.

(20) Wang, Z. L. *Mater. Today* **2004**, 26–33.

(21) Huang, M. H.; Mao, S.; Feick, H.; Yan, H.; Wu, Y.; Kind, H.; Weber, E.; Russo, R.; Yang, P. *Science* **2001**, *292*, 1897–1899.

(22) Umar, A.; Ra, H.; Jeong, J.; Suh, E.; Hahn, Y. *Korean J. Chem. Eng.* **2006**, *23*, 499–501.

(23) Umar, A.; Kim, S. H.; Lee, Y.-S.; Nahm, K. S.; Hahn, Y. B. *J. Cryst. Growth* **2005**, *282*, 131–136.

(24) Hughes, W. L.; Wang, Z. L. *Appl. Phys. Lett.* **2003**, *82*, 2886.

(25) Zhang, B. P.; Binh, N. T.; Wakatsuki, K.; Segawa, Y.; Yamada, Y.; Usami, N.; Kawasaki, M.; Koinuma, H. *Appl. Phys. Lett.* **2004**, *84*, 4098.

(26) Shen, G. Z.; Bando, Y.; Liu, B. D.; Golberg, D.; Lee, C.-J. *Adv. Funct. Mater.* **2006**, *16*, 410–416.

(27) Dietz, R. E.; Hopfield, J. J.; Thomas, D. G. *J. Appl. Phys.* **1961**, *32*, 2282.

(28) Mizukoshi, A.; Ozawa, J.; Shirakawa, S.; Nakano, K. *IEEE Trans. Power Appar. Syst.* **1983**, *PAS-102*.

(29) Fichou, D.; Kossanyi, J. *J. Electrochem. Soc.* **1986**, *133*, 1607–1616.

(30) Baskoutas, S.; Bester, G. *J. Phys. Chem. A* **2011**, *115*, 15862–15867.

(31) Chien, C.-T.; Wu, M.-C.; Chen, C.-W.; Yang, H.-H.; Wu, J.-J.; Su, W.-F.; Lin, C.-S.; Chen, Y.-F. *Appl. Phys. Lett.* **2008**, *92*, 223102.

(32) Zhu, H.; Yang, D.; Zhang, H. *Inorg. Mater.* **2006**, *42*, 1210–1214.

(33) Mitra, S. S.; Bryant, J. I. *J. Phys.* **1965**, *26*.

(34) Calleja, J. M.; Cardona, M. *Phys. Rev. B* **1977**, *16*, 3753–3761.

(35) Umar, A.; Kim, S. H.; Kim, J. H.; Park, Y. K.; Hahn, Y. B. *Mater. Lett.* **2007**, *61*, 4954–4958.

(36) Li, C.; Hong, G.; Wang, P.; Yu, D.; Qi, L. *Chem. Mater.* **2009**, *21*, 891–897.

(37) Decremps, F.; Pellicer-Porres, J.; Saitta, A.; Chervin, J.-C.; Polian, A. *Phys. Rev. B* **2002**, *65*, 092101.

(38) Wang, X.; Huo, K.; Zhang, F.; Hu, Z.; Chu, P. K.; Tao, H.; Wu, Q.; Hu, Y.; Zhu, J. *J. Phys. Chem. C* **2009**, *113*, 170–173.

(39) Chawla, S.; Karar, N.; Chander, H. *Phys. B Condens. Matter* **2010**, *405*, 198–203.

(40) Johnson, J. C.; Yan, H.; Yang, P.; Saykally, R. J. *J. Phys. Chem. B* **2003**, *107*, 8816–8828.

(41) Wang, X.; Summers, C. J.; Wang, Z. L. *Nano Lett.* **2004**, *4*, 423–426.

(42) Ho, C.-H.; Li, J.-S.; Chen, Y.-J.; Wu, C.-C.; Huang, Y.-S.; Tiong, K.-K. *J. Alloys Compd.* **2009**, *480*, 50–53.

(43) Kinadjian, N.; Achard, M.; Julián-lópez, B.; Maugey, M.; Poulin, P.; Prouzet, E.; Backov, R. *Adv. Funct. Mater.* **2012**, *22*, 3994–4003.

Chapter 3

(1) Kinadjian, N.; Le Bechec, M.; Pigot, T.; Dufour, F.; Durupthy, O.; Bentaleb, A.; Prouzet, E.; Lacombe, S.; Backov, R. *Eur. J. Inorg. Chem.* **2012**, 5350–5359.

(2) Landmann, M.; Rauls, E.; Schmidt, W. G. *J. Phys. Condens. Matter* **2012**, *24*, 195503.

(3) Nie, X.; Zhuo, S.; Maeng, G.; Sohlberg, K. *Int. J. Photoenergy* **2009**, *2009*, 1–22.

(4) Mo, S.; Ching, W. *Phys. Rev. B. Condens. Matter* **1995**, *51*, 13023–13032.

(5) Zhang, H.; Banfield, J. F. *J. Phys. Chem. B* **2000**, *120*, 3481–3487.

(6) Shklover, V.; Nazeeruddin, M.; Zakeeruddin, S. M.; Barbé, C.; Kay, A.; Haibach, T.; Steurer, W.; Hermann, R.; Nissen, H.; Gratzel, M. *Chem. Mater.* **1997**, *9*, 430–439.

(7) Burnside, S. D.; Shklover, V.; Barbé, C.; Comte, P.; Arendse, F.; Brooks, K.; Gratzel, M. *Chem. Mater.* **1998**, *10*, 2419–2425.

(8) Magne, C.; Dufour, F.; Labat, F.; Lancel, G.; Durupthy, O.; Cassaignon, S.; Pauporté, T. *J. Photochem. Photobiol. A Chem.* **2012**, *232*, 22–31.

(9) Berger, T.; Sterrer, M.; Diwald, O.; Knözinger, E. *Chemphyschem* **2005**, *6*, 2104–2112.

(10) Fujishima, A.; Zhang, X.; Tryk, D. *Surf. Sci. Rep.* **2008**, *63*, 515–582.

(11) Hoffmann, M. R.; Martin, S. T.; Choi, W.; Bahnemannt, D. W. *Chem. Rev.* **1995**, *95*, 69–96.

(12) Coronado, J. M.; Kataoka, S.; Tejedor-Tejedor, I.; Anderson, M. A. *J. Catal.* **2003**, *219*, 219–230.

(13) Kasuga, B. T.; Hiramatsu, M.; Hoson, A.; Sekino, T.; Niihara, K. *Adv. Mater.* **1999**, *11*, 1307–1311.

(14) Liu, S. M.; Gan, L. M.; Liu, L. H.; Zhang, W. D.; Zeng, H. C. *Chem. Mater.* **2002**, *14*, 1391–1397.

(15) Zhang, L.; Yu, J. C. *Chem. Commun.* **2003**, 2078–2079.

(16) Shibata, H.; Ogura, T.; Mukai, T.; Ohkubo, T.; Sakai, H.; Abe, M. *J. Am. Chem. Soc.* **2005**, *127*, 16396–16397.

(17) Yuan, Z.; Ren, T.; Vantomme, A.; Su, B.-L. *Chem. Mater.* **2004**, 5096–5106.

(18) On, D. T. *Langmuir* **1999**, *15*, 8561–8564.

(19) Antonelli, D. M. *Microporous Mesoporous Mater.* **1999**, *30*, 315–319.

(20) Yun, H.; Miyazawa, K.; Zhou, H.; Honma, I.; Kuwabara, M. *Adv. Mater.* **2001**, *13*, 1377–1380.

(21) Yuan, Z.-Y.; Ren, T.-Z.; Su, B.-L. *Adv. Mater.* **2003**, *15*, 1462–1465.

(22) Luo, H.; Wang, C.; Yan, Y. *Chem. Mater.* **2003**, *15*, 3841–3846.

(23) Zhou, Y.; Antonietti, M. *J. Am. Chem. Soc.* **2003**, *125*, 14960–14961.

(24) Blin, J.-L.; Léonard, A.; Yuan, Z.-Y.; Gigot, L.; Vantomme, A.; Cheetham, A. K.; Su, B.-L. *Angew. Chem. Int. Ed. Engl.* **2003**, *42*, 2872–2875.

(25) Coakley, K. M.; Liu, Y.; McGehee, M. D.; Frindell, K. L.; Stucky, G. D. *Adv. Funct. Mater.* **2003**, *13*, 301–306.

(26) Antonelli, D. M.; Ying, J. Y. *Angew. Chemie Int. Ed.* **1995**, *34*, 2014–2017.

(27) Wang, K.; Yao, B.; Morris, M. A.; Holmes, J. D. *Chem. Mater.* **2005**, *17*, 4825–4831.

(28) Kirsch, B. L.; Richman, E. K.; Riley, A. E.; Tolbert, S. H. *J. Phys. Chem. B* **2004**, *108*, 12698–12706.

(29) Madhugiri, S.; Sun, B.; Smirniotis, P. G.; Ferraris, J. P.; Balkus, K. J. *Microporous Mesoporous Mater.* **2004**, *69*, 77–83.

(30) Li, D.; Xia, Y. *Nano Lett.* **2003**, *3*, 555–560.

(31) Nuansing, W.; Ninmuang, S.; Jarernboon, W.; Maensiri, S.; Seraphin, S. *Mater. Sci. Eng. B* **2006**, *131*, 147–155.

(32) Liu, Z.; Sun, D. D.; Guo, P.; Leckie, J. O. *Nano Lett.* **2007**, *7*, 1081–1085.

(33) Zhang, Y. X.; Li, G. H.; Jin, Y. X.; Zhang, Y.; Zhang, J.; Zhang, L. D. *Chem. Phys. Lett.* **2002**, *365*, 300–304.

(34) Caruso, R. A.; Schattka, J. H.; Greiner, A. *Adv. Mater.* **2001**, *13*, 1577–1579.

(35) Lei, Y.; Zhang, L. D.; Meng, G. W.; Li, G. H.; Zhang, X. Y.; Liang, C. H.; Chen, W.; Wang, S. X. *Appl. Phys. Lett.* **2001**, *78*, 1125.

(36) Xiang, B.; Zhang, Y.; Wang, Z.; Luo, X. H.; Zhu, Y. W.; Zhang, H. Z.; Yu, D. P. *J. Phys. D. Appl. Phys.* **2005**, *38*, 1152–1155.

(37) Backov, R. *Soft Matter* **2006**, *2*, 452.

(38) Prouzet, E.; Khani, Z.; Bertrand, M.; Tokumoto, M.; Guyot-Ferreol, V.; Tranchant, J.-F. *Microporous Mesoporous Mater.* **2006**, *96*, 369–375.

(39) Prouzet, E.; Ravaine, S.; Sanchez, C.; Backov, R. *New J. Chem.* **2008**, *32*, 1284.

(40) Brun, N.; Ungureanu, S.; Deleuze, H.; Backov, R. *Chem. Soc. Rev.* **2011**, *40*, 771–788.

(41) Nicole, L.; Rozes, L.; Sanchez, C. *Adv. Mater.* **2010**, *22*, 3208–3214.

(42) Vigolo, B.; Pénicaud, A.; Coulon, C.; Sauder, C.; Pailler, R.; Journet, C.; Bernier, P.; Poulin, P. *Science (80-.).* **2000**, *290*, 1331–1334.

(43) Biette, L.; Carn, F.; Maugey, M.; Achard, M.-F.; Maquet, J.; Steunou, N.; Livage, J.; Serier, H.; Backov, R. *Adv. Mater.* **2005**, *17*, 2970–2974.

(44) Serier, H.; Achard, M.-F.; Babot, O.; Steunou, N.; Maquet, J.; Livage, J.; Leroy, C. M.; Backov, R. *Adv. Funct. Mater.* **2006**, *16*, 1745–1753.

(45) Dexmer, J.; Leroy, C. M.; Binet, L.; Heresanu, V.; Launois, P.; Steunou, N.; Coulon, C.; Maquet, J.; Brun, N.; Livage, J.; Backov, R. *Chem. Mater.* **2008**, *20*, 5541–5549.

(46) Leroy, M.; Achard, M.; Babot, O.; Steunou, N.; Masse, P.; Livage, J.; Binet, L.; Brun, N.; Backov, R. *Chem. Mater.* **2007**, *19*, 3988–3999.

(47) Brun, N.; Leroy, C. M.; Dexmer, J.; Serier, H.; Carn, F.; Biette, L.; Backov, R. *Comptes Rendus Chim.* **2010**, *13*, 154–166.

(48) Sugimoto, T.; Zhou, X.; Muramatsu, A. *J. Colloid Interface Sci.* **2003**, *259*, 43–52.

(49) Sakurada, I. *Polyvinyl Alcohol Fibres*; International Fiber Science and Technology, Ed.; M. Dekker.; New York, 1985; p. vol. 6.

(50) Miaudet, P.; Derré, A.; Maugey, M.; Zakri, C.; Piccione, P. M.; Inoubli, R.; Poulin, P. *Science* **2007**, *318*, 1294–1296.

(51) *Natl. Bur. Stand. Monogr.* **1969**, *25*, 83.

(52) *Natl. Bur. Stand. Monogr.* **1969**, *25*, 82.

(53) Rouquerol, J.; Avnir, D.; Fairbridge, C. W.; Everett, D. H.; Haynes, J. H.; Pernicone, N.; Ramsay, J. D. F.; Sing, K. S. W.; Unger, K. K. *Pure Appl. Chem.* **1994**, *66*, 1739–1758.

(54) Weidner, V. R.; Hsia, J. J. *J. Opt. Soc. Am.* **1981**, *71*, 856–861.

(55) Henderson, M. A. *Surf. Sci. Rep.* **2011**, *66*, 185–297.

(56) Peral, J.; Ollis, D. F. *J. Catal.* **1992**, *136*, 554–565.

(57) Besov, A. S.; Vorontsov, A. V. *Catal. Commun.* **2008**, *9*, 2598–2600.

(58) Vincent, G.; Marquaire, P. M.; Zahraa, O. *J. Photochem. Photobiol. A Chem.* **2008**, *197*, 177–189.

(59) Avnir, D.; Jaroniec, M. *Langmuir* **1989**, *5*, 1431–1433.

(60) Prouzet, E.; Boissière, C.; Kim, S. S.; Pinnavaia, T. J. *Microporous Mesoporous Mater.* **2009**, *119*, 9–17.

Chapter 4

(1) Leroy, M.; Achard, M.; Babot, O.; Steunou, N.; Masse, P.; Livage, J.; Binet, L.; Brun, N.; Backov, R. *Chem. Mater.* **2007**, *19*, 3988–3999.

(2) Sakurada, I. *Polyvinyl Alcohol Fibres*; International Fiber Science and Technology, Ed.; M. Dekker.; New York, 1985; p. vol. 6.

(3) Mercader, C.; Denis-Lutard, V.; Jestin, S.; Maugey, M.; Derre, A.; Poulin, P. *J. Appl. Polym. Sci.* **2012**, *125*, 191–196.

(4) Zhang, J.; Chen, Z.; Wang, Z.; Zhang, W.; Ming, N. *Mater. Lett.* **2003**, *57*, 4466–4470.

(5) Kinadjian, N.; Le Bechec, M.; Pigot, T.; Dufour, F.; Durupthy, O.; Bentaleb, A.; Prouzet, E.; Lacombe, S.; Backov, R. *Eur. J. Inorg. Chem.* **2012**, 5350–5359.

(6) Rouquerol, J.; Avnir, D.; Fairbridge, C. W.; Everett, D. H.; Haynes, J. H.; Pernicone, N.; Ramsay, J. D. F.; Sing, K. S. W.; Unger, K. K. *Pure Appl. Chem.* **1994**, *66*, 1739–1758.

(7) Prouzet, E.; Boissiere, C.; Kim, S.; Pinnavaia, T. *Microporous Mesoporous Mater.* **2009**, *119*, 9–17.

(8) Mercader, C. "*Filage continu de fibres de nanotubes de carbone : de la solidification aux propriétés finales*", Thèse, Université de Bordeaux 1, 2010.

(9) Henderson, M. A. *Surf. Sci. Rep.* **2011**, *66*, 185–297.

Chapter 5

(1) Badaire, S.; Pichot, V.; Zakri, C.; Poulin, P.; Launois, P.; Vavro, J.; Guthy, C.; Chen, M.; Fischer, J. E. *J. Appl. Phys.* **2004**, *96*, 7509.

(2) Tran, H. D.; Li, D.; Kaner, R. B. *Adv. Mater.* **2009**, *21*, 1487–1499.

(3) Acik, M.; Baristiran, C.; Sonmez, G. *J. Mater. Sci.* **2006**, *41*, 4678–4683.

(4) Yang, X.; Li, L. *Synth. Met.* **2010**, *160*, 1365–1367.

(5) Yoon, H.; Jang, J. *Adv. Funct. Mater.* **2009**, *19*, 1567–1576.

(6) Zhang, X.; Manohar, S. K. *J. Am. Chem. Soc.* **2004**, *126*, 12714–12715.

(7) Tran, H. D.; Li, D.; Kaner, R. B. *Adv. Mater.* **2009**, *21*, 1487–1499.

(8) Martin, C. R. *Acc. Chem. Res.* **1995**, *28*, 61–68.

(9) Liu, Z.; Zhang, X.; Poyraz, S.; Surwade, S. P.; Manohar, S. K. *J. Am. Chem. Soc.* **2010**, *132*, 13158–13159.

(10) Mehdinia, A.; Aziz-Zanjani, M. O.; Ahmadifar, M.; Jabbari, A. *Biosens. Bioelectron.* **2013**, *39*, 88–93.

(11) Dubal, D. P.; Patil, S. V.; Jagadale, A. D.; Lokhande, C. D. *J. Alloys Compd.* **2011**, *509*, 8183–8188.

(12) Lee, D. U.; Pradhan, D.; Mouawia, R.; Oh, D. H.; Heinig, N. F.; Leung, K. T.; Prouzet, E. *Chem. Mater.* **2010**, *22*, 218–225.

(13) Yoon, H.; Jang, J. *Adv. Funct. Mater.* **2009**, *19*, 1567–1576.

(14) Mehdinia, A.; Aziz-Zanjani, M. O.; Ahmadifar, M.; Jabbari, A. *Biosens. Bioelectron.* **2013**, *39*, 88–93.

(15) Cosgrove, T.; Hughes, R.; Fermin, D.; Riley, J.; Eastman, J.; Eastoe, J.; Vincent, B.; van Duijneveldt, J.; Reynolds, P.; Kwamena, N.-O. A.; Reid, J. P.; Richardson, R.; Barlett, P.; Davis, S.; Briscoe, W. *Colloid Science: Principles, Methods and Appliactions*; Cosgrove, T., Ed.; Wiley.; University of Bristol, 2010.

(16) Israelachvili, J. N.; Mitchell, D. J.; Ninham, B. W. *J. Chem. Soc. Faraday Trans. II* **1976**, *72*, 1525–1568.

(17) Griffin, W. C. *J. Soc. Cosmet. Chem.* **1949**, *1*, 311–326.

(18) Davies, J. T. *Proc. 2nd Int. Cong. Surf. Act.* **1959**, *1 Butterwo*, 426–438.

(19) Israelachvili, J. *Colloids Surf. A* **1994**, *91*, 1–8.

(20) Winsor, P. A. *Trans. Faraday Soc.* **1948**, *44*, 376–398.

(21) Kresge, C. T.; Leonowicz, M. E.; Roth, W. J.; Vartuli, J. C.; Beck, J. S. *Nature* **1992**, *359*, 710–712.

(22) Beck, J. S.; Vartuli, J. C.; Roth, W. J.; Leonowicz, M. E.; Kresge, C. T.; Schmitt, K. D.; Chu, C. T.-W.; Olson, D. H.; Sheppard, E. W.; McCullen, S. B.; Higgins, J. B.; Schlenkert, J. L. *J. Am. Chem. Soc.* **1992**, *114*, 10834–10843.

(23) Attard, G. S.; Glyde, J. C.; Göltner, C. G. *Nature* **1995**, *378*, 366–368.

(24) Attard, G. S.; Corker, J. M.; Göltner, C. G.; Henke, S.; Templer, R. H. *Angew. Chemie Int. Ed. English* **1997**, *36*, 1315–1317.

(25) Attard, G. S.; Edgar, M.; Goltner, C. G. *Acta Mater.* **1998**, *46*, 751–758.

(26) Attard, G. S.; Coleman, N. R. B.; Elliott, J. M. In *Mesoporous Molecular Sieves*; Bonneviot, L.; Beland, F.; Danumah, C.; Giasson, S.; Kaliaguine, S., Eds.; Amsterdam, Lausanne, New York, Oxford, Shannon, Singapore, Tokyo, 1998; Vol. 117, pp. 89–94.

(27) Ramos, L.; Fabre, P. *Langmuir* **1997**, *13*, 682–686.

(28) Surendran, G.; Tokumoto, M. S.; Pena dos santos, E.; Remita, H.; Ramos, L.; Kooyman, P. J.; Santilli, C. V.; Bourgaux, C.; Dieudonne, P.; Prouzet, E. *Chem. Mater.* **2005**, *17*, 1505–1514.

(29) Skotheim, T.; Inganas, O.; Prejza, J.; Lundstrom, I. *Mol. Cryst. Liq. Cryst.* **1982**, *83*, 1361–1371.

(30) Intelmann, C. M.; Syritski, V.; Tsankov, D.; Hinrichs, K.; Rappich, J. *Electrochim. Acta* **2008**, *53*, 4046–4050.

(31) Lee, A. S.; Peteu, S. F.; Ly, J. V; Requicha, A. A. G.; Thompson, M. E.; Zhou, C. *Nanotechnology* **2008**, *19*, 165501.

(32) Lee, D. U.; Pradhan, D.; Mouawia, R.; Oh, D. H.; Heinig, N. F.; Leung, K. T.; Prouzet, E. *Chem. Mater.* **2010**, *22*, 218–225.

(33) Figueiredo Neto, A. M.; Salinas, S. *The Pysics of Lyotropic Liquid Crystals: Phase Transition and Structural properties*; Oxford University Press, Ed.; New York, 2005.

(34) Pena dos Santos, E.; Tokumoto, M. S.; Surendran, G.; Remita, H.; Bourgaux, C.; Dieudonné, P.; Prouzet, E.; Ramos, L. *Langmuir* **2005**, *21*, 4362–4369.

(35) Daniel, C.; Hamley, I. W.; Mingvanish, W.; Booth, C. *Macromolecules* **2000**, *33*, 2163–2170.

(36) Auvray, X.; Perche, T.; Anthore, R.; Petipas, C. *Langmuir* **1991**, 2385–2393.

General conclusion and perspectives

(1) Kinadjian, N.; Achard, M.-F.; Julián-lópez, B.; Maugey, M.; Poulin, P.; Prouzet, E.; Backov, R.; Julian-Lopez, B. *MRS Proc.* **2013**, *1512*, mrsf12–1512–ff04–33.

(2) Kinadjian, N.; Le Bechec, M.; Pigot, T.; Dufour, F.; Durupthy, O.; Bentaleb, A.; Prouzet, E.; Lacombe, S.; Backov, R. *Eur. J. Inorg. Chem.* **2012**, 5350–5359.

(3) Mercader, C.; Denis-Lutard, V.; Jestin, S.; Maugey, M.; Derre, A.; Poulin, P. *J. Appl. Polym. Sci.* **2012**, *125*, 191–196.

(4) Kinadjian, N.; Nallet, F.; Ly, I.; Bentaleb, A.; Backov, R.; Prouzet, E. *J. Colloid Interface Sci.* **2013**, *submitted.*